Ultra-cold atoms in shell and ring structures

Andrew Elbourn

A thesis presented for the degree of
Doctor of Philosophy

Department of Physics and Astronomy
University of Sussex
United Kingdom
June 2022

Declaration

I hereby declare that the results presented in this thesis are the product of my own independent research and that, to the best of my knowledge, all the relevant sources have been appropriately acknowledged. In addition, this thesis has not been and will not be submitted in whole or in part to another University for the award of any other degree.

Andrew Elbourn

Abstract

This thesis looks at the three-dimensional dynamics of wave packets within the context of atomic trapping. We study three-dimensional dynamics from a theoretical standpoint, a field of high interest due to the emergence of quantum atom-based technologies, including quantum atomic metrology. In particular, we look at the dynamics of freely expanding wave packets at the point of release from an atom trapping scheme consisting of different geometries. We derive a new methodology for generating analytic expressions for the free expansion of these wave functions that utilise the infinite summation of individually expanding and interacting Gaussian distributions. We can then demonstrate that the resulting expressions show high fidelity to results obtained through numerical simulation of the freely-expanding Gaussian and hollow shell wave packets, validating the methodology used. The advantages of these analytic expressions are three-fold. Firstly, the method does not rely on intermediary time steps allowing for a quick system evaluation. Secondly, having an analytic expression allows for a greater understanding of the system's behaviour. In particular, we can now analyse the system's interference fringes and more easily predict the impact various properties have on the overall system. Finally, the analytical model is not subject to the pitfalls of numerical simulation such as numerical drift, high dependence on the choice of time step and considerations such as cross-boundary and boundary interactions. In developing these expressions, we observe the emergence of interference fringes, particularly a region of high wave-function density that developed in the centre of the hollow shell and toroidal wave packets. Following on from this, we look at how an initial asymmetry in the starting parameters of the system affects the resulting free expansion. In particular, we look to simulate the effects of microgravity on the hollow shell and how tilting affects the toroidal wave packet.

Additionally, this thesis studies atom dynamics in the hollow shell. We use a Kapitza-style, driven inverted pendulum, technique to generate a stable region above the equatorial plane in a classical atomic-scaled system. We demonstrated that it

is possible to achieve a stable inverted position on an atomic scale, even when the system has a degree of elasticity. We demonstrate that the capture angle for such a system is quite broad and can even be just above the equatorial plane in some cases. We demonstrate that achieving a stable inverted position for a wide range of starting variables is possible. Additionally, we demonstrate that in-situ cooling of the system may be possible by linearly reducing the driving frequency of the system. This phenomenon is experimentally interesting since it may lead to a new technique for systemic cooling, allowing for prolonged lifetimes and a reduction in evaporation rate. We also demonstrate that it is possible to localise a pendulum through multi-directional driving, allowing for more refined control and manipulation of the system. After demonstrating the viability of an inverted pendulum on the scale of an atom trapping scheme, we then took steps to improve the model to reflect an atomic system better to see whether such a technique could be applicable in atomic trapping systems. In testing this idea, we found that when modulating an atomic quadrupole trap in the manner outlined for the mechanical system, the system did not readily result in a stable region in the inverted position. Instead, we found that throughout all the parameters tested, the trap operated in a linear regime when vertically driven, meaning that for these parameters, the Kapitza-style driving was insufficient to stabilise the north pole in this system. Instead, we were able to find an alternative approach utilising a time-averaged adiabatic potential at the north pole of the trapping potential, which led to stable systems and might be utilised instead of the vertical Kapitza-style driving.

Acknowledgments

I want to extend my gratitude to all those who have helped and supported me through my research and without whom I would not have been able to finish this thesis. Firstly I would like to thank my supervisor Barry Garraway who was always available to check ideas and point me in the right direction while allowing me the freedom to explore and test my ideas. I would also like to thank my second supervisor, German Sinuco-Leon, who provided helpful insight and guidance and gave me feedback on some of the posters I was preparing for conferences.

I want to thank Jean-Marc Martin and Gwyn Wilson. They provided helpful discussion and input to help me formulate my ideas and approach and provided a sounding board to verify whether I was talking nonsense or had an idea.

I would also like to thank the University of Sussex and the Quantum Technology Hub, who provided and funded my PhD without whom I would not have had the opportunity to research my thesis.

I want to thank my family for all that they have done to support me through this thesis. You helped create a relaxing and helpful environment for me during the final stages of writing my thesis. In addition, you were there to provide support and encouragement throughout the entire process.

Finally, I would like to thank all my friends who provided all the support and encouragement I needed throughout my thesis. Without your support and encouragement, this thesis would have been significantly harder to complete.

Contents

List of Figures

Chapter 1

Introduction

At the turn of the 20^{th} Century, a seismic shift in physics occurred due to the emergence of quantum mechanics. It was developed to explain phenomena that classical mechanics could not; its roots began towards the end of the previous century with the quantisation of light by Max Planck [1] while he was studying black body radiation. Albert Einstein later hypothesised that light consisted of individual particles [2], later dubbed photons, in order to explain the photoelectric effect where light liberates electrons from a material. Louis de Broglie [3] later proposed the theory that matter can behave as both a wave and a particle under certain circumstances. This concept was later built on by the work of Werner Heisenberg, Max Born, and Pascual Jordan with the development of matrix mechanics [4, 5, 6] and Erwin Schrödinger, who first developed wave mechanics and the well-known Schrödinger equation [7]. Werner Heisenberg went on to form the foundations of the uncertainty principle [8], which was later expanded upon by Earle Hesse Kennard [9], and Hermann Weyl (who attributed his result to Pauli) [10].

Since discovering quantum mechanics, there has been much interest in utilising quantum mechanisms within technology. As such, a large variety of different applications have been considered and developed. These technologies utilise a range of quantum phenomena to exceed the capabilities of purely classical systems. Possible applications include geosensing [11, 12, 13], the measurement of fundamental constants [14, 15, 16, 17], studying microgravity [18, 19, 20], inertial navigation

[21, 20, 22], quantum radar [23, 24] and medical and biological imaging [25, 26]. Many of these quantum technologies utilise atomic trapping schemes to isolate and control groups of atoms in order to interrogate them and learn about the various properties of the system. Many trapping schemes utilise a form of matter called a Bose-Einstein condensate. This Bose-Einstein condensate is a gas consisting of low-density bosons cooled to extremely low temperatures, close to absolute zero. The theory of Bose-Einstein condensates was based on a paper by Satyendra Nath Bose [27, 28] on quantum statistics that Albert Einstein used to predict the condensate's existence [29]. What is special about a Bose-Einstein condensate is that it consists of a large proportion of atoms that occupy the lowest quantum state. As a result, the Bose-Einstein condensate will exhibit some quantum properties, particularly wavefunction interference, which can be observed on a macroscopic scale. These Bose-Einstein condensates were first isolated by Eric Cornell and Carl Wiemann [30] using rubidium atoms in 1995, which was soon followed by Wolfgang Ketterle [31], who managed the same feat with sodium. These Bose-Einstein condensates (BECs) are now extensively used in quantum technology. In conjunction with the creation of Bose-Einstein condensates, the manipulation and trapping of these atoms have grown as a field of study, and the use of magnetic or laser fields to manipulate atoms and molecules has led to the awarding of several Nobel prizes [32]. In particular, laser cooling and trapping [33, 34, 35] has been utilised to trap billions of neutral atoms and molecules and then cool them to temperatures just above absolute zero so that quantum phenomena might be observed. Due to these techniques, the ultra-cooled atoms are isolated from their environment, which is vital to maintain since they would be lost immediately as they contact anything not in this state. Through evaporative cooling of the most energetic particles, a Bose-Einstein condensate may be observed in these trapping schemes.

The focus of this thesis has been to study the three-dimensional dynamics of wave packets within the context of atom trapping schemes. With the field of quantum technology and atomic trapping being an ever-broadening one, there are plenty of

applications for which a clear and detailed understanding of the inner dynamics is perhaps not fully explored. Therefore, we look to apply numerical and analytical techniques to understand better two particular systems: the free expansion of wave packets and an investigation into the feasibility of atomic trapping schemes utilising an inverted elastic pendulum technique.

The first of these, the free expansion of three-dimensional wave packets, is an area of interest since free expansion could be used to prove the presence of a Bose-Einstein condensate within the atomic trap prior to release since the Bose-Einstein condensate will form interference fringes. This expansion could be used as part of a validation process. However, for this to be experimentally viable, we need to understand how the wave packet expands. In particular, it is useful to know how the initial trapping geometry affects the rate of expansion, the time it takes for visible fringes to emerge and the expected emergent features. Additionally, the free expansion of these wave packets allows for the potential exploration of other inherent properties of the system, given that the resulting interference pattern is highly dependent on the system's initial conditions. Such a mechanism might be used to study microgravity through the use of a hollow shell potential. In this system, microgravity should warp the initial shape of the wave packet, which is then amplified in the generated interference fringes. Some work looking at the free-expansion of toroidal wave-packets has already been undertaken; of particular note, some papers have looked at the two-dimensional free-expansion of ring wave-packets, [36, 37, 38], although some of these results are dependent on limiting assumptions on the system. In addition to this, C. Ryu *et al.* [39] have done some numerical simulations on thin toroidal wave-packets in three dimensions. Although this is an area of interest, we are currently unaware of any analytical expressions to describe the free-expansion behaviour of these geometries in three dimensions. Additionally, we will explore some of the properties of these free-expanding wave packets, particularly the interference fringe behaviour and visibility, to better understand what to expect upon studying these systems experimentally.

Another area of interest is in applying the principles of the inverted pendulum to an atom-trapping scheme to stabilise atoms around the north pole of a trapping potential, a position which on its own is gravitationally unstable. The inverted pendulum, also known as the Kapitza or Stephenson pendulum depending on the source, is a well-known and established mechanical phenomenon. It consists of a rigid pendulum with an oscillating pivot point such that the inverted position is stable. First described by Andrew Stephenson in 1908 [40] the reasons for stability were not fully understood until 1951 when P. L. Kapitza provided analytical insight into the system [41, 42]. Landau and Lifshitz later published a paper equating the stability to the pendulum being in an effective potential due to the driving of the system [43]. The stability of this inverted pendulum system has been studied extensively over the years, with many papers investigating various aspects of this system [44, 45, 46]. A modified version of the system where we replace the fixed rod with spring has been studied in both two [47, 48] and three dimensions [49]. Thus far, the study of the inverted pendulum seems to have largely been in the context of mechanical systems. We want to apply the inverted pendulum principles to systems on the scale of atomic traps. In particular, we will consider a system on the scale of an atom trap [50] that takes the form of a magnetic quadrupole [51, 52, 53]. A magnetic quadrupole trap dresses atoms in a quadrupole field leading to the production of an adiabatic potential. Such a magnetic quadrupole confines atoms within a system with a degree of elasticity. As such, we shall consider the system to be in the form of an elastic pendulum for our initial model. Elastic pendulums also have a long history, with the first known study of the elastic pendulum appearing to have been made by A. Vitt and G. Gorelik in 1933 [54]. The elastic pendulum has subsequently been a system of research interest with many papers looking at the system, including the following sources [55, 56, 57].

In chapter 2 of this thesis, we will be looking at a methodology for generating analytical expressions for the free expansion of three-dimensional wave-packets typical of the ones that one would see as a wave packet is released from an atomic trap.

We employ a system of taking the integral over an infinite number of individual Gaussian wave-packets that individually interact with one another and themselves. During free expansion, a wave packet will undergo self-interactions leading to the emergence of interference fringes. If observed, these fringes can be used to prove the presence of a Bose-Einstein condensate in the original atomic trap, which helps to validate the results obtained. We mainly focus on the toroidal and hollow shell wave packets due to their quantum rotational and gravitational sensors applications. We show how to extract the interference patterns from these expressions and determine their visibility.

In chapter 3, we take our analytical expressions and compare our results to those that can be achieved through numerical simulations, comparing the fidelity of our results. Additionally, we appraise the impact of various initial conditions on the behaviour of these systems and look at how best to optimise experimental parameters to give the best chance of observing these phenomena. Finally, we take a look at how atomic Gross-Pitaevskii [58] interactions in the system impact the overall results. We narrow down under which conditions these may be considered negligible and how they change the observed results.

In chapter 4, we apply the methodology to various systems and geometries to further test the capabilities of this approach. We cover systems that form various geometries and those in a state of asymmetry. Additionally, we study an approximation of the methodology where instead of taking an integral of an infinite number of wave packets, we take a limited number of Gaussians and the accuracy one might expect to obtain.

In chapter 5, we turn our attention to this thesis's second area of study. In this chapter, we will be looking at the feasibility of utilising an inverted elastic pendulum mechanism on an atomic trapping scale. An inverted elastic pendulum utilises a vertical driving motion to maintain a stable inverted position. We take a classical system and scale it to the size of an atom trapping scheme. We then study the stability of such a system by defining a stability region and testing its robustness

when it comes to initial conditions.

In chapter 6, we look at variations in the system. In particular, we study a multi-directional driving of the system, which allows for fine location control over the pendulum allowing for a changing of the stable regions away from the inverted position to other similarly gravitationally unfavourable positions. We also look at a mechanism for reducing the driving frequency, which leads to in-situ cooling of the system. This mechanism could provide a way to reduce the system's total energy through an alternative to evaporative cooling, which is the approach most used presently but has downsides in the reduction of atoms within the system. We test this phenomenon and ascertain what factors impact it and how much energy loss one might expect through this mechanism.

In chapter 7, we then implement the Kapitza-style vertical driving of the system to an atomic quadrupole trap. This system does not appear to produce stable results with the same variables utilised in the mechanical atomic trapping scale system. We found that this resulted from the system occupying a "linear" regime over these parameters meaning that the atom was not stabilising at the north pole of the trapping potential. We subsequently explore an alternative approach, utilising a horizontal driving at the north pole, finding that this approach could produce stable systems where a Kapitza-style driving could not.

Chapter 2

Three-dimensional expansion of wave packets

2.1 Introduction

First demonstrated nearly thirty years ago [59, 60, 61], matter-wave interferometry provides the framework to make ever more sensitive and precise measurements, achieving significant improvements over classical, light-based methods. Principally, Bose-Einstein condensates (BECs) are used in matter-wave interferometry due to a large proportion of atoms in a BEC occupying the lowest quantum state. Therefore, a BEC will exhibit macroscopic quantum behaviour such as wave packet interference. There are many possible applications of matter-wave interferometry including geosensing [11, 12, 13], the measurement of fundamental constants [14, 15, 16, 17], studying microgravity [18, 19, 20] and inertial navigation [20, 21, 22]. In this thesis chapter, we will mainly use inertial navigation as our background; specifically, inertial navigation that utilises Sagnac effect interferometry [62]. Briefly, the Sagnac effect utilises two propagating wave packets injected into a ring-shaped waveguide. These wave packets propagate in opposite directions around the ring, completing several full cycles. Rotation of the system will induce a path difference between the two wave packets so that a phase shift can be measured when they recombine. From

this phase-shift, it is possible to calculate the angular velocity using the following formula [63]:

$$\Omega = \frac{\delta\phi\lambda v}{8\pi A}, \tag{2.1}$$

with Ω the angular velocity, $\delta\phi$ the phase shift, λ the wavelength of the wave packet used, v the wave speed and A the enclosed area. It must be noted that, for matter-waves, the measurement of the angular velocity does not depend on the velocity of the atoms since this will cancel with the wavelength.

One of the key components required to achieve Sagnac effect in matter-wave interferometry is a ring-shaped waveguide [64]. Due to how intrinsic these waveguides are there are a large number of groups working on their development [65, 66, 67, 68, 69, 70, 71, 72]. Two significant recent results are the successful manipulation of two spin-states [73], which would allow controlled independent propagation of two wave packets within the same guide, and the demonstration of a highly smooth wave-guide which exhibits almost excitationless acceleration [74].

Another geometry of great experimental interest is that of the hollow shell. It is believed that the hollow shell geometry lends itself well to studying micro-gravity [75]. Although not terrestrially viable under Earth-like gravitational conditions, these hollow shells could be used to measure and understand microgravity in orbit above the earth. The resulting free-expansion interference patterns of the hollow shells depend highly on the system's initial conditions, making them an ideal candidate for the study of microgravity. As such there is a current experiment [76] in situ at the NASA Cold Atom Laboratory (CAL) [77] aboard the International Space Station (ISS). Some work has been done on these hollow shells previously, looking at the expansion [78], critical temperature [79] and the breathing modes [80].

One area of interest with both geometries is the behaviour of the wave packets under free expansion. As stated above, with the hollow shell, the free expansion provides a framework by which microgravity may be studied. With toroidal wave packets, the observation of self-interference fringes experimentally proves the pres-

ence of a BEC within the system. Additionally, the free expansion of these wave packets allows for the potential exploration of other inherent properties of the system, given that the resulting interference pattern is highly dependent on the system's initial conditions. Some work looking at the free-expansion of toroidal wave packets has already been undertaken; of particular note, some papers have looked at the two-dimensional free-expansion of ring wave packets, [36, 37, 38]. However, some of these results depend on limiting system assumptions. In addition to this, C. Ryu *et al.* [39] have done some numerical simulations on thin toroidal wave packets in three dimensions. Additionally, L. A. Toikka [38] looked at the free expansion of the toroidal wave packet and was able to arrive at an approximate expression utilising a manipulation of the Wigner function to describe the two-dimensional expansion of such a system.

In this thesis chapter, we will derive expressions for the free-expanding toroidal and hollow shell wave packets, obtaining expressions for the location and visibility of the emergent interference fringes. The focus of the first part of this thesis is to derive and then verify, through comparison to other techniques, equations to describe the free expansion of both the toroidal and hollow shell wave packets. In this chapter, we will assume that the wave packets are formed of a dilute gas and thus a system with minimal atomic interactions.

2.2 The Free-Expansion of the Toroidal wave packet

We recognised a lack of an analytic expression to describe the free expansion of a toroidal wave packet, so we sought to derive our own. Furthermore, we hoped to describe the free expansion of a toroidal wave-function that did not utilise Fourier transforms of the function into momentum-space, such as in the Split-Step Fourier Method (SSFM) [81]. Instead, we approximate the wave packet by utilising the infinite summation of interacting Gaussians in real space. This approach is an

extension of a method pioneered by J. Janszky [82] who utilised a similar approach to Gaussian wave packets in phase space of a one-dimensional system. We build upon this idea by employing the concept within real three-dimensional space to generate our wave functions.

The basis of our methodology is constructing our wave packet geometry from an infinite number of interacting and expanding individual Gaussian wave packets and then integrating these through the geometry of the final wave function we wish to create. The steps we outline here results in a wave function for the three-dimensional wave packet. However, a similar approach could be used to produce a wave-function density instead, details of which can be found in appendix A of this thesis. The method detailed in this appendix is similar to the one outlined here but does not include phase details since we are dealing with a density function. This other method may be preferable depending on the system and if the shape of the wave packet is the primary concern. We will start by utilising the toroidal wave packet geometry, but this methodology may be applied to different systems and geometries. It must be noted that some of the integration steps may not always be possible depending on the geometry; however, a numerical integration, although not preferable, should still render valuable results with the advantage of avoiding an iterative process to understand the fate of the system.

Starting with our Gaussian wave packet, we know that this, while undergoing free expansion, has a natural time-dependent spreading function. First, we need to define a scaled time variable τ, scaled to the Gaussian wave packet's dispersion time. We define this scaled time variable, τ, as

$$\tau = \frac{t}{t_d}, \tag{2.2}$$

with t_d the dispersion time-scale and t the time in seconds. We define the dispersion time-scale as

$$t_d = \frac{2m\sigma_0^2}{\hbar}, \tag{2.3}$$

where m is the mass of the wave packet, σ_0 the initial width of the Gaussian at time $t = 0$ and $\hbar$ the familiar Planck constant, the mass we will typically be used for numerical work in this thesis is the mass of rubidium-87 since it is commonly used in atomic-trapping schemes due to its properties being conducive to the production of a Bose-Einstein condensate. We can now, utilising our scaled time variable, write a general expression for the natural spreading of a Gaussian wave packet in the following manner:

$$\sigma(\tau) = \sigma_0\sqrt{1+\tau^2}. \tag{2.4}$$

It is useful at this point to define a complex width with phase as such,

$$\tilde{\sigma}(\tau) = \sqrt{\sigma_0\sigma(\tau)}e^{i\theta_\tau/2}, \tag{2.5}$$

where θ_τ can be found from the scaled time τ using

$$\tan(\theta_\tau) = \tau. \tag{2.6}$$

If we start with a one-dimensional wave packet, located at the origin then this has the following form:

$$\psi_{GWP}(x,\tau) = \frac{\sqrt{\sigma_0}}{(2\pi)^{\frac{1}{4}}\tilde{\sigma}(\tau)}\exp\left(-\frac{x^2}{4\tilde{\sigma}(\tau)^2}\right) \tag{2.7}$$

Substituting equation (2.5) into equation (2.7) we can rewrite equation (2.7) as

$$\psi_{GWP}(x,\tau) = \frac{1}{(2\pi)^{\frac{1}{4}}\sqrt{\sigma(\tau)}}\exp\left(-\frac{i\theta_\tau}{2}\right)\exp\left(-\frac{x^2(e^{-i\theta_\tau/2})^2}{4\sigma_0\sigma(\tau)}\right). \tag{2.8}$$

In order to remove the nested exponential functions we will use equation (2.6) to convert our $\exp(-\theta_\tau/2)$ function. We can rewrite equation (2.6) in terms of expo-

nential function with

$$\tau = \frac{i\left(\exp\left(-2i\theta_\tau\right) - 1\right)}{\left(\exp\left(-2i\theta_\tau\right) + 1\right)}. \tag{2.9}$$

We rearrange this function for the exponential and take the square root which results in the following expression:

$$\exp(-i\theta_\tau/2)^2 = \frac{1 - i\tau}{\sqrt{1+\tau^2}}. \tag{2.10}$$

We can rewrite the square root utilising equation (2.4), therefore,

$$\exp(-i\theta_\tau/2)^2 = \frac{\sigma_0\left(1 - i\tau\right)}{\sigma(\tau)}. \tag{2.11}$$

By substituting equation (2.11) into equation (2.8) we obtain the expression

$$\psi_{GWP}(x,\tau) = \frac{1}{(2\pi)^{\frac{1}{4}}\sqrt{\sigma(\tau)}} \exp\left(-\frac{i\theta_\tau}{2}\right) \exp\left(-\frac{x^2(1-i\tau)}{4\sigma(\tau)^2}\right). \tag{2.12}$$

Equation (2.12) can be rewritten in the following manner:

$$\psi_{GWP}(x,\tau) = \frac{1}{(2\pi)^{\frac{1}{4}}\sqrt{\sigma(\tau)}} \exp\left(-\frac{x^2}{4\sigma(\tau)^2} + i\frac{x^2\tau}{4\sigma(\tau)^2} - \frac{i\theta_\tau}{2}\right). \tag{2.13}$$

Now that we have a one-dimensional equation we can formalise a two-dimensional function with

$$\psi_{2DGWP}(x,y,\tau) = \frac{\sigma_0}{\sqrt{2\pi}\tilde{\sigma}(\tau)^2} \exp\left[-\frac{(x-x_0)^2 + (y-y_0)^2}{4\tilde{\sigma}(\tau)^2}\right]. \tag{2.14}$$

Doing similar substitutions as we performed in the one-dimensional equation we can

rewrite it in the following manner:

$$\begin{aligned}\psi_{2DGWP}(x,y,\tau) =& \frac{1}{\sqrt{2\pi}\sigma(\tau)} \exp\left(-i\theta_\tau\right) \\ & \times \exp\left[-\frac{(x-x_0)^2+(y-y_0)^2}{4\sigma(\tau)^2}\right] \\ & \times \exp\left[i\tau\frac{(x-x_0)^2+(y-y_0)^2}{4\sigma(\tau)^2}\right].\end{aligned} \tag{2.15}$$

Now that we have the basis for our methodology, we apply it to the toroidal wave packet. We start with the two-dimensional expression but need to convert it to polar coordinates. We centre the 2D GWP at the coordinates $x_0 = R\cos(\theta')$, $y_0 = R\sin(\theta')$ and then integrate over the angle θ', where R is the large radius of the desired torus and θ' is the angular location of one of the chosen Gaussian distributions. We will start with the two-dimensional equation in the form of equation (2.14) and insert our wave packet locations x_0 and y_0. We then integrate this function over the angle θ', which is the same as taking the infinite summation of Gaussians around a ring. This integral is performed between $\theta' = 0$ and $\theta' = 2\pi$ meaning that we have the expression

$$\psi_{2DGWP} = \frac{\sigma_0}{\sqrt{2\pi}\tilde{\sigma}(\tau)^2}\int_0^{2\pi} \exp\left(-\frac{(x-R\cos(\theta'))^2+(y-R\sin(\theta'))^2}{4\tilde{\sigma}(\tau)^2}\right) d\theta'. \tag{2.16}$$

Due to symmetry we are able to convert $x \to r$ where r is the radial coordinate and $y \to 0$. Making these replacements and expanding our function we get the following un-normalised expression for the two-dimensional torus:

$$\tilde{\psi}_{\text{2dtorus}}(r,\tau) = \frac{\sigma_0}{\sqrt{2\pi}\tilde{\sigma}(\tau)^2}\int_0^{2\pi} \exp\left(-\frac{r^2-2rR\cos(\theta')+R^2}{4\tilde{\sigma}(\tau)^2}\right) d\theta'. \tag{2.17}$$

We now use the Bessel function I_0 integral identity

$$I_0(z) = \frac{1}{\pi}\int_0^{\pi} \exp(z\cos(\theta))\, d\theta \tag{2.18}$$

in order to integrate our expression. Utilising this expression we get a two-dimensional

wave-function for the torus in the following form:

$$\tilde{\psi}_{\text{2dtorus}}(r,\tau) = \frac{1}{N}\frac{\sqrt{2\pi}\sigma_0}{\tilde{\sigma}(\tau)^2}\exp\left(-\frac{r^2+R^2}{4\tilde{\sigma}(\tau)^2}\right) I_0\left(\frac{rR}{2\tilde{\sigma}(\tau)^2}\right), \tag{2.19}$$

where N is some normalisation factor. To find the normalisation factor N we must solve the expression,

$$\int_0^\infty |\psi_{\text{2dtorus}}(r,\tau)|^2\, 2\pi r\, dr = 1. \tag{2.20}$$

In doing so we obtain the expression

$$\psi_{\text{2dtorus}}(r,\tau) = \frac{1}{\sqrt{2\pi}\sigma(\tau)}\exp\left(-\frac{r^2+R^2}{4\tilde{\sigma}(\tau)^2}+\frac{R^2}{8\sigma_0^2}-i\theta_\tau\right)\frac{I_0\left(\frac{rR}{2\tilde{\sigma}(\tau)^2}\right)}{\sqrt{I_0\left(\frac{R^2}{4\sigma_0^2}\right)}} \tag{2.21}$$

for the normalised wave equation. To convert our two-dimensional model into a three-dimensional model we simply multiply the two-dimensional torus by the one-dimensional Gaussian wave packet, $\psi_{\text{3dtorus}}(r,z,\tau) = \psi_{\text{2dtorus}}(r,\tau)\psi_{\text{GWP}}(z)$ giving the following expression:

$$\begin{aligned}\psi_{\text{3dtorus}}(r,z,\tau) =& \frac{1}{\sqrt{2\pi}\sigma(\tau)}\exp\left(-\frac{r^2+R^2}{4\tilde{\sigma}(\tau)^2}+\frac{R^2}{8\sigma_0^2}-i\theta_\tau\right)\frac{I_0\left(\frac{rR}{2\tilde{\sigma}(\tau)^2}\right)}{\sqrt{I_0\left(\frac{R^2}{4\sigma_0^2}\right)}} \\ &\times \frac{1}{(2\pi)^{\frac{1}{4}}\sqrt{\sigma(\tau)}}\exp\left(-\frac{z^2}{4\tilde{\sigma}(\tau)^2}-\frac{i\theta_\tau}{2}\right).\end{aligned} \tag{2.22}$$

This expression may be simplified further to give

$$\begin{aligned}\psi_{\text{3dtorus}}(r,z,\tau) =& \frac{1}{(2\pi)^{\frac{3}{4}}\sigma(\tau)^{\frac{3}{2}}}\exp\left(-\frac{r^2+R^2+z^2}{4\tilde{\sigma}(\tau)^2}+\frac{R^2}{8\sigma_0^2}-\frac{3i\theta_\tau}{2}\right) \\ &\times \frac{I_0\left(\frac{rR}{2\tilde{\sigma}(\tau)^2}\right)}{\sqrt{I_0\left(\frac{R^2}{4\sigma_0^2}\right)}}.\end{aligned} \tag{2.23}$$

This equation appears to be in a similar form to that found by Toikka [38]; however, this approach utilises a truncated series expansion and an approximation of

the ground state in order to generate the final expression. We found that our expression at time $t = 0$ is a better approximation of the ground state than a Gaussian distribution placed at the torus radius. We found this by numerically simulating the ground state and then comparing our equation at $t = 0$ to the simulated ground state and the estimated ground state. This behaviour is partly because the ground state estimate does not consider the curvature of the ring.

2.3 Limits of the toroidal wave equation

Having found an equation for the free-expanding torus, we want to look at how the wave equation behaves in its limits. To study this behaviour we start by taking our wave function and rewriting it to replace all terms of $\tilde{\sigma}(\tau)$ giving

$$\begin{aligned}\psi_{\text{3dtorus}}(r,z,\tau) =& \frac{1}{(2\pi)^{\frac{3}{4}}\sigma(\tau)^{\frac{3}{2}}} \exp\left(-\frac{(r^2+R^2+z^2)(1-i\tau)}{4\sigma(\tau)^2} + \frac{R^2}{8\sigma_0^2} - \frac{3i\theta_\tau}{2}\right) \\ & \times \frac{I_0\left(\frac{rR(1-i\tau)}{2\sigma(\tau)^2}\right)}{\sqrt{I_0\left(\frac{R^2}{4\sigma_0^2}\right)}}.\end{aligned} \tag{2.24}$$

Having now obtained an expression for the three-dimensional free-expanding toroidal wave packet, we wish to understand how that wave packet behaves towards its limits. In particular, we want to know how the wave packet behaves at $r \to 0$ and as $r \to \infty$. Furthermore, we want to understand which parts of the equation dominate at each of these limits, which will help us better understand what is going on with the system. So we start with our equation (2.24) we ignore any terms which are not dependent on r. Additionally, we will ignore the normalisation constant since we want to study the behaviour of the system. By ignoring these terms, we are left with a simplified expression for the wave function with

$$\psi(r,z,\tau) \propto \exp\left(-\frac{r^2(1-i\tau)}{4\sigma(\tau)^2}\right) I_0\left(\frac{rR(1-i\tau)}{2\sigma(\tau)^2}\right). \tag{2.25}$$

As we can see, we have just an exponential function multiplied by the modified

Bessel function dependent on the variable r. We will start by looking at the small argument limit of both functions. For the Bessel function, the small argument limit can be written as

$$\lim_{x\to 0} I_0(x(A-iB)) = 1 + \frac{x^2}{4}(A-iB)^2 + \mathcal{O}(x^4). \tag{2.26}$$

Whereas for the exponential function we get the following expansion:

$$\lim_{x\to 0} \exp(-x^2(a-ib)) = 1 + x^2(-a+ib) + \mathcal{O}(x^4). \tag{2.27}$$

Substituting in our parameters for a, A, b and B we get the limits,

$$\lim_{r\to 0} I_0\left(\frac{rR(1-i\tau)}{2\sigma(\tau)^2}\right) = 1 + \frac{r^2R^2}{16\sigma(\tau)^4}(1-i\tau)^2 + \mathcal{O}(r^4), \tag{2.28}$$

and

$$\lim_{r\to 0} \exp\left(-\frac{r^2(1-i\tau)}{4\sigma(\tau)^2}\right) = 1 - \frac{r^2}{4\sigma(\tau)^2}(1-i\tau) + \mathcal{O}(r^4). \tag{2.29}$$

Multiplying these two functions together and only considering terms up to order r^2 the small argument limit for our wave equation becomes

$$\lim_{r\to 0} \psi(r,z,\tau) \propto 1 - \frac{r^2}{4\sigma(\tau)^2}(1-i\tau)\left(1 - \frac{R^2}{4\sigma(\tau)^2}(1-i\tau)\right) + \mathcal{O}(r^4). \tag{2.30}$$

In this small argument limit we can see that we have a parabola centred on the origin and that we have no other peaks in this limit. In this limit we now have an expression for the wave-function and may wish to find an expression for the wave-function density. The complex conjugate of the small argument limit may be written as

$$\lim_{r\to 0} \psi(r,z,\tau)^* \propto 1 - \frac{r^2}{4\sigma(\tau)^2}(1+i\tau)\left(1 - \frac{R^2}{4\sigma(\tau)^2}(1+i\tau)\right) + \mathcal{O}(r^4). \tag{2.31}$$

Therefore the wave-function density takes an equation of the form:

$$\lim_{r\to 0} |\psi(r,z,\tau)|^2 \propto= 1 - \frac{r^2}{2\sigma(\tau)^2}\left(1 - \frac{R^2}{4\sigma(\tau)^2}\left(1-\tau^2\right)\right) + \mathcal{O}(r^4). \tag{2.32}$$

We have an expression for the spreading of the wave-function in equation (2.4) which we can substitute into equation (2.32) so that the small argument limit may be written as

$$\lim_{r\to 0} |\psi(r,z,\tau)|^2 \propto 1 - \frac{2r^2}{4\sigma_0^2\left(1+\tau^2\right)}\left(1 - \frac{R^2}{4\sigma_0^2\left(1+\tau^2\right)}\left(1-\tau^2\right)\right) + \mathcal{O}(r^4). \tag{2.33}$$

To progress beyond this point, we need to consider relative values for σ_0 and R. In atomic systems a reasonable value for these parameters might be $\sigma_0 \approx 10^{-6}$ and $R \approx 10^{-5}$, therefore $R^2/4\sigma_0^2 > 1$. In fact, this statement is always true since if the width was greater than the radius; then the resulting system would not be in the form of a torus. Here we look at how the centre of the system evolves with time; in particular, we want to demonstrate analytically that initially and at early time values, the system will have a local minimum located at $r = 0$. This minimum transforms as time progresses to a local maximum which we call the central interference fringe. In the limit $\tau \to 0$, the ratio

$$\frac{1-\tau^2}{1+\tau^2} \to 1, \tag{2.34}$$

whereas, in the limit $\tau \to \infty$, the ratio

$$\frac{1-\tau^2}{1+\tau^2} \to -1. \tag{2.35}$$

These properties mean that the system will initially start as a parabola and will subsequently transition into an inverted parabola. This behaviour is in agreement with the emergence of a central fringe, as noted by C. Ryu *et al.* [39] in their analysis of a thin toroidal wave packet. This inversion is a characteristic of the exponential function dominating the system's behaviour. Therefore, near the ring's centre, the

system's dominant properties might be inferred from the exponential term. We can now turn our attention to the large argument limit of our expression. Again we look at our component functions, taking a limit of these as $r \to \infty$. We know the exponential will tend towards zero in this limit, which is expected. The Bessel function will then operate as a variation on this. In the limit $r \to \infty$, the Bessel function can be approximated as

$$\begin{aligned}\lim_{x\to\infty} I_0\left(x(A-iB)\right) = &\cos\left(\frac{\pi}{4}+x(B+iA)\right)\left(\frac{2}{\sqrt{-2\pi x(B+iA)}}\right)\\ &+\mathcal{O}\left(\frac{1}{x^{\frac{3}{2}}}\right).\end{aligned} \tag{2.36}$$

By substituting in our expressions for A and B we find that we have the limit to the Bessel function of

$$\begin{aligned}\lim_{r\to\infty} I_0\left(\frac{Rr}{2\sigma(\tau)^2}(1-i\tau)\right) = &\cos\left(\frac{\pi}{4}+\frac{rR}{2\sigma(\tau)^2}(\tau+i)\right)\left(\frac{2\sigma(\tau)}{\sqrt{-\pi Rr(\tau+i)}}\right)\\ &+\mathcal{O}\left(\frac{1}{x^{\frac{3}{2}}}\right).\end{aligned} \tag{2.37}$$

We can see from this that this part of the wave-function behaves like a cosine function which the exponential function will suppress as $r \to \infty$. Therefore, this indicates that the further away from the centre, the more the Bessel function properties will dictate the shape of the wave function with a suppressive exponential term. As time progresses, the width of the exponential term will increase, and, as a result, the magnitude of the wave function will increase over time for parts of the wave packet located away from the centre. This property is an expected result since the wave function will become decreasingly localised and spread out as time progresses.

2.4 Locations and visibility of the interference fringes for the toroidal wave packet

We now want to look at the interference fringes, categorising their location and relative visibility. We start yet again with equation (2.24). To find these properties we need to take the density of the wave equation since the density represents what an observer will see experimentally. The density function is found by multiplying the wave equation by its complex conjugate, $|\psi|^2 = \psi\psi^*$, for our toroidal wave equation this results in the expression

$$|\psi_{3\text{dtorus}}|^2 = \frac{1}{(2\pi)^{\frac{3}{2}}\sigma(\tau)^3}\exp\left(-\frac{(r^2+R^2+z^2)}{2\sigma(\tau)^2}+\frac{R^2}{4\sigma_0^2}\right)\frac{\left|I_0\left(\frac{rR(1-i\tau)}{2\sigma(\tau)^2}\right)\right|^2}{I_0\left(\frac{R^2}{4\sigma_0^2}\right)}. \quad (2.38)$$

From this, we need to isolate the oscillating properties of the function to isolate the location of the various peaks. We know from the simulation that we expect a peak in the centre at $r = 0$, but we do not have an expression for the other interference peak locations, so we need to find this. The only sinusoidal component is the complex Bessel function. We can approximate the Bessel function through the identity

$$|I_0(A+iB)|^2 = |I_0(A)|^2|I_0(iB)|^2 + |2\sum_{k=1}^{\infty} I_k(A)I_k(iB)|^2 \quad (2.39)$$

It can be stated that $|I_k(A)|^2 < |I_0(A)|^2$ [83], in the small argument limit $|I_0(A)|^2 \to 1$ and $|I_k(A)|^2 \to 0$ for $k \geq 1$. We are therefore able to approximate the Bessel function with a complex argument as

$$|I_0(A+iB)|^2 \approx |I_0(A)|^2|I_0(iB)|^2 \quad (2.40)$$

For our system we can substitute in

$$A = \frac{rR}{2\sigma(\tau)^2} \quad (2.41)$$

and

$$B = \frac{-rR\tau}{2\sigma(\tau)^2}. \tag{2.42}$$

This gives an overall approximation of the Bessel function of

$$\left| I_0\left(\frac{rR(1-i\tau)}{2\sigma(\tau)^2}\right)\right|^2 \approx \left| I_0\left(\frac{rR}{2\sigma(\tau)^2}\right)\right|^2 \left| I_0\left(\frac{-irR\tau}{2\sigma(\tau)^2}\right)\right|^2. \tag{2.43}$$

We can rewrite the modified Bessel function of the first order with imaginary arguments in the form of a Bessel function of the first kind (J_0) using $I_0(-ix) = J_0(x)$. In the large argument limit the Bessel function of the first kind can be written as

$$J_0(x) = \sqrt{\frac{2}{\pi x}} \sin\left(x + \frac{\pi}{4}\right). \tag{2.44}$$

As per equation (2.43) this term is squared giving a characteristic oscillatory behaviour in the form of a sine squared function. This $\sin^2(x + \pi/4)$ function has local maxima at $x = \pi n - 3\pi/4$ and a local minima at $x = \pi n - \pi/4$ with n being a positive integer and represents the number of the fringe with the fringe closest to the centre taking the number one, the next furthest out two and so on. We can obtain the locations of these local maxima and local minima by rearranging them for r. By equating the local maxima to the argument of the sine function in equation (2.44) we find that

$$\frac{\tau R r_{\max}}{2\sigma(\tau)^2} = \pi n - \frac{3\pi}{4}, \text{ for } n \geq 1. \tag{2.45}$$

Through rearranging terms we find that the radial location of the local maxima is therefore located at

$$r_{\max} = \frac{2\pi\sigma(\tau)^2}{\tau R}\left(n - \frac{3}{4}\right), \text{ for } n \geq 1. \tag{2.46}$$

Similarly we can find a local minimum in a similar manner by equating the expression for the local minima with the argument of the sine function in equation (2.44)

$$\frac{\tau R r_{\min}}{2\sigma(\tau)^2} = \pi n - \frac{\pi}{4}, \text{ for } n \geq 1. \tag{2.47}$$

Through a rearrangement of terms we find that we have an expression for the location of the local minima for the system with

$$r_{\min} = \frac{2\pi\sigma(\tau)^2}{\tau R}\left(n - \frac{1}{4}\right), \text{ for } n \geq 1. \tag{2.48}$$

We now have all the local maxima and local minima of the $\sin^2$ function and, by extension, the Bessel proportion of the wave function; however, there is one more peak that is not accounted for using this approach. Due to the exponential term, there is another maximum located at $r = 0$. This peak effects the other peaks; specifically, the first local maxima becomes superseded by the maxima located at the origin. The first maxima from the Bessel function we disregard and replace with a peak located at the origin. Therefore, overall, we have the following locations for all of the local maxima and minima in the following manner:

$$r_{\max} = 0, \text{ for } n = 1, \tag{2.49}$$

$$r_{\max} = \frac{2\pi\sigma(\tau)^2}{\tau R}\left(n - \frac{3}{4}\right), \text{ for } n \geq 2 \tag{2.50}$$

and

$$r_{\min} = \frac{2\pi\sigma(\tau)^2}{\tau R}\left(n - \frac{1}{4}\right), \text{ for } n \geq 1. \tag{2.51}$$

These then are substituted into our wave-function in equation (2.24) to find the wave-function value at the local maxima and minima of the wave-function. The visibility of the local maxima can then be calculated by measuring the relative

difference between the local maxima and their adjacent minima. It must be noted that after the first peak, all maxima have two adjacent minima that do not have the same magnitude; therefore, to find the relative visibility, we need to consider both and take the bigger of the two local minima. We define the relative visibility of each maxima with respect to its adjacent minima as

$$\nu = \frac{|\psi_{\max}(r,z,\tau)|^2 - |\psi_{\min}(r,z,\tau)|^2}{|\psi_{\max}(r,z,\tau)|^2 + |\psi_{\min}(r,z,\tau)|^2}. \tag{2.52}$$

By substituting the locations of the local maxima and minima of the wave equation into the density function, we obtain the following expressions for the density at these locations:

$$\begin{aligned}\psi_{\max}(0,z,\tau) =& \frac{1}{(2\pi)^{\frac{3}{4}}\sigma(\tau)^{\frac{3}{2}}\sqrt{I_0\left(\frac{R^2}{4\sigma_0^2}\right)}} \\ &\times \exp\left(-\frac{(R^2+z^2)(1-i\tau)}{4\sigma(\tau)^2} + \frac{R^2}{8\sigma_0^2} - \frac{3i\theta_\tau}{2}\right), \text{ for } n=1\end{aligned} \tag{2.53}$$

$$\begin{aligned}\psi_{\text{3dtorus}}(r_{\max},z,\tau) =& \frac{1}{(2\pi)^{\frac{3}{4}}\sigma(\tau)^{\frac{3}{2}}} \frac{I_0\left(\frac{\pi}{\tau}\left(n-\frac{3}{4}\right)(1-i\tau)\right)}{\sqrt{I_0\left(\frac{R^2}{4\sigma_0^2}\right)}} \\ &\times \exp\left(-\frac{\left(\left(\frac{2\pi\sigma(\tau)^2}{\tau R}\left(n-\frac{3}{4}\right)\right)^2 + R^2 + z^2\right)(1-i\tau)}{4\sigma(\tau)^2}\right) \\ &\times \exp\left(\frac{R^2}{8\sigma_0^2} - \frac{3i\theta_\tau}{2}\right), \text{ for } n \geq 2\end{aligned} \tag{2.54}$$

$$\begin{aligned}\psi_{\text{3dtorus}}(r_{\min},z,\tau) =& \frac{1}{(2\pi)^{\frac{3}{4}}\sigma(\tau)^{\frac{3}{2}}}\frac{I_0\left(\frac{\pi}{\tau}\left(n-\frac{1}{4}\right)(1-i\tau)\right)}{\sqrt{I_0\left(\frac{R^2}{4\sigma_0^2}\right)}} \\ &\times\exp\left(-\frac{\left(\left(\frac{2\pi\sigma(\tau)^2}{\tau R}\left(n-\frac{1}{4}\right)\right)^2+R^2+z^2\right)(1-i\tau)}{4\sigma(\tau)^2}\right) \\ &\times\exp\left(\frac{R^2}{8\sigma_0^2}-\frac{3i\theta_\tau}{2}\right),\ \text{for } n\geq 1\end{aligned} \tag{2.55}$$

Since we are looking at the relative visibility of the interference fringes we ignore any common multiplier terms since these will cancel in the final result. In doing so we simplify the wave equations at these local maxima and minima so that

$$\tilde{\psi}_{\max}(0,z,\tau)=1,\ \text{for } n=1, \tag{2.56}$$

$$\begin{aligned}\tilde{\psi}_{\text{3dtorus}}(r_{\max},z,\tau) =& I_0\left(\frac{\pi}{\tau}\left(n-\frac{3}{4}\right)(1-i\tau)\right) \\ &\times\exp\left(-\frac{\left(\left(\frac{2\pi\sigma(\tau)^2}{\tau R}\left(n-\frac{3}{4}\right)\right)^2\right)(1-i\tau)}{4\sigma(\tau)^2}\right), \\ &\text{for } n\geq 2\end{aligned} \tag{2.57}$$

and

$$\begin{aligned}\tilde{\psi}_{\text{3dtorus}}(r_{\min},z,\tau) =& I_0\left(\frac{\pi}{\tau}\left(n-\frac{1}{4}\right)(1-i\tau)\right) \\ &\times\exp\left(-\frac{\left(\left(\frac{2\pi\sigma(\tau)^2}{\tau R}\left(n-\frac{1}{4}\right)\right)^2\right)(1-i\tau)}{4\sigma(\tau)^2}\right), \\ &\text{for } n\geq 1\end{aligned} \tag{2.58}$$

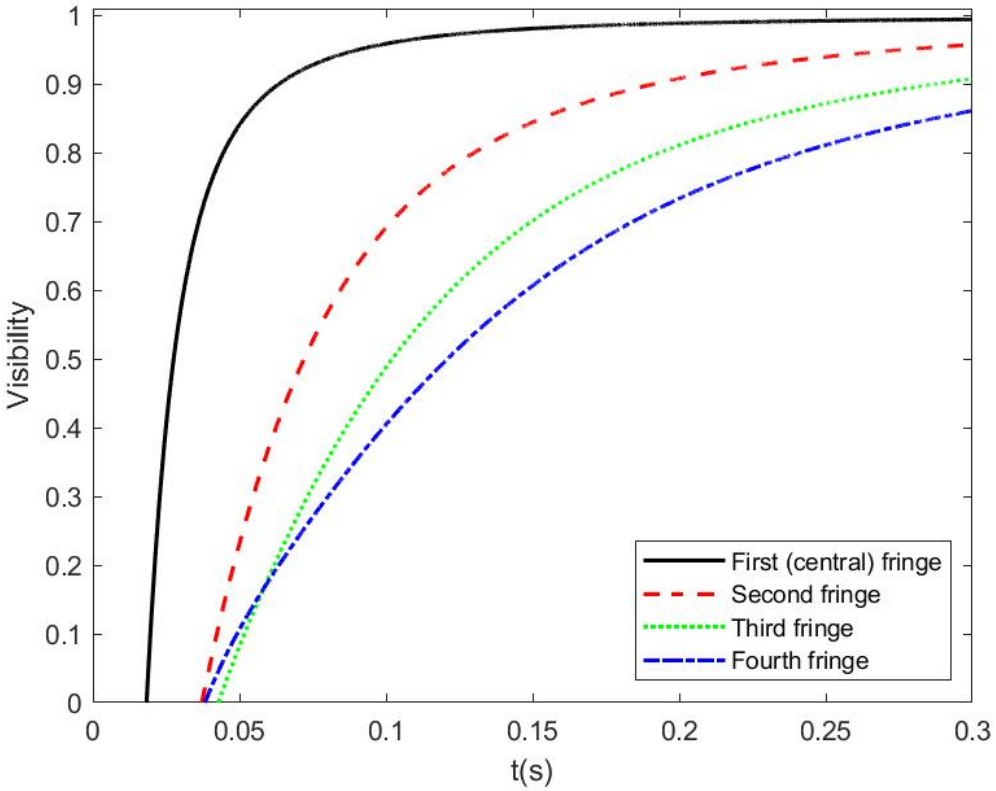

Figure 2.1: Visibility of the first four fringes against time graph for an initial torus with $R = 20$ μm and width $\sigma = 2$ μm. The visibility is initially zero at time $t = 0$ since the location of the local maxima, as defined by the sinusoidal component of the wave function, has a lower density than the location of the local minima but as the wave packet expands and the fringes develop the density at the local maxima will become greater than that of the local minima and the visibility of the fringe will start to increase as time progresses. This, therefore, shows the point at which the fringe emerges at the location specified.

In figure 2.1, we plot the time evolution of the peak visibility for the first four interference peaks. From figure 2.1, we can see that initially, all fringes have zero visibility, but as time progresses, the visibility increases, approaching an asymptotic limit. We can see clearly that the first, central, fringe has the highest visibility of just under 0.8, with all subsequent fringes having increasingly lower visibility. Experimentally it is clear that to observe the fringes best, it is necessary to wait for a short time, in this particular set-up, around 0.1 seconds, before imaging the system. This required waiting time decreases as the initial radius and the ratio between the initial and width decreases.

2.5 Overall behaviour of the free expanding toroidal wave packet

In the previous sections of this chapter, we have focused on specific properties of the wave equation; we now want to look at the overall behaviour of the system. In figure 2.2 and figure 2.3 we present some of the resultant graphs using our equation. Whenever results are presented in this thesis chapter, we have used results consistent with rubidium-87 (Rb-87) due to its prevalent experimental use. We also looked at experimentally viable parameters on size and width wherever possible.

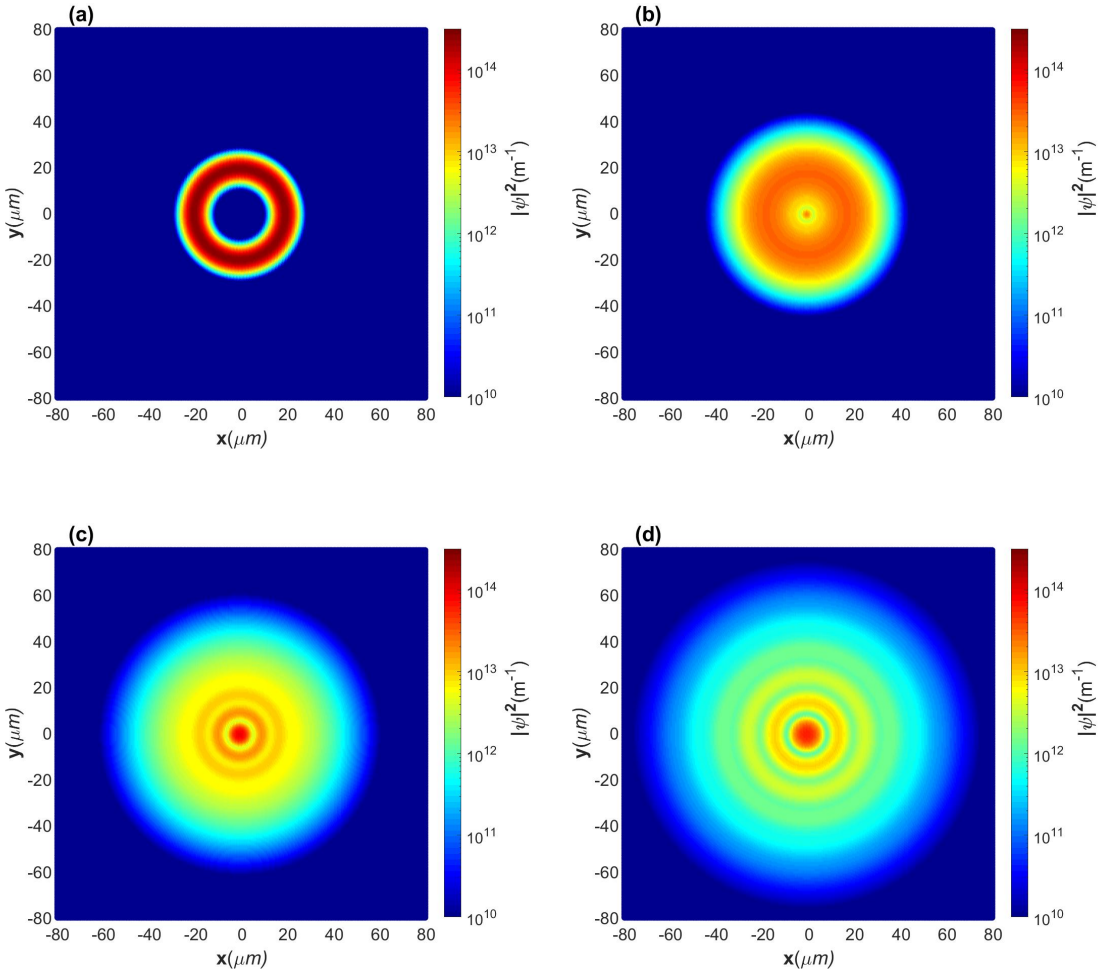

Figure 2.2: Cross-section of toroidal wave packet of radius $R = 20$ μm on the plane $z = 0$ and at times (a) $t = 0$ s, (b) $t = 0.033$ s, (c) $t = 0.067$ s and (d) $t = 0.1$ s. These results are for the free-expansion of rubidium-87 with an initial width of $\sigma = 2$ μm.

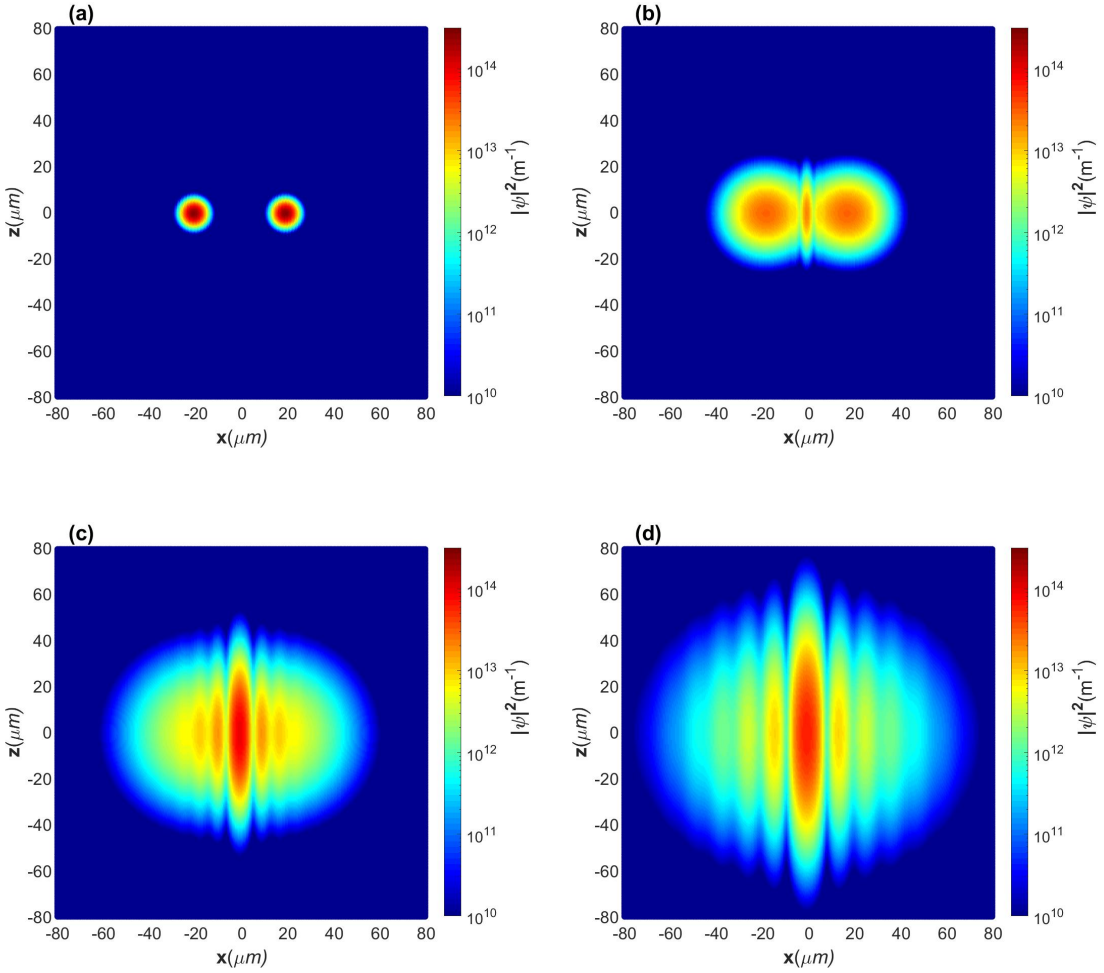

Figure 2.3: Cross-section of toroidal wave packet of radius $R = 20$ μm on the plane $y = 0$ and at times (a) $t = 0$ s, (b) $t = 0.033$ s, (c) $t = 0.067$ s and (d) $t = 0.1$ s. These results are for the free-expansion of rubidium-87 with an initial width of $\sigma = 2$ μm.

From the cross-sections in figure 2.2 and figure 2.3, it can be seen that, after some time, the free-expanding toroidal wave packet forms a central, high-density column. C. Ryu *et al.* [39] also noted the presence of a central column when looking at the expansion of thin tori. Our results demonstrate that this is not a unique property of thin discs but also occurs with thicker toroidal wave packets. This central peak results from interferences between parts of the wave packet at different sides of the torus. This central peak or fringe, now that we have demonstrated its presence, is something we want to study further in this section. The long-term behaviour of the toroidal wave-packet mirrors is that once the fringes have emerged they will remain

present, with the visibility of these fringes tending towards an asymptotic limit. As the wave-packet expands the peak density of the wave-packet will decrease as it spreads.

Having looked at the free expansion of a specific toroidal wave packet, we then varied the radii of our wave packets and looked to see the time at which the central column emerges. We define the emergence time as the time at which the wave-function density at the centre exceeds that at the initial radius, so that the inequality $|\psi_{\text{torus}}(r = R, z = 0, t)|^2 < |\psi_{\text{torus}}(r = 0, z = 0, t)|^2$ holds.

From figure 2.4(a), we see that as the radius of the torus increases, the time taken for the emergence of the central column also increases non-linearly. We also find a dependence on the ratio of the initial width (σ) and the wave packet's initial radius (R). In figure 2.4(b) we plot the ratio $\sigma : R$ against the time of emergence. We find that the time the central column emerges increases as the ratio $\sigma : R$ increases until it reaches a peak at approximately $\sigma = 0.33R$. This trend seems to be independent of the initial radius. Upon reaching the peak, there is a fall in the time taken for the central column to emerge. This property is consistent with the fact that the central hole in the toroidal wave packet will begin to close for larger widths. In theory, it would be best to design an experiment so that either the width of the torus is very narrow or very broad to see the interferences as early as possible; however, both of these approaches come with their own challenges. In particular, if the width of the initial torus is increased too much, then the torus ceases to be a torus, with the centre hole filling in. As a result, if the initial state is too broad, the shape can best be described as a biconcave disc instead of the desired torus. If, however, one wishes to generate a torus with a very narrow initial width, then generating such a potential to trap the atoms begins to get challenging, and there is a limit to how narrow it is possible to generate trapping potentials for such an experiment. From figure 2.4(a), we note that to observe the emergence of a central column experimentally, where a typical drop time of approximately 20 ms is what might be typically expected on a benchtop experiment, an initial radius of

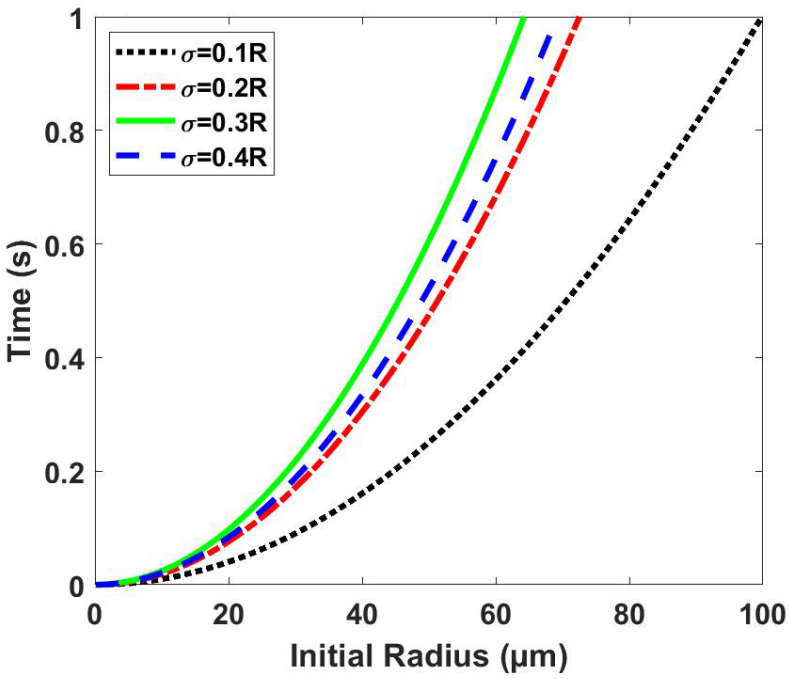

(a)

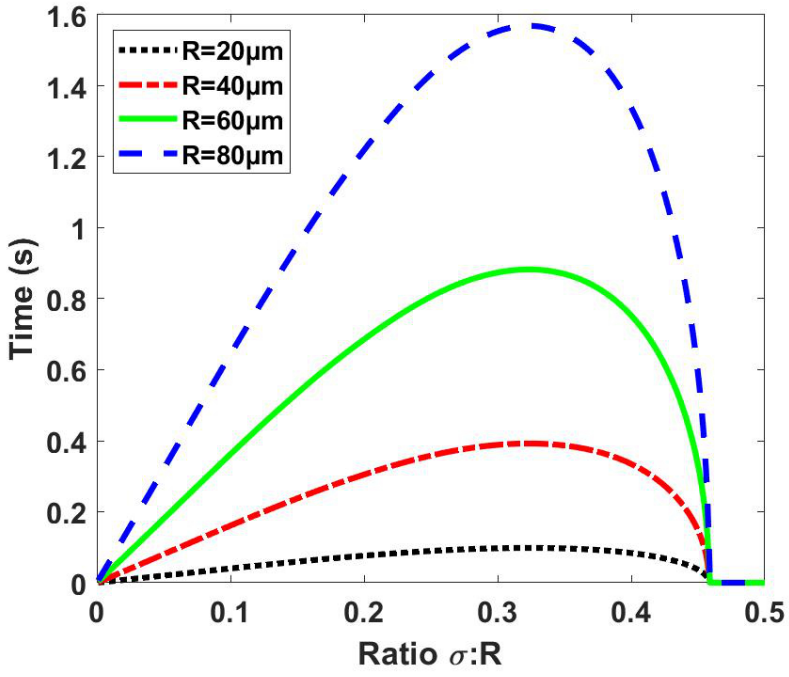

(b)

Figure 2.4: Graphs showing the time at which the central peak emerges for Rb87. (a) is generated with a fixed ratio of width σ to radius R. (b) is generated for a fixed radius with a varying width to radius ratio.

approximately 10 μm would be required. By reducing the initial width of the wave packet, it would be possible to observe this phenomenon for slightly larger initial

radii. However, this drop time might be extended beyond the 20 ms through the use of a drop tower such as the ZARM drop tower at the University of Bremen [84] and the Einstein-Elevator at the Leibniz Universität, Hannover [85]. Additionally, longer drop times might be achieved through parabolic flight such as the experiments being performed by Bouyer *et al.* [86].

2.6 Variations on the symmetrical toroidal wave packet

Having looked at the symmetrical torus, we now turn our attention to some slight variations in the initial state. Firstly we will look at an initial system whose radial width is different from the width in the z-axis. Therefore, this difference in the z-axis width allows the study of flat tori like those considered by C. Ryu *et al.* [39] or for a tall torus, which would more resemble a hollow tube. When sliced vertically, this consideration would result in a torus-like geometry with an elliptical cross-section. In this approach, we shall define two widths and two expansion rates by extension. The first, which we shall label as σ_{xy}, is the initial width of the wave packet in x and y and σ_z is the width in z. Later in this chapter, we will discuss what happens if the system is such that the width is not the same in all directions. As a starting point, we will be utilising our equation for the two-dimensional ring and multiplying it with a Gaussian wave packet in the z plane with different widths and rates of expansion in that direction. From equation (2.21) and equation (2.12) we have the following expression for the two dimensional torus:

$$\psi_{\text{2dtorus}}(r,\tau) = \frac{1}{\sqrt{2\pi}\sigma_{xy}(\tau)} \exp\left(-\frac{r^2+R^2}{4\tilde{\sigma}_{xy}(\tau)^2} + \frac{R^2}{8\sigma_0^2} - i\theta_\tau\right) \frac{I_0\left(\frac{rR}{2\tilde{\sigma}_{xy}(\tau)^2}\right)}{\sqrt{I_0\left(\frac{R^2}{4\sigma_{xy}^2}\right)}}, \quad (2.59)$$

with

$$\sigma_{xy}(\tau) = \sigma_{xy}\sqrt{1+\tau^2} \quad (2.60)$$

and

$$\tilde{\sigma}_{xy}(\tau) = \sigma_{xy}\sqrt{1+i\tau}. \tag{2.61}$$

The Gaussian distribution in z can then be written as

$$\psi_{GWP}(z,\tau) = \frac{1}{(2\pi)^{\frac{1}{4}}\sqrt{\sigma_z(\tau)}} \exp\left(-\frac{i\theta_\tau}{2}\right) \exp\left(-\frac{z^2(1-i\tau)}{4\sigma_z(\tau)^2}\right). \tag{2.62}$$

As we did before in section 2.2 the final wave-function is simply equal to

$$\psi_{\text{3dtorus}} = \psi_{\text{2dtorus}}(r,\tau) \times \psi_{GWP}(z,\tau). \tag{2.63}$$

This gives a final wave-function in the following form:

$$\begin{aligned}\psi_{\text{3dtorus}} =& \frac{\exp\left(\frac{R^2}{8\sigma_0^2}\right)\exp\left(-\frac{3i\theta_\tau}{2}\right)}{(2\pi)^{\frac{3}{4}}\sigma_{xy}(\tau)\sqrt{\sigma_z(\tau)}} \exp\left(-\frac{(r^2+R^2)(1-i\tau)}{4\sigma_{xy}(\tau)^2} - \frac{z^2(1-i\tau)}{4\sigma_z(\tau)^2}\right) \\ &\times \frac{I_0\left(\frac{rR(1-i\tau)}{2\sigma_{xy}(\tau)^2}\right)}{\sqrt{I_0\left(\frac{R^2}{4\sigma_{xy}^2}\right)}}\end{aligned} \tag{2.64}$$

This process obtains an analytic function due to the wave-function's separability of the z-component. The resultant wave equation can be used to describe the free expansion of a torus which is almost flat in the z direction, like the system studied by C. Ryu *et al.* [39]. Alternatively, it can also be used to describe a tall torus that stretches into the z direction.

Repeating the same process, but this time with a decoupling of the widths in x and y, does not result in a function which can be analytically integrated so easily. We start with the Gaussian wave packet in x, y and z with

$$\psi_{GWP}(x,\tau) = \frac{1}{(2\pi)^{\frac{1}{4}}\sqrt{\sigma_x(\tau)}} \exp\left(-\frac{i\theta_\tau}{2}\right) \exp\left(-\frac{x^2(1-i\tau)}{4\sigma_x(\tau)^2}\right), \tag{2.65}$$

$$\psi_{GWP}(y,\tau) = \frac{1}{(2\pi)^{\frac{1}{4}}\sqrt{\sigma_y(\tau)}} \exp\left(-\frac{i\theta_\tau}{2}\right) \exp\left(-\frac{y^2(1-i\tau)}{4\sigma_y(\tau)^2}\right) \tag{2.66}$$

and

$$\psi_{GWP}(z,\tau) = \frac{1}{(2\pi)^{\frac{1}{4}}\sqrt{\sigma_z(\tau)}} \exp\left(-\frac{i\theta_\tau}{2}\right) \exp\left(-\frac{z^2(1-i\tau)}{4\sigma_z(\tau)^2}\right). \tag{2.67}$$

As before, we want theses Gaussians to be located on a torus therefore we need to perform a transformation of the x and y coordinate such that they are Gaussian distributions centred at x_0 and y_0 respectively. This relocation of the Gaussian gives the wave packets in x, y and z as

$$\psi_{GWP}(x,\tau) = \frac{1}{(2\pi)^{\frac{1}{4}}\sqrt{\sigma_x(\tau)}} \exp\left(-\frac{i\theta_\tau}{2}\right) \exp\left(-\frac{(x-x_0)^2(1-i\tau)}{4\sigma_x(\tau)^2}\right), \tag{2.68}$$

$$\psi_{GWP}(y,\tau) = \frac{1}{(2\pi)^{\frac{1}{4}}\sqrt{\sigma_y(\tau)}} \exp\left(-\frac{i\theta_\tau}{2}\right) \exp\left(-\frac{(y-y_0)^2(1-i\tau)}{4\sigma_y(\tau)^2}\right) \tag{2.69}$$

and

$$\psi_{GWP}(z,\tau) = \frac{1}{(2\pi)^{\frac{1}{4}}\sqrt{\sigma_z(\tau)}} \exp\left(-\frac{i\theta_\tau}{2}\right) \exp\left(-\frac{z^2(1-i\tau)}{4\sigma_z(\tau)^2}\right) \tag{2.70}$$

respectively. Taking the product of these three functions gives us a three-dimensional Gaussian centred at $x = x_0$, $y = y_0$ and $z = 0$ with different widths in x, y and z. The resulting combined three dimensional expression is therefore,

$$\begin{aligned}\psi_{3dGWP}(x,y,z,\tau) =& \frac{1}{(2\pi)^{\frac{3}{4}}\sqrt{\sigma_x(\tau)\sigma_y(\tau)\sigma_z(\tau)}} \exp\left(-\frac{3i\theta_\tau}{2}\right) \\ &\times \exp\left(-\frac{(x-x_0)^2}{4\sigma_x(\tau)^2} - \frac{(y-y_0)^2}{4\sigma_y(\tau)^2} - \frac{z^2}{4\sigma_z(\tau)^2}\right) \\ &\times \exp\left(i\tau\left[\frac{(x-x_0)^2}{4\sigma_x(\tau)^2} + \frac{(y-y_0)^2}{4\sigma_y(\tau)^2} + \frac{z^2}{4\sigma_z(\tau)^2}\right]\right).\end{aligned} \tag{2.71}$$

We can now set the location of the Gaussian by making the substitutions

$$x_0 = R\cos(\theta') \tag{2.72}$$

and

$$y_0 = R\sin(\theta') \tag{2.73}$$

The resulting expression we integrate through the angle θ'. Since the system is asymmetric we are not able to use symmetry to simplify our expression as we did in equation (2.17). Therefore, without a clear simplification, we are left with an integral

$$\begin{aligned}\psi_{3dGWP}(x,y,z,\tau) =& \frac{1}{(2\pi)^{\frac{3}{4}}\sqrt{\sigma_x(\tau)\sigma_y(\tau)\sigma_z(\tau)}}\exp\left(-\frac{3i\theta_\tau}{2}\right)\\ &\times\int_0^{2\pi}\exp\left(-\frac{(x-R\cos(\theta'))^2}{4\sigma_x(\tau)^2}-\frac{(y-R\sin(\theta'))^2}{4\sigma_y(\tau)^2}\right)\\ &\times\exp\left(i\tau\left[\frac{(x-R\cos(\theta'))^2}{4\sigma_x(\tau)^2}+\frac{(y-R\sin(\theta'))^2}{4\sigma_y(\tau)^2}\right]\right)\\ &\times\exp\left(-\frac{z^2}{4\sigma_z(\tau)^2}\right)\exp\left(i\tau\frac{z^2}{4\sigma_z(\tau)^2}\right)d\theta'\end{aligned} \tag{2.74}$$

which does not appear to have an analytical solution or an identity that we can use to solve the integration. Numerical integration would be the likely course of action here. Although this would mean that we no longer have a purely analytic expression, it would still have advantages over numerical simulation methods. These benefits include the fact that it is a non-iterative approach, so errors associated with minor discrepancies compound with each iteration. A result can be found for one specific time value without finding all the intermediary values. We will be exploring other systems where integration may not always be possible in chapter 4 of this thesis.

2.7 The Free-Expansion of the Hollow Shell wave packet

The methodology to form the three-dimensional hollow shell follows from the one-dimensional Gaussian wave packet in equation (2.13). Although we detail the alternative approach in appendix B, we will include an alternative method that finds a wave-density function as we did with the toroidal wave packet. We start with a three-dimensional Gaussian wave packet located at $x = x_0$, $y = y_0$ and $z = z_0$. By shifting the location of the Gaussian wave packet then we can rewrite the expression as

$$\begin{aligned}\psi_{\text{3DGWP}}(x,y,z,\tau) =& \frac{\sigma_0^{\frac{3}{2}}}{(2\pi)^{\frac{3}{4}}\tilde{\sigma}(\tau)^3} \\ & \times \exp\left(-\frac{(x-x_0)^2+(y-y_0)^2+(z-z_0)^2}{4\tilde{\sigma}(\tau)^2}\right).\end{aligned} \tag{2.75}$$

This Gaussian we locate on the surface of a sphere with

$$x_0 = R\sin(\phi')\cos(\theta'), \tag{2.76}$$

$$y_0 = R\sin(\phi')\sin(\theta') \tag{2.77}$$

and

$$z_0 = R\cos(\phi'). \tag{2.78}$$

We will then integrate through the angles θ' and ϕ' to generate our hollow shell wave function. The resulting integral expression is in the form of the expression

$$\begin{aligned}\psi_{\text{hs}}(x,y,z,\tau) =& \frac{\sigma_0^{\frac{3}{2}}}{(2\pi)^{\frac{3}{4}}\tilde{\sigma}(\tau)^3}\frac{1}{N}\int_0^{2\pi} d\theta' \int_0^{\pi} \\ & \times \exp\left(-\frac{(x-R\sin(\phi')\cos(\theta'))^2+(y-R\sin(\phi')\sin(\theta'))^2}{4\tilde{\sigma}(\tau)^2}\right) \\ & \times \exp\left(-\frac{(z-R\cos(\phi'))^2}{4\tilde{\sigma}(\tau)^2}\right)\sin(\phi')\,d\phi',\end{aligned} \tag{2.79}$$

where N is a yet to be determined normalisation constant. Due to symmetry we can set $x = y = 0$ and $z = r$. This substitution gives the modified expression

$$\begin{aligned}\psi_{\text{hs}}(r,\theta',\phi',\tau) =& \frac{\sigma_0^{\frac{3}{2}}}{(2\pi)^{\frac{3}{4}}\tilde{\sigma}(\tau)^3}\frac{1}{N}\int_0^{2\pi} d\theta' \\ & \times \int_0^{\pi} \exp\left(-\frac{r^2+R^2\cos^2(\phi')-2Rr\cos(\phi')}{4\tilde{\sigma}(\tau)^2}\right) \\ & \times \exp\left(-\frac{r^2+R^2\cos^2(\phi')-2Rr\cos(\phi')}{4\tilde{\sigma}(\tau)^2}\right)\sin(\phi')\,d\phi'.\end{aligned} \tag{2.80}$$

This function may be expanded and simplified using the fact that $R^2 = R^2\sin^2(\phi')\cos^2(\theta') + R^2\sin^2(\phi')\sin^2(\theta') + R^2\cos^2(\phi')$. This gives us the final integral

$$\begin{aligned}\psi_{\text{hs}}(r,\theta',\phi',\tau) =& \frac{\sigma_0^{\frac{3}{2}}}{(2\pi)^{\frac{3}{4}}\tilde{\sigma}(\tau)^3}\frac{1}{N} \\ & \times \int_0^{2\pi} d\theta' \int_0^{\pi} \exp\left(-\frac{R^2+r^2-2Rr\cos(\phi')}{4\tilde{\sigma}(\tau)^2}\right)\sin(\phi')\,d\phi'.\end{aligned} \tag{2.81}$$

Integrating with respect to θ' gives us an extra 2π term since the function has no θ' dependency. This leaves the following integral function:

$$\psi_{\text{hs}}(r,\phi',\tau) = \frac{(2\pi)^{\frac{1}{4}}\sigma_0^{\frac{3}{2}}}{\tilde{\sigma}(\tau)^3}\frac{1}{N}\int_0^{\pi} \exp\left(-\frac{R^2+r^2-2Rr\cos(\phi')}{4\tilde{\sigma}(\tau)^2}\right)\sin(\phi')\,d\theta'. \tag{2.82}$$

To integrate this with respect to θ' we can use the identity

$$\int_0^{\pi} \exp(-A+B\cos(\phi'))\sin(\phi')d\phi = \frac{2}{B}\sinh(B)\exp(-A). \tag{2.83}$$

Utilising this identity with

$$A = \frac{R^2 + r^2}{4\tilde{\sigma}(\tau)^2} \tag{2.84}$$

and

$$B = \frac{Rr}{2\tilde{\sigma}(\tau)^2} \tag{2.85}$$

for our system gives us the final integrated expression

$$\psi_{\text{hs}}(r,\tau) = \frac{4(2\pi)^{\frac{1}{4}}\sigma_0^{\frac{3}{2}}}{Rr\tilde{\sigma}(\tau)}\frac{1}{N}\exp\left(-\frac{R^2+r^2}{4\tilde{\sigma}(\tau)^2}\right)\sinh\left(\frac{Rr}{2\tilde{\sigma}(\tau)^2}\right). \tag{2.86}$$

Utilising equation (2.5) and equation (2.10) we can remove the $\tilde{\sigma}$ term from our expression by substituting

$$\tilde{\sigma}(\tau)^2 = \frac{\sigma(\tau)^2}{1 - i\tau}. \tag{2.87}$$

The resulting expression for the free expanding hollow shell is therefore

$$\psi_{\text{hs}}(r,\tau) = \frac{4(2\pi)^{\frac{1}{4}}\sigma_0^{\frac{3}{2}}}{Rr\tilde{\sigma}(\tau)}\frac{1}{N}\exp\left(-\frac{(R^2+r^2)(1-i\tau)}{4\sigma(\tau)^2}\right)\sinh\left(\frac{Rr(1-i\tau)}{2\sigma(\tau)^2}\right). \tag{2.88}$$

To understand the behaviour of the system better we choose to rewrite the sinh function with a complex argument in terms of hyperbolic and trigonemtric functions. We achieve this by making the substitution

$$\sinh(A - iB) = \sinh(A)\cos(B) - i\cosh(A)\sin(B). \tag{2.89}$$

This substitution gives us the un-normalised wave equation

$$\begin{aligned}\psi_{\text{hs}}(r,\tau) =& \frac{4(2\pi)^{\frac{1}{4}}\sigma_0^{\frac{3}{2}}}{\tilde{\sigma}(\tau)rR}\frac{1}{N}\Bigg[\exp\left(-\frac{(r^2+R^2)(1-i\tau)}{4\sigma(\tau)^2}\right)\\ &\times\left(\sinh\left(\frac{rR}{2\sigma(\tau)^2}\right)\cos\left(\frac{rR\tau}{2\sigma(\tau)^2}\right)\right.\\ &\left.-i\cosh\left(\frac{rR}{2\sigma(\tau)^2}\right)\sin\left(\frac{rR\tau}{2\sigma(\tau)^2}\right)\right)\Bigg],\end{aligned} \tag{2.90}$$

with the normalisation factor N taking the form

$$N = \sqrt{\frac{32\pi^2\sigma_0^2}{R^2}\left(1-\exp(-\frac{R^2}{2\sigma_0^2})\right)}. \tag{2.91}$$

This gives us the following final equation for the wave-function:

$$\begin{aligned}\psi_{\text{hs}}(r,\tau) =& \frac{\exp\left(-\frac{i\theta_\tau}{2}\right)}{2^{\frac{1}{4}}\pi^{\frac{3}{4}}r\sqrt{\sigma(\tau)\left(1-\exp\left(-\frac{R^2}{2\sigma_0^2}\right)\right)}}\Bigg[\exp\left(-\frac{(r^2+R^2)(1-i\tau)}{4\sigma(\tau)^2}\right)\\ &\times\left(\sinh\left(\frac{rR}{2\sigma(\tau)^2}\right)\cos\left(\frac{rR\tau}{2\sigma(\tau)^2}\right)\right.\\ &\left.-i\cosh\left(\frac{rR}{2\sigma(\tau)^2}\right)\sin\left(\frac{rR\tau}{2\sigma(\tau)^2}\right)\right)\Bigg],\end{aligned} \tag{2.92}$$

given $\tilde{\sigma}(\tau) =$
$\sqrt{\sigma(\tau)\sigma_0}\exp(i\theta_\tau/2)$.

2.8 Limits of the hollow shell wave equation

We now again wish to understand the properties of the system both close to and far out from the origin. Taking our wave function in equation (2.92) we focus only on

those terms which are dependent on the radial location r such that

$$\begin{aligned}\psi_{\rm hs}(r,\tau) \propto & \frac{1}{r}\Bigg[\exp\left(-\frac{r^2(1-i\tau)}{4\sigma(\tau)^2}\right) \\ & \times\left(\sinh\left(\frac{rR}{2\sigma(\tau)^2}\right)\cos\left(\frac{rR\tau}{2\sigma(\tau)^2}\right)\right. \\ & \left.-i\cosh\left(\frac{rR}{2\sigma(\tau)^2}\right)\sin\left(\frac{rR\tau}{2\sigma(\tau)^2}\right)\right)\Bigg].\end{aligned} \tag{2.93}$$

In the small argument limit as $r \to 0$ the sine function tends towards 0 and the cosine function tends towards 1. This therefore means in the limit $r \to 0$

$$\lim_{r\to 0}\psi_{\rm hs}(r,\tau) \propto \frac{1}{r}\left[\exp\left(-\frac{r^2(1-i\tau)}{4\sigma(\tau)^2}\right)\left(\sinh\left(\frac{rR}{2\sigma(\tau)^2}\right)\right)\right]. \tag{2.94}$$

We can now separate out the various functions. In particular the hyperbolic sine function has the following series expansion in this limit:

$$\lim_{r\to 0}\sinh\left(\frac{rR}{2\sigma(\tau)^2}\right) = \frac{rR}{2\sigma(\tau)^2} + \mathcal{O}(r^3). \tag{2.95}$$

This will cancel with the $1/r$ term leading to the expression

$$\lim_{r\to 0}\psi_{\rm hs}(r,\tau) \propto \left[\exp\left(-\frac{r^2(1-i\tau)}{4\sigma(\tau)^2}\right)\frac{R}{2\sigma(\tau)^2}\right]. \tag{2.96}$$

Already we can see at the origin, like the toroidal wave packet, the exponential term will dominate the properties of the wave-function. The exponential function itself has a series expansion at $r = 0$, as seen in the toroidal wave packet, in the following form:

$$\lim_{x\to 0}\exp\left(-\frac{r^2(1-i\tau)}{4\sigma(\tau)^2}\right) = 1 - \frac{r^2}{4\sigma(\tau)^2}(1-i\tau) + \mathcal{O}(r^4). \tag{2.97}$$

Again, given the reappearance of the exponential function, initially, the system will take the form of a parabola which, as time progresses, will invert, leading to the emergence of the expected central interference fringe. Finally, in the large argument

limit, the $1/r$ portion of the function and the exponential portion will suppress the wave function further away from the origin. Therefore the characteristic behaviour of the wave function in this limit is dictated by the cosine and sine functions.

2.9 Locations and visibility of the interference fringes for the hollow shell wave packet

As before, we would like to know the location and relative visibility of the interference fringes. Therefore, we define a complex conjugate of the above wave function as follows:

$$\begin{aligned}\psi_{\text{hs}}(r,\tau)^* =& \frac{\exp\left(\frac{i\theta_\tau}{2}\right)}{2^{\frac{1}{4}}\pi^{\frac{3}{4}} r\sqrt{\sigma(\tau)\left(1-\exp\left(-\frac{R^2}{2\sigma_0^2}\right)\right)}}\Bigg[\exp\left(-\frac{(r^2+R^2)(1+i\tau)}{4\sigma(\tau)^2}\right) \\ &\times\left(\sinh\left(\frac{rR}{2\sigma(\tau)^2}\right)\cos\left(\frac{rR\tau}{2\sigma(\tau)^2}\right)\right. \\ &\left.+\, i\cosh\left(\frac{rR}{2\sigma(\tau)^2}\right)\sin\left(\frac{rR\tau}{2\sigma(\tau)^2}\right)\right)\Bigg].\end{aligned} \tag{2.98}$$

The density function given by, $|\psi|^2 = \psi\psi^*$, can now be found. We note that in order to do this we must use the fact $(\sinh(A)\cos(B) - i\cosh(A)\sin(B))(\sinh(A)\cos(B) + i\cosh(A)\sin(B)) = \frac{1}{2}(\cosh(2A) - \cos(2B))$. As a result we can rewrite the density function as

$$\begin{aligned}|\psi_{\text{hs}}(r,\tau)|^2 =& \frac{1}{(2\pi)^{\frac{3}{2}} r^2\sigma(\tau)\left(1-\exp\left(-\frac{R^2}{2\sigma_0^2}\right)\right)}\Bigg[\exp\left(-\frac{(r^2+R^2)}{2\sigma(\tau)^2}\right) \\ &\times\left(\cosh\left(\frac{rR}{\sigma(\tau)^2}\right)-\cos\left(\frac{rR\tau}{\sigma(\tau)^2}\right)\right)\Bigg].\end{aligned} \tag{2.99}$$

From this expression, we can extract the oscillatory cos term. As was the case with the toroidal wave packet, we note that a central fringe emerges at $r = 0$. This time the central fringe will supersede both the first local maxima and minima as dictated by the cosine portion of the expression. For a function $-\cos(x)$ it has local

maxima located at $x = 2\pi n + \pi$ and local minima at $x = 2\pi n$. From this, we can obtain an expression for the radial locations of these local maxima and minima by equating the argument of the cosine function with the local maxima and minima expressions for the cosine function. We can then rearrange these expressions for r to find these locations. In particular, the local maxima of the cosine function gives us the expression

$$2\pi n + \pi = \frac{r_{\max} R\tau}{\sigma(\tau)^2}, \text{ for } n \geq 2. \tag{2.100}$$

This expression can then be rearranged for r giving

$$r_{\max} = \frac{\pi\sigma(\tau)^2}{R\tau}(2n+1), \text{ for } n \geq 2. \tag{2.101}$$

Similarly, the local minima of the cosine function gives us

$$2\pi n = \frac{r_{\min} R\tau}{\sigma(\tau)^2}, \text{ for } n \geq 1, \tag{2.102}$$

which can be rearranged for r to give

$$r_{\min} = \frac{\pi\sigma(\tau)^2}{R\tau}(2n), \text{ for } n \geq 1. \tag{2.103}$$

Now that we have the locations for our local maxima and local minima, we can then substitute these back into our wave function to get the value of that function. We use the same form of equation (2.52) as before. We must note that in order to substitute in $r = 0$, we need to know the following limits:

$$\lim_{r\to 0} \frac{1}{r} \exp(-Ar^2) \sinh(Br) \cos(Cr) = B \tag{2.104}$$

and

$$\lim_{r\to 0} \frac{1}{r} \exp(-Ar^2) \cosh(Br) \sin(Cr) = C. \tag{2.105}$$

Therefore, the wave equation at the local maxima and minima can be written as

$$\begin{aligned}\psi_{\text{hs}}(r=0,\tau) =& \frac{\exp\left(-\frac{i\theta_\tau}{2}\right)}{2^{\frac{1}{4}}\pi^{\frac{3}{4}}\sqrt{\sigma(\tau)\left(1-\exp\left(-\frac{R^2}{2\sigma_0^2}\right)\right)}} \\ & \times\left[\exp\left(-\frac{(R^2)(1-i\tau)}{4\sigma(\tau)^2}\right)\left(\frac{R}{2\sigma(\tau)^2}-\frac{iR\tau}{2\sigma(\tau)^2}\right)\right], \\ & \text{for } n=1,\end{aligned} \tag{2.106}$$

$$\begin{aligned}\psi_{\text{hs}}(r_{\max},\tau) =& \frac{R\tau\exp\left(-\frac{i\theta_\tau}{2}\right)}{2^{\frac{1}{4}}\pi^{\frac{7}{4}}\sigma(\tau)^{\frac{3}{2}}(2n+1)\sqrt{\left(1-\exp\left(-\frac{R^2}{2\sigma_0^2}\right)\right)}} \\ & \times\left[\exp\left(-\frac{\left(\left(\frac{\pi\sigma(\tau)^2}{R\tau}(2n+1)\right)^2+R^2\right)(1-i\tau)}{4\sigma(\tau)^2}\right)\right. \\ & \times\left(\sinh\left(\frac{\pi(2n+1)}{2\tau}\right)\cos\left(\frac{\pi(2n+1)}{2}\right)\right. \\ & \left.\left.-i\cosh\left(\frac{\pi(2n+1)}{2\tau}\right)\sin\left(\frac{\pi(2n+1)}{2}\right)\right)\right], \\ & \text{for } n\geq 2\end{aligned} \tag{2.107}$$

and

$$\begin{aligned}\psi_{\text{hs}}(r_{\min},\tau) =& \frac{R\tau\exp\left(-\frac{i\theta_\tau}{2}\right)}{2^{\frac{5}{4}}\pi^{\frac{7}{4}}\sigma(\tau)^{\frac{3}{2}}n\sqrt{\left(1-\exp\left(-\frac{R^2}{2\sigma_0^2}\right)\right)}} \\ & \times\left[\exp\left(-\frac{\left(\left(\frac{2n\pi\sigma(\tau)^2}{R\tau}\right)^2+R^2\right)(1-i\tau)}{4\sigma(\tau)^2}\right)\right. \\ & \left.\times\left(\sinh\left(\frac{\pi n}{\tau}\right)\cos(\pi n)-i\cosh\left(\frac{\pi n}{\tau}\right)\sin(\pi n)\right)\right], \\ & \text{for } n\geq 1.\end{aligned} \tag{2.108}$$

Since we are looking at the relative visibility we are able to cancel any common

multipliers giving us the final expressions for the wave equations:

$$\tilde{\psi}_{\mathrm{hs}}(r=0,\tau)=\left(\frac{1}{2\sigma(\tau)}-\frac{i\tau}{2\sigma(\tau)}\right),\ \text{for } n=1, \tag{2.109}$$

$$\begin{aligned}\tilde{\psi}_{\mathrm{hs}}(r_{\max},\tau)=&\frac{\tau}{\pi\,(2n+1)}\Bigg[\exp\left(-\frac{\left(\left(\frac{\pi\sigma(\tau)^2}{R\tau}(2n+1)\right)^2\right)(1-i\tau)}{4\sigma(\tau)^2}\right)\\&\times\left(\sinh\left(\frac{\pi(2n+1)}{2\tau}\right)\cos\left(\frac{\pi(2n+1)}{2}\right)\right.\\&\left.-i\cosh\left(\frac{\pi(2n+1)}{2\tau}\right)\sin\left(\frac{\pi(2n+1)}{2}\right)\right)\Bigg],\\&\text{for } n\geq 2\end{aligned} \tag{2.110}$$

and

$$\begin{aligned}\tilde{\psi}_{\mathrm{hs}}(r_{\min},\tau)=&\frac{\tau}{2\pi n}\Bigg[\exp\left(-\frac{\left(\left(\frac{2n\pi\sigma(\tau)^2}{R\tau}\right)^2\right)(1-i\tau)}{4\sigma(\tau)^2}\right)\\&\times\left(\sinh\left(\frac{\pi n}{\tau}\right)\cos\left(\pi n\right)-i\cosh\left(\frac{\pi n}{\tau}\right)\sin\left(\pi n\right)\right)\Bigg],\\&\text{for } n\geq 1\end{aligned} \tag{2.111}$$

These terms can then be substituted into the visibility, ν, formula

$$\nu=\frac{\psi_{\max}(r,z,\tau)-\psi_{\min}(r,z,\tau)}{\psi_{\max}(r,z,\tau)+\psi_{\min}(r,z,\tau)}. \tag{2.112}$$

Giving us an expression for the relative visibility for each of the emergent interference fringes. We can use this expression to plot this property of the system in figure 2.5.

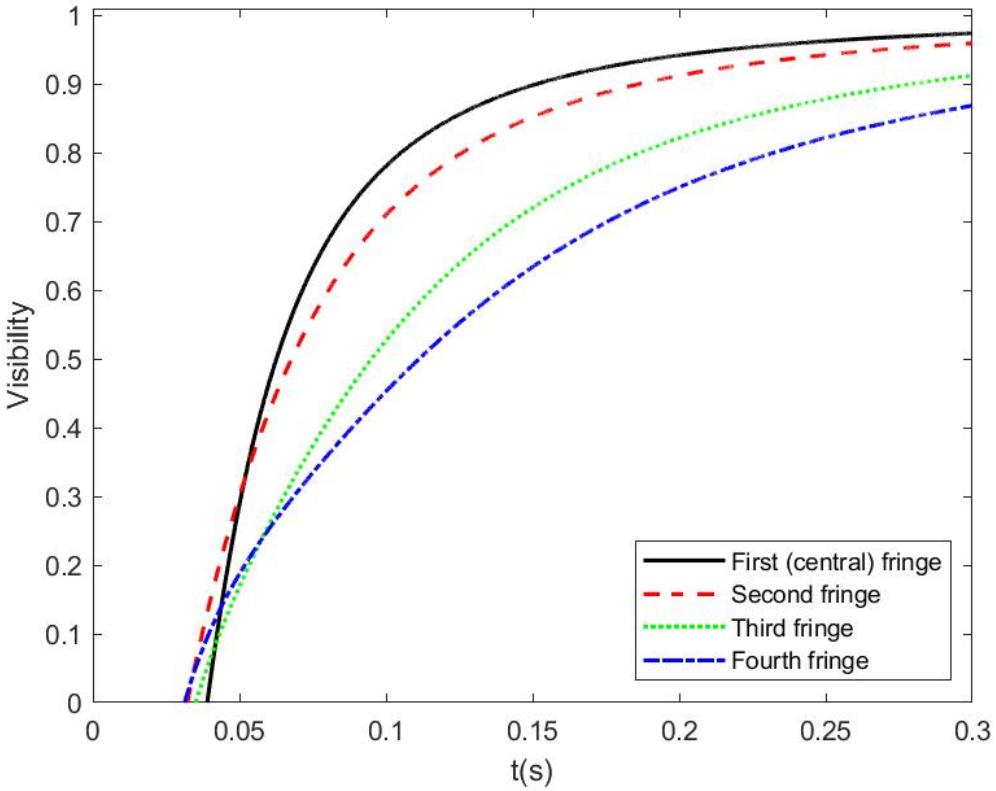

Figure 2.5: Visibility of the first four fringes against time graph for an initial hollow shell with $R = 20$ μm and width $\sigma = 2$ μm. The visibility is initially zero at time $t = 0$ since the location of the local maxima, as defined by the sinusoidal component of the wave function, has a lower density than the location of the local minima but as the wave packet expands and the fringes develop the density at the local maxima will become greater than that of the local minima and the visibility of the fringe will start to increase as time progresses. This, therefore, shows the point at which the fringe emerges at the location specified.

As in figure 2.1, we see in figure 2.5 that initially, the visibility of the fringes is zero and then increases asymptotically. This time we observe that the first fringe has greater visibility than in figure 2.1 whereas all subsequent fringes have lower visibility than in figure 2.1. This lower visibility means the geometry of the hollow shell wave packet suppresses subsequent interference fringes more than the toroidal geometry. As with the torus, experimentally, a waiting time of approximately 0.1 seconds is required to achieve the highest visibility. As the initial radius and the ratio between the initial radius and width decrease, this waiting time decreases.

2.10 Overall behaviour of the free expanding hollow shell wave packet

Having established an expression for the visibility of the fringes, we now turn our attention to results generated using our expression for the hollow shell. In figure 2.6 we plot our expression at various time values.

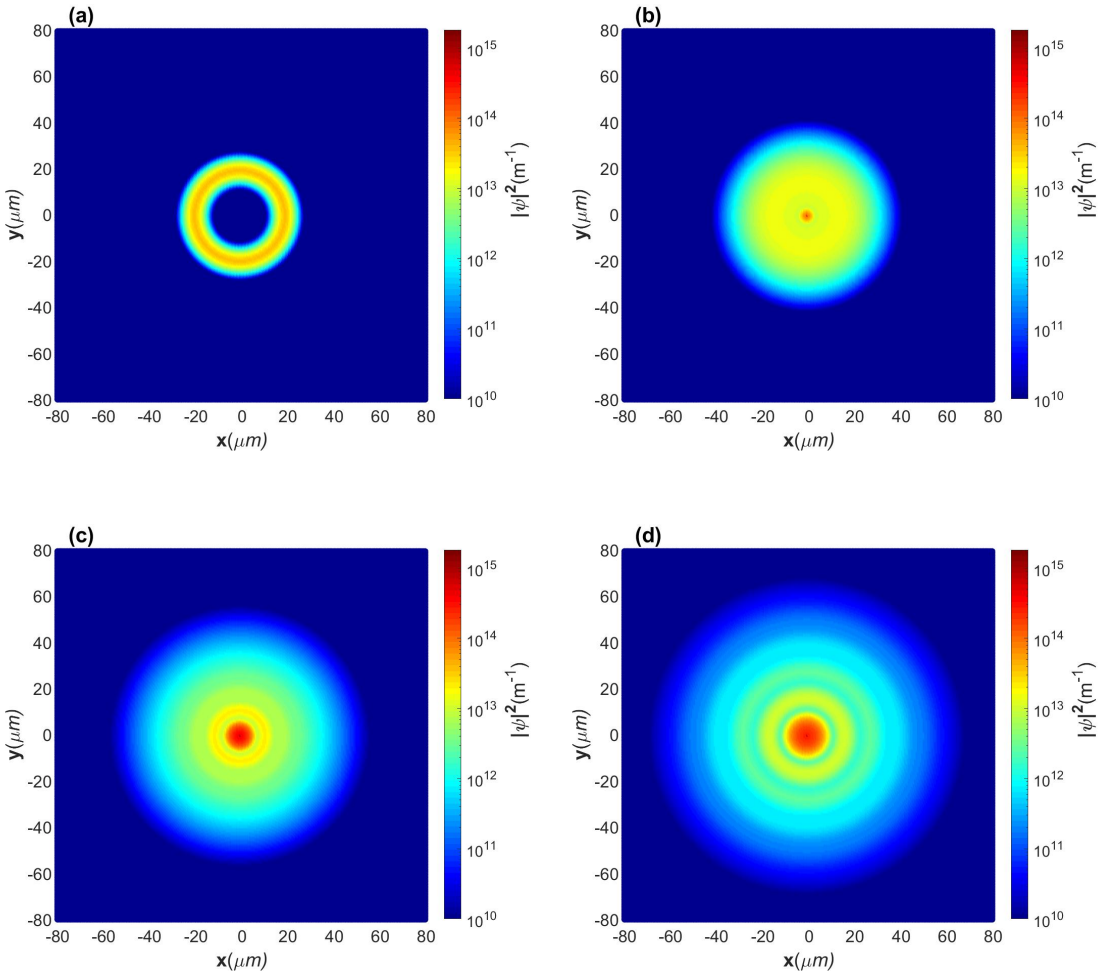

Figure 2.6: Cross-section of hollow shell wave packet of radius $R = 20$ μm on the plane $y = 0$ and at times (a) $t = 0$ s, (b) $t = 0.001$ s, (c) $t = 0.01$ s and (d) $t = 0.1$ s. These results are for the free-expansion of rubidium-87 with an initial width of $\sigma = 2$ μm.

As observed previously, the hollow shell will expand to form a high-density core with the free expansion of a toroidal wave packet. However, due to the spherical symmetry, this core will not extend out into a column like the toroidal case due to

the spherical symmetry of the hollow shell geometry. The long-term behaviour of the hollow shell wave-packet mirrors that of the toroidal in that once the fringes have emerged they will remain present, with the visibility of these fringes tending towards an asymptotic limit. As the wave-packet expands the peak density of the wave-packet will decrease as it spreads.

2.11 Conclusions

In conclusion, we have derived expressions for the free-expansion of both the toroidal (2.24) and hollow shell (2.92) wave packets in three dimensions. Additionally, we have derived expressions for the fringe visibility for both systems, demonstrating their asymptotic nature, allowing for a greater understanding of what might be expected experimentally. The visibility expressions might also help design experiments to look specifically at the free expansion of these geometries to obtain high visibility interference fringes.

Chapter 3

Numerical approach to the dynamics of tori and hollow shells

3.1 Introduction to Methodology

The Split-Step Fourier Method (SSFM) [81] is a well-established pseudo-spectral method used to solve non-linear differential equations. The method takes small time steps, treating the linear and non-linear terms separately. The linear steps are performed in momentum space, whereas the non-linear steps get performed in position space; therefore, it is necessary to utilise Fourier transforms to switch between the two. By repeated implementation of the algorithm, it is possible to simulate the evolution of a wave function in time for any given potential. The standard Split-Step Fourier Method takes the following form:

$$\Psi(r, t + \Delta t) = \mathcal{F}^{-1}\left[\exp\left(-\frac{i\Delta t k\hbar}{2m}\right)\mathcal{F}\left(\Psi(r,t)\exp\left(-\frac{i\Delta t V}{\hbar}\right)\right)\right]. \tag{3.1}$$

With $\mathcal{F}$ the Fourier transform, $\mathcal{F}^{-1}$ the inverse Fourier transform, $\Psi(r,t)$ the wave-function at time t, Δt the time step, k the momentum space coordinate, V the potential function and m the mass of a single atom. After each step of the algorithm we replace $\Psi(r,t)$ with the output $\Psi(r, t+\Delta t)$. For the free-expanding wave function simulation, we assume that the wave packet is not in a potential and, therefore,

$V = 0$. By making this substitution the equation (3.1) becomes

$$\Psi_{\text{free-expansion}}(r, t + \Delta t) = \mathcal{F}^{-1}\left[\exp\left(-\frac{i\Delta t k\hbar}{2m}\right)\mathcal{F}\left(\Psi(r,t)\right)\right]. \tag{3.2}$$

However, before we simulate the free expansion, we want to find the ground state of the wave function. We could use an approximation of the ground state, assuming that the wave function will form a Gaussian distribution with a width determined by the initial width of the atomic trap; however, we have found that at least with our spherically symmetric toroidal and hollow shell potentials, that this is not quite the best as the curvature affects the overall shape. Instead, we choose to find the ground state numerically and simulate the expansion from this numerically found ground state once this has been found. The method we employ to find the ground state is an imaginary time propagation [87] starting with a flat wave function that is uniform within our simulated region. We will be replacing our t in the Split-Step Fourier Method algorithm with $-it$. This imaginary time propagation causes a convergence on the ground state, which we can then use as the input for the numerically simulated expansion. Before substituting $-it$ for t, we note using a variation on the standard SSFM algorithm. Specifically, we will split the real space propagation portion into two, and Strang splitting [88] the momentum space portion. This is due to this approach being more accurate with Deiterding *et al.* [89] finding that this approach has an accuracy of order $\mathcal{O}\Delta t^2$ compared to $\mathcal{O}\Delta t$ for the more common approach. Since we aim to get as accurate results as possible without the simulation taking so long, we decide to use this approach to have more accurate results without decreasing the time step interval. We note that although we have utilised Strang splitting which would appear to add an extra exponential term it is possible to combine the final exponential of one iteration of the loop with the first exponential of the subsequent iteration to reduce the number of exponentials evaluated to two. Coupling this with the increased order of accuracy helps to contribute to a shorter run time for the simulations compared to the non-Strang splitting approach. The algorithm to find

the ground state is as follows:

$$\begin{aligned}\Psi(r,t+\Delta t) = &\exp\left(-\frac{\Delta t\left(V+g\left|\Psi(r,t)\right|^2\right)}{2\hbar}\right)\\ &\times\mathcal{F}^{-1}\left[\exp\left(-\frac{\Delta t k\hbar}{2m}\right)\right.\\ &\left.\times\mathcal{F}\left(\Psi(r,t)\exp\left(-\frac{\Delta t\left(V+g\left|\Psi(r,t)\right|^2\right)}{2\hbar}\right)\right)\right]\end{aligned} \tag{3.3}$$

We chose to stop the algorithm when the maximum difference between $\Psi(r,t)$ and $\Psi(r,t+\Delta t)$ was less than 10^{-3} which seemed to give us the ground state to a suitable degree of accuracy. Once we find the ground state, we can then numerically simulate the system and compare it to our analytic expression.

3.2 Simulating results

We must be careful when utilising a numerical methodology like this, as there are various pitfalls we need to avoid. Firstly, simulations of this nature tend to balance between ensuring high accuracy through smaller time steps and increasing the density of data points used and reasonable run times to generate enough results in a reasonable time. We used the University of Sussex's High-Performance Computing (HPC) cluster, which allowed for a higher number of data points and smaller time steps than might be reasonably utilised on a desktop computer. This access to the HPC cluster also allowed for multiple simulations to run concurrently. Another property we needed to be careful with was the size of the simulated box. Again, we need to be careful because the boundary of the simulated box is continuous and cross-boundary interactions can occur. Therefore, we need to ensure that the simulation box is large enough to make the cross-boundary interactions negligible, at least during the emergence of the interference fringes. We found that a box size four times the wave-packet initial diameter was sufficient to minimise cross-boundary interactions over the simulated interval. However, it must be noted that the longer the simulation continues beyond the emergence of the self-interference, the more sig-

nificant the impact that the cross-boundary interactions have. Equally important is to choose the correct point density while simulating our system, if the grid spacing is not small enough then a portion of the wave function may lie at the boundaries of momentum space causing aliasing to occur. We chose to use a $256 \times 256 \times 256$ grid since we found that this gave a sufficiently small spatial grid spacing to prevent aliasing from occurring over the course of our simulations. With our choice of box size, and point density we find that the size of the wave packet is significantly smaller in volume than the size of the momentum space simulated. Additionally, we did not observe the emergence of artifacts within our simulations which would indicate that the grid size selected was causing aliasing to occur. We now want to compare the results from our equations to those generated using SSFM. We will compare the density function from the density function generated through SSFM with our density function and measure the fidelity, which indicates how much two wave functions overlap. The formula we used to calculate the fidelity is [90]

$$F(\rho, \sigma) = \left| \iiint \sqrt{\psi_\rho^* \psi_\sigma} dx dy dz \right|^2 . \tag{3.4}$$

We plot this fidelity for various starting conditions in figure 3.1.

From figure 3.1(a) and figure 3.1(c), we see that we have an initial fidelity of slightly less than unity, which is universal across all the radii used. The reason for this is that there is a slight discrepancy in the initial conditions of both models. This discrepancy, as can be seen in figure 3.1(b) and figure 3.1(d), is dependent on the ratio between the initial width and the initial radius. The smaller this ratio is, the higher the initial fidelity measured. This trend indicates that the smaller the ratio is, the more accurate our expression is. Despite this property, our results still have relatively high fidelity for larger width/radius ratios. Across all radii used, we get an initial increase in fidelity, with the fidelity being within 10^{-4} of one. A total overlap of the two density functions indicates a total agreement in the limit where the fidelity is one. In figure 3.1(a), we observe that the point of maximum fidelity seems to correspond to the time at which the central column emerges in figure 2.4.

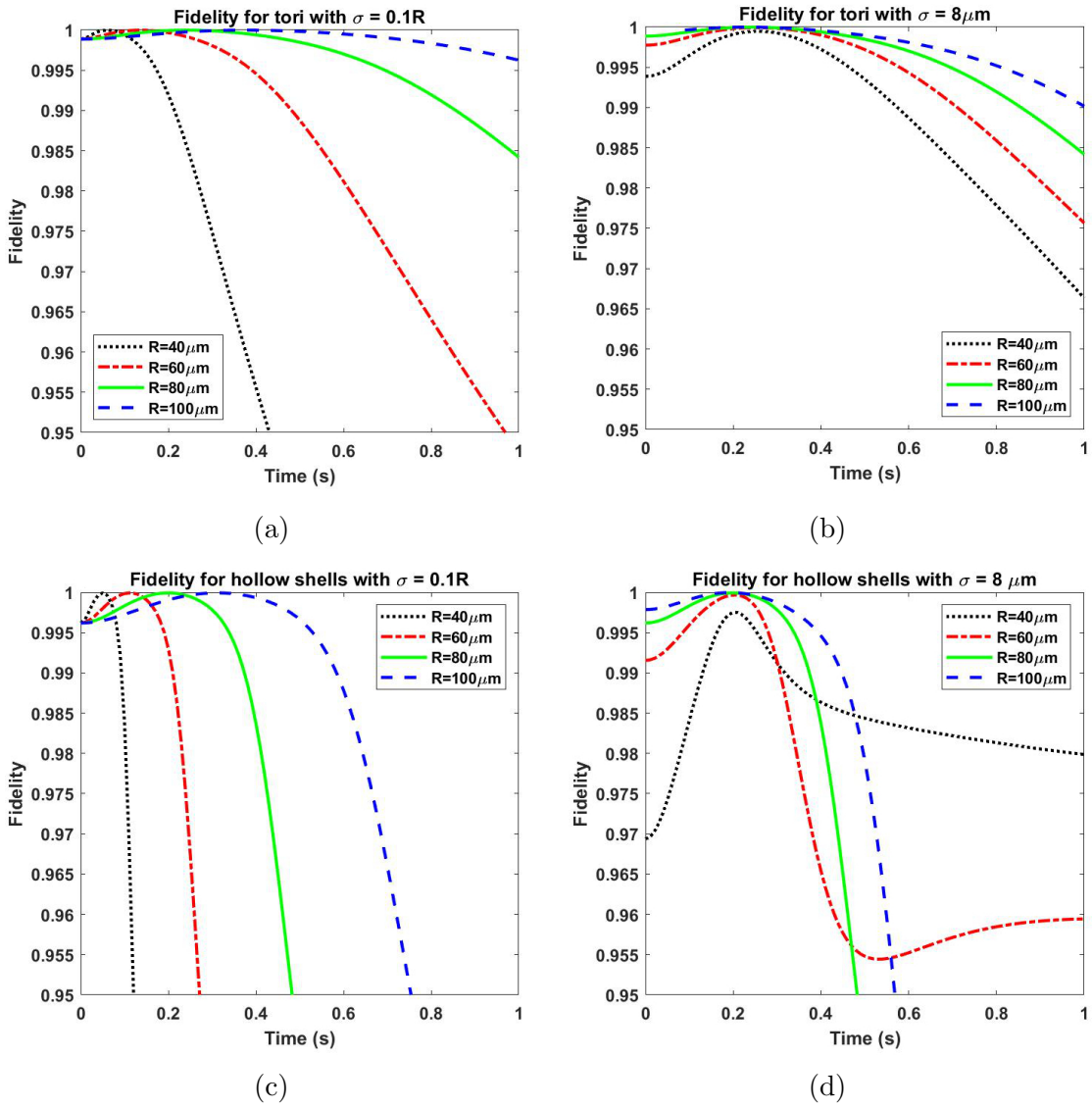

Figure 3.1: The time-evolution of the fidelity when comparing our equations, equation (2.24) and equation (2.92), with those generated by the SSFM. (a) and (b) compare our expression for a toroidal wave-packet with the results of the SSFM with (a) at a fixed ratio of $\sigma = 0.1R$ and (b) at a fixed width of $\sigma = 8$ μm. (c) and (d) compare our expression for a hollow shell wave-packet with the results of the SSFM with (c) at a fixed ratio of $\sigma = 0.1R$ and (d) at a fixed width of $\sigma = 8$ μm.

This occurrence means we can have almost total confidence in our results for the interference as we observe that our equations have a fidelity to the SSFM of one as the central feature emerges. Upon reaching this maximum value, we observe a drop-off in the fidelity. We largely attribute this drop in fidelity to one of the limitations of the SSFM, namely periodic boundary conditions.

Indeed, we find in our SSFM calculations that we get significant cross-boundary interactions occurring. These interactions increase in magnitude as time progresses.

The cross-boundary interactions are model, not experiment, specific, this is a significant problem with this approach, but there is no such problem with our equations. One approach to reducing this issue would be to use a larger simulation space; however, either the run time of the simulation must be sacrificed or the density of points simulated over. Another approach would be to use absorbing boundary conditions, eliminating cross-boundary interactions when using the SSFM. We found that when the central column emerges, the density of the wave-function at the boundaries approached 0.1% of the maximum density within the volume before rapidly increasing. In figure 3.1(a) and figure 3.1(c) we have a fixed ratio between the initial width and radius across all radii. Therefore, the trends observed can be considered the same but for a scaling factor. In figure 3.1(b) and figure 3.1(d) we fixed the width of the initial wave-packet and plotted the fidelity for various different radii. We observe that we still get similar trends with fixed σ/R ratios, as we still see an initial increase in fidelity as it approaches one before dropping off. In figure 2.4 we found that the rate of expansion was dependent on the ratio of the initial width to radius, in figure 3.1(b) and figure 3.1(d) we also find that the fidelity is dependent on this σ/R ratio. We notice that the fidelity drops sharply when comparing our hollow shell models to our toroidal ones. This property was expected, given the spherical symmetry of the hollow shell wave-packets, as more cross-boundary interactions will occur initially as more of the wave-packet will hit the boundary when placed in the same volume as the tori. Having plotted the time evolution of the fidelity, we now focus on the fidelity at the time of emergence for the central fringe. We plot this fidelity for various starting conditions in figure 3.2.

From figure 3.1, we observe that we have an overall very high fidelity when comparing our equations to SSFM simulations with fidelity over 0.9997 for both geometries when the initial radius is greater than 2.5 μm. With results this high, our method appears to provide an excellent approximation of the systems in question. We note from figure 3.1(a) and figure 3.1(b) that the fidelity is slightly higher for the hollow shell when comparing them to similar toroidal systems. However, we note

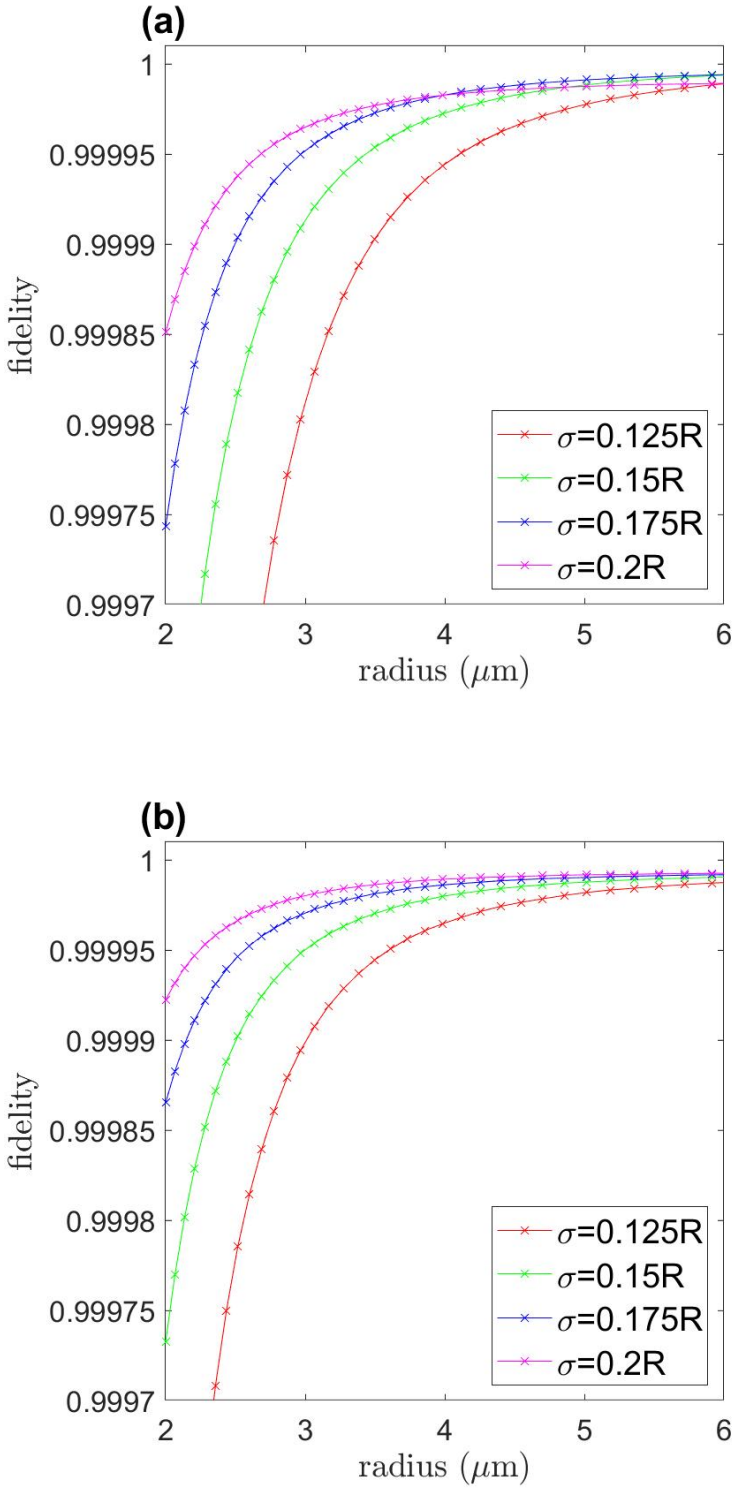

Figure 3.2: The fidelity of various simulations at the time of emergence for the central fringe. We compare our analytical expressions to numerical simulations. We then plot the initial radius against fidelity for wave-functions of various widths. In (a) we plot the fidelity for the toroidal wave packets and in (b) we plot it for hollow shells.

that the fidelity seems to reach an asymptotic limit as the initial radius increases in both geometries. We also note that the greater the initial width, the higher the fidelity. This property means that for all but very narrow and very small systems, our methodology produces results that are an excellent approximation for the free expansion of such systems.

Overall, our results demonstrate that our analytic expressions are in close agreement with the results obtained through the SSFM. Furthermore, the high fidelity indicates that our equations provide viable alternatives to SSFM for these specific wave packets. We also note that our equations have the advantage of not dealing with cross-boundary interactions, which would not occur experimentally. Another advantage of our approach is that we can separate it into expansion and interference terms, allowing for a greater understanding of how the system behaves and the effect changing specific initial parameters will have on it.

3.3 Gross-Pitaevskii interactions

One property present in a physical system that we have not yet explored is the interaction energy between individual atoms. In a Bose-Einstein condensate, the dynamics of the individual atoms will be dictated by three different energies, kinetic energy, the potential field and interaction energy. Our model and approach have neglected this interaction energy and have just considered non-interacting kinetic particles in a potential field. However, in an actual system, the atoms that form the Bose-Einstein condensate will be weakly interacting via atomic coupling. The Gross-Pitaevskii equation [58, 91] is one way that these interactions can be included in a wave equation. The Gross-Pitaevskii equation is a variation on the non-interacting Hamiltonian that utilises a pseudo-potential model to include these atomic interactions. If a system is perfectly condensed with all atoms in a Bose-Einstein condensate state, or in other words, if all atoms occupy the lowest quantum state with each atom having the same wave-function $\phi(\mathbf{r})$. The condensate can then

be described by a mean-field utilising the Hartree-Fock method [92] such that,

$$\Psi(\mathbf{r}_1, \mathbf{r}_2 \dots \mathbf{r}_N) = \phi(\mathbf{r}_1)\phi(\mathbf{r}_2) \dots \phi(\mathbf{r}_N). \tag{3.5}$$

We must now define a mean-field energy, U_0 as

$$U_0 = \frac{4\pi\hbar^2 a_{12}}{m}, \tag{3.6}$$

where a_{12} is the mean scattering length, and m is the mass of a single atom within the condensate. The scattering length is a property that needs to be found experimentally. The mean-field energy forms a pseudo-potential and gives us the Hamiltonian of the system in the form

$$H = \sum_{i=1}^{N} \left(\frac{\mathbf{p}_i^2}{2m} + V(\mathbf{r}_i) \right) + U_0 \sum_{i<j} \delta(\mathbf{r}_i - \mathbf{r}_j). \tag{3.7}$$

This Hamiltonian has the regular kinetic, $\mathbf{p}^2/2m$ and potential $V(\mathbf{r}_i)$ with an added pseudo-potential U_0 which sums all the interactions between atoms in the system and δ the Dirac delta function. Then, utilising the Hartree-Fock method and assuming the particle density is equal to the absolute square of the wave function, we arrive at the following wave function:

$$\left(-\frac{\hbar^2}{2m}\nabla^2 + V(\mathbf{r}) + g\left|\psi(\mathbf{r})\right|^2 \right) \psi(\mathbf{r}) = \mu\psi(\mathbf{r}), \tag{3.8}$$

with g being the non-linear coupling constant. This wave-equation thus describes the ground-state of the system. The mean-field energy is multiplied by the number of atoms N giving the non-linear coupling constant as

$$g = NU_0 = \frac{4\pi\hbar^2 N a_{12}}{m}. \tag{3.9}$$

The addition of Gross-Pitaevskii to the Split-Step Fourier Method requires a small adjustment to the algorithm. Previously we outlined a split-step Fourier method

with imaginary time propagation and a potential term to find the wave-function groundstate before performing the free-expansion simulation [89]. We will be utilising a similar method to simulate the Gross-Pitaevskii wave function. Again, we will be utilising the two half steps in the potential term to have greater accuracy without increasing the number of spatial points utilised. The only modifications we need to make to the groundstate finding algorithm is an adjustment to the potential term and a conversion to real-time propagation. The modification to the potential term is a simple addition of the mean-field energy term multiplied by the current wave-function density, meaning that we can make the transformation

$$V(\mathbf{r},t) \rightarrow V(\mathbf{r},t) + g\left|\psi\right|^2 \tag{3.10}$$

in our algorithm. We will be utilising the scattering length of rubidium-87 as found by Egorov *et al.* [93], since rubidium-87 is a common isotope used experimentally. The algorithm we will be using in full therefore is as follows:

$$\begin{aligned}\Psi(r,t+\Delta t) = &\exp\left(-\frac{i\Delta t\left(V+g\left|\Psi(r,t)\right|^2\right)}{2\hbar}\right)\\ &\times\mathcal{F}^{-1}\left[\exp\left(-\frac{i\Delta t k\hbar}{2m}\right)\right.\\ &\left.\times\mathcal{F}\left(\Psi(r,t)\exp\left(-\frac{i\Delta t\left(V+g\left|\Psi(r,t)\right|^2\right)}{2\hbar}\right)\right)\right],\end{aligned} \tag{3.11}$$

with $\mathcal{F}$ the Fourier transform and $\mathcal{F}^{-1}$ the inverse Fourier transform and Δt the time step and k the momentum space coordinate. Under the free expansion, the potential term V is set to zero. Although this is relatively straightforward for the Split-Step Fourier Method numerical approach, the same cannot be said for our approach in chapter 2. This difficulty is because the Gross-Pitaevskii is a non-linear differential equation, which makes solutions challenging to obtain. Solutions thus far have been found for free-particle, sometimes called the Hartree approximation [94] and the soliton [95, 96], but neither of these are applicable for our systems.

Additionally, there are a couple of approximations that have also been made in

the Thomas-Fermi approximation [97, 98] and the Bogoliubov approximation [99]. The Thomas-Fermi approximation applies only if the atomic density is so large that the kinetic energy term may be neglected. This kinetic energy term is usually comparatively negligible since, at ultra-cold temperatures, the atomic velocities are very low, however, this assumption does not hold for the systems we are considering since the number of atoms might reasonably be expected to be in the 10^4 atom range. Therefore the kinetic energy term is not negligible when compared to the Gross-Pitaevskii interaction term. The Bogoliubov approximation assumes that the wave function may be approximated by adding a small perturbation to the wave function at equilibirum. The free expansion of a wave function does not hold since the wave function deviates considerably from the equilibrium. We, therefore, do not have an established method of introducing Gross-Pitaevskii interactions into our methodology. We, therefore, need to understand what effect the Gross-Pitaevskii interactions have on the system and compare these to our original methodology, which omits these considerations. That way, we can better define under what conditions our approach remains a good approximation of the Gross-Pitaevskii expansion. We will measure the numerical simulation's fidelity or overlap with our analytic expressions. In particular, we will be looking at the toroidal system and how the number of atoms and the expansion rate affects our methodology compared to Gross-Pitaevskii numerical simulations. In figure 3.3, we plot the infidelity against time for several different systems with a different number of atoms. We have chosen to use infidelity, equal to one minus fidelity, since we can then put a log scale on the infidelity axis to differentiate the different lines better.

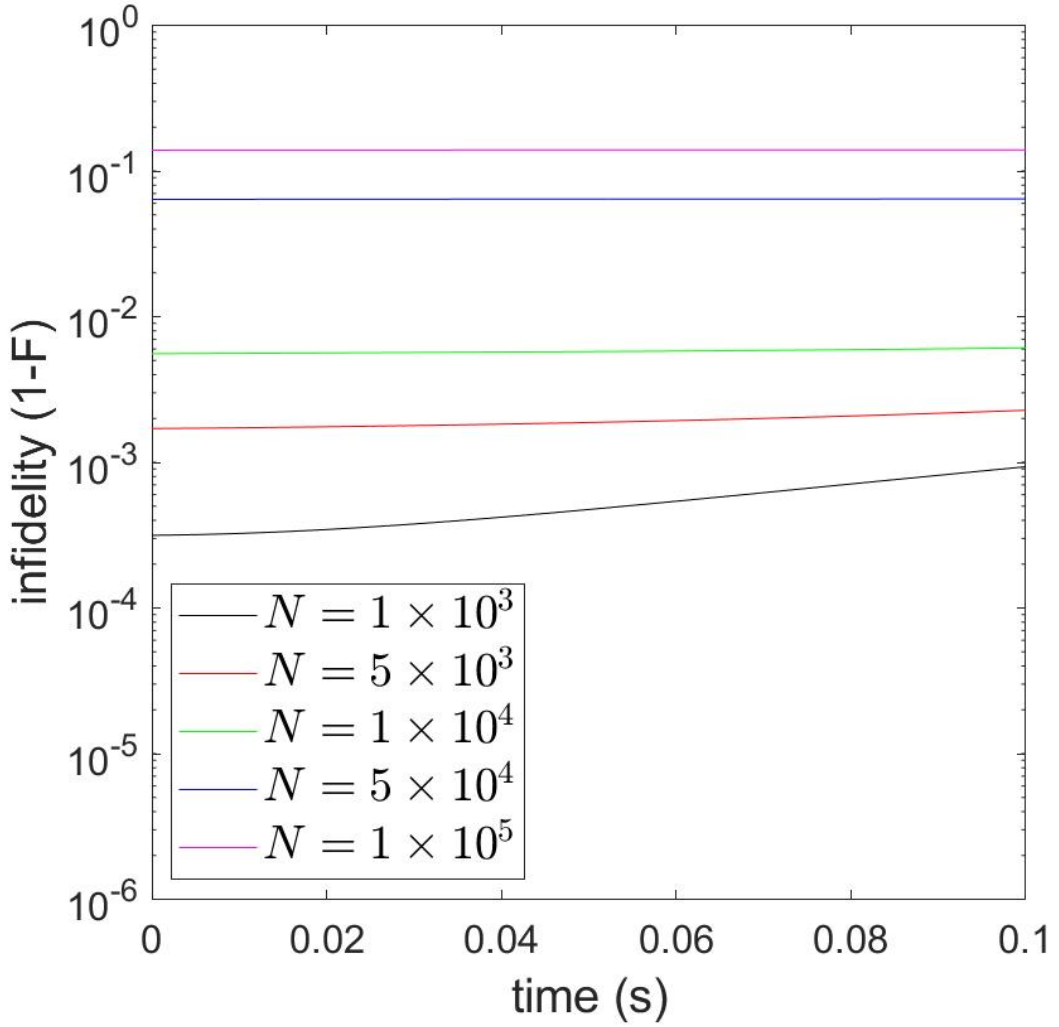

Figure 3.3: Here, we plot 1-fidelity against time for a different number of atoms. These results are obtained by comparing a Gross-Pitaevskii numerical simulation to our non-Gross-Pitaevskii analytical approach. In this simulation, we used a toroidal wave packet with a radius of 50 μm and a width of 5 μm.

From figure 3.3, we see that the fewer the number of atoms, the higher the fidelity; this we expect since the more atoms, the more interactions and the more the system will divert from the non-Gross-Pitaevskii system. Nevertheless, the fidelity remains relatively high, with systems containing 10^4 atoms or fewer maintaining a fidelity above 0.995. Even at 10^5 atoms, the fidelity does not drop below 0.9. Therefore, this trend indicates that although Gross-Pitaevskii interactions affect the overall system, this is often not significant until the emergence of interference fringes. In figure 3.4, we plot the fidelity comparison for systems of a different ra-

dius to see how Gross-Pitaevskii interactions impact this system. The smaller the radius, the greater the Gross-Pitaevskii interactions and the greater deviation of the system from the non-Gross-Pitaevskii system. We also see that the smaller the radius, the faster the systems differ. In conjunction with our findings regarding the number of particles, this result suggests that our analytic expression works best when the wave packet is at a lower density, as was expected, and has a larger initial radius. Our methodology in chapter 2 does not provide a straightforward way to include any Gross-Pitaevskii interactions; however, results indicate the difference between Gross-Pitaevskii and non-Gross-Pitaevskii systems is not significant with the caveats outlined before. Suppose an expression was found for the free expansion of a Gaussian wave packet with Gross-Pitaevskii interactions. In that case, this could be utilised in our methodology to overcome discrepancies for the limited shortcomings of our approach, particularly for small wave packets and systems with a large number of atoms.

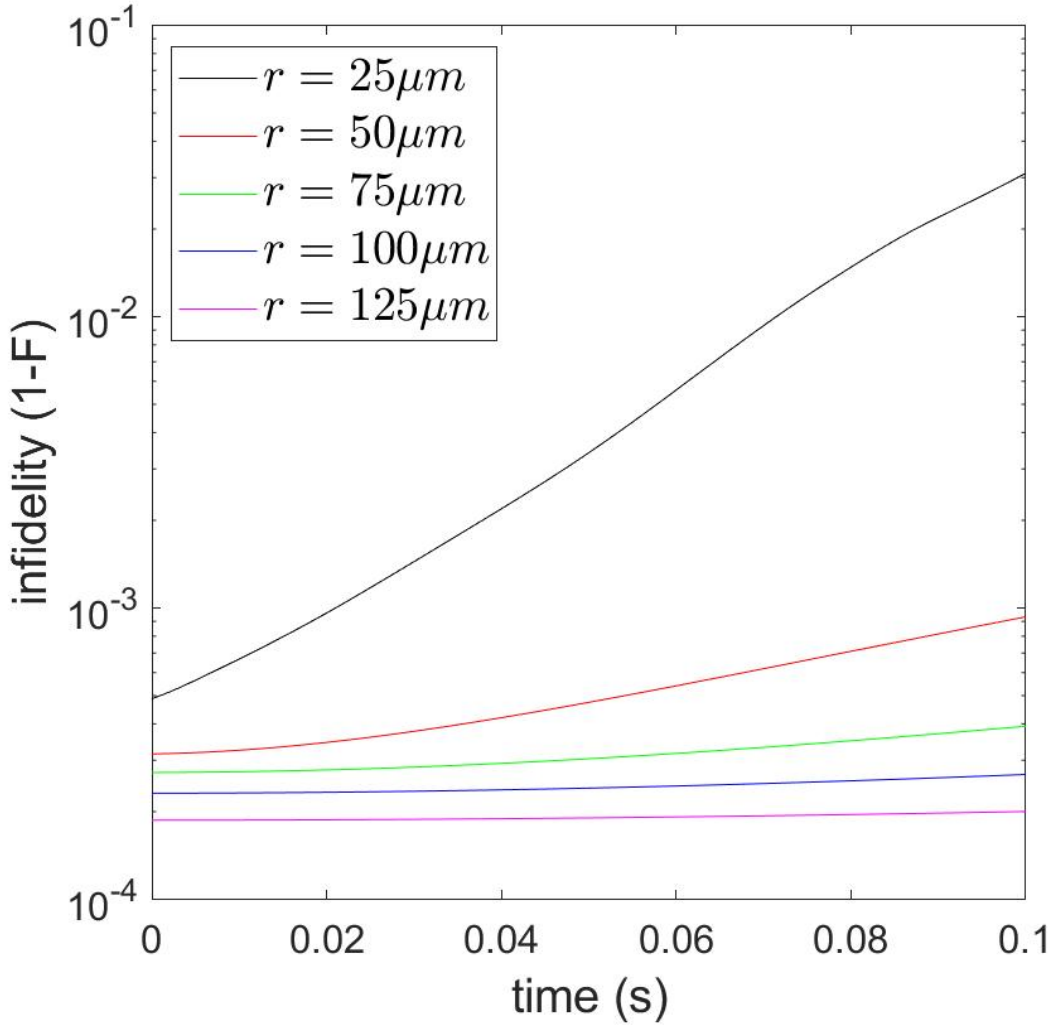

Figure 3.4: Here we plot 1-fidelity against time for different initial radius'. These results are obtained by comparing a Gross-Pitaevskii numerical simulation to our non Gross-Pitaevskii analytical approach. We utilise a fixed width to radius ratio of 0.1 and 10^3 atoms.

3.4 Conclusions

We have then demonstrated that our results mirror those achieved through the implementation of the SSFM, with direct comparisons yielding a high fidelity across all results. For most of the systems tested, we found that our fidelity exceeded 0.99 over the initial expansion of the system, with a consistent drop-off in fidelity occurring as the wave function began to expand over the edges of the box, causing

cross-boundary interactions to occur. Furthermore, we observed that in both systems, a high-density central peak emerges, which in the toroidal geometry produces a central column. This central peak depended on the initial radius (R) and its ratio with the initial width (σ). We noted a high fidelity at the time of emergence for the central fringe in both systems, with fidelity over 0.9997 in most simulated systems. In addition, we found that the larger the initial width and the larger the initial radius, the higher the fidelity we recorded at the time of emergence for the central fringe. Finally, we looked at the overall effect that Gross-Pitaevskii interactions had on the overall behaviour of the system. We found that systems with a high density of atoms deviated more from the results of our equations which did not include such coupling. We also found that the smaller the initial radius was, the more the Gross-Pitaevskii caused the simulations to deviate from our results. However, we found that the fidelity remained relatively high, particularly in the larger and less dense systems with fewer than 10^3 atoms and widths greater than 50 μm remaining within 10^{-3} of a fidelity of one.

Chapter 4

Asymmetric freely-expanding wave-packets

4.1 Introduction

In the previous two chapters of this thesis, we have been looking at two symmetric systems; however, there is significant experimental interest in asymmetric systems. As discussed previously in this thesis, the interference fringe generated from a freely expanding Bose-Einstein condensate depends on the system's initial state. This property can be utilised to determine the system's original state after the free expansion of the condensate. Therefore, understanding the dynamics of these asymmetric systems is something we want to achieve with our methodology. Thus far, we have just been considering symmetrical systems. Therefore it is equally important to check that our approach is still valid when the system does not have this circular symmetry. Demonstrating that our methodology is still valid in the asymmetric system would further demonstrate the versatility of the approach used. In this chapter of the thesis, we will be focusing on how gravity might affect the initial geometry of both the hollow shell and toroidal wave packets. Firstly, we will be simulating the effects of tilting the toroidal wave packet on the interference fringes generated by adding a gradient to the width of the torus. This tilting will cause an asymmetry in

the initial state, affecting the system's dynamics and, in particular, the interference fringes generated. Secondly, we will look at microgravity's effects on the hollow shell system. This micro-gravity will result in a deformation of the initial state, and the subsequent interference pattern generated should be highly dependent on this deformation. As a result, this might be used to study and measure micro-gravity in experiments like those being tested at the NASA cold atom laboratory on the International Space Station [77]. In this chapter, we will be looking at both systems, observing how the interference pattern is affected and testing the validity of our methodology against numerical simulations of the same systems.

We note that due to the nature of the Gaussian distributions, it may not always be possible to analytical solve the integral for the system. Therefore analytical solutions may be restricted to systems with symmetry. We will have to employ numerical integration to obtain our wave packets' dynamics when this is the case. This lack of an analytical solution to the integral does mean that extracting specific properties like the location and the visibility of the fringes is more complex but does not invalidate some of the other benefits of our approach over a purely simulated system. In particular, we still are not required to find intermediary time values and, as such, can identify the shape of the wave packet at any given time after the point of release. Additionally, we do not have to consider the time step utilised, the interactions with the simulation environment or numerical drift. When performing a numerical integration of the system, we need to establish how quickly the numerical integration converges to the solution and, therefore, how many spatial steps we must perform to describe the system accurately. This chapter will examine two variations of the initial state in tilted toroidal and tilted hollow shell wave packets. We aim to demonstrate that our methodology might be applied to asymmetric systems, detailing one particular approach to show our methodology's versatility.

4.2 Numerical integration of the tilted torus

In order to determine how quickly the numerical integration converges on the solution, we will look at the two geometries we have outlined in chapters 2 and 3 of this thesis, namely the hollow shell and the toroidal wave-packet. We have already established that our analytical solution has a high fidelity or overlap compared to the system's simulated ground state. We will use this property to test the convergence of the numerical integration. We use imaginary time propagation to find the ground state for the hollow shell and toroidal system. We then compare a numerical integration of the same system at time zero with various integration spatial steps and measure the resulting fidelity or overlap between the numerically integrated system and the numerically determined ground-state. We will then utilise this fidelity result to determine the number of spatial steps we will be utilising in our numerical integration of the system. When selecting the number of spatial steps, we needed to consider the balance between the accuracy of the integration and the time taken to perform the integration. This balance is essential with the hollow shell wave function since this requires integration over both θ and ϕ. Therefore the run time can suffer rapidly as the number of spatial steps utilised in the numerical integration increases. As outlined in a previous chapter of this thesis, the ground state for our wave function may be found numerically through imaginary time propagation utilising the split-step Fourier methodology. Through iterating this approach, the wave function will converge on the ground state for the system. To test our numerical integration, we perform this ground state finding algorithm until the maximum change in the wave function falls below a certain tolerance level. In our case, we utilise a maximum difference of 10^{-3}, which is sufficiently smaller than the maximum amplitude of the system, which typically is of the order 10^7 meaning that we obtain a ground state that is accurate to approximately ten digits which we feel is sufficiently accurate. This accuracy is an absolute accuracy of the system and not a relative error. We then want to compare this ground state to our numerically integrated equation. We will start by looking at the toroidal wave packet. The integral that we will be

numerically testing is in the following form:

$$\begin{aligned}\psi_{\text{torus}} =& \frac{\sigma_0^{\frac{3}{2}}}{(2\pi)^{\frac{3}{4}}\tilde{\sigma}(\tau)^3}\exp\left(-\frac{z^2}{4\tilde{\sigma}(\tau)^2}\right) \\ &\times\int_0^{2\pi}\exp\left(-\frac{(x-R\cos(\theta'))^2+(y-R\sin(\theta'))^2}{4\tilde{\sigma}(\tau)^2}\right)d\theta'.\end{aligned} \tag{4.1}$$

In order to numerically integrate our expression we shall replace the integration term with a summation term which we need to evaluate such that

$$\begin{aligned}\psi_{\text{approx}} =& \frac{\sigma_0^{\frac{3}{2}}}{(2\pi)^{\frac{3}{4}}\tilde{\sigma}(\tau)^3}\exp\left(-\frac{z^2}{4\tilde{\sigma}(\tau)^2}\right) \\ &\times\sum_{n=0}^{n_{\max}}\frac{1}{2}\left(\theta'_{n+1}-\theta'_n\right)\left(\Psi\left(\theta'_{n+1}\right)+\Psi\left(\theta'_n\right)\right),\end{aligned} \tag{4.2}$$

with Ψ the integrand, $n_{\max}$ the total number of spatial steps used in the integration which we are looking to determine. Typically, the angles at which the summation is evaluated would be equally spaced and therefore,

$$\theta'_n = \frac{2\pi n}{n_{\max}} \tag{4.3}$$

and

$$\theta'_{n+1} = \frac{2\pi(n+1)}{n_{\max}}. \tag{4.4}$$

The integrand therefore takes on the following form:

$$\Psi(\theta') = \exp\left(-\frac{(x-R\cos(\theta'))^2+(y-R\sin(\theta'))^2}{4\tilde{\sigma}(\tau)^2}\right). \tag{4.5}$$

We then renormalise the resulting function and find the fidelity or overlap between the approximate wave function obtained through numerical integration and the ground state found through numerical simulation. Finally, we calculate the fidelity for these two wave functions using the same expression as before in equation (3.4).

Given that we want the fidelity to be as close to one as possible, we introduce

the term infidelity, which is simply one minus the fidelity. With infidelity, the closer to zero the value is, the better the result and the closer the two wave functions are to perfectly overlapping one another. Plotting the infidelity for our toroidal system as a function of the number of spatial steps, $n_{\max}$, used in the integration, we obtain figure 4.1 which we can use to see how quickly the numerical integration converges on the ground state for the system.

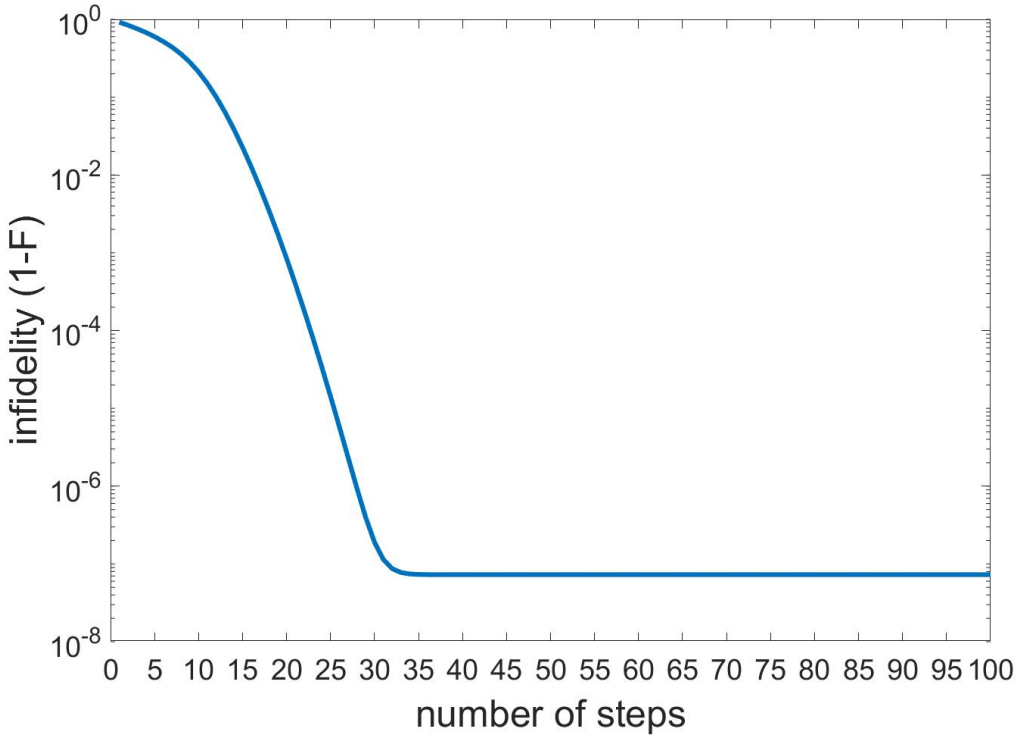

Figure 4.1: Infidelity when comparing our numerical integration of the torus to the simulated ground-state of the system. We utilise a torus with a radius of 20 μm and a width of 2 μm.

From figure 4.1 we see that with just a single spatial step, the infidelity is very high, almost at a value of one, but as the number of spatial steps increases, the infidelity decreases until we reach an infidelity of approximately 10^{-7} at around thirty-five spatial steps at which point the infidelity no longer begins to grow. This plateauing of the infidelity is because we compare our numerical integration to a simulated ground state. There is liable to be some discrepancy between the two systems, with an infidelity of around 10^{-7} in this system. Due to the plateauing of the infidelity, we will utilise thirty-six spatial steps in our numerical integration since

the improvement in infidelity beyond this number of spatial steps becomes negligible. To visualise how the number of spatial steps affects the overall shape of the wave function, we plot the same system utilised to find the infidelity of the numerical integration. In figure 4.4(a) we use nine spatial steps in the numerical integration and in figure 4.4(b) we use thirty-six spatial steps to the numerical integration. Our results become much smoother with the greater number of integration spatial steps. By thirty-six spatial steps, we obtain a wave function that appears much like what we might expect from a toroidal wave function, confirming what we see when measuring the infidelity with the system's ground state.

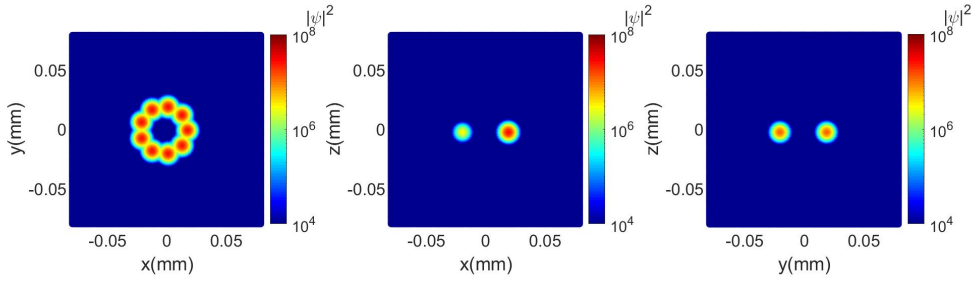

(a)

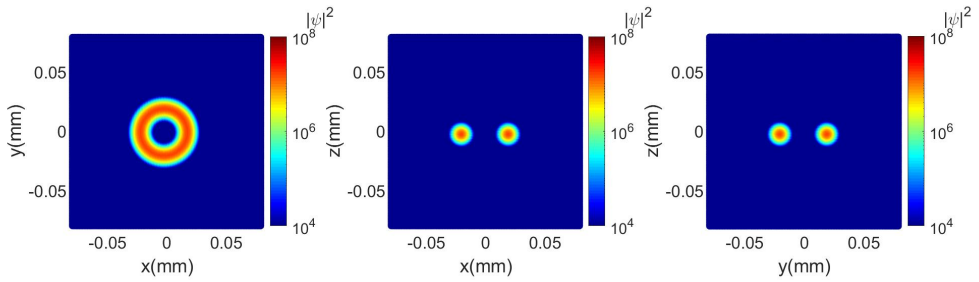

(b)

Figure 4.2: In (a), we plot the toroidal system with $n_{\max} = 9$ spatial steps in the integration. We see that there are 9 distinct Gaussian distributions spaced equally around the ring. Each spatial step of the integration process adds an additional Gaussian onto the ring with each Gaussian equally spread out. In (b), we increase the number of spatial steps to $n_{\max} = 36$ and observe that the wave function is a lot smoother, hence the infidelity is much lower than in (a).

4.3 Numerical integration of the hollow shell

Now that we understand the toroidal wave function, we focus on the hollow shell. The approach we use for this system is similar to the one utilised with the toroidal

wave function; however, unlike with the torus, we have a double integral that we must evaluate. The integral that we need to evaluate for the hollow shell takes the following form:

$$\begin{aligned}\psi_{\text{hs}}(x,y,z,\tau) =& \frac{\sigma_0^{\frac{3}{2}}}{(2\pi)^{\frac{3}{4}}\tilde{\sigma}(\tau)^3}\int_0^{2\pi} d\theta' \\ &\times \int_0^{\pi} \exp\left(-\frac{(x-R\sin(\phi')\cos(\theta'))^2}{4\tilde{\sigma}(\tau)^2}\right) \\ &\times \exp\left(-\frac{(y-R\sin(\phi')\sin(\theta'))^2}{4\tilde{\sigma}(\tau)^2}\right) \\ &\times \exp\left(-\frac{(z-R\cos(\phi'))^2}{4\tilde{\sigma}(\tau)^2}\right)\sin(\phi')\,d\phi'.\end{aligned} \tag{4.6}$$

This function has a dependence on both θ' and ϕ', and as a result, we need to integrate over both of these parameters. We therefore replace the two integrals with summations such that

$$\begin{aligned}\psi_{\text{approx}} =& \frac{\sigma_0^{\frac{3}{2}}}{(2\pi)^{\frac{3}{4}}\tilde{\sigma}(\tau)^3}\sum_{m=0}^{m_{\max}}\sum_{n=0}^{n_{\max}}\frac{1}{4}\left(\phi'_{m+1}-\phi'_m\right)\left(\theta'_{n+1}-\theta'_n\right) \\ &\times\left[\Psi\left(\theta'_{n+1},\phi'_{m+1}\right)+\Psi\left(\theta'_n,\phi'_{m+1}\right)+\Psi\left(\theta'_{n+1},\phi'_m\right)+\Psi\left(\theta'_n,\phi'_m\right)\right],\end{aligned} \tag{4.7}$$

with Ψ the integrand, $n_{\max} = m_{\max}$ the total number of spatial steps used in the integration which we are looking to determine. Typically, the angles at which the summation is evaluated would be equally spaced and therefore,

$$\theta'_n = \frac{2\pi n}{n_{\max}}, \tag{4.8}$$

$$\theta'_{n+1} = \frac{2\pi(n+1)}{n_{\max}}, \tag{4.9}$$

$$\phi'_n = \frac{\pi n}{n_{\max}} \tag{4.10}$$

and

$$\phi'_{n+1} = \frac{\pi(n+1)}{n_{\max}}. \tag{4.11}$$

With these substitutions the resulting integrand takes on the form of

$$\begin{aligned}\Psi(\theta', \phi') = &\exp\left(-\frac{(x - R\sin(\phi')\cos(\theta'))^2 + (y - R\sin(\phi')\sin(\theta'))^2}{4\tilde{\sigma}(\tau)^2}\right) \\ &\times \exp\left(-\frac{(z - R\cos(\phi'))^2}{4\tilde{\sigma}(\tau)^2}\right)\sin(\phi').\end{aligned} \tag{4.12}$$

Again, we shall look at the infidelity of the system when comparing the numerical integration to the ground state as shown in figure 4.3.

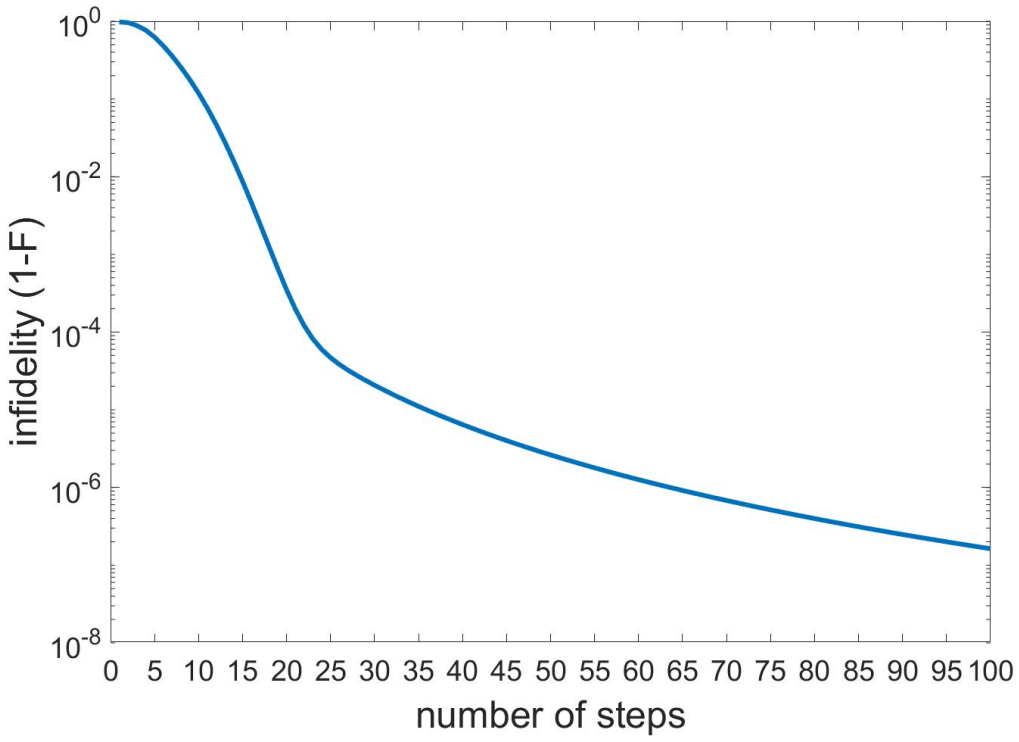

Figure 4.3: Infidelity when comparing our numerical integration of the hollow shell to the simulated ground-state of the system. We utilise a torus with a radius of 20 μm and a width of 2 μm. All other parameters are appropriate for the trapping of a rubidium-87 Bose-Einstein condensate.

We see that again, the infidelity is close to one for one spatial step in the numerical integration, but this drops. We do not observe the same plateauing as in the torus case in figure 4.1, but we observe a change in gradient at around twenty to

twenty-five spatial steps. With the hollow shell case, the spatial step size is critical for a numerical method since, unlike in the toroidal case, we have a double integral; as a result, the total number of spatial steps over the entire calculation is squared since we need to do the integration in both θ' and ϕ'. We do not want to select too many spatial steps since the numerical integration run time will increase rapidly. Equally, we want to maintain a good degree of accuracy so that we have confidence in our results and so they reflect the system's actual behaviour as best as possible. As a compromise between these two considerations, we again select thirty-six spatial steps since this is the first value with an infidelity lower than 10^{-5} giving us a strong degree of accuracy without having to calculate too many spatial steps in total. We wish to see how the number of spatial steps utilised in the numerical integration affects the overall result. As in figure 4.4(a) and in figure 4.4(b), we will be using the same initial radius and width, but this time in a hollow shell geometry. We will also use both 9 and 36 spatial steps in the integration. Our results become much smoother with the greater number of integration spatial steps. By thirty-six spatial steps, we obtain a wave function that appears much like what we might expect from a toroidal wave function, confirming what we see when measuring the infidelity with the system's ground state.

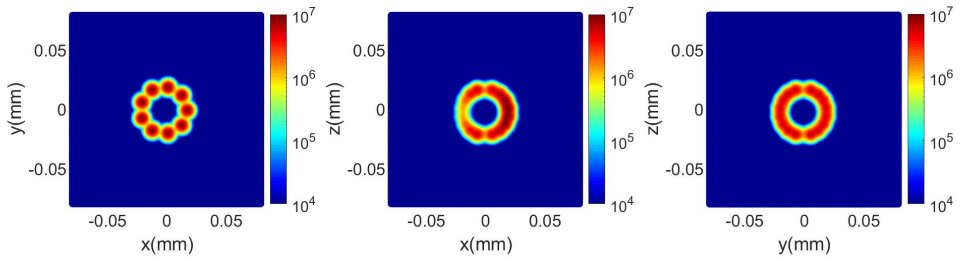

(a)

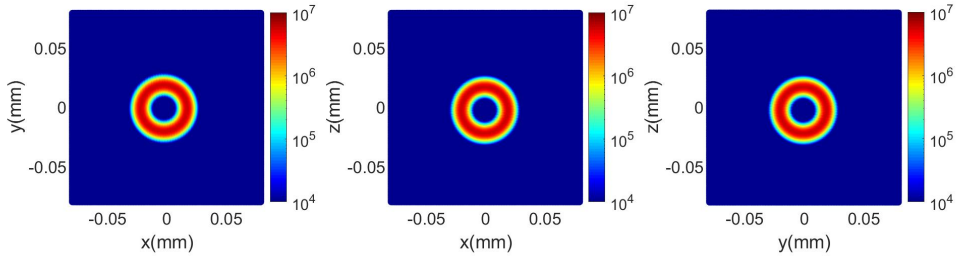

(b)

Figure 4.4: In (a), we plot the hollow shell system with 9 spatial steps in the integration. We see a distinct number of Gaussian distributions spaced equally around the ring. Each spatial step of the integration process adds an additional Gaussian onto the ring with each Gaussian equally spread out. We see in the x-z graph for the nine spatial step integration that there is an asymmetry. This asymmetry is due to selecting an odd number of spatial steps meaning that on one side of the shell one Gaussian lies directly on the line $z = 0$ whereas at the other end the Gaussian is either just above or below this plane, hence the asymmetry. In (b), we increase the number of spatial steps to 36. Again, we observe that the wave function is much smoother, hence why the infidelity is much lower than the system with only 9 spatial steps in the numerical integration.

Having now selected the number of spatial steps we will be using in our systems' numerical integration; we can now turn our attention to asymmetric variations in these two systems.

4.4 Tilted ring trap

Having established our numerical integration methodology and spatial step number selection, we now focus on variations on the toroidal wave packet. In particular, we will use a tilted ring so that most of the wave function collects to one side. We wish to characterise this tilting effect on the overall initial shape of the system

and then observe the impact that this new geometry has on the overall interference pattern generated when this new wave function is allowed to expand freely. We know that these interference fringes are highly dependent on the initial state and that properties of the original state might be obtained by studying the resulting interference fringes. Therefore, we want to test whether this is the case and observe any characteristic phenomena due to this asymmetry. Additionally, we look to demonstrate that our methodology generates reliable results for such an asymmetric system, further demonstrating the versatility of our approach.

We will apply a Gaussian weighting function in θ' located somewhere on the toroidal ring and with a standard deviation to achieve our tilted ring. This exponential weighting is what we might expect to see for a tilted ring in the ground state with a peak density at the point of lowest gravitational potential energy and a Gaussian-like decrease in density the further away from this gravitational minimum. We found that applying this Gaussian weighting function appeared to give a good approximation of the ground-state when we applied a gravitational gradient to our system. We tested this by adding a gravitational gradient to a potential and utilising our imaginary time propagation to find the ground-state. This standard deviation may be changed or manipulated to affect the amount of tilting that the torus undergoes, with a smaller standard deviation leading to highly tilted tori. Specifically, we will be multiplying our wave function with the following tilting function:

$$F(\theta') = \exp\left(-\frac{(\theta' - \theta_0)^2}{2\sigma_{\theta'}}\right), \tag{4.13}$$

with θ_0 the location of the maximum amplitude of the wave function, we will assume that $\theta_0 = \pi$ so that the minimum width of the ring is located at $x = R$ and $y = 0$, where R is the radius of the ring and $\sigma_{\theta'}$ the angular width of the Gaussian. This

biasing gives us an overall wave function

$$\begin{aligned}\psi_{\text{tilted-torus}}(x,y,z,\tau) =& \frac{\sigma_0^{\frac{3}{2}}}{(2\pi)^{\frac{3}{4}}\tilde{\sigma}(\tau)^3}\exp\left(-\frac{z^2}{4\tilde{\sigma}(\tau)^2}\right) \\ &\times \int_0^{2\pi}\exp\left(-\frac{(x-R\cos(\theta'))^2+(y-R\sin(\theta'))^2}{4\tilde{\sigma}(\tau)^2}\right) \\ &\times \exp\left(-\frac{(\theta'-\theta_0)^2}{2\sigma_{\theta'}}\right)d\theta'.\end{aligned} \tag{4.14}$$

This expression does not have an analytical solution in its current formulation. We utilise the numerical integration approach, as seen in section 4.2, to understand how this system behaves as it undergoes free expansion. Before looking at this free expansion, we first focus on the system's initial state. In figure 4.5, we plot the wave function at time zero for different tilting widths to see the initial state of the wave function.

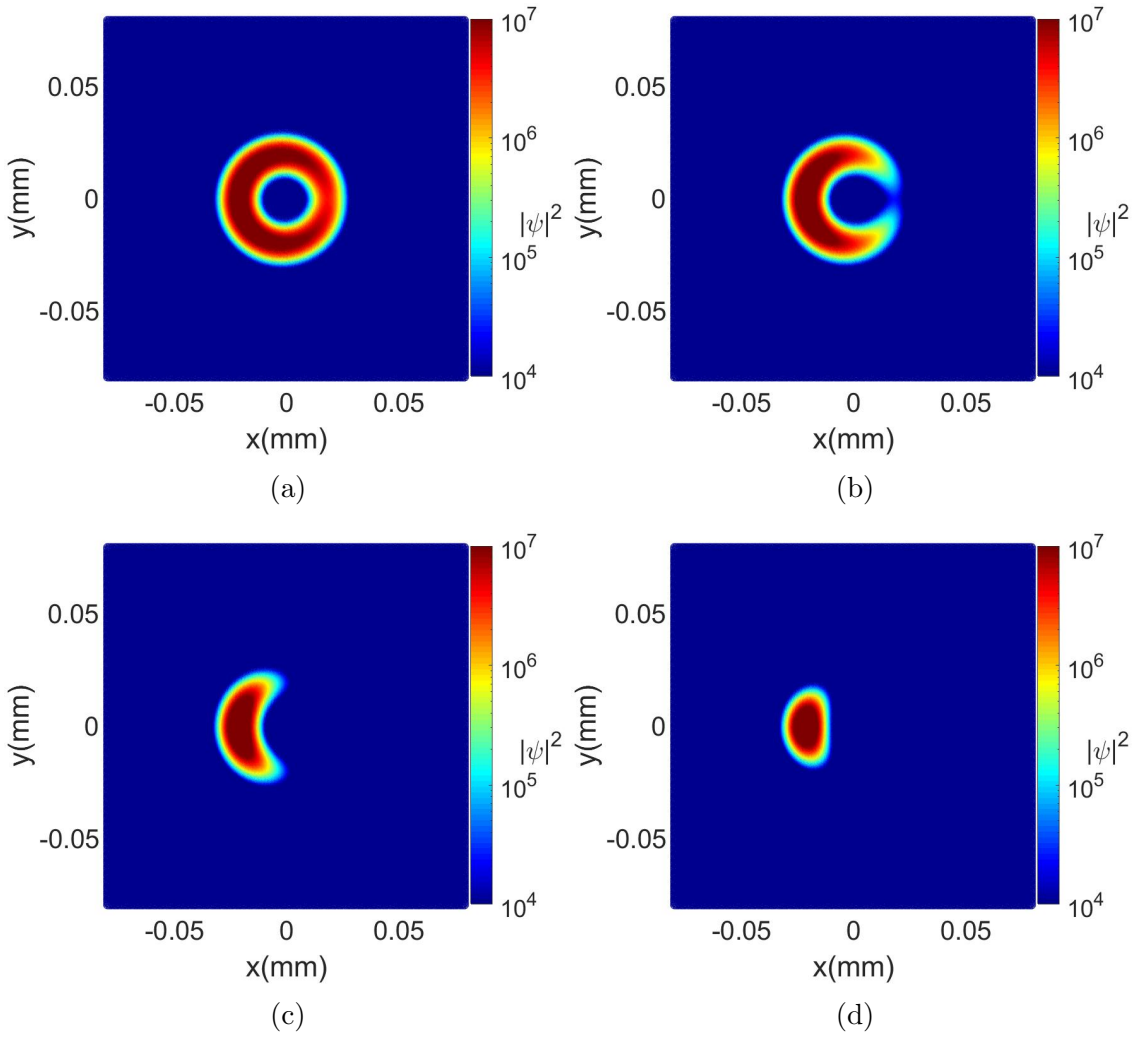

Figure 4.5: Cross-section in the x-y plane of the tilted torus with varying tilt widths at time $t = 0$ s. We utilise a torus that has a radius of 20 μm and a width of 2 μm. All other parameters are appropriate for the trapping of a rubidium-87 Bose-Einstein condensate. (a) $\sigma_{\theta'} = \frac{\pi}{2}$, (b) $\sigma_{\theta'} = \frac{\pi}{4}$, (c) $\sigma_{\theta'} = \frac{\pi}{8}$ and (d) $\sigma_{\theta'} = \frac{\pi}{16}$.

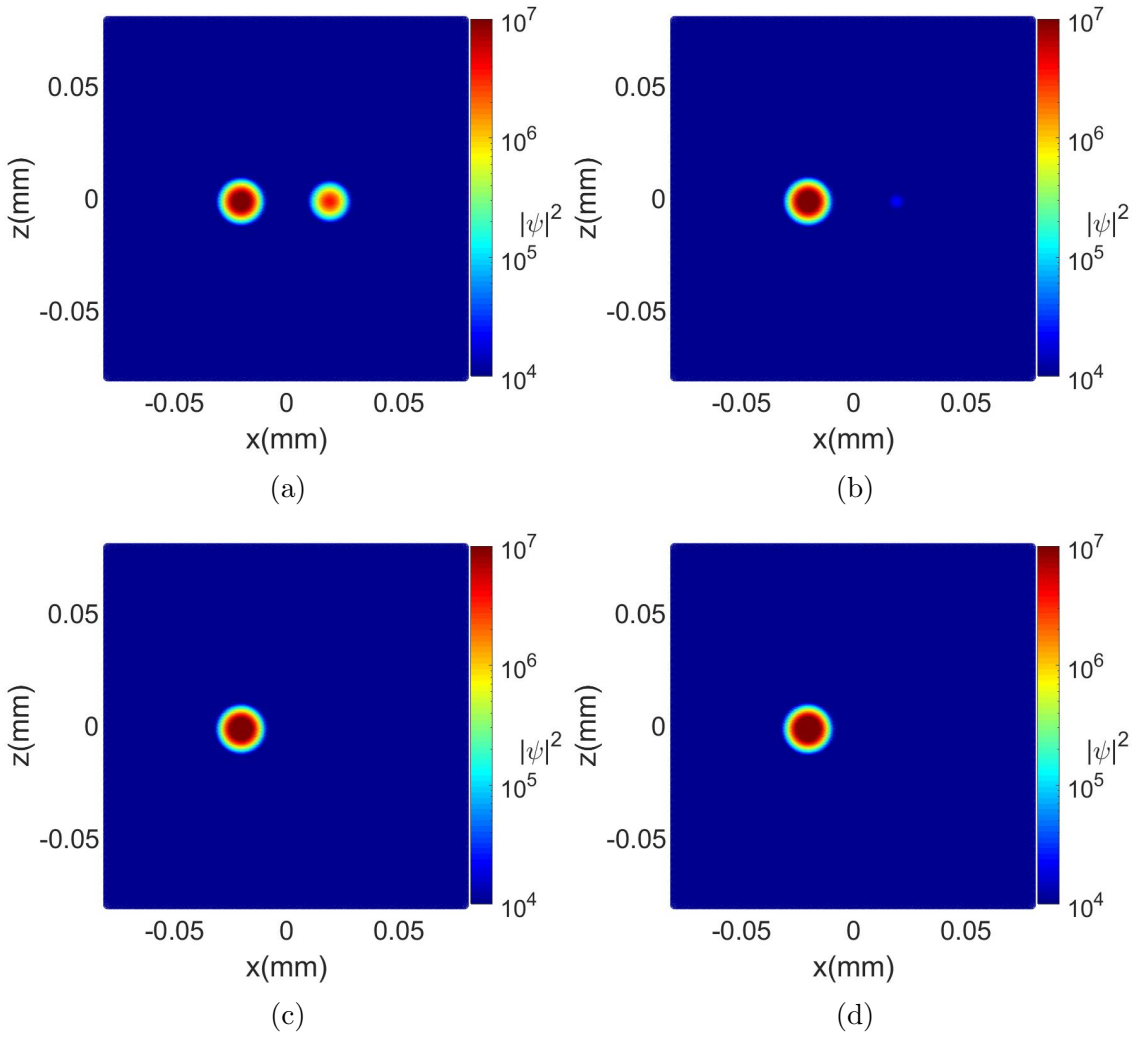

Figure 4.6: Cross-section in the x-z plane of the tilted torus with varying tilt widths at time $t = 0$ s. We utilise a torus that has a radius of 20 μm and a width of 2 μm. All other parameters are appropriate for the trapping of a rubidium-87 Bose-Einstein condensate. (a) $\sigma_{\theta'} = \frac{\pi}{2}$, (b) $\sigma_{\theta'} = \frac{\pi}{4}$, (c) $\sigma_{\theta'} = \frac{\pi}{8}$ and (d) $\sigma_{\theta'} = \frac{\pi}{16}$.

From figure 4.5, we can see that the majority of the wave packet is located in the lower portion of the trapping geometry when tilted, but a portion of the wave function remains located at the highest point in the trap. We can also see that as the width of this biasing Gaussian decreases, the more we find the wave-function is localised to the minimum position and the smaller the proportion of the ring that the wave-function occupies. The wave function is asymmetric with this function, indicating that it is possible to probe other systems with our methodology. If we then take the same systems but check the evolution of their shape after the point of release, we will observe the resulting interference fringes generated by this tilting.

In particular, we shall be looking at the system when $t = 0.05$ seconds. At this time in the symmetric system, the central fringe emerges.

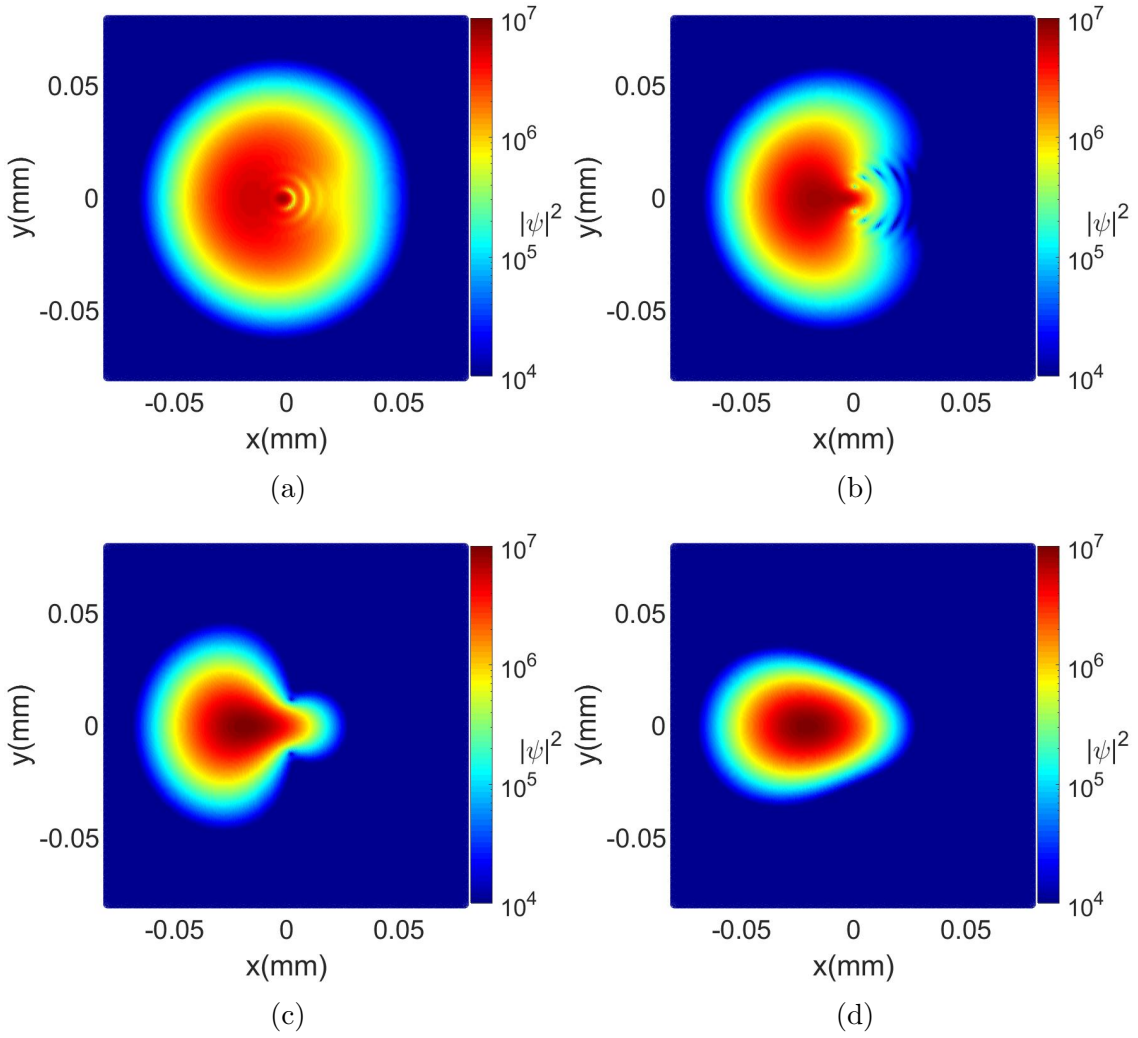

Figure 4.7: Cross-section in the x-y plane of the tilted torus with varying tilt widths at time $t = 0.05$ s. We utilise a torus that has a radius of 20 μm and a width of 2 μm. All other parameters are appropriate for the trapping of a rubidium-87 Bose-Einstein condensate. (a) $\sigma_{\theta'} = \frac{\pi}{2}$, (b) $\sigma_{\theta'} = \frac{\pi}{4}$, (c) $\sigma_{\theta'} = \frac{\pi}{8}$ and (d) $\sigma_{\theta'} = \frac{\pi}{16}$.

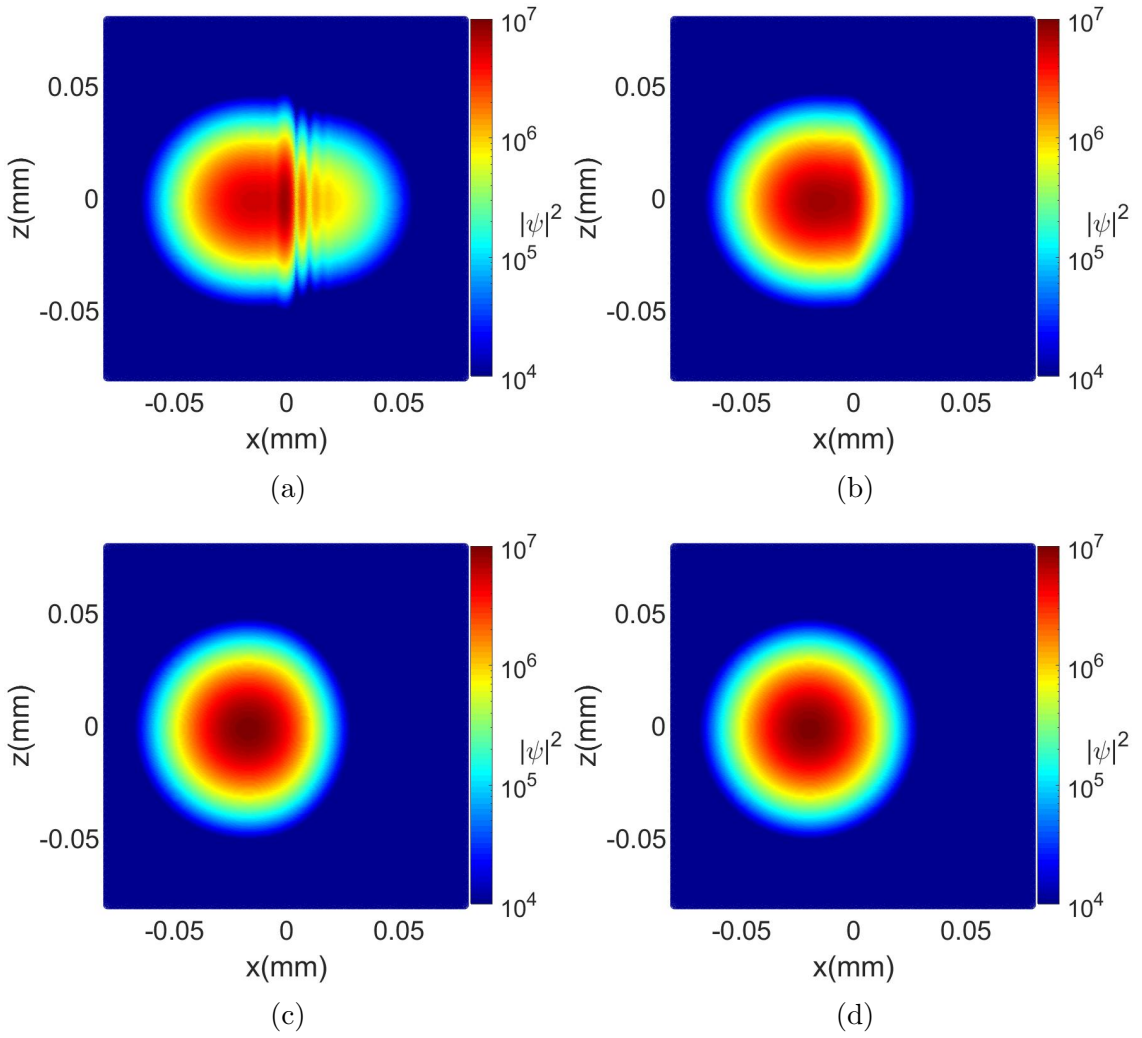

Figure 4.8: Cross-section in the x-z plane of the tilted torus with varying tilt widths at time $t = 0.05$ s. We utilise a torus that has a radius of 20 μm and a width of 2 μm. All other parameters are appropriate for the trapping of a rubidium-87 Bose-Einstein condensate. (a) $\sigma_{\theta'} = \frac{\pi}{2}$, (b) $\sigma_{\theta'} = \frac{\pi}{4}$, (c) $\sigma_{\theta'} = \frac{\pi}{8}$ and (d) $\sigma_{\theta'} = \frac{\pi}{16}$.

We can see in figures 4.7-4.8 that the first three systems still exhibit interference fringes but are wildly different in appearance. In particular, we note in figures 4.7-4.8(b) and figures 4.7-4.8(c) we get the emergence of some anti-nodes that appear to radiate out from the centre of the ring. In figures 4.7-4.8(a), we get a clear wave pattern forming that radiates from the centre, and we can see the remnants of the high-density central region as noted in the symmetrical system. This central peak has almost disappeared in figures 4.7-4.8(b) and does not appear to be present in either figures 4.7-4.8(c) or figures 4.7-4.8(d). In figures 4.7-4.8(d) in particular, we find that there appears to be little in the way of self-interference, indicating that

the small proportion of wave-function located opposite the maximum amplitude of the system is sufficiently small in this system that the interference fringes we are familiar with seeing are no longer visible. If we look at the x-z plane, we see the familiar vertical interference fringes in figures 4.7-4.8(a) that we observe in the symmetrical system. However, for the following wave functions, this feature no longer appears, and by figures 4.7-4.8(d), the wave function in this plane has the appearance of a Gaussian wave-packet. As predicted, we see that the resulting systems form significantly different outcomes under free expansion. This property, therefore, could be utilised to understand the starting state of the system prior to free expansion.

One property we are keen to take a closer look at is the emergence of these anti-nodes that we observe in figures 4.7-4.8(c) in particular. In figures 4.9-4.11, we focus on the anti-nodes of the system. In figures 4.7-4.8, we see that the anti-nodes emerge when the initial width $\sigma_{\theta'}$ is between $\pi/2$ and $\pi/8$ so we will focus in on this area and extend the time scale of the simulation to see how the anti-nodes differ in these systems.

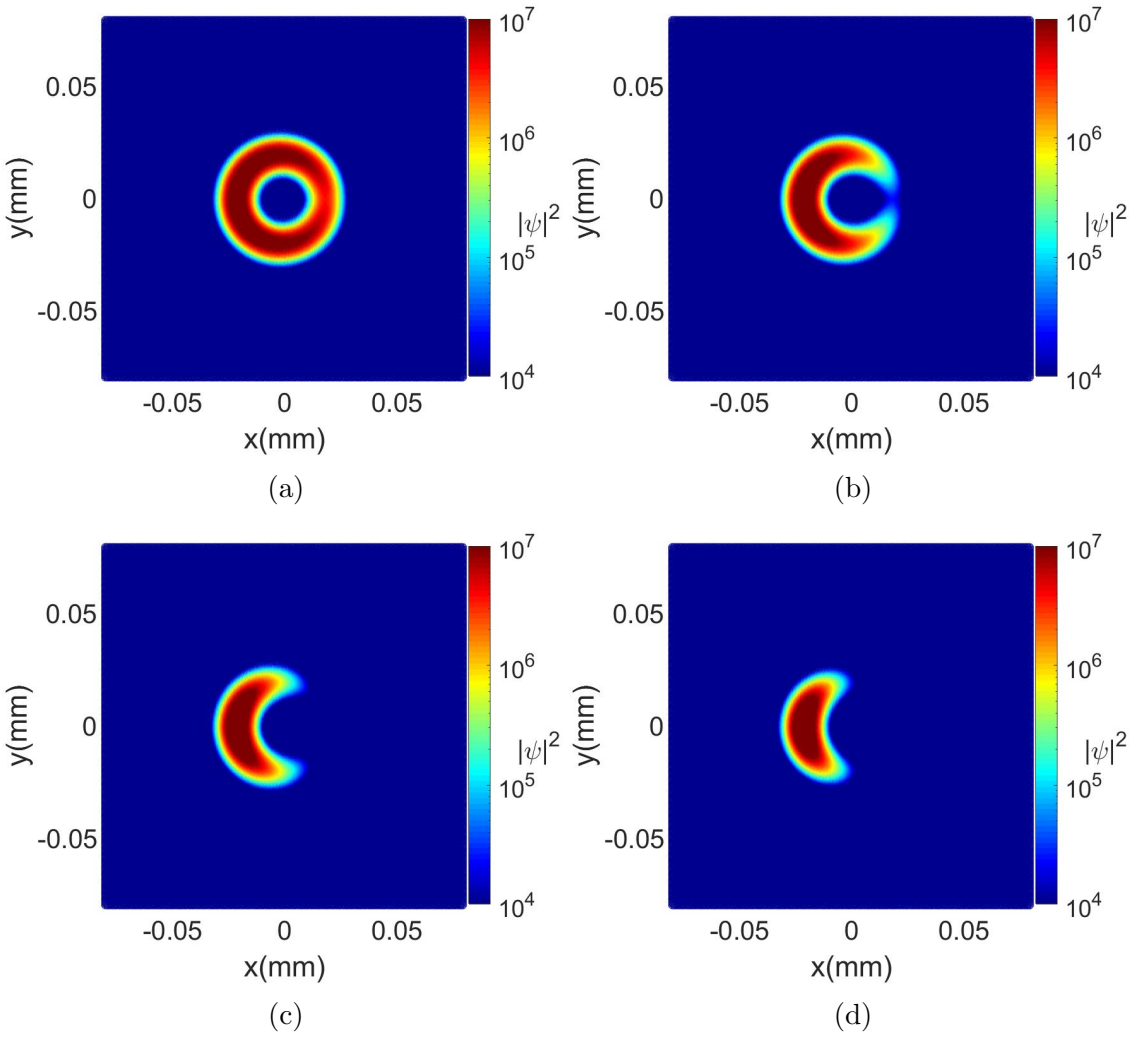

Figure 4.9: Cross-section in the x-y plane of the tilted torus with varying tilt widths at time $t = 0$ s. This time we are focusing on the anti-nodes for the system. All four of the following initial conditions appear to exhibit these anti-nodes as the wave function expands. We note that all four of these systems initialise with a relatively high density along the $x = 0$ line which is means that we observe these anti-nodes emerge in these systems but not for an initial width of $\pi/16$. We utilise a torus that has a radius of 20 μm and a width of 2 μm. All other parameters are appropriate for the trapping of a rubidium-87 Bose-Einstein condensate. (a) $\sigma_{\theta'} = \frac{\pi}{2}$, (b) $\sigma_{\theta'} = \frac{\pi}{4}$, (c) $\sigma_{\theta'} = \frac{\pi}{6}$ and (d) $\sigma_{\theta'} = \frac{\pi}{8}$.

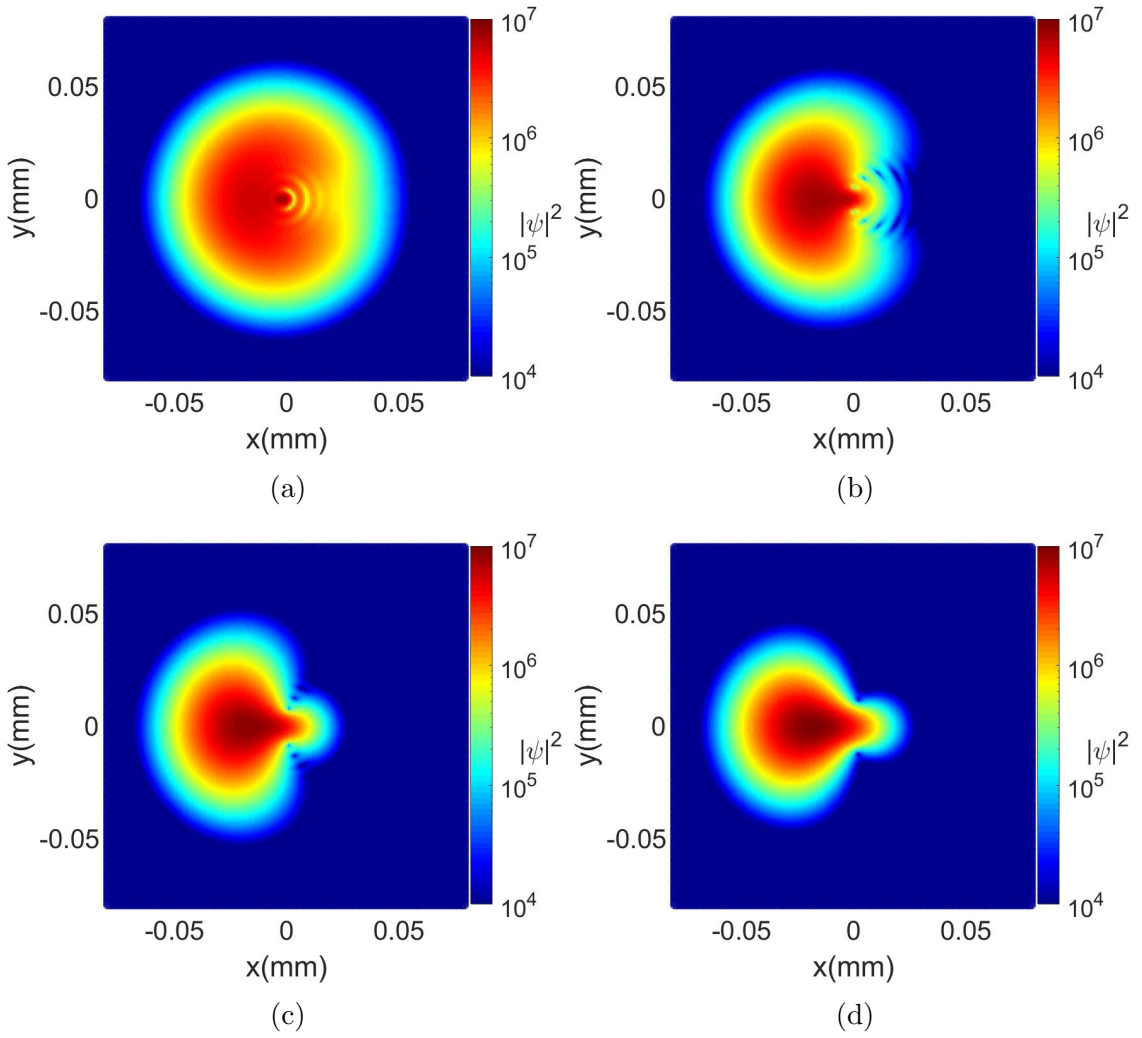

Figure 4.10: Cross-section in the x-y plane of the tilted torus with varying tilt widths at time $t = 0.05$ s. Again we see the emergence of these anti-nodes occurring with (a) having a ripple like pattern, in (b) the contrast in this ripple increases, in (c) the ripples break off forming diagonal pockets of low density and by (d) the number of anti-nodes is reduced to two. We utilise a torus that has a radius of 20 μm and a width of 2 μm. All other parameters are appropriate for the trapping of a rubidium-87 Bose-Einstein condensate. (a) $\sigma_{\theta'} = \frac{\pi}{2}$, (b) $\sigma_{\theta'} = \frac{\pi}{4}$, (c) $\sigma_{\theta'} = \frac{\pi}{6}$ and (d) $\sigma_{\theta'} = \frac{\pi}{8}$.

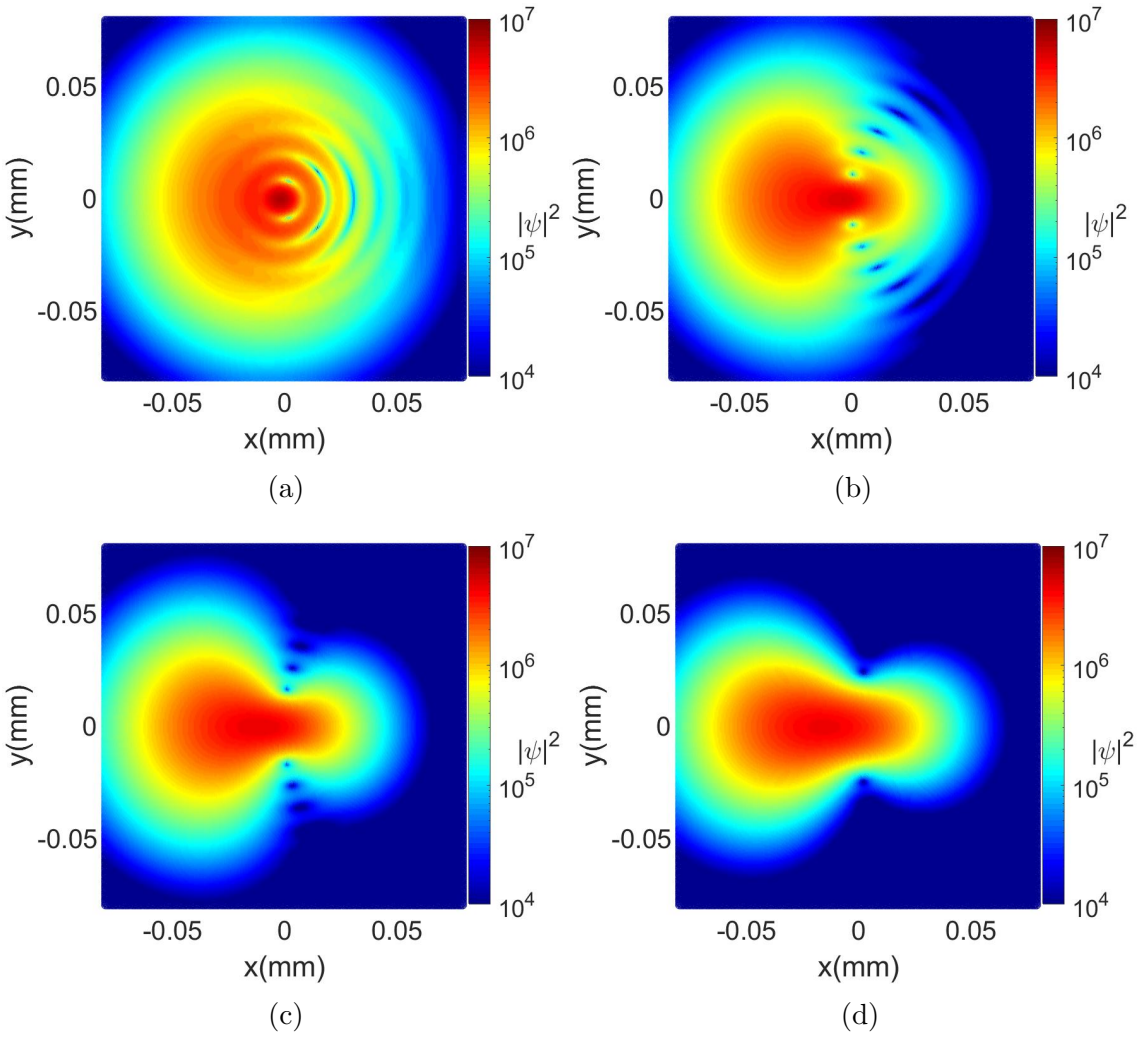

Figure 4.11: Cross-section in the x-y plane of the tilted torus with varying tilt widths at time $t = 0.1$ s. By increasing the time value we can see how in (b) the low density regions has begun to split off into a series of anti-nodes along the diagonal as in (c). We utilise a torus that has a radius of 20 μm and a width of 2 μm. All other parameters are appropriate for the trapping of a rubidium-87 Bose-Einstein condensate. (a) $\sigma_{\theta'} = \frac{\pi}{2}$, (b) $\sigma_{\theta'} = \frac{\pi}{4}$, (c) $\sigma_{\theta'} = \frac{\pi}{6}$ and (d) $\sigma_{\theta'} = \frac{\pi}{8}$.

In figures 4.10-4.11(a), we see that the anti-nodes do not appear to be present; instead, we see the ripple of interference fringes emanating from the centre of the ring out towards the region of lowest density in the initial state. When the angle $\sigma_{\theta'}$ is decreased in figures 4.9-4.11(b) and 4.9-4.11(c) we see that the ripples observed in figures 4.9-4.11(a) begin to form areas of increasingly low density that emanate from the centre of the system. In figures 4.9-4.11(b) these low density regions look to be in a similar location to the troughs in the ripple observed in figures 4.9-4.11(a). By shrinking the angle $\sigma_{\theta'}$ to $\frac{\pi}{6}$, these low-density regions break off into isolated spots

located on either side of the x-axis and travel out diagonally. As time progresses, the angle of these anti-nodes with respect to the x-axis increases. However, we see that if the angle $\sigma_{\theta'}$ becomes too small in figures 4.10-4.11(d) then the anti-nodes do not begin to form. This lack of anti-nodes is due to the reduction in self-interference within these systems. The characteristic anti-nodes can no longer form because they are formed from this self-interference. In particular, the anti-nodes are a feature of the asymmetry of the system and are dependent on the system's initial state. This feature appears to be unique to the asymmetric system since it is not a property we observed in previous chapters of this thesis when considering the symmetric system. This property is a clear indication of the asymmetry of the system. It might be used to identify the system's initial tilt or gradient since its behaviour depends on this property.

In the latter part of this chapter, we will compare our analytical results with numerical integration against those achieved utilising a numerical simulation of the same initial state. However, before doing this, we want to look at the asymmetric hollow shell system first.

4.5 Hollow shell with micro-gravity

Having demonstrated how the tilted ring wave function behaves, we now focus on the second of our two models in the hollow shell. This system, in particular, is of interest regarding experiments that aim to measure micro-gravity. Adding a gravitational gradient to our system will result in a deformation of the ground state of the system and, therefore, by extension, the interference pattern generated upon release from the trapping potential. We will again be using the same approach discussed in the toroidal geometry with a biasing function dependent on the angle ϕ' where ϕ' is the angle to the vertical. By making this choice, we will assume that the gravitational acceleration direction is directly down. The bias that we will be using takes the

following form:

$$F(\phi') = \exp\left(-\frac{(\phi' - \phi_0)^2}{2\sigma_{\phi'}}\right), \tag{4.15}$$

with $\phi_0 = \pi$ and $\sigma_{\phi'}$ the width of the Gaussian. We use this function to multiply our expression for the hollow shell prior to the integration to add a gradient or bias to make the resulting wave-function asymmetric. With this bias we obtain an expression for the wave equation in the following form:

$$\begin{aligned}\psi_{\text{tilted-hs}}(x, y, z, \tau) =& \frac{\sigma_0^{\frac{3}{2}}}{(2\pi)^{\frac{3}{4}}\tilde{\sigma}(\tau)^3} \int_0^{2\pi} d\theta' \int_0^{\pi} \\ & \exp\left(-\frac{(x - R\sin(\phi')\cos(\theta'))^2 + (y - R\sin(\phi')\sin(\theta'))^2}{4\tilde{\sigma}(\tau)^2}\right) \\ & \times \exp\left(-\frac{(z - R\cos(\phi'))^2}{4\tilde{\sigma}(\tau)^2}\right) \exp\left(-\frac{(\phi' - \phi_0)^2}{2\sigma_{\phi'}}\right) \sin(\phi')\, d\phi'.\end{aligned} \tag{4.16}$$

This function does not appear to have an analytical solution, so we need to numerically integrate the function using the algorithm outlined in equation (4.7). Finally, we can obtain a wave function for our tilted hollow shell to see how this system behaves under free expansion.

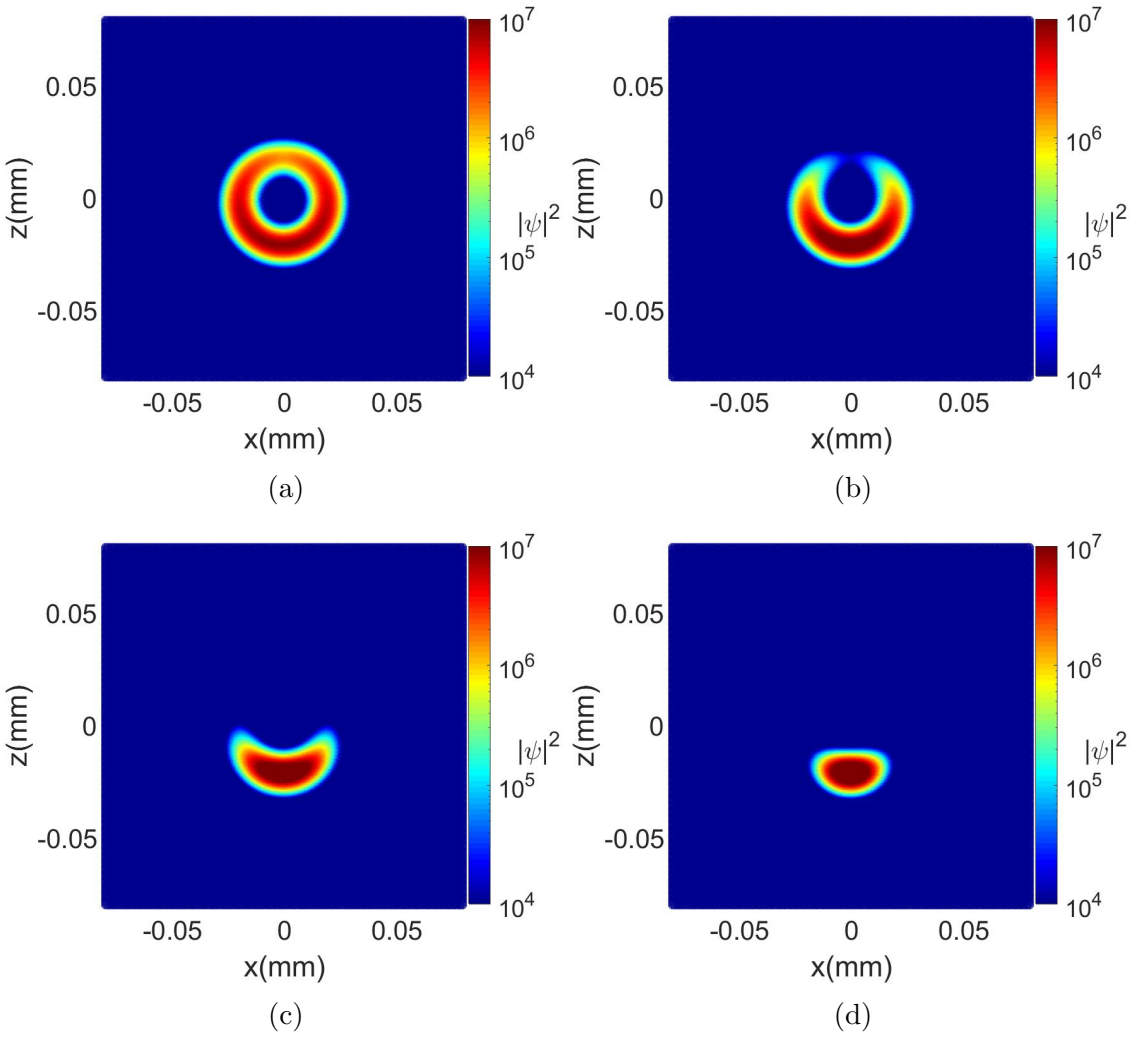

Figure 4.12: Cross-section in the x-z plane of the tilted hollow shell with varying tilt widths at time $t = 0$. We utilise a torus that has a radius of $20\mu m$ and a width of $2\mu m$. All other parameters are appropriate for the trapping of a rubidium-87 Bose-Einstein condensate. (a) $\sigma_{\theta'} = \frac{\pi}{2}$, (b) $\sigma_{\theta'} = \frac{\pi}{4}$, (c) $\sigma_{\theta'} = \frac{\pi}{8}$ and (d) $\sigma_{\theta'} = \frac{\pi}{16}$.

In figure 4.12, we see that we are getting very similar results to those we obtained for the toroidal system in figure 4.8, with a clear bias in the wave function at the bottom of the shell. Given that we are applying the same weighting function to the function, we expected this since the cross-section of both systems in an x-z or y-z plane for the hollow shell system and the x-y plane in the toroidal system will be largely similar. This similarity in the systems means we expect the starting system to be similar in appearance. We would also expect that the cross-sections for both systems might look fairly similar once expanded, at least when comparing the x-y plane for the toroidal system and the x-z or y-z planes of the hollow shell systems.

In figure 4.13 we plot the system at a time $t = 0.05$ seconds.

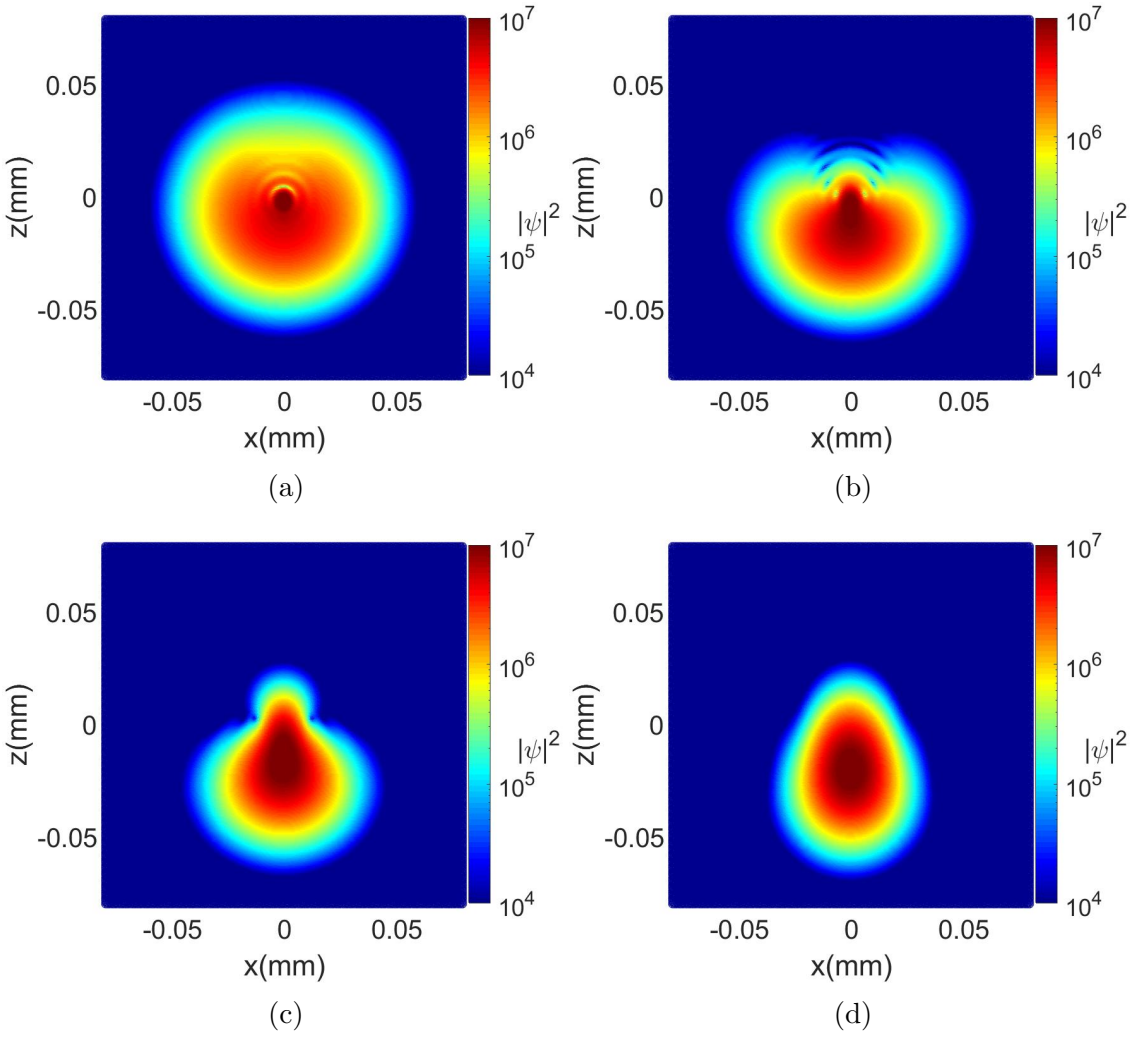

Figure 4.13: Cross-section in the x-z plane of the tilted hollow shell with varying tilt widths at time $t = 0.05$ s. We utilise a torus that has a radius of 20 μm and a width of 2 μm. All other parameters are appropriate for the trapping of a rubidium-87 Bose-Einstein condensate. (a) $\sigma_{\theta'} = \frac{\pi}{2}$, (b) $\sigma_{\theta'} = \frac{\pi}{4}$, (c) $\sigma_{\theta'} = \frac{\pi}{8}$ and (d) $\sigma_{\theta'} = \frac{\pi}{16}$.

We can see clearly in figure 4.13 that we can make many comparisons to figures 4.7-4.8 with the wave function making a very similar appearance in both systems in their retrospective planes. The real difference in the two systems arises in the x-z plane of the toroidal system as the toroidal wave packet allows for the free expansion in the z-direction due to the initial system not having portions of the wave function in this direction. This property results in the vertical peaks observed in the first free-expansion figures. In the hollow shell system, there is no such space for the wave packet to expand into due to the symmetry, which means that we do not observe

this same phenomenon in this system. The key features of the anti-nodes emerging and how if the initial biasing is too narrow, the interference fringes do not appear to emerge are present in both systems. Having looked at both the hollow shell and toroidal wave functions, picking out key features that emerge, we must now test the rate at which the systems diverge from the numerical simulation to confirm the accuracy of these results.

4.6 Comparison to the numerical simulation

Having demonstrated that we can obtain results for asymmetric systems, we now want to compare our results to numerical simulations of the same systems. In doing so, we can test the validity of our methodology against the numerical approach, allowing us to see how the two approaches diverge over time and to what extent. We will take each of our simulated systems at a time equal to zero to test this. We will then numerically simulate these systems utilising the SSFM outlined in previous chapters of this thesis. We will then compare these numerical simulations to our integral at various time values up until the time of emergence of the central fringe for the symmetric systems at $t = 0.05$ seconds. We will again look at the infidelity between these two results as a function of time. This infidelity tells us the rate of divergence between these two approaches. We are using the same starting state for both the numerical simulation and the equation; therefore, at time zero, the infidelity will also be zero but should increase as time progresses. For the tilted toroidal system, when we plot this infidelity against time in figure 4.14, which we will discuss below.

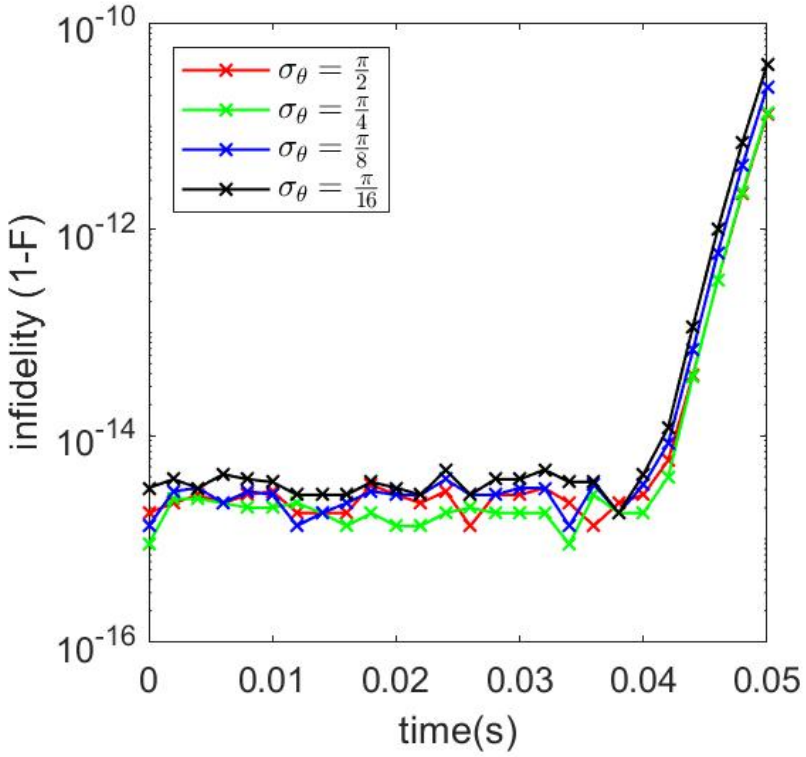

Figure 4.14: Infidelity when comparing our numerical integration of the torus to the simulated system at varying time values. All variables are consistent with those used in figure 4.5 and figure 4.7. We limited the time frame of these simulations to exclude cross-boundary interactions in the numerical simulation, which leads to a divergence in the two models that is dependent on the simulation environment and not the dynamical evolution of the system as would be observed experimentally. The variations observed initially in the infidelity is likely due to numerical fluctuations and are low in magnitude.

From this figure, we can see that the divergence in our two approaches is minimal with a fidelity measuring of the order 10^{-11}. This value indicates that there is little difference between the numerically simulated results and those obtained through the numerical integration of our analytical expression. However, as the wave function reaches the time at which the central fringe emerges in the symmetric system, there is an increase in infidelity. We were expecting to see this property due to the cross-boundary interactions present in our simulation. Nevertheless, the two systems remain in close agreement with one another with a high fidelity. In figure 4.14, we see that the smaller the width of the biasing Gaussian, the greater the level of infidelity as the time approaches $t = 0.05$ seconds. This property is likely because the

initial state has a higher density as the same amount of wave function is contained within a smaller volume due to the tilting. This increase in density leads to a greater rate of expansion, and therefore one would expect the cross-boundary interactions to be stronger at this time.

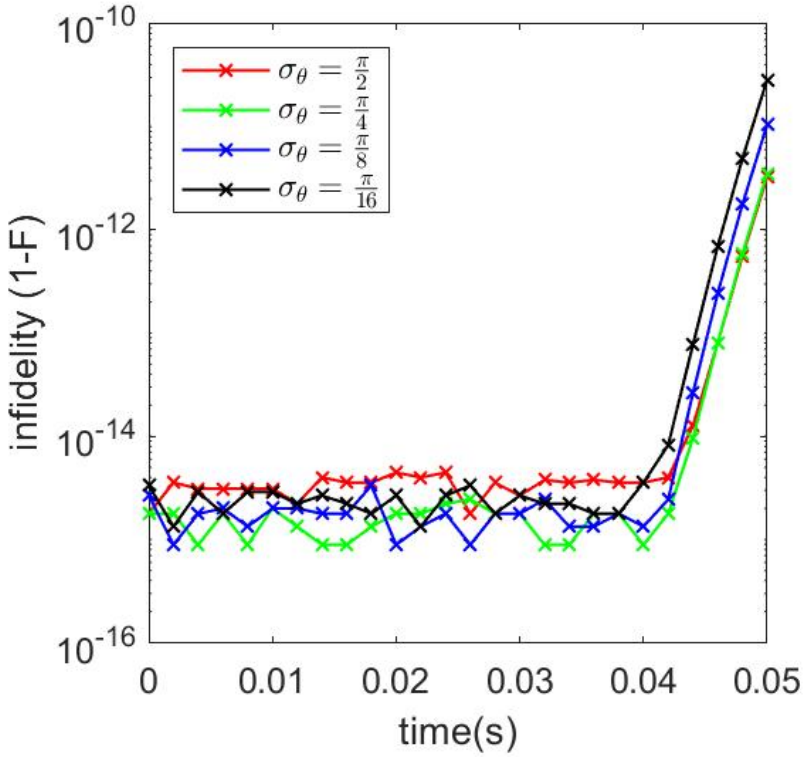

Figure 4.15: Infidelity when comparing our numerical integration of the hollow shell to the simulated system at varying time values. All variables are consistent with those used in figure 4.12 and figure 4.13. We limited the time frame of these simulations so as to exclude cross-boundary interactions in the numerical simulation, which leads to a divergence in the two models that is dependent on the simulation environment and not the dynamical evolution of the system as would be observed experimentally. The variations observed initially in the infidelity is likely due to numerical fluctuations and are low in magnitude.

We repeat the same checks for the hollow shell. In figure 4.15, we plot the infidelity over time for the hollow shells. Again we find that in figure 4.15 that the infidelity drift over time is minimal with the same increase as the wave-function approaches the time of emergence for the central peak in the symmetric system. Furthermore, we again see that the more the wave-function is biased towards one location, the quicker the divergence, again consistent with the higher density of the

initial state leading to a greater expansion rate. Overall, both results demonstrate that the drift between the two approaches is minimal and that they are in close agreement with one another.

4.7 Conclusions

We have shown how our methodology might be applied to an asymmetric system whilst maintaining a high fidelity or agreement to numerical simulations of the same system. We have found that it is not always possible to find an analytical solution to the integral generated by our methodology. However, we have demonstrated that a numerical integration method might be applied in these situations and that this numerical integration converges upon the solution fairly quickly. In particular, we found that, in the two types of systems that we have tested in this chapter, within thirty-six spatial steps or Gaussians, the numerical integration of our equation has an infidelity of less than 10^{-5} to the numerically simulated ground-state. This infidelity indicates that the two approaches are in close agreement with one another, with very little difference between the two systems. We then demonstrated that the divergence of our analytical approach compared to numerical simulations of the same asymmetric system is very small. This divergence does increase over time, but this is likely due to cross-boundary interactions arising in the numerical simulations. We have demonstrated the versatility of our approach and how it might be applied to asymmetric systems whilst maintaining some of the advantages over the numerical approach. These advantages include not requiring the evaluation of intermediate time spatial steps. This non-iterative approach means minor inaccuracies do not compound with the number of spatial steps while maintaining a high fidelity with our numerical simulations. We will now turn our attention to a different system for the remainder of this thesis, namely, looking at how the driving of a potential can generate stable atom trapping schemes where the region of stability is unfavourable without the driving.

Chapter 5

The atomic scale elastic inverted pendulum

5.1 Introduction

The inverted pendulum, also known as the Kapitza or Stephenson pendulum, is a well-known mechanical phenomenon whereby oscillations of a rigid pendulum may lead to the inverted position becoming stable. First described by Andrew Stephenson in 1908 [40], the reasons for stability were not fully understood until 1951 when P. L. Kapitza provided the analytical insight [41, 42]. Landau and Lifshitz later described this stability via an effective potential [43]. The stability of this inverted pendulum has proven to be of high interest, with many papers dedicated to various aspects and properties of the system [44, 45, 46]. Another pendulum phenomenon that has been studied extensively is the behaviour of an elastic pendulum, with perhaps the first study on it being made in 1933 by A. Vitt and G. Gorelik [54] with many subsequent papers on this topic [55, 56, 57, 100]. The combination of the two pendulums has received some study in both two [47, 48] and three dimensions [49, 100].

For the most part, those studies of the inverted pendulum were in the context of a mechanical system; in contrast, we are interested in seeing whether this mechanism might apply to an atomic system to generate atomic trapping schemes with stable

gravitationally unfavourable positions. In particular, we will consider a system on the scale of a magnetic quadrupole atom trap [50, 51, 52, 53]. A magnetic quadrupole generates an adiabatic potential which confines atoms with a degree of elasticity so our model will reflect this through use of the elastic inverted pendulum. Therefore, we aim to demonstrate the feasibility of the elastic inverted pendulum on an atomic trapping scale, understanding the stability regions. In figure 5.1, we show a diagram of the approximate system we shall be using in this chapter. This figure assumes that the pendulum has a radial trapping frequency ω and a spring constant κ. The pendulum is driven vertically with $u = A\cos(\Omega t)$ with A the driving amplitude and Ω the driving frequency. Finally, we consider the system to have a radial trapping frequency ω. We shall be using a comoving Cartesian reference frame to minimise erratic movement, which can cause problems when numerically simulating systems of this nature. In section 2 of this chapter, we will derive the equations of motion for an inverted elastic pendulum. We will then, in section 3, look at how the system behaves and test the system's stability, including varying the starting conditions, to demonstrate the system's robustness. Also, in section 3, we will look at two different driving methods which demonstrate interesting results, namely multi-dimensional driving, which leads to finer pendulum bob localisation and linearly reduces the driving frequency leading to total system energy loss. In this chapter, we will use m as the mass of the pendulum, θ as the pendulum's angle with the vertical, r the length of the pendulum, ℓ_0 as the rest length of the pendulum and u as the current height of the pendulum's fulcrum above the rest height. Now that we have defined the system, we need to define the system's equations of motion.

5.2 Equations of Motion

Starting with the two-dimensional system, we will be using many of the same steps as utilised by Lynch [100] as a guide. Using a comoving reference frame as the resulting equation can be approximated as a Mathieu equation [101] gives us some

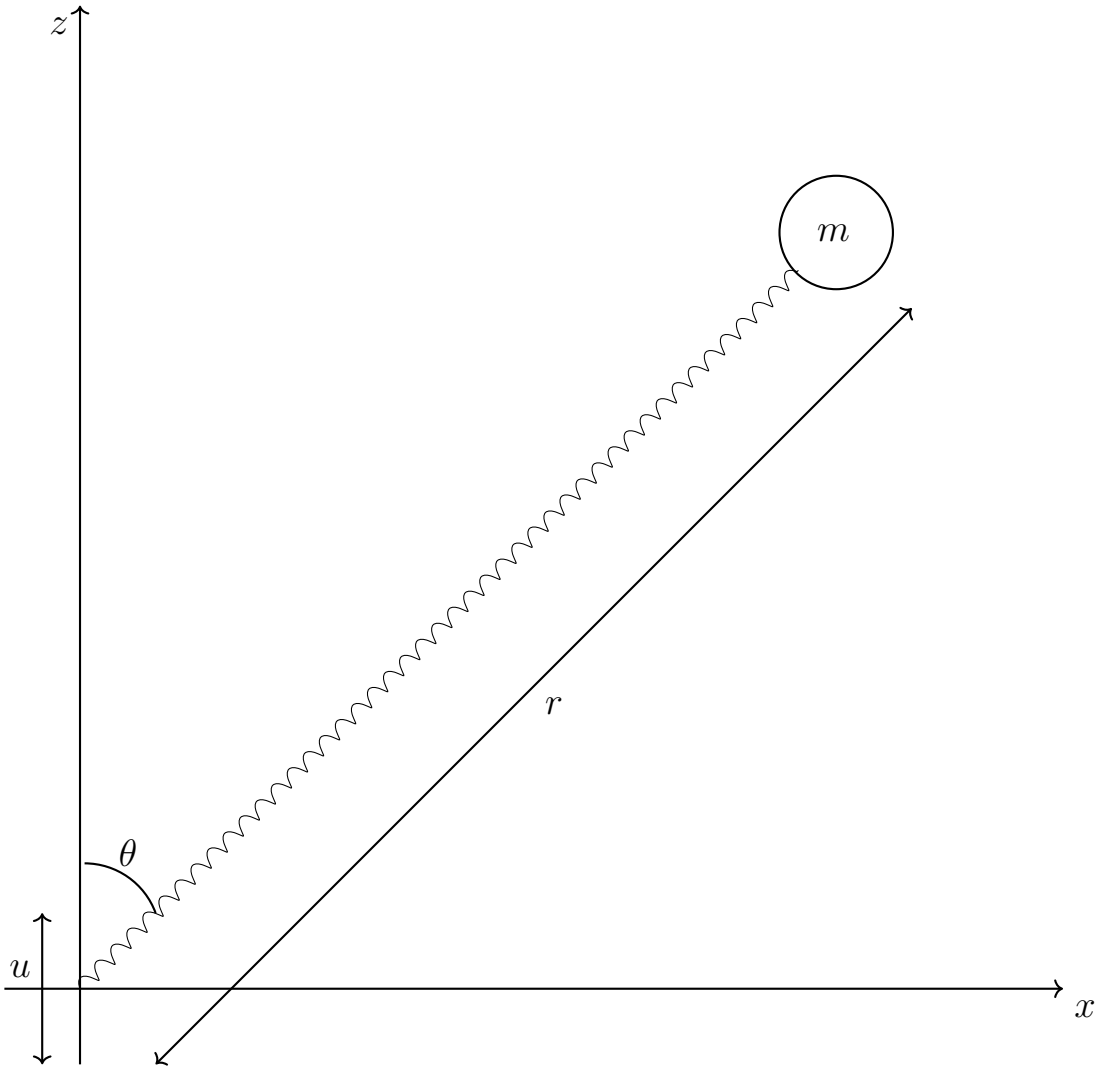

Figure 5.1: Diagram of the inverted elastic pendulum inside a co-moving Cartesian reference frame. θ is the angle of the pendulum to the vertical, u is the time dependent vertical displacement of the pendulums fulcrum, m the mass of the pendulum and r the time-dependent length of the pendulum consisting of a rest length ℓ_0 and an extension $\delta\ell$.

insight into regions of stability. Mathieu equations are in the following form:

$$\frac{\partial^2 y}{\partial x^2} + (a - 2q\cos(x))y = 0. \tag{5.1}$$

Mathieu functions tend to appear in periodic oscillation problems and are, therefore, well studied with clearly defined regions of stability and instability. For example, in figure 5.2, the grey-shaded areas are unstable, whereas the white areas are stable. A characteristic Mathieu function defines the bounds on each region.

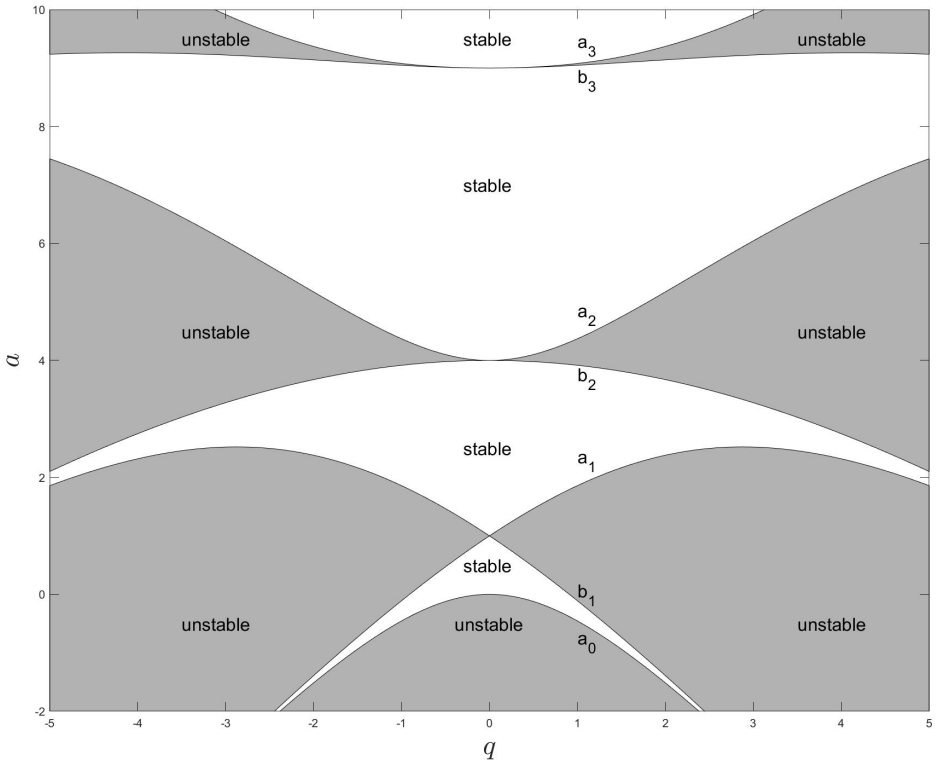

Figure 5.2: Graph showing the first four stable regions of the Mathieu equation. The areas that are shaded grey are unstable whereas those in white are stable solutions to the Mathieu equation.

Most of the literature on the inverted pendulum utilises a polar coordinate system. Here we present this approach to this system before discussing why we have chosen not to use this in obtaining our results. In polar coordinates, the Lagrangian of the system can be written in the following manner when in the comoving reference frame; note that in this reference frame, in such a system, the acceleration

of the pivot point is added to the gravitational acceleration in the $z-$direction of the pendulum bob. The reason for choosing a comoving frame is two-fold; firstly, in the comoving frame, the dynamics of the pendulum will be less erratic since, in the lab reference frame, there are two motions, one from the oscillation of the pendulum pivot point and the second from the oscillations due to the spring. In the comoving frame, we have just the spring dynamics to deal with, and as a result, the behaviour is less erratic. This choice of coordinates makes simulating the system easier since erratic behaviour often means that minor errors compound quicker to deviate the system from what might be observed experimentally. Secondly, from an analytic perspective, the choice of the comoving frame allows for a linearisation later, which we will be using to find an approximate region of stability for the system. We start here in the comoving frame by defining a Lagrangian equation for the system. The Lagrangian is simply the difference between the system's kinetic and potential energy. The kinetic energy is in the form $\frac{1}{2}mv^2$. There are two sources of potential energy, gravitational and spring energy, with gravitational energy mg and spring potential $\frac{1}{2}\kappa\delta x$ where δx is the relative extension from the rest length. In the comoving reference frame, the acceleration of the pivot point is added to the gravitational acceleration. All of this leads to the following expression for the two-dimensional Lagrangian of a driven spring pendulum in polar coordinates:

$$L = \frac{m}{2}\left[\left(\frac{dr}{dt}\right)^2 + \left(r\frac{d\theta}{dt}\right)^2\right] - m\left(g + \frac{d^2u}{dt^2}\right)r\cos\theta - \frac{\kappa}{2}(r-\ell_0)^2, \tag{5.2}$$

where κ is the spring constant of the system and all other variables as defined previously. Setting $u = A\cos(\Omega t)$ with A the amplitude of oscillation and Ω the frequency. We can utilise Lagrangian mechanics to obtain equations of motion for the system. The Euler-Lagrange equations for a Lagrangian state that,

$$\frac{d}{dt}\left(\frac{\partial L}{\partial \dot{\mathbf{x}}}\right) - \frac{\partial L}{\partial \mathbf{x}} = 0, \tag{5.3}$$

where $\mathbf{x}$ is a time-dependent variable, $\dot{\mathbf{x}}$ the time-derivative of this variable and

L is the Lagrangian function. If we start with our initial Lagrangian for a two-dimensional elastic pendulum in polar coordinates,

$$L = \frac{m}{2}\left[\dot{r}^2 + r^2\dot{\theta}^2\right] - m\,(g + \ddot{u})\,r\cos\theta - \frac{\kappa}{2}(r - \ell_0)^2, \tag{5.4}$$

we can then derive the equations of motion for this system. Firstly, we will consider the equations of motion for r. The first or derivative of the Lagrangian in terms of r gives us

$$\frac{\partial L}{\partial r} = mr\left(\frac{\partial\theta}{\partial t}\right)^2 - m\left(g + \frac{\partial^2 u}{\partial t^2}\right)\cos(\theta) - \kappa(r - \ell_0) \tag{5.5}$$

and the second order derivative gives us

$$\frac{d}{dt}\frac{\partial L}{\partial \dot{r}} = m\ddot{r}. \tag{5.6}$$

Substituting these expressions into equation (5.3) gives us an equation of motion for the system in r of

$$\frac{\partial^2 r}{\partial t^2} = r\left(\frac{\partial\theta}{\partial t}\right)^2 - \left(g + \frac{\partial^2 u}{\partial t^2}\right)\cos(\theta) - \frac{\kappa}{m}(r - \ell_0). \tag{5.7}$$

Next we look at the θ term. We find that the first order derivative of the Lagrangian is

$$\frac{\partial L}{\partial \theta} = mr\left(g + \frac{\partial^2 u}{\partial t^2}\right)\sin(\theta) \tag{5.8}$$

and the second order derivative is

$$\frac{d}{dt}\frac{\partial L}{\partial \dot{\theta}} = \frac{d}{dt}mr^2\frac{\partial\theta}{\partial t} = mr^2\frac{\partial^2\theta}{\partial t^2} + 2mr\frac{\partial r}{\partial t}\frac{\partial\theta}{\partial t}. \tag{5.9}$$

This gives the following expression for the time evolution of θ:

$$\frac{\partial^2\theta}{\partial t^2} = \frac{1}{r}\left((g+\ddot{u})\sin(\theta) - 2\dot{r}\dot{\theta}\right) \tag{5.10}$$

The driving term u we will substitute with a cosine driving term of

$$u = A\cos(\Omega t) \rightarrow \ddot{u} = -A\Omega^2\cos(\Omega t), \tag{5.11}$$

with A the driving amplitude and Ω the driving frequency. This driving motion gives the final expression for the equation of motion in the comoving reference frame of

$$\frac{\partial^2 r}{\partial t^2} = r\left(\frac{\partial\theta}{\partial t}\right)^2 - \left(g - A\Omega^2\cos(\Omega t)\right)\cos(\theta) - \frac{\kappa}{m}(r-\ell_0) \tag{5.12}$$

and

$$\frac{\partial^2\theta}{\partial t^2} = \frac{1}{r}\left((g - A\Omega^2\cos(\Omega t))\sin(\theta) - 2\frac{\partial r}{\partial t}\frac{\partial\theta}{\partial t}\right). \tag{5.13}$$

If we assume that the effect that the spring has on the system is negligible, then the equations may be linearised [48] in the following manner to obtain an of motion the angle θ that is in the form of a Mathieu equation. The linearization results in the expression

$$\frac{\partial^2\theta}{\partial\tau^2} - \frac{1}{1-\omega_0^2/\omega_s^2}\left[\frac{\omega_0^2}{\Omega^2} - \frac{A}{\ell_0}\cos(\tau)\right]\theta = 0, \tag{5.14}$$

whereby $\tau = \Omega t$, $\omega_0 = \sqrt{\frac{g}{\ell_0}}$ is the oscillating frequency and $\omega_s = \sqrt{\frac{\kappa}{m}}$ the spring frequency. Details of this linearization may be found in works by Ryland and Meirovitch[49] and Mazzilli [47]. The equation of motion for the radius can also be linearised. Arinstein and Gitterman [48] in their paper created a dimensionless relative contraction of the pendulum (R) in the following form:

$$R = \frac{r}{\ell_0} - \left(1 + \frac{\omega_0^2}{\omega_s^2}\right). \tag{5.15}$$

The linearised equation of motion for the relative contraction is in the following form,

$$\frac{\partial^2 R}{\partial \tau^2} + \frac{\omega_s^2}{\Omega^2} R = A\cos(\tau) \tag{5.16}$$

With the equations of motion for the angle θ in the form of a Mathieu equation, we can apply Mathieu equation knowledge to obtain an expression for the stable regions of the system. A typical Mathieu equation takes the form of the expression

$$w'' + (a - 2q\cos(2z))\, w = 0. \tag{5.17}$$

Comparing this to our expression for θ in equation (5.14) we find that we have

$$a = -\frac{g}{\Omega^2\left(\ell_0 - \frac{g}{\omega^2}\right)} \tag{5.18}$$

and

$$q = -\frac{2A}{\ell_0 - \frac{g}{\omega^2}}. \tag{5.19}$$

Redoing the Mathieu stability plot in figure 5.2 to reflect the parameters of our system, we then obtain a Mathieu stability plot utilising the properties of the inverted elastic pendulum in figure 5.3 for the parameters A and $\frac{g}{\Omega^2}$. The Mathieu equation has well-established stability regions, determining initial system conditions leading to a stable inverted elastic pendulum. In addition to this, Landau and Lifshitz [43] also state that for a pendulum to be stable in the inverted position, the inequality

$$A^2\Omega^2 > 2g\ell_0 \tag{5.20}$$

must be satisfied. In addition to this condition, there are a further two conditions

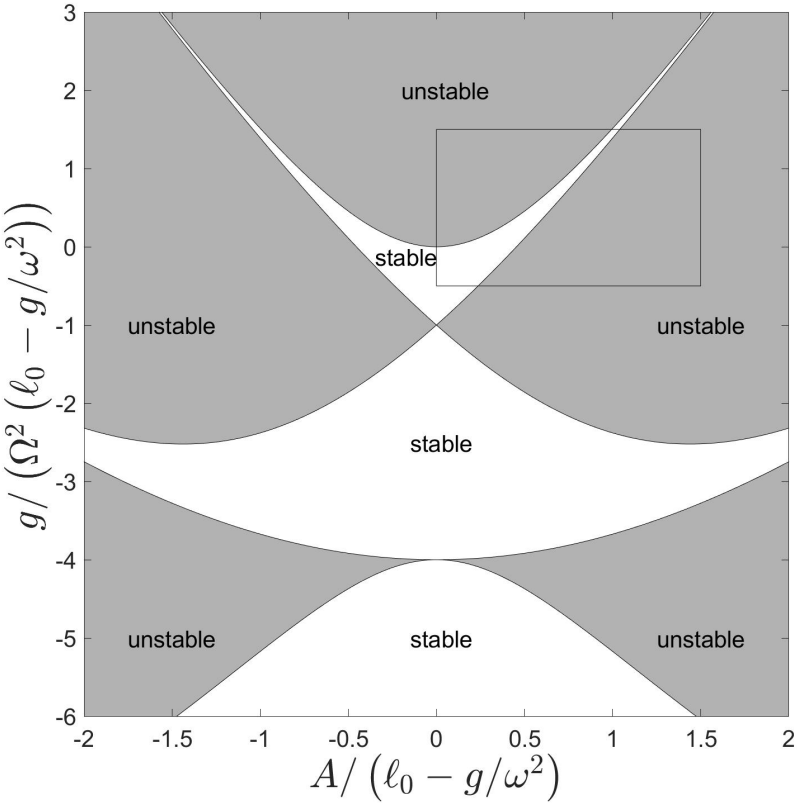

Figure 5.3: Stability of the equations of motion for the inverted pendulum. This graph was generated using $g = 9.81$ ms^{-1}, $\omega = 2.5 \times 10^4$ rad/s and $\ell_0 = 1 \times 10^{-5}$ m. The gray regions represent unstable variable combinations. In figure 5.4 we zoom in on the highlighted box which is where we might expect to find atom-trapping scale systems.

which we must consider. Firstly the driving amplitude must be less than the length of the pendulum. If this is not the case, the system quickly becomes overdriven and, therefore, more chaotic. Secondly, the driving frequency must be less than the trapping frequency. Otherwise, the system begins to break down. With these conditions established for the classical mechanical system, we can now turn our attention to a system consistent with an atom trap scale. With a system consistent with atom trapping, we have a fixed mass $m \sim 10^{-25}$. We might reasonably expect a broad range of feasible conditions for an atomic system. In table 5.5, we outline approximate ranges for the variables that one might reasonably expect to utilise experimentally. We have then focused on testing systems that fall within these ranges. With the above parameters, the system returns values of a and q in the

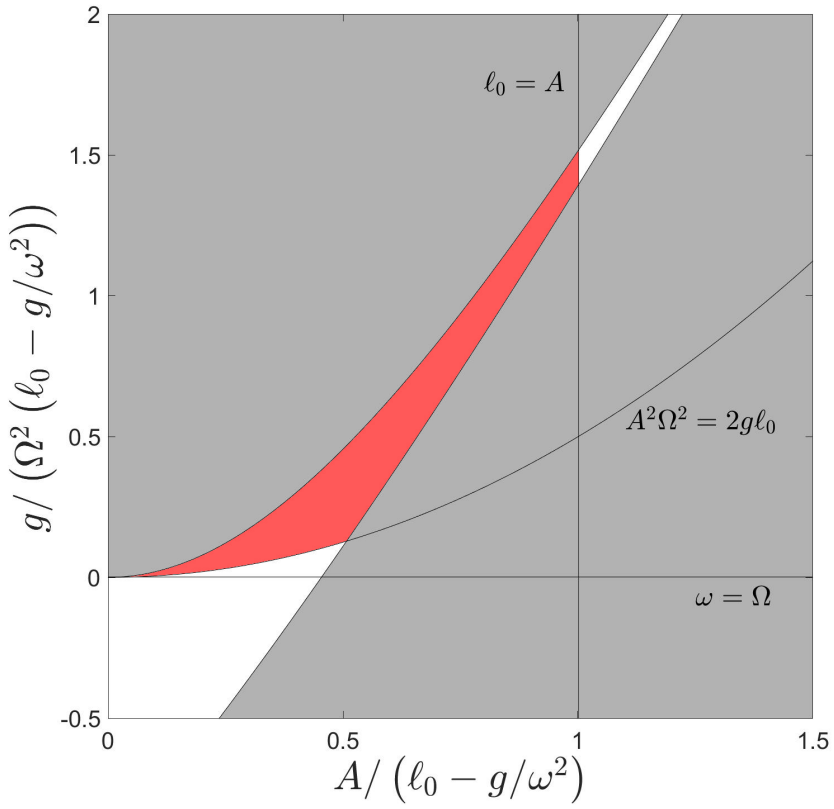

Figure 5.4: The grey regions represent unstable variable combinations. The red region is the predicted stable region within which we might expect to find a typical atomic system. We plot the stability regions of the Mathieu equation with our linearised equations of motion; the square represents the area where we might expect atomic systems to lie.

Mathieu equation, which are both negative for the most part. These quantities mean that the system lies in and around the first stability zone of the Mathieu equation, the boundary conditions of which are as follows [102]:

$$a_0(q) = -\frac{1}{2}q^2 + \frac{7}{128}q^4 - \frac{29}{2304}q^6 + \frac{68687}{18874368}q^8 + \cdots \tag{5.21}$$

and

$$a_1(q) = 1 + q - \frac{1}{8}q^2 - \frac{1}{64}q^3 - \frac{1}{1536}q^4 + \frac{11}{36864}q^5 + \frac{49}{589824}q^6 + \frac{55}{9437184}q^7 - \frac{83}{35389440}q^8 + \cdots . \tag{5.22}$$

A significant problem with this approach is that the system has to be linearised

Ω	$10^2 < \Omega < 10^5$ rad/s
ω	$10^3 < \omega < 10^6$ rad/s
ℓ_0	$10^{-6} < \ell_0 < 10^{-2}$ m
A	$10^{-8} < A < 10^{-3}$ m

Figure 5.5: Table showing the variable ranges over which the Mathieu equation is stable for our particular setup.

to obtain equations of motion. It is unclear whether this approximation will hold on the scale of an atomic trapping system; thus, any stability regions obtained using this method can only serve as a guide. Thus far, we have confined our pendulum to two dimensions. As the system is a pendulum, we can expect it to behave with an oscillatory motion. If the system is initially in the xz-plane, we would expect the motion to remain in this plane provided that the system is not initialised with an initial velocity in the ϕ-direction azimuthal angular direction. However, given that we want to study a system intended to emulate an experimental system, we want to introduce initial velocities in ϕ to see how the system behaves if the system is not initially at rest to test the robustness of the system. We will be covering this robustness in more detail later in this chapter, but we present the equations of motion here. An additional benefit to simulating the system in three dimensions is being able to simulate the system with an initial velocity in ϕ, which does not appear to affect the stability of the system but does make it easier to see the path of the pendulum as it evolves over time when plotted. This velocity allows us to see and understand the dynamics of the pendulum better when the pendulum follows a fairly consistent path and therefore overlaps itself over several cycles.

Additionally, we choose to utilise a Cartesian coordinate system over the perhaps more natural spherical coordinate system. This choice is because in polar coordinates, if the pendulum is primarily confined to an $x-z$-plane, when the pendulum passes over the vertical, the value of ϕ very rapidly will flip from positive to negative. This rapid shift in ϕ can lead to problems while simulating the system. Therefore, we choose to utilise a Cartesian coordinate system to avoid these problems. The Lagrangian in a three-dimensional Cartesian coordinate system in a lab-based reference

frame is as follows:

$$\begin{aligned} L =& \frac{m}{2}\left[\left(\frac{\partial x}{\partial t}\right)^2+\left(\frac{\partial y}{\partial t}\right)^2+\left(\frac{\partial z}{\partial t}\right)^2\right]-mz\left(g-A\Omega^2\cos\left(\Omega t\right)\right) \\ & -\frac{\kappa}{2}\left(\sqrt{x^2+y^2+z^2}-\ell_0\right)^2 \end{aligned} \tag{5.23}$$

We now apply Lagrangian dynamics principals to find the equations of motion. These equations of motions can be found utilising Lagrangian mechanics which states that

$$\frac{d}{dt}\frac{\partial L}{\partial \dot{x}}-\frac{\partial L}{\partial x}=0, \tag{5.24}$$

$$\frac{d}{dt}\frac{\partial L}{\partial \dot{y}}-\frac{\partial L}{\partial y}=0 \tag{5.25}$$

and

$$\frac{d}{dt}\frac{\partial L}{\partial \dot{z}}-\frac{\partial L}{\partial z}=0. \tag{5.26}$$

By substituting in the Lagrangian in equation (5.23) to the above expressions we can find the equations of motion for the system. Firstly, the first derivative of the Lagrangian in terms of x results in the expression

$$\frac{\partial L}{\partial x}=\kappa x\left(1-\frac{\ell_0}{\sqrt{x^2+y^2+z^2}}\right) \tag{5.27}$$

and the second derivative gives the expression.

$$\frac{d}{dt}\frac{\partial L}{\partial \dot{x}}=m\frac{\partial^2 x}{\partial t^2} \tag{5.28}$$

From these we therefore find the equation of motion for the system in x is

$$\frac{\partial^2 x}{\partial t^2}=\frac{\kappa x}{m}\left(\frac{\ell_0}{\sqrt{x^2+y^2+z^2}}-1\right). \tag{5.29}$$

The same process can be repeated for both y

$$\frac{\partial^2 y}{\partial t^2} = \frac{\kappa y}{m}\left(\frac{\ell_0}{\sqrt{x^2+y^2+z^2}} - 1\right) \tag{5.30}$$

and z

$$\frac{\partial^2 z}{\partial t^2} = \frac{\kappa z}{m}\left(\frac{\ell_0}{\sqrt{x^2+y^2+z^2}} - 1\right) - g + A\Omega^2\cos(\Omega t) \tag{5.31}$$

with results analogous across the three coordinates. The equation of motion in the z coordinate has an additional cosine term which is the result of the vertical driving of the system.

Having acquired equations of motion in the comoving reference frame in Cartesian coordinates, we now want to understand the system's dynamics. We have already outlined a linearisation in polar coordinates to find a stability region utilising a Mathieu equation. However, we have identified that this has utilised an approximation based on the assumption that the spring component does not significantly impact the system's dynamics. In our atomic scale system, it is not clear whether this is a valid approximation that we can make. If we do not make the linearisation approximation, the equations are in a form without a straightforward way to form the equation for the time evolution of x, y and z. Therefore, we want to test whether the linearisation is appropriate and produces accurate results. To test this, we will be utilising a numerical simulation approach. One consideration we want to make when choosing our methodology is that we wish to include an adaptive time step into our algorithm. The desire for an adaptive time step is due to a pendulum system with periods of both high and low velocities.

While at a high velocity, we want the time step to be smaller to reduce errors, whereas, at low velocity, we want to have larger time steps to ensure simulation run-time is not too high. A typical approach for numerical simulation is utilising a Runge-Kutta approach [103]. The standard Runge-Kutta algorithm does not naturally include an adaptive time step, but we can use a modified version of this,

namely, the Runge-Kutta-Fehlberg algorithm (RKF45) [104]. This algorithm utilises an $\mathcal{O}(h^4)$ with an $\mathcal{O}(h^5)$ error estimator where h is the time step. The error estimator is used to set the adaptive time step by comparing the error estimator to a user-defined acceptable error range. When using this method, we want to be using both an upper and lower bound on this error since if the error is too small, one can afford to increase the time step to improve run times. Suppose it is above the acceptable error threshold. In that case, the time step can be reduced, and the current iteration is repeated until the error returns to an acceptable level. This RKF45 algorithm starts with an expression for the initial state of the system in

$$\frac{\partial y_i}{\partial x} = f_i\left(x, y_1, y_2, \cdots y_n\right). \tag{5.32}$$

From this we calculate the following intermediary steps so that

$$k_1 = hf\left(x, y\right), \tag{5.33}$$

$$k_2 = hf\left(x + \frac{1}{4}h, y + \frac{1}{4}k_1\right), \tag{5.34}$$

$$k_3 = hf\left(x + \frac{3}{8}h, y + \frac{3}{32}k_1 + \frac{9}{32}k_2\right), \tag{5.35}$$

$$k_4 = hf\left(x + \frac{12}{13}h, y + \frac{1932}{2197}k_1 - \frac{7296}{2197}k_2 + \frac{7296}{2197}k_3\right), \tag{5.36}$$

$$k_5 = hf\left(x + h, y + \frac{439}{216}k_1 - 8k_2 + \frac{3680}{513}k_3 - \frac{845}{4104}k_4\right) \tag{5.37}$$

and

$$k_6 = hf\left(x + \frac{1}{2}h, y - \frac{8}{27}k_1 + 2k_2 - \frac{3544}{2565}k_3 + \frac{1859}{4104}k_4 - \frac{11}{40}k_5\right). \tag{5.38}$$

This results in a new value of y in the form:

$$y(x+h) = y(x) + \frac{16}{135}k_1 + \frac{6656}{12825}k_3 + \frac{28561}{56430}k_4 - \frac{9}{50}k_5 + \frac{2}{55}k_6 \tag{5.39}$$

An estimation of the truncation error can be found by substituting these same intermediary steps into the expression

$$TE = \left| \frac{1}{360}k_1 - \frac{128}{4275}k_3 - \frac{2187}{75240}k_4 + \frac{1}{50}k_5 + \frac{2}{55}k_6 \right|. \tag{5.40}$$

This truncation error can help us check whether the step size is too large and adjust this accordingly. Applying our Runge-Kutta-Fehlberg algorithm to these equations of motion, we can simulate the evolution of our system. For full details, please refer to the appendix C. The reason for this change in the coordinate system and reference frame is that the simulation time dramatically reduces, and the movement in the coordinates x, y and z are less erratic than their spherical coordinate counterparts. We can convert our results into spherical coordinates if desired using a simple coordinate transformation. The Runge-Kutta method works for first-order differential equations; therefore, we have to rewrite each of the expressions as first-order differential equations by introducing the following identities:

$$X = \frac{\partial x}{\partial t}, \tag{5.41}$$

$$Y = \frac{\partial y}{\partial t} \tag{5.42}$$

and

$$Z = \frac{\partial z}{\partial t}. \tag{5.43}$$

As a result we now have six, interdependent, first order differential equations with

the other three accompanying expressions being

$$\frac{\partial^2 X}{\partial t^2} = \frac{\kappa x}{m}\left(\frac{\ell_0}{\sqrt{x^2+y^2+z^2}} - 1\right), \tag{5.44}$$

$$\frac{\partial^2 Y}{\partial t^2} = \frac{\kappa y}{m}\left(\frac{\ell_0}{\sqrt{x^2+y^2+z^2}} - 1\right) \tag{5.45}$$

and

$$\frac{\partial^2 Z}{\partial t^2} = \frac{\kappa z}{m}\left(\frac{\ell_0}{\sqrt{x^2+y^2+z^2}} - 1\right) - g + A\Omega^2\cos(\Omega t). \tag{5.46}$$

We have used MATLAB run on the University of Sussex's High-Performance Computing cluster (HPC) for our numerical simulations. The HPC allowed us to perform multiple simulations simultaneously, and the time it takes to run the simulations is shorter than possible on a conventional desktop computer. For this thesis, we set a tolerance range of $10^{-3} > \text{error} > 10^{-6}$; this tolerance range seemed to give a good balance between efficient run times and accuracy. We also wanted to prioritise accuracy over run time when possible; as such, our requirements were more stringent on the upper bound so that if any of the six equations fell above the tolerance, then the whole step was rejected, and the time step decreased. On the other hand, we only increased the time step with the lower bound if every equation fell below the tolerance. This decision was to ensure that we did not end up in a loop whereby one parameter fell below the minimum tolerance and, therefore, the time step was increased, only to find that this caused one of the equations to have too large an error and the time step having to be decreased back down to the previous increment. One valuable property to study is the energy of the system. Since all equations thus far have been in the comoving frame, we need to convert our parameters back into the lab frame. Since this system is only being driven vertically, the x and y portions do not need to be modified, but the equations in z must be changed.

In particular,

$$z_{\text{lab}} = z_{\text{comoving}} + A\cos(\Omega t) \tag{5.47}$$

which, when differentiated, gives us

$$\left(\frac{\partial z}{\partial t}\right)_{\text{lab}} = \left(\frac{\partial z}{\partial t}\right)_{\text{comoving}} - A\Omega\sin(\Omega t). \tag{5.48}$$

The equations for the kinetic and potential energy in the lab reference frame, utilising the comoving values for x, y and z are as follows:

$$KE_{\text{lab}} = \frac{m}{2}\left(\left(\frac{\partial x}{\partial t}\right)^2 + \left(\frac{\partial y}{\partial t}\right)^2 + \left(\left(\frac{\partial z}{\partial t}\right) - A\Omega\sin(\Omega t)\right)^2\right) \tag{5.49}$$

$$\begin{aligned} PE_{\text{lab}} =& mg\left(z_{\text{comoving}} + A\cos(\Omega t)\right) \\ \textit{and} \qquad & + \frac{\kappa}{2}\left(\sqrt{x^2 + y^2 + \left(z_{\text{comoving}} + A\cos(\Omega t)\right)^2} - \ell_0\right)^2. \end{aligned} \tag{5.50}$$

The system's total energy in the lab reference frame is the sum of these two expressions.

5.3 Numerical simulations of the elastic inverted pendulum

Now that we have the equations for motion and our numerical simulation methodology, we can generate results based on a wide range of variables. We put limits on the four variables Ω, ω, A and ℓ_0 that fall within what we consider experimentally viable for an atom trap. The variables we selected were the same as seen in Table 5.5. Testing various combinations of these variables will help us build an image of this system's stable regions. For our simulations, we consider a system stable if it remains above the horizontal over a period of one second. By remaining above the

horizontal over a period of one second, the system is demonstrating that the mechanics involved can maintain its inverted position over the time period since, with the absence of driving in the initial system, the pendulum will naturally fall below the horizontal due to the effects of gravity much before the one second has elapsed. Figure 5.6 shows the typical path of a stable set of variables and is what we might expect to see in similarly stable systems:

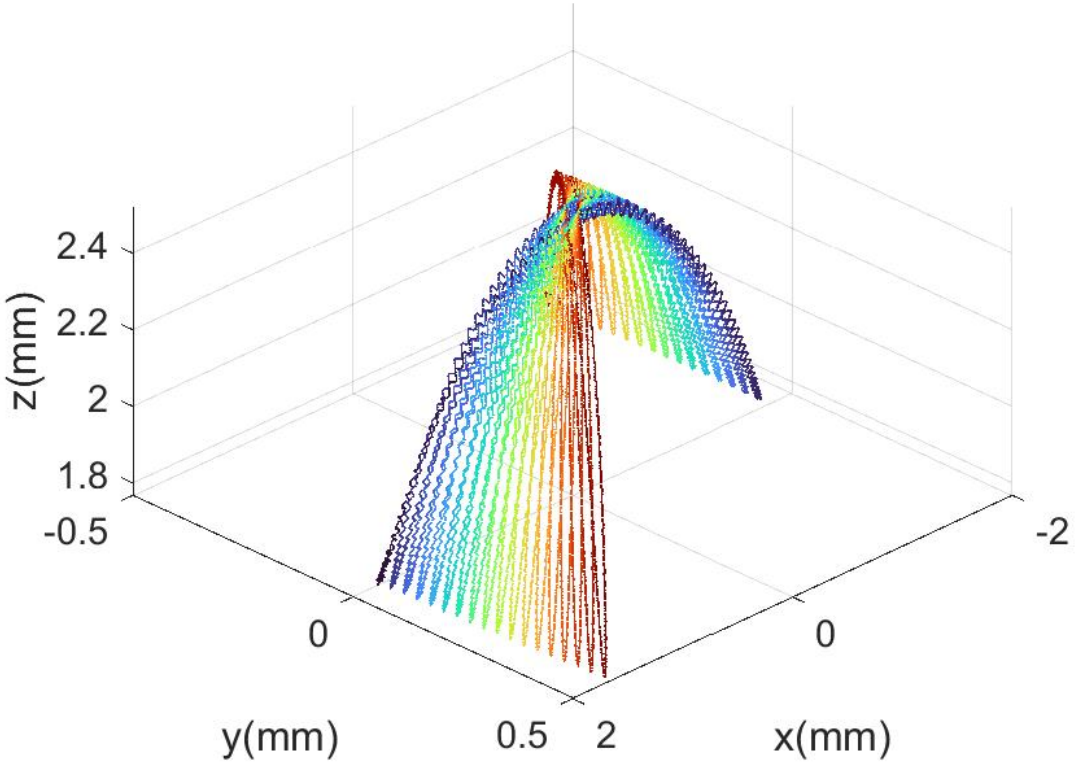

Figure 5.6: Typical trajectory of a stable system in three dimensions with the following parameters. The initial angle $\theta = \frac{\pi}{4}$, driving frequency $\Omega = 16000$ rad/s, ω the radial trapping frequency 25000 rad/s, rest length 2.5×10^{-3} m and driving amplitude $A = 2.5 \times 10^{-5}$ m. These four parameters were selected because we consider this to form a very stable system. By this, we mean that despite the relatively large angle of $\theta = \frac{\pi}{4}$, the pendulum remains in the vertical position, oscillating side to side, over a period of one second. The blue represents the start of the simulation and the red the end; yellow is somewhere in the middle with our colour scale. Additionally, we have induced a velocity, initially in the y-direction of 1 ms^{-1}. This velocity ensures that the typical path will rotate around the vertical axis to improve the clarity of the diagram. This velocity does not seem to affect the stability of the pendulum.

Figure 5.6 shows that the typical path forms a shell-like path that avoids the pole. We can see little variation in the x-z plane, where the system forms a smooth arc. However, we observe that in the y-z plane, the system will vary, forming a shell-like path that avoids the pole. We might expect these variable ranges to lead to results in and around the Mathieu equation's first stability region. We note that if we simulate a system and find that it is stable at a fixed initial angle θ, we would expect, given that we initialise the system at rest, that the system is also stable when initialised at a smaller initial angle. Using the upper and lower bound of the first stable region of the Mathieu equation and the inequality

$$A^2\Omega^2 > 2g\ell_0, \tag{5.51}$$

which defines the stable inverted positions. We obtain a good idea of which combinations we might expect to be stable. We can then test these using our numerical simulations to determine the validity of these conditions, given that we made some assumptions in generating these conditions. We then compare the theoretically stable variable combinations with simulated results. Firstly we will look at the two-dimensional case. Each time we simulated the two-dimensional system, the pendulum was initially at rest and placed at $\theta = 10^{-5}$. The red points represent combinations of variables that remain stable for one second under these conditions in figure 5.7. The black dots refer to theoretically stable variable combinations that, when simulated, produced unstable systems. The opacity of the black dots is dependent on the number of variable combinations, which proved unstable. Plotting all two-variable combinations together produces figure 5.7, In the top-left graph of figure 5.7, we can see a well-defined line of an unstable variable combination of variables where $\omega > \Omega$. This line, therefore, indicates that to improve the chances of stability, ω has to be greater than Ω. This condition is not a hard and fast rule since some combinations defy this inequality but remain stable. Additionally, when we look at the bottom right results, we see a clearly defined line again. This time, it would appear that ℓ_0 must be two orders of magnitude greater than A. Repeating

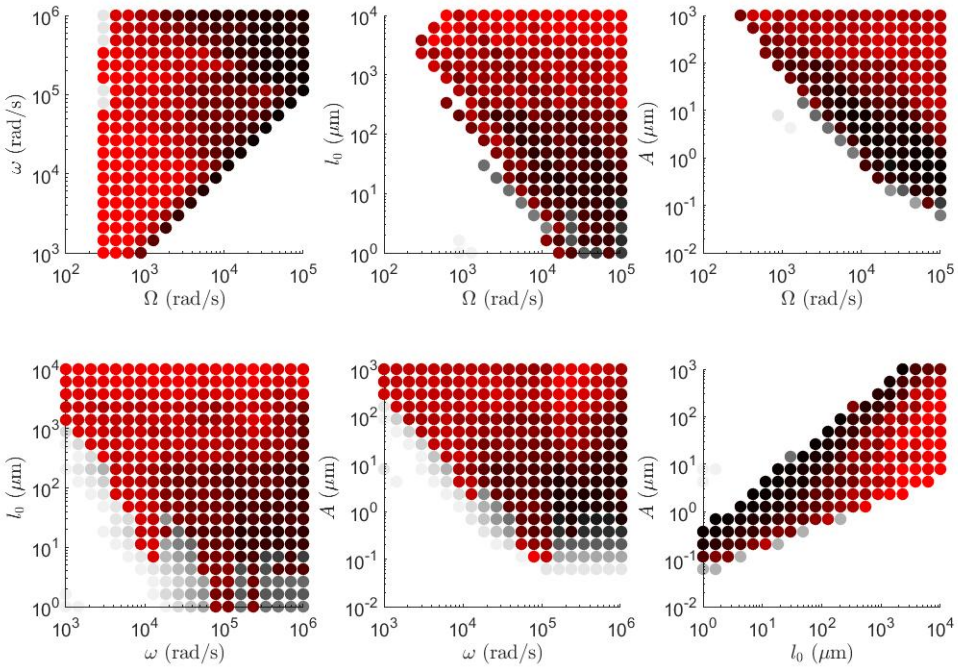

Figure 5.7: Theoretically stable combinations of variables were simulated stable in the two-dimensional system. The axis of the above graphs utilises a logarithmic scale so that we might capture a wide range of highly varying different systems, all of which the Mathieu model predicts to be stable. The red dots represent variable combinations that we found to be stable, and the black dots represent systems that theoretically should be stable but proved not to be when simulated. The opacity on the black dots corresponds to the number of systems with the darker the dots, the more the number of systems we predict stable, but we find are simulated unstable.

the same simulations in three dimensions produces the same results as expected, with an equal number of stable and unstable points as in the two-dimensional simulations. Other than the two trends mentioned prior, the only other thing to note from our results is that there does appear to be a slight tendency that the smaller the values of A and ℓ_0, the more likely the system is to be unstable. The graphs in the top middle, top right, bottom left, and bottom middle all have darker zones that increase in intensity as the value of A and ℓ_0 decreases.

5.4 System robustness

One important principle to understand is how robust the stability of the inverted pendulum systems is. In particular, we need to ascertain whether the system is

not precisely at rest or the starting location of the pendulum is not at the precise angle. These are important considerations to make if such a system is experimentally viable.

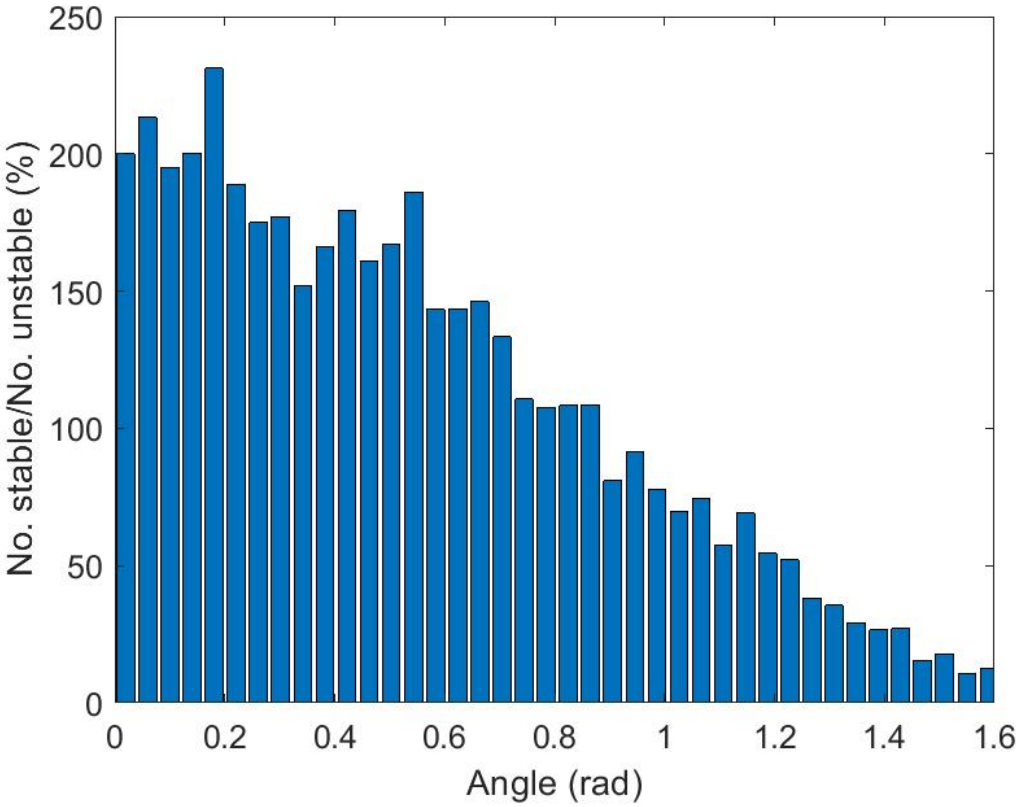

Figure 5.8: Histogram of the percentage difference between the number of stable systems over the number of unstable systems over a range of angles between zero and $\frac{\pi}{2}$. In total, we simulated 12200 systems. Once simulated at a random initial angle, we allocated the results into 40 bins representing different initial angles and then sorted these into stable and unstable results. In each of these tests of robustness, we are utilising the systems we simulated in figure 5.7, which we found to be stable at an initial angle of $\theta = 10^{-5}$ radians and at rest. All systems were initialised at rest.

In our idealised system, it is essential to understand how robust the system is and how dependent it is on the starting conditions. Does a slight deviation of the starting conditions lead to an unstable system? For example, suppose a system is sensitive to the starting conditions. In that case, it may be experimentally challenging, whereas we describe it as robust if it is relatively unreactive to such changes in initial conditions.

When discussing robustness, two properties may vary from the ideal experimen-

tally, the initial positions and velocities. We start by looking at the system's response to an initial velocity in the r direction. In figures 5.9-5.10 we look at what happens when an initial velocity in r is introduced into the system. In figure 5.9, we took approximately twelve thousand systems that we had demonstrated to be stable when initialised without any initial velocities. We gave each one a randomised starting velocity within a range of ± 100 ms^{-1}. In this figure, we can see that there are more systems stable the closer the initial velocity in r is to zero, with a sharp peak at this value of over twice as many stable systems to unstable systems around this value. As the velocity increases, so do the chances that the system becomes unstable, with around a third of systems with an initial velocity of approximately ± 100 ms^{-1} being unstable. If we repeat this process over a shorter range of velocities as in figure 5.10, we see that with a low initial starting velocity, most systems will be stable in this range. This property indicates that the system is relatively unreactive to an initial velocity in the r direction at low velocities. However, if the velocity increases, the system is more likely to become unstable. This feature is likely due to the system's increased energy, leading to instability emerging.

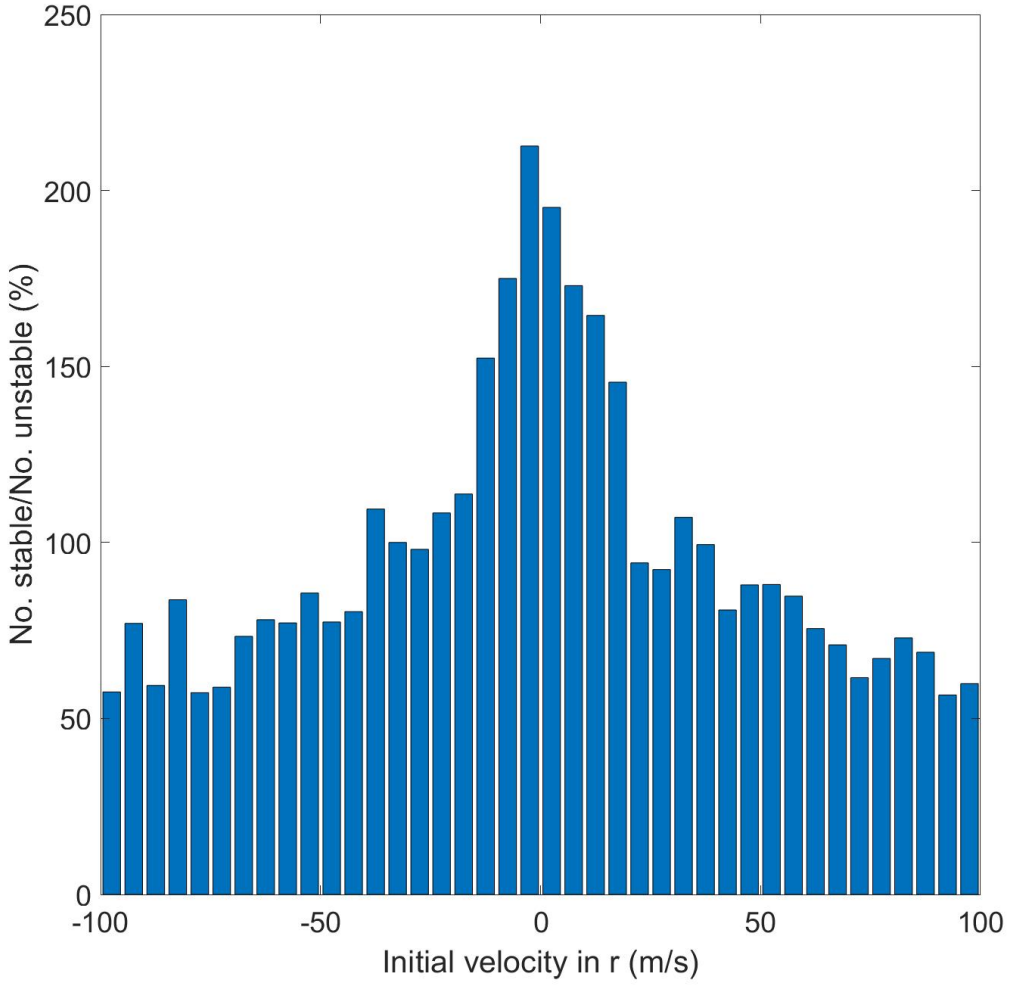

Figure 5.9: Histogram of the percentage difference between the number of stable systems over the number of unstable systems over a range of initial velocities in r between ± 100 ms^{-1}. In total, we simulated 12200 systems. Once simulated at a random initial angle, we allocated the results into 40 bins representing different initial angles and then sorted these into stable and unstable results. In each of these tests of robustness, we are utilising the systems we simulated in figure 5.7, which we found to be stable at an initial angle of $\theta = 10^{-5}$ radians and at rest. These systems were initialised with only a component of velocity in r and were static in both θ and ϕ.

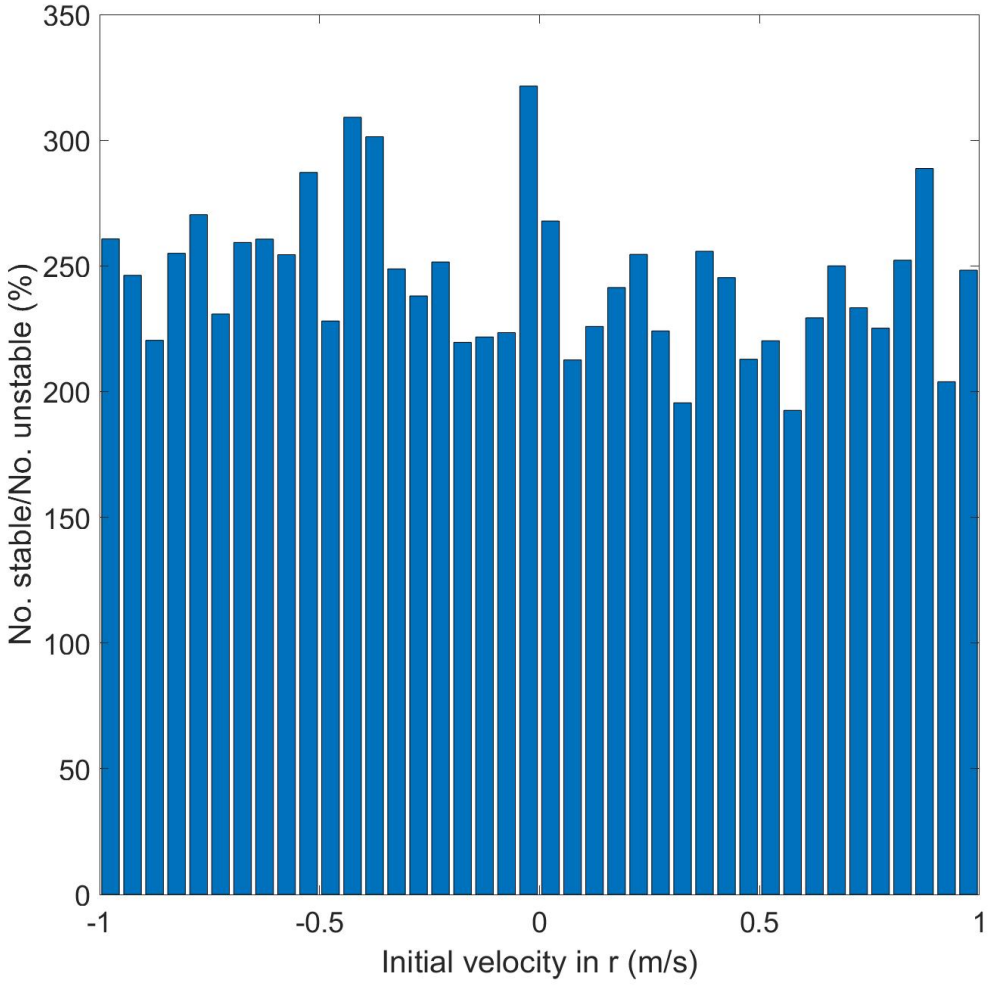

Figure 5.10: Histogram of the percentage difference between the number of stable systems over the number of unstable systems over a range of initial velocities in r between ± 1 ms^{-1}. In total, we simulated 12200 systems. Once simulated at a random initial angle, we allocated the results into 40 bins representing different initial angles and then sorted these into stable and unstable results. In each of these tests of robustness, we are utilising the systems we simulated in figure 5.7, which we found to be stable at an initial angle of $\theta = 10^{-5}$ radians and at rest. These systems were initialised with only a velocity component in r and were static in both θ and ϕ.

Repeating this test with an initial velocity in θ, we find a similar trend emerges. In figure 5.11, we see a peak in the number of stable systems as the initial velocity nears zero rad/s but drops off as the initial velocity increases. By focusing on smaller initial velocities in figure 5.12, we again see that most systems remain stable when only a small initial velocity is applied to the system, which agrees with the results

observed with the initial velocities in r.

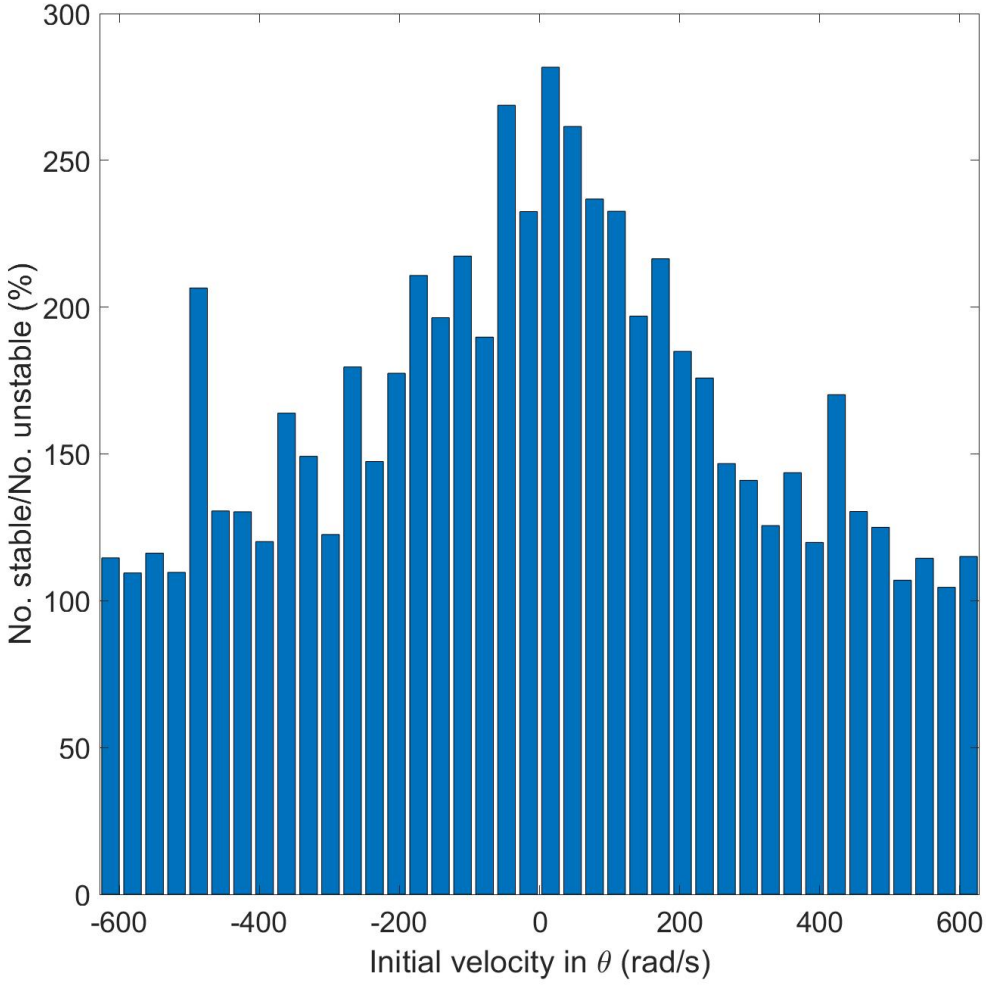

Figure 5.11: Histogram of the percentage difference between the number of stable systems over the number of unstable systems over a range of initial velocities in θ between ± 600 rad/s. In total, we simulated 12200 systems. Once simulated at a random initial angle, we allocated the results into 40 bins representing different initial angles and then sorted these into stable and unstable results. In each of these tests of robustness, we are utilising the systems we simulated in figure 5.7, which we found to be stable at an initial angle of $\theta = 10^{-5}$ radians and at rest. These systems were initialised with only a velocity component in θ and were static in both r and ϕ.

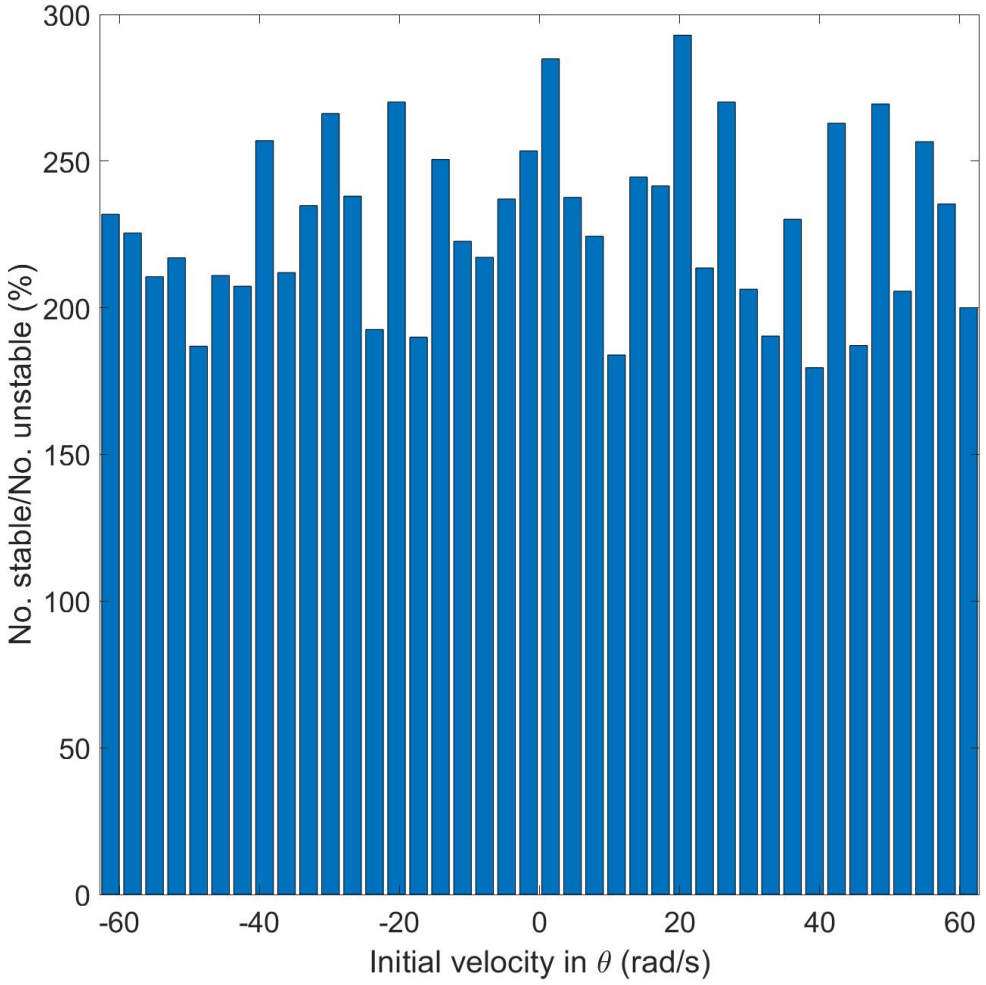

Figure 5.12: Histogram of the percentage difference between the number of stable systems over the number of unstable systems over a range of initial velocities in θ between ± 60 rad/s. In total, we simulated 12200 systems. Once simulated at a random initial angle, we allocated the results into 40 bins representing different initial angles and then sorted these into stable and unstable results. In each of these tests of robustness, we are utilising the systems we simulated in figure 5.7, which we found to be stable at an initial angle of $\theta = 10^{-5}$ radians and at rest. These systems were initialised with only a velocity component in θ and were static in both r and ϕ.

However, if we repeat the test with an initial velocity in ϕ, we find that no such trend emerges, with most systems stable even with an initial velocity of 6000 rad/s. Since the velocity is tangential to the direction of gravity, it does not appear to have much impact on the system's overall stability. Of course, some systems will become unstable, but this is due to the increase in the system's total energy rather than the

dynamics induced by this new velocity.

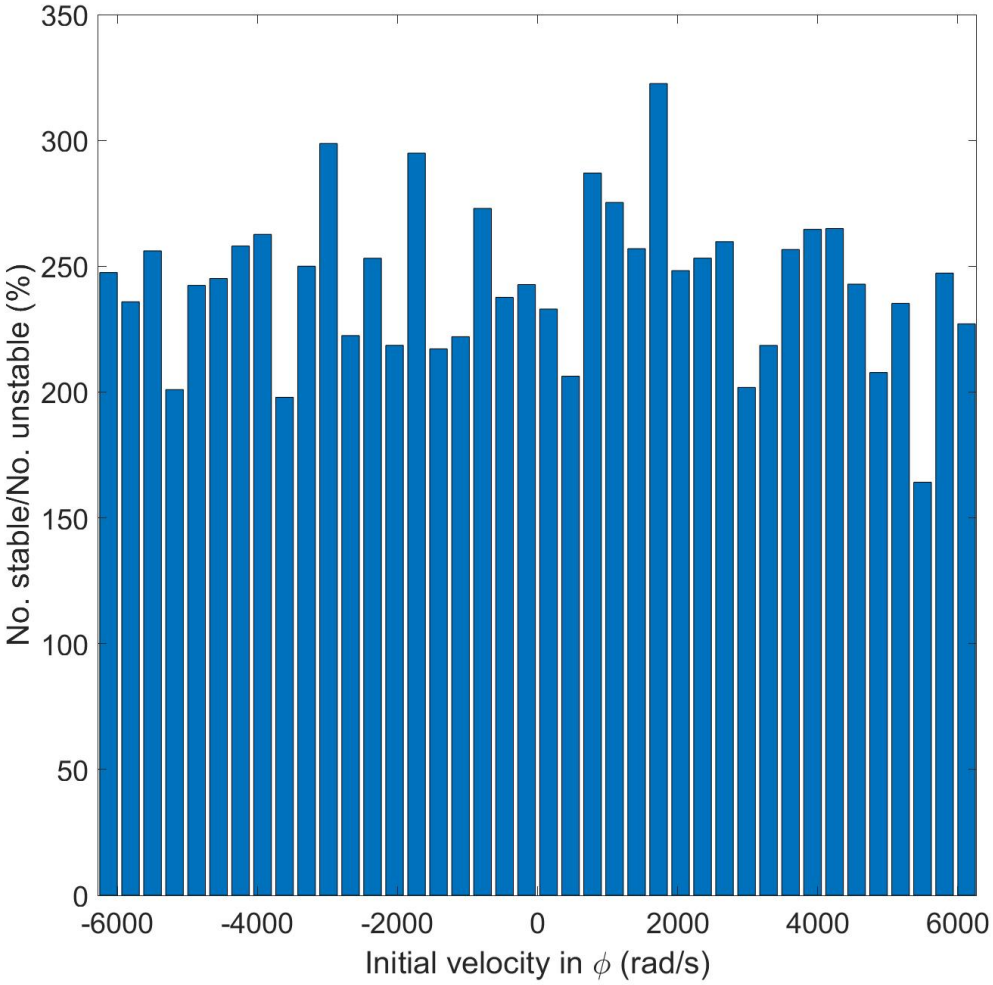

Figure 5.13: Histogram of the percentage difference between the number of stable systems over the number of unstable systems over a range of initial velocities in ϕ between ± 6000 rad/s. In total, we simulated 12200 systems. Once simulated at a random initial angle, we allocated the results into 40 bins representing different initial angles and then sorted these into stable and unstable results. In each of these tests of robustness, we are utilising the systems we simulated in figure 5.7, which we found to be stable at an initial angle of $\theta = 10^{-5}$ radians and at rest. These systems were initialised with only a component of velocity in ϕ and were static in both r and θ.

The final property that we wish to examine is the effect stretching or compressing the system in its initial state has on the overall stability. By stretching or compressing the system, we are introducing more energy into the system and, therefore, would expect that this will lead to some systems becoming unstable. In figure 5.14,

we test whether the amount the system is compressed or extended affects whether or not the system remains stable or whether the act of doing so alone is enough to induce instability.

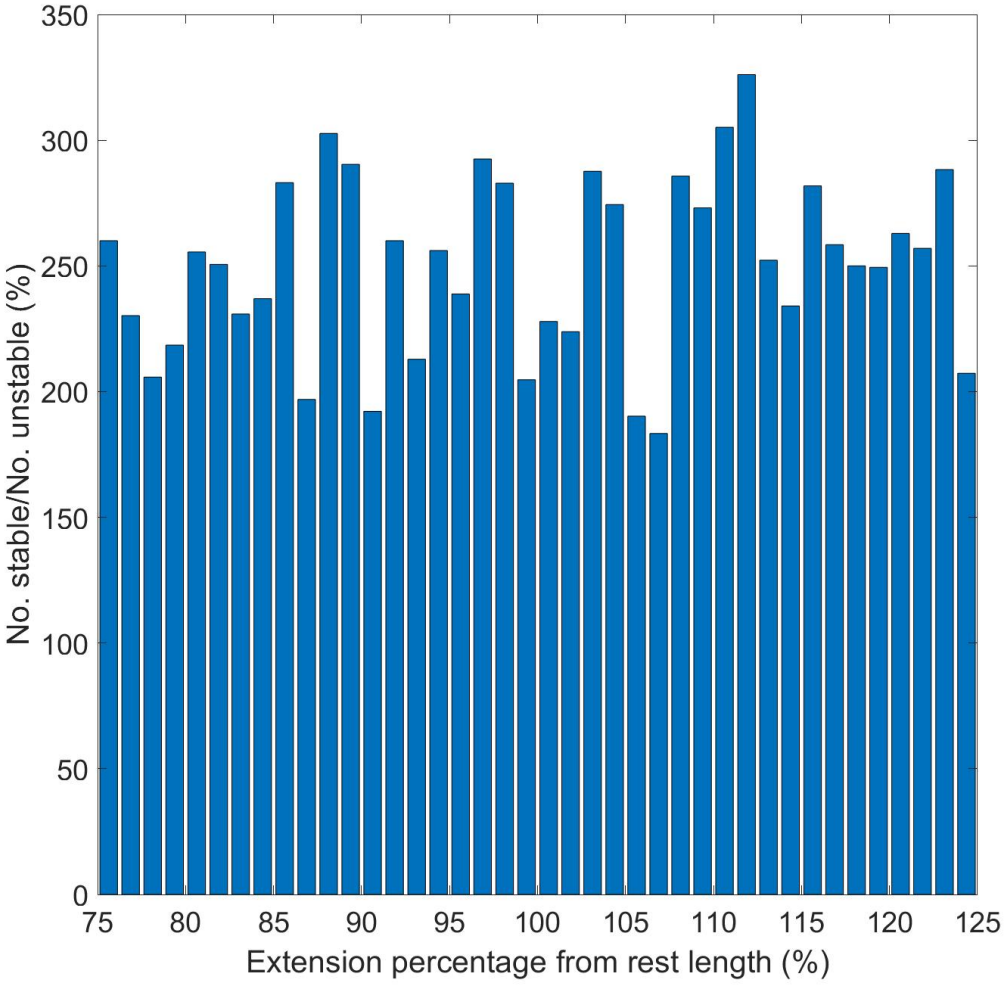

Figure 5.14: Histogram of the percentage difference between the number of stable systems over the number of unstable systems over a range of initial extensions in the initial length of the pendulum between 75% and 125% of the initial rest length of the pendulum. In total, we simulated 12200 systems. Once simulated at a random initial angle, we allocated the results into 40 bins representing different initial angles and then sorted these into stable and unstable results. In each of these tests of robustness, we are utilising the systems we simulated in figure 5.7, which we found to be stable at an initial angle of $\theta = 10^{-5}$ radians and at rest. All systems are initialised at rest.

We can see that in figure 5.14 that there does not appear to be any significant increase in the number of unstable systems when stretching or compressing the initial

state, with around two-thirds of all systems remaining stable with any amount of compression or extension. As a result, we can conclude that the amount the system is compressed or stretched does not significantly impact the stability over this range. We note that if the system is compressed or stretched in the extreme by over a factor of two in either direction, then the system tends to be unstable since the amount of potential energy introduced into the system is, therefore, very high. We have not extensively tested this level of compression since the more that the initial state is stretched or compressed in its initial state, the more rapidly that the system will oscillate, which can lead to a significant increase in the time it takes to simulate the system with our adaptive time step algorithm. Since we are considering slight variations to the initial state to simulate, not quite initialising the system with the exact parameters, we did not feel that we needed to explore beyond the ranges we have looked at here.

Overall, we find that the system can be relatively robust regarding the initial conditions. We found that the most significant contributor to instability is the starting angle of the system, with a larger starting angle much more likely to end up being unstable when simulated. We also found that, in general, the system is likely to remain stable if initialised with a starting velocity; however, if the system has too high a starting velocity in r or θ, then we see that the system tends to become more unstable. The system did not seem to be particularly sensitive to the amount of compression/extension of the initial state nor the initial velocity in ϕ indicating that these do not affect stability beyond introducing more kinetic and potential energy into the system.

5.5 Conclusion

In conclusion, we have demonstrated that it is possible to have a stable elastic pendulum in the inverted position on the scale of an atomic trap. We have shown that such an elastic system can be stable in two and three dimensions. We also demonstrated systemic cooling by reducing the system's driving frequency. Further

investigation into this cooling mechanism is required. In particular, we want to test this cooling on models that consider the collisions between atoms and the geometry of a oblate spheroid to reflect an experimental system closer. Another aspect we looked at was the robustness of the stable system. We found that, in general, the system was not overly dependent on the starting velocities of the system except that the velocity in θ needed to be directed towards the pole to avoid the system becoming unstable. We were able to show that the system is dependent on the starting angle θ and radius r. The larger the starting angle θ, the more likely the system was to be stable, and the further the starting radius was from the rest length, the more unstable the system appeared to be. Finally, we developed equations of motion to describe the shaking of the system in three dimensions. We then tested several scenarios. Of note, we found that by shaking the system at the same frequency and amplitude in all three dimensions; it was possible to isolate the pendulum to one relatively localised point, finding that it oscillated between $\frac{\pi}{4}$ and $\frac{\pi}{2}$. This localisation indicates potential for different results depending on the system's driving mechanism and requires further investigation. We hope to study some more exotic shaking motions to see what is possible in future research. We will also improve our model by changing to a oblate spheroid geometry and introducing collisions of atoms within the system.

Chapter 6

System variations on the inverted elastic pendulum

In the previous chapter, we looked at the feasibility of an atomic trapping scale inverted elastic pendulum as a possible mechanism for generating new atomic trapping schemes where a wave packet inside a trapping potential may occupy locations that would otherwise be gravitationally unfavourable to it. This chapter will take these same systems and vary some of the system's parameters and conditions to observe new phenomena, which may prove experimentally helpful. In particular, we will cover three different system types; firstly, we shall look at a possible method for in-situ cooling of the trapped atoms through the linear reduction in the driving frequency. We will look at systems where the driving is performed in multiple directions instead of just in the vertical. Finally, we will be looking at systems that start with a high angular velocity in the ϕ direction and see what path these pendulums take. All three of these variations might be of interest experimentally as they allow for the creation of stable systems and fine control over the pendulum beyond what is possible with a Kapitza mechanism.

6.1 Systemic cooling

One of the current issues with atomic trapping schemes is their longevity. Once a Bose-Einstein condensate is placed within a potential field, the BEC will begin to heat up, and the system's total energy increases. If overheated, the atoms will cease to be a BEC anymore, leading to a loss of the quantum properties needed to measure the system. As such, a method of evaporative cooling is commonly used whereby the higher energy atoms of the system are allowed to evaporate off, leaving behind those atoms in a lower energy state. This property leads to a steady loss of atoms from the system over time which reduces the lifetime of the atomic trapping scheme. This evaporative cooling is the primary mechanism used to prolong the BEC's lifetime. However, suppose another method of in-situ cooling for atomic traps can be found. In that case, it is worth exploring as an option to be used in conjunction with the evaporative cooling process. While studying our inverted elastic pendulum system, we found that we were able to see a reduction in the system's total energy by linearly decreasing the trapping frequency of the system, provided that the system was initially in a stable inverted position and that the final system was also stable if the pendulum had been initialised in this state. In particular, we define a time-dependent driving frequency

$$\Omega(t) = \Omega_0 - \delta\Omega t, \tag{6.1}$$

where Ω_0 is the initial trapping frequency, and $\delta\Omega$ is the change in Ω per second. We then replace the Ω term in equation (5.46). We make the substitution after the equations have been found using Lagrangian mechanics. This approach is an approximation since the driving frequency is time-dependent; however, we justify this by looking at the second derivative of the driving term of the equation,

$$\begin{aligned}\frac{\partial^2}{\partial t^2}\cos\left((\Omega_0 - \delta\Omega t)t\right) =& 2\delta\Omega \sin\left((\Omega_0 - \delta\Omega t)t\right) \\ &- \left(\Omega_0 - \delta\Omega t\right)^2 \cos\left((\Omega_0 - \delta\Omega t)t\right).\end{aligned} \tag{6.2}$$

For systems on an atomic trapping scale $\Omega_0 \approx 10^5\ rad/s$ and $\delta\Omega \approx 10^4\ rad/s$, as a result, $2\delta\Omega \ll (\Omega_0 - \delta\Omega t)^2$ for time $t \leq 1$ which is the time scale over which we apply the change in driving frequency. Since there is a limit to which the driving frequency may be reduced and still have a stable system if a longer time was desired for the reduction in the driving frequency, the rate at which the frequency decreases would have to scale inversely to the time. If we now simulate the system utilising our familiar Runge-Kutta-Fehlberg algorithm with this replacement, we can study the system's dynamics. In figure 6.1, we plot the evolution of the system in which the driving frequency linearly reduces, This property could lead to in-situ cooling of

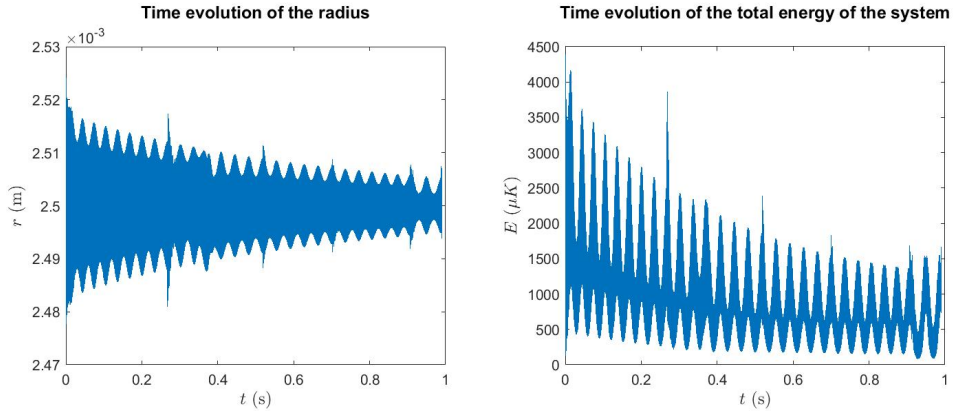

Figure 6.1: Systemic cooling with the following parameters used to generate figure 5.6. The initial angle $\theta = \frac{\pi}{4}$, driving frequency $\Omega = 16000$ rad/s, the radial trapping frequency 25000 rad/s, rest length 2.5×10^{-3} m and driving amplitude $A = 2.5\times10^{-5}$ m. Additionally, we reduced the driving frequency by 5000 rad/s over one second of simulation. The time evolution of the radius graph is plotted in the co-moving frame, whereas the total energy we derive for the lab reference frame.

atoms within a Kapitza-style atom trap by modifying the driving frequency. This cooling phenomenon seems to occur by smoothly reducing the driving frequency in a system where all variable combinations are stable. Starting in an unstable configuration or increasing the driving frequency leads to heating and instability. With a smooth change in the driving frequency, the system's average total energy decreases linearly over time. We observed this phenomenon in both two and three dimensions. The drift observed in the polar angle is down to the system's tolerances since reducing the tolerances also reduces the angular drift.

We acknowledge that the system we are testing is only an approximation utilis-

ing a mechanical system with certain assumptions made, including that the system is a spherical atom trap and there is no heating due to particle interactions. Nevertheless, in this idealised system, we have shown that systemic energy loss due to vertical oscillations is possible and requires further investigation using models that reflect experimental methods more closely. One additional test of these results is to verify that we see this same property emerging when we look at this system using a different approach. In the following section, we will derive an approximate expression for the time evolution of the relative contraction R and the angle θ utilising the Mathieu approximation as used by Arinstein and Gitterman [48].

6.2 Time-dependent equations for R and θ utilising the linearised Mathieu approximation

Demonstrating the energy loss in utilising a different approach is essential in establishing the phenomenon as more than a quirk of the methodology employed. Unfortunately, the nature of the equations of motion does not allow for precise analytical expressions for the time-dependent evolution of the radius and angle of the system. In this section, we derive an approximate form for these expressions. In the next section, we will introduce a time-dependency to the driving frequency to verify our results. We start with the equations of motion that we found in a previous chapter in the form of equation (5.16) and equation (5.14). We shall make a couple of substitutions to make the analytic process easier. Firstly, we define a pendulum frequency as

$$\omega_0^2 = \frac{g}{\ell_0}. \tag{6.3}$$

Next, we define a relative contraction of the pendulum, as in equation (5.15), in the following manner:

$$R = \frac{r}{\ell_0} - \left(1 + \frac{\omega_0^2}{\omega^2}\right). \tag{6.4}$$

Finally we define a dimensionless time quantity as,

$$\tau = \Omega t. \tag{6.5}$$

Making these substitutions and linearising the second order differential equations as outlined by Ryland and Meirovitch [49] and Mazzilli [47] giving the following expressions for R as in equation (5.16) and θ as in equation (5.14) in the comoving reference frame:

$$\frac{\partial^2 R}{\partial \tau^2} + \frac{\omega^2}{\Omega^2} R = A\cos(\tau) \tag{6.6}$$

and

$$\frac{\partial^2 \theta}{\partial \tau^2} - \frac{1}{1 - \frac{\omega_0^2}{\omega^2}} \left[\frac{\omega_0^2}{\Omega^2} - \frac{A}{\ell_0}\cos(\tau)\right] \theta = 0. \tag{6.7}$$

Firstly, let us solve for R; we know that the solution has the following form with c_1 and c_2 being constants that initial conditions can define

$$R(\tau) = \frac{A\Omega^2 \cos(\tau)}{\omega^2 - \Omega^2} + c_1 \cos\left(\frac{\omega\tau}{\Omega}\right) + c_2 \sin\left(\frac{\omega\tau}{\Omega}\right). \tag{6.8}$$

We assume that the system is initially placed with the pendulum having no extension and is therefore at its rest length ℓ_0. Therefore, at $\tau = 0$ and $r = \ell_0$,

$$R(0) = \frac{\ell_0}{\ell_0} - \left(1 + \frac{\omega_0^2}{\omega^2}\right). \tag{6.9}$$

Simplifying fully this expression gives us

$$R(0) = -\frac{\omega_0^2}{\omega^2}, \tag{6.10}$$

Substituting in $\tau = 0$, we get the following expression for constant c_1 once we have rearranged the expression:

$$c_1 = -\frac{\omega_0^2}{\omega^2} - \frac{A\Omega^2}{\omega^2 - \Omega^2} \tag{6.11}$$

This expression, therefore, gives the following expression for the time-dependent relative contraction of the system,

$$R(\tau) = \frac{A\Omega^2 \cos(\tau)}{\omega^2 - \Omega^2} - \left(\frac{\omega_0^2}{\omega^2} + \frac{A\Omega^2}{\omega^2 - \Omega^2}\right) \cos\left(\frac{\omega\tau}{\Omega}\right) + c_2 \sin\left(\frac{\omega\tau}{\Omega}\right). \tag{6.12}$$

We now need a second known system state to find an expression for c_2. We will assume that the system is initially at rest, meaning that at $\tau = 0$, the velocity of R is $R'(\tau) = 0$. Taking the derivative of equation (6.12), we find

$$R'(\tau) = -\frac{A\Omega^2 \sin(\tau)}{\omega^2 - \Omega^2} + \frac{\omega}{\Omega}\left(\frac{\omega_0^2}{\omega^2} + \frac{A\Omega^2}{\omega^2 - \Omega^2}\right) \sin\left(\frac{\omega\tau}{\Omega}\right) + \frac{\omega c_2}{\Omega} \cos\left(\frac{\omega\tau}{\Omega}\right). \tag{6.13}$$

Substituting in $\tau = 0$ and $R'(0) = 0$ we find

$$0 = \frac{\omega c_2}{\Omega}. \tag{6.14}$$

Since $\frac{\omega}{\Omega} \neq 0$, $c_2 = 0$, therefore, we have a time dependent expression for the relative contraction of the pendulum in the form of

$$R(\tau) = \frac{A\Omega^2 \cos(\tau)}{\omega^2 - \Omega^2} - \left(\frac{\omega_0^2}{\omega^2} + \frac{A\Omega^2}{\omega^2 - \Omega^2}\right) \cos\left(\frac{\omega\tau}{\Omega}\right). \tag{6.15}$$

We can now convert this expression back to an expression for the length of the

pendulum in terms of time t in the comvoing reference frame giving the expression

$$r(t) = \ell_0 \left[\frac{A\Omega^2 \cos(\Omega t)}{\omega^2 - \Omega^2} - \left(\frac{\omega_0^2}{\omega^2} + \frac{A\Omega^2}{\omega^2 - \Omega^2} \right) \cos(\omega t) + \left(1 + \frac{\omega_0^2}{\omega^2} \right) \right] \tag{6.16}$$

as the time dependent length of the pendulum. We now seek to find an expression for the angle θ. We first recognise that we have an expression for the angle θ that is in the form of the following Mathieu expression:

$$\frac{\partial^2 \theta}{\partial \tau^2} + [\alpha + \beta \cos(\tau)]\, \theta = 0, \tag{6.17}$$

with

$$\alpha = -\frac{1}{1 - \frac{\omega_0^2}{\omega^2}} \frac{\omega_0^2}{\Omega^2} \tag{6.18}$$

and

$$\beta = \frac{1}{1 - \frac{\omega_0^2}{\omega^2}} \frac{A}{\ell_0}. \tag{6.19}$$

The solution to this Mathieu equation is therefore

$$\theta(\tau) = c_1 \mathrm{Ce}\left[4\alpha, -2\beta, \frac{\tau}{2} \right] + c_2 \mathrm{Se}\left[4\alpha, -2\beta, \frac{\tau}{2} \right], \tag{6.20}$$

with Ce the even Mathieu characteristic function and Se the odd Mathieu characteristic function. Substituting back in α and β with a fixed initial angle θ_0, giving the following expression at $\tau = 0$:

$$\begin{aligned} \theta_0 = c_1 \mathrm{Ce}&\left[-\frac{4}{1 - \frac{\omega_0^2}{\omega^2}} \frac{\omega_0^2}{\Omega^2},\ -\frac{2}{1 - \frac{\omega_0^2}{\omega^2}} \frac{A}{\ell_0},\ 0 \right] \\ + c_2 \mathrm{Se}&\left[-\frac{4}{1 - \frac{\omega_0^2}{\omega^2}} \frac{\omega_0^2}{\Omega^2},\ -\frac{2}{1 - \frac{\omega_0^2}{\omega^2}} \frac{A}{\ell_0},\ 0 \right]. \end{aligned} \tag{6.21}$$

We know that we can remove the odd characteristic function from equation (6.21)

since

$$\mathrm{Se}\left[4\alpha,\ -2\beta,\ 0\right] = 0. \tag{6.22}$$

This therefore gives the following expression for the constant c_1 in the form of

$$c_1 = \frac{\theta_0}{\mathrm{Ce}\left[-\frac{4}{1-\frac{\omega_0^2}{\omega^2}}\frac{\omega_0^2}{\Omega^2},\ -\frac{2}{1-\frac{\omega_0^2}{\omega^2}}\frac{A}{\ell_0},\ 0\right]}. \tag{6.23}$$

Again we are now assuming that the system is initially at rest, therefore, at $\tau = 0$, $\theta' = 0$. This gives us the expression

$$0 = c_2\frac{\Omega}{2}\mathrm{Se}'\left[-\frac{4}{1-\frac{\omega_0^2}{\omega^2}}\frac{\omega_0^2}{\Omega^2},\ -\frac{2}{1-\frac{\omega_0^2}{\omega^2}}\frac{A}{\ell_0},\ 0\right]. \tag{6.24}$$

Therefore $c_2 = 0$ and

$$\begin{aligned}\theta(\tau) =& \frac{\theta_0}{\mathrm{Ce}\left[-\frac{4}{1-\frac{\omega_0^2}{\omega^2}}\frac{\omega_0^2}{\Omega^2},\ -\frac{2}{1-\frac{\omega_0^2}{\omega^2}}\frac{A}{\ell_0},\ 0\right]} \\ &\times \mathrm{Ce}\left[-\frac{4}{1-\frac{\omega_0^2}{\omega^2}}\frac{\omega_0^2}{\Omega^2},\ -\frac{2}{1-\frac{\omega_0^2}{\omega^2}}\frac{A}{\ell_0},\ \frac{\tau}{2}\right].\end{aligned} \tag{6.25}$$

Substituting back in our expression for τ we arrive at the following expression for θ in the comoving reference frame gives us

$$\begin{aligned}\theta(t) =& \frac{\theta_0}{\mathrm{Ce}\left[-\frac{4}{1-\frac{\omega_0^2}{\omega^2}}\frac{\omega_0^2}{\Omega^2},\ -\frac{2}{1-\frac{\omega_0^2}{\omega^2}}\frac{A}{\ell_0},\ 0\right]} \\ &\times \mathrm{Ce}\left[-\frac{4}{1-\frac{\omega_0^2}{\omega^2}}\frac{\omega_0^2}{\Omega^2},\ -\frac{2}{1-\frac{\omega_0^2}{\omega^2}}\frac{A}{\ell_0},\ \frac{\Omega t}{2}\right].\end{aligned} \tag{6.26}$$

6.3 Adding a time-dependency to the driving frequency

Now that we have approximate expressions for R and θ we now look to add a time-dependency to the driving frequency. To do this we will be making the substitution

$$\Omega = \Omega_0 - \delta\Omega t, \tag{6.27}$$

where Ω_0 is the initial driving frequency and $\delta\Omega$ is the decrease in driving frequency per second. Making this substitution into equation (6.16) and equation (6.26) results in the expressions

$$\begin{aligned} r(t) =& \ell_0 \left[\frac{A\left(\Omega_0 - \delta\Omega t\right)^2 \cos((\Omega_0 - \delta\Omega t)\, t)}{\omega^2 - \left(\Omega_0 - \delta\Omega t\right)^2} \right. \\ & \left. - \left(\frac{\omega_0^2}{\omega^2} + \frac{A\left(\Omega_0 - \delta\Omega t\right)^2}{\omega^2 - \left(\Omega_0 - \delta\Omega t\right)^2} \right) \cos\left(\omega t\right) + \left(1 + \frac{\omega_0^2}{\omega^2} \right) \right] \end{aligned} \tag{6.28}$$

and

$$\begin{aligned} \theta(t) =& \frac{\theta_0}{\mathrm{Ce}\left[-\frac{4}{1-\frac{\omega_0^2}{\omega^2}} \frac{\omega_0^2}{\left(\Omega_0 - \delta\Omega t\right)^2},\ -\frac{2}{1-\frac{\omega_0^2}{\omega^2}} \frac{A}{\ell_0},\ 0 \right]} \\ & \times \mathrm{Ce}\left[-\frac{4}{1-\frac{\omega_0^2}{\omega^2}} \frac{\omega_0^2}{\left(\Omega_0 - \delta\Omega t\right)^2},\ -\frac{2}{1-\frac{\omega_0^2}{\omega^2}} \frac{A}{\ell_0},\ \frac{\left(\Omega_0 - \delta\Omega t\right) t}{2} \right]. \end{aligned} \tag{6.29}$$

We can now find potential, kinetic and total system energy expressions. These can be found by substituting these new expressions for r and θ into

$$E_p = mg\left(r\cos(\theta) + A_z \cos((\Omega_0 - \delta\Omega t)\, t)\right) + \frac{1}{2}\kappa\left(r - \ell_0\right)^2 \tag{6.30}$$

and

$$\begin{aligned} E_k =& \frac{1}{2}m\Bigg[\left(r\frac{\partial\theta}{\partial t}\cos\left(\theta\right)+\frac{\partial r}{\partial t}\sin(\theta)\right)^2 \\ &+\left(\left(\frac{\partial r}{\partial t}\cos(\theta)-\frac{\partial\theta}{\partial t}r\sin(\theta)\right)-A_z\left(\Omega_0-\delta\Omega t\right)\sin(\left(\Omega_0-\delta\Omega t\right)t)\right)^2\Bigg] \end{aligned} \tag{6.31}$$

Sometimes it is useful to rewrite the Mathieu function as an expansion. We can do this if we assume that the following term is much less than one,

$$1 \gg \left|-\frac{2}{1-\frac{\omega_0^2}{\omega^2}}\frac{A}{\ell_0}\right| \tag{6.32}$$

This inequality will hold for atomic trapping schemes, and therefore, the expansion holds. The expansion of the Mathieu function [105] is as follows:

$$\begin{aligned} Ce\left(a_r(q),q,z\right) \propto& \cos(rq)+\frac{q}{4}\left(\frac{\cos((r-2)z)}{r-1}-\frac{\cos((r+2)z)}{r+1}\right) \\ &+\frac{q^2}{32}\left(\frac{\cos((r-4)z)}{(r-2)(r-1)}-\frac{2(r^2+1)\cos(rz)}{(r-1)^2(r+1)^2}\right. \\ &\left.+\frac{\cos((r+4)z)}{(r+2)(r+1)}\right)+\mathcal{O}(q^3), \end{aligned} \tag{6.33}$$

with r a property of the Mathieu even value [106] which itself can be written as an expansion in the following manner:

$$a_r(q) \propto r^2+\frac{q^2}{2(r-1)(r+1)}+\mathcal{O}(q^4). \tag{6.34}$$

With both of these approximations, we can have an expression for the even Mathieu characteristic function that is easier to manipulate. Therefore we can obtain an expression for the total energy of the system. Finally, we can plot this equation as a time function to see if we observe the same drop in system energy observed with our numerical simulation.

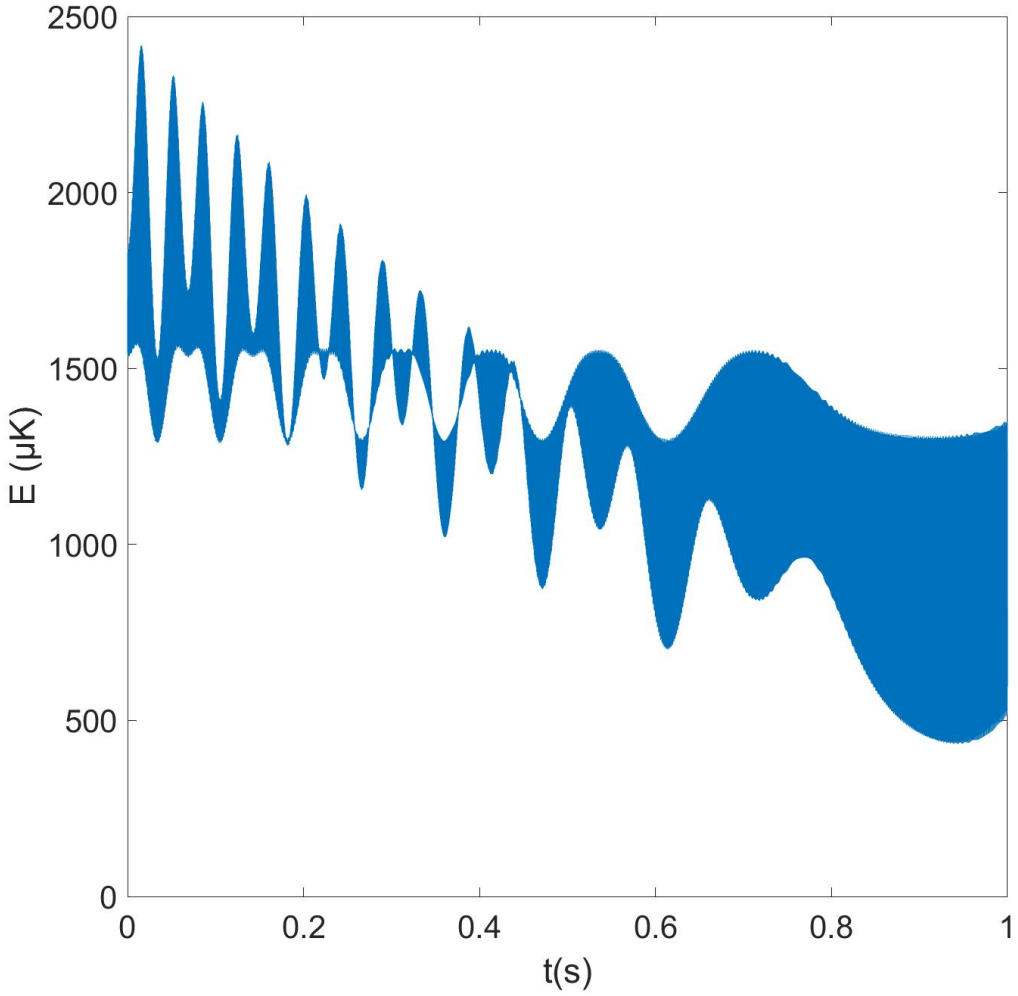

Figure 6.2: Systemic cooling using the Mathieu approximation for the system with the same parameters as used to generate figure 5.6. The initial angle $\theta = \frac{\pi}{4}$, driving frequency $\Omega = 16000$ rad/s, the radial trapping frequency 25000 rad/s, rest length 2.5×10^{-3} m and driving amplitude $A = 2.5 \times 10^{-5}$ m. Additionally, we reduced the driving frequency by 5000 rad/s over one second of simulation. These input conditions are the same as those used in our simulation in figure 6.1.

In figure 6.2, we plot the time evolution of the total energy using the same parameters as utilised when we numerically simulated figure 6.1. We are not expecting to achieve the same result in both graphs since the two approaches are different and are based on different system assumptions; however, we would expect them to observe similar trends, particularly a loss of energy. In both figure 6.2 and figure 6.1, we observe that over one second that the maximum amplitude of the total energy decreases over time. This trend indicates that this property is not a consequence of

our approach since it is present in two different approaches to the system, so we can be fairly confident that this is a physical property of the system.

6.4 Multi-directional driving

One related system we can test using a similar methodology is multi-directional shaking, where we drive the system in both the vertical and horizontal planes. We choose to look at such a system since the ability to drive the system in multiple directions opens up the possibility of localising a pendulum to a specific region that is not necessarily located directly in the vertical position. This approach opens up the possibility for greater control over the pendulum's behaviour. Simulating such system driving is essential, and observing the effects from a numerical approach. In the case of three-dimensional shaking of the atom trap, we will be using a non-moving reference frame. We used the co-moving frame initially with the vertically oscillating pendulum. This choice is because the resulting equations approximate a Mathieu equation that tells us about the system's behaviour and predicts stable configurations of variables. However, when we shake the system in three dimensions, the system is unlikely to be in the form of a Mathieu equation. We already saw that some simplifications are necessary to get an equation in the form of a Mathieu equation in the single-dimensional shaking. Adding more shaking dimensions will likely lead to even more simplification of the system to obtain the Mathieu equation form. Therefore, we will abandon this approach and continue in the stationary frame. The Lagrangian of the system is similar to that shown in equation (5.23) but with additional driving terms so that

$$\begin{aligned} L =& \frac{m}{2}\left[\left(\frac{\partial x}{\partial t}\right)^2+\left(\frac{\partial y}{\partial t}\right)^2+\left(\frac{\partial z}{\partial t}\right)^2\right]-mz\left(g-A_z\Omega_z^2\cos\left(\Omega_z t\right)\right) \\ &+mxA_x\Omega_x^2\cos(\Omega_x t)+myA_y\Omega_y^2\cos(\Omega_y t)-\frac{\kappa}{2}\left(\sqrt{x^2+y^2+z^2}-\ell_0\right)^2. \end{aligned} \tag{6.35}$$

From this Lagrangian we obtain the following equations of motion

$$\frac{\partial^2 x}{\partial t^2} = \frac{\kappa x \ell_0}{m\sqrt{x^2+y^2+z^2}} - \frac{\kappa x}{m} + A_x \Omega_x^2 \cos(\Omega_x t), \tag{6.36}$$

$$\frac{\partial^2 y}{\partial t^2} = \frac{\kappa y \ell_0}{m\sqrt{x^2+y^2+z^2}} - \frac{\kappa y}{m} + A_y \Omega_y^2 \cos(\Omega_y t) \tag{6.37}$$

and

$$\frac{\partial^2 z}{\partial t^2} = \frac{\kappa z \ell_0}{m\sqrt{x^2+y^2+z^2}} - \frac{\kappa z}{m} - g + A_z \Omega_z^2 \cos(\Omega_z t). \tag{6.38}$$

We can now simulate the system using the same Runge-Kutta-Fehlberg algorithm outlined previously. If we take a stable system like that which we used to generate figure 5.6 but introduce a driving at the same frequency, amplitude and phase in both the x and y directions as well, we instead produce figure 6.3. In this figure, we can see that the system remains stable and confines the pendulum bob to a specific region on the surface of a sphere. In addition, we note the exclusion of two wedges from the spherical cap the pendulum is tracing out with its path. These wedges seem to be a driving feature since we ran the simulation for 10 seconds and the pendulum bob traced over the rest of the spherical cap multiple times during the simulation. The fact that we are still able to produce a stable system with an exotic driving scheme indicates that this may prove to be an area of future research which is beyond the scope of this paper but indicates that this is something worth pursuing with the possibility for fine control over the pendulum bob. In addition to testing these two systems, we were also able to test a system with vibrations only in the x and y directions; however, this did not prove to be very stable; although we had a few oscillations, the system quickly decayed from any stable position. Further investigation of other vibrational systems should now be possible with our current equations of motion. Further exploration is required to find other possible vibrating schemes that could lead to the emergence of a stable system.

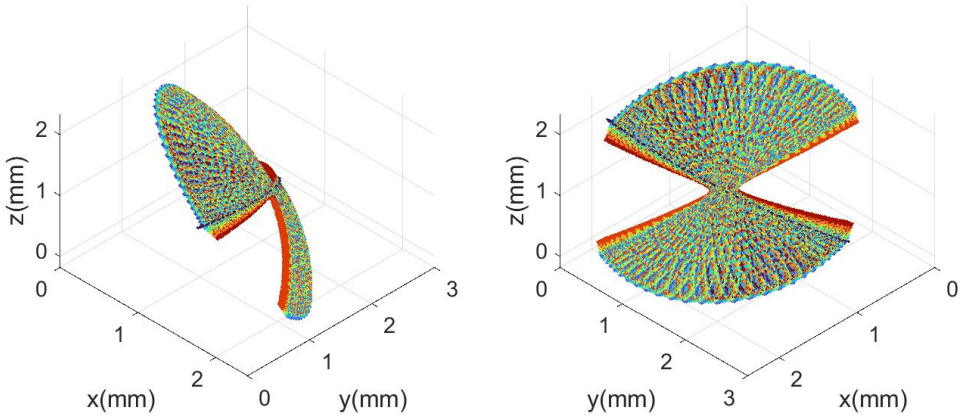

Figure 6.3: Typical trajectory of a stable system in three dimensions with the following parameters. The initial angle $\theta = \frac{\pi}{4}$, driving frequencies $\Omega_x = \Omega_y = \Omega_z = 16000$ rad/s, the radial trapping frequency 25000 rad/s, rest length 2.5×10^{-3} m and driving amplitude $A_x = A_y = A_z = 2.5 \times 10^{-5}$ m. The colour scale goes from blue at time $t = 0$ seconds through yellow to red at $t = 10$ seconds. The graph shows a typical path over 10 seconds with both plots taken simultaneously but at different angles.

6.5 Conclusions

In this chapter, we looked at some variations on the mechanical Kapitza pendulum on an atomic trapping scale. In particular, we looked at a mechanism by which the system's total energy is reduced through the reduction in the vertical driving of the pendulum. We demonstrated that this approach leads to stable systems that remain in the inverted position but whose total energy is reduced while the driving frequency of the system is similarly reduced. We then demonstrated that this result could also be seen numerically utilising the linearised approximation of the system, further confirming our results. Additionally, we looked at a variation on the driving scheme whereby the system is driven in multiple directions. We found that we were able to control the location of the pendulum through the use of this multi-directional driving, and it could be an approach that is used to manipulate the location of a pendulum.

Chapter 7

The atomic Kapitza pendulum and an alternative approach

7.1 Introduction

Having explored the mechanical Kapitza system for an elastic pendulum on the scale of an atomic trapping scheme, we now focus on replicating this result in a system that better reflects existing trapping schemes. In particular, we look at an atomic trapping scheme in the quadrupole. In this scheme, an atom is trapped within a potential shell with an oblate spheroid geometry. Furthermore, this shell is governed by an instantaneous dressed potential [65, 51] for such a system as given by the following expression:

$$V(x,y,z,t) = m'_F\hbar\sqrt{\left[\omega_0(x,y,z,t) - \omega_{rf}(t)\right]^2 + (\Omega_0(x,y,z,t))^2} + mgz, \qquad (7.1)$$

where ω_0 is the Larmor frequency, $\omega_{rf}(t)$ is the RF frequency, and Ω_0 is the Rabi coupling frequency. Additionally, m'_F is the magnetic quantum number of the total atomic spin in the rf-dressed frame. In our case, we are looking at a system containing rubidium-87 atoms, which, in its ground state, has an F value of either 1 or 2. Typically we choose $m'_F = F$. For this purpose, we will set $m_F = 1$. The other constants in our expression are $\hbar$, the familiar reduced Planck constant, m, the

mass of our rubidium-87 and g, the gravitational acceleration. The dressed potential is then dependent on the following frequencies: ω_0, the Larmor frequency, ω_{rf} the radio frequency and Ω_0 the Rabi frequency. Each of these frequencies are functions dependent on the system. Here we will consider the case of a quadrupole field used by Lesanovsky and von Klitzing [65]. We do not have a spherical trap; instead, the trapping geometry forms an oblate spheroid whose major radius is twice the length of its minor radius. Another related system is an Ioffe-Pritchard trap [107], which is similar to the quadrupole except that this is in the form of a oblate spheroid. We will not be investigating the latter system in this thesis. However, the general principles applied here for the quadrupole should carry through to the Ioffe-Pritchard system, albeit with a slightly different geometry. In these trapping schemes, the atoms are contained within and manipulated within this potential. In particular, a modulation to the rf-field might be introduced to manipulate the atom's positioning within the potential. One particular approach is to modulate the rf-field in the z-direction to generate a potential where an atom might be trapped at the equator of the potential rather than at the south pole.

In our eventual system, we will be looking to shake the potential such that we can maintain a stable region in the inverted position; as such, we will include this shaking from the off. In addition to this, the conventional atomic trapping scheme as outlined by Garraway and Perrin [51] and Lesanovsky and von Klitzing [65] generates a trapping scheme which has a hole located at the north pole of the system this is something we wish to avoid with our trapping scheme since this is the desired location for the atoms in our new trap, as such this will have to be adapted. We start by writing expressions for the Larmor frequency,

$$\omega_0(x, y, z, t) = \alpha\sqrt{x^2 + y^2 + 4(z - z_0(t))^2} \tag{7.2}$$

with

$$\alpha = \frac{g_F \mu_B b'}{\hbar}. \tag{7.3}$$

In this expression for α μ_B is the Bohr magneton, b' the gradient of our quadrupole and g_F is the Landé g factor. The Landé g factor is typically $\pm 1/2$ for a system that utilises rubidium-87. The modulation of the quadrupole means that we might consider the centre of the quadrupole field to oscillate vertically in lab frame so that

$$z_0(t) = \frac{B_m}{2b'} \sin(\omega_m t), \tag{7.4}$$

with B_m the modulation amplitude for the B-field and ω_m the modulation frequency. In our new model, we propose utilising a constant radio-frequency. This constant radio-frequency differs from the system described by Lesanovsky and von Klitzing [65], whose rf-field oscillated with the following behaviour:

$$\omega_{rf}(t) = \omega_{rf} \sqrt{1 + \left(\frac{\alpha B_m}{b' \omega_{rf}}\right)^2 \sin^2(\omega_m t)}, \tag{7.5}$$

where ω_{rf} the rf modulation frequency. Finally, we look at the Rabi frequency term. Again our approach differs from Garraway and Perrin [51] and Lesanovsky and von Klitzing [65]. In these works, the Rabi frequency is defined as

$$\Omega_0(x, y, z, t) = \frac{|\alpha B_{rf}|}{2b'} \sqrt{1 - u_z(\rho, z, t)^2}, \tag{7.6}$$

where B_{rf} is the magnitude of the Rabi frequency and u_z the direction of the magnetic field. For a linearly polarised system, u_z can be written as

$$u_z(\rho, z, t) = \frac{-2(z - z_0(t))}{\sqrt{\rho^2 + 4(z - z_0(t))^2}}. \tag{7.7}$$

We note that in this system, B_{rf} is non-static and is defined as,

$$B_{rf} = B_1 \sqrt{1 + \left(\frac{\alpha B_m}{b' \omega_{rf}}\right)^2 \sin^2(\omega_m t)}. \tag{7.8}$$

A system driven in such a way will generate a stable region located at the equator if the driving frequency, ω_m, is much greater than the rf-coupling frequency Ω_0. In

this regime, the system acts as if it were under a potential that can be found by taking the time average of the modulating potential field with

$$V_{TA}(\mathbf{r}) = \frac{1}{\tau}\int_0^\tau V_m(\mathbf{r},t)dt, \tag{7.9}$$

where τ is the period of modulation and is equal to $\tau = 2\pi\omega_m^{-1}$. This is referred to as a Time-Averaged Adiabatic Potential and has been realised experimentally [65, 108, 73, 109]. The net outcome is that, through modulation, it is possible to generate a stable system. We collect all the above terms together to form a Lagrangian for the system to find the equations of motion. We can then utilise our Runge-Kutta-Fehlberg algorithm to simulate the system's dynamics and see how it behaves. The Lagrangian for the system takes the following form:

$$\begin{aligned} L =& \frac{m}{2}\left(\left(\frac{\partial x}{\partial t}\right)^2 + \left(\frac{\partial y}{\partial t}\right)^2 + \left(\frac{\partial z}{\partial t}\right)^2\right) - mgz \\ & - m'_F\hbar\left[\frac{\alpha^2\gamma(t)B_1^2}{4b'^2}\left(1 - \frac{2\zeta(t)}{\sqrt{x^2+y^2+4\zeta(t)^2}}\right)^2\right. \\ & \left. + \left(\omega_{rf}\lambda(t) - \alpha\sqrt{x^2+y^2+\zeta(t)^2}\right)^2\right]^{\frac{1}{2}}. \end{aligned} \tag{7.10}$$

We define the parameters $\zeta(t)$, $\gamma(t)$ and $\lambda(t)$ as

$$\zeta(t) = z - \frac{B_m}{2b'}\sin(\omega_m t), \tag{7.11}$$

$$\gamma(t) = 1 + \frac{\alpha B_m}{b'\omega_{rf}}\sin^2(\omega_m t) \tag{7.12}$$

and

$$\lambda(t) = \sqrt{1 + \frac{\alpha^2 B_m^2\sin^2(\omega_m t)}{b'^2\left(\omega_{rf}\right)^2}}. \tag{7.13}$$

$\zeta(t)$ is a modification of the evolution of the z coordinate to include the vertical

driving of the system and $\gamma(t)$ and $\lambda(t)$ two time dependent terms we have defined in order to simplify the system.

Utilising Lagrangian mechanics this gives the following equations of motion for the system:

$$\frac{\partial x}{\partial t} = X, \tag{7.14}$$

$$\frac{\partial y}{\partial t} = Y, \tag{7.15}$$

$$\frac{\partial z}{\partial t} = Z, \tag{7.16}$$

$$\begin{aligned}\frac{\partial X}{\partial t} =& -\frac{\alpha\hbar m'_F x}{m} \\ &\times \frac{\alpha + \frac{\alpha B_1^2\gamma(t)\zeta(t)^2}{b'^2(x^2+y^2+4\zeta(t)^2)^2} - \frac{\lambda(t)\omega_{rf}}{\sqrt{x^2+y^2+4\zeta(t)^2}}}{\sqrt{\frac{\alpha^2 B_1^2\gamma(t)}{4b'^2}\left(1-\frac{4\zeta(t)^2}{x^2+y^2+4\zeta(t)^2}\right)+\left(\lambda(t)\omega_{rf}-\alpha\sqrt{x^2+y^2+4\zeta(t)^2}\right)^2}},\end{aligned} \tag{7.17}$$

$$\begin{aligned}\frac{\partial Y}{\partial t} =& -\frac{\alpha\hbar m'_F y}{m} \\ &\times \frac{\alpha + \frac{\alpha B_1^2\gamma(t)\zeta(t)^2}{b'^2(x^2+y^2+4\zeta(t)^2)^2} - \frac{\lambda(t)\omega_{rf}}{\sqrt{x^2+y^2+4\zeta(t)^2}}}{\sqrt{\frac{\alpha^2 B_1^2\gamma(t)}{4b'^2}\left(1-\frac{4\zeta(t)^2}{x^2+y^2+4\zeta(t)^2}\right)+\left(\lambda(t)\omega_{rf}-\alpha\sqrt{x^2+y^2+4\zeta(t)^2}\right)^2}}\end{aligned} \tag{7.18}$$

and

$$\begin{aligned}\frac{\partial Z}{\partial t} =& -g-\frac{\alpha\hbar m'_F \zeta(t)}{m} \\ &\times \frac{4\alpha - \frac{\alpha B_1^2\gamma(t)(x^2+y^2)}{b'^2(x^2+y^2+4\zeta(t)^2)^2} - \frac{4\lambda(t)\omega_{rf}}{\sqrt{x^2+y^2+4\zeta(t)^2}}}{\sqrt{\frac{\alpha^2 B_1^2\gamma(t)}{4b'^2}\left(1-\frac{4\zeta(t)^2}{x^2+y^2+4\zeta(t)^2}\right)+\left(\lambda(t)\omega_{rf}-\alpha\sqrt{x^2+y^2+4\zeta(t)^2}\right)^2}}.\end{aligned} \tag{7.19}$$

From these equations of motion, we apply our Runge-Kutta-Fehlberg algorithm to

demonstrate its stability and dynamics. In figure 7.2 we plot a typical path of an atom trapped in this potential.

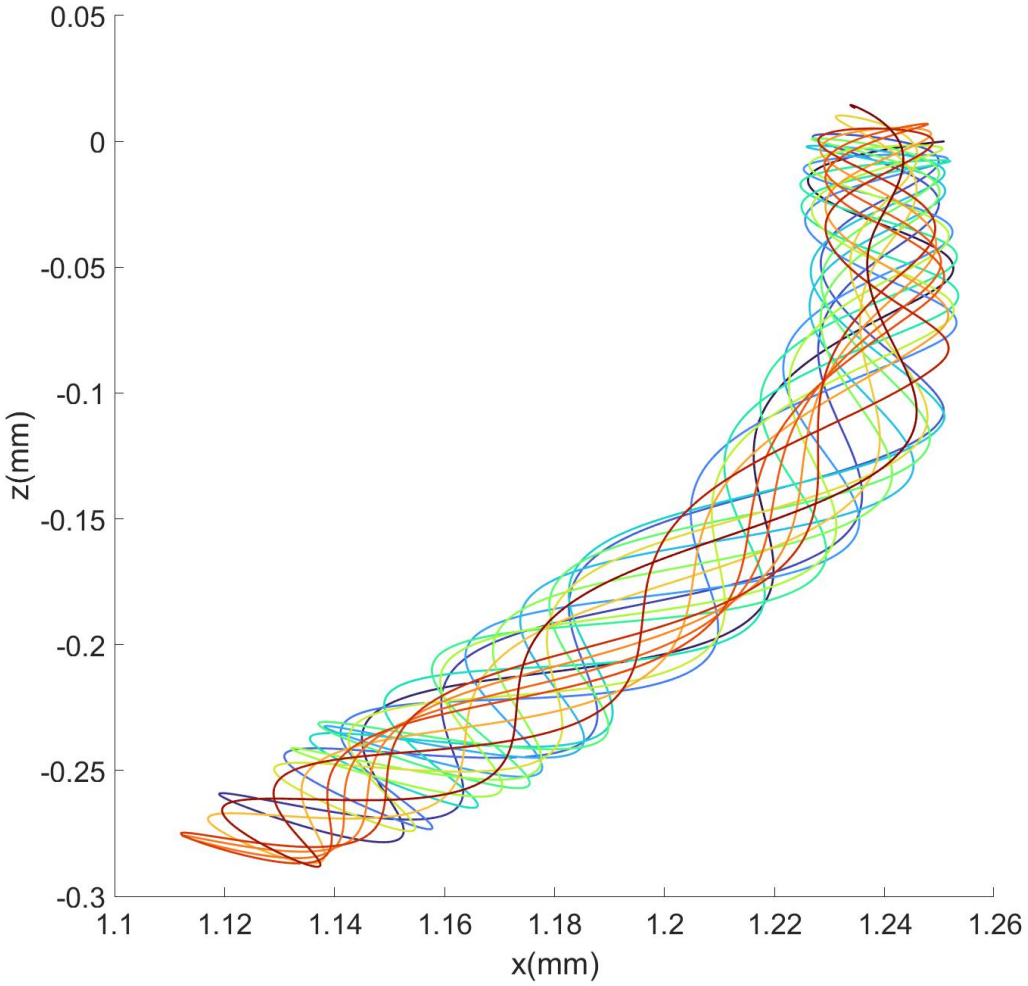

Figure 7.1: Typical path of a stable system with the atom trapped at the equator of the potential. We set the initial position of the atom at $x = 1.2508$ mm and $z = 0$ mm, setting $B_m = 2.5 \times 10^{-5}$ T, $\omega_{rf} = 5.5 \times 10^7$ rad/s, $B_{rf} = 1.3191 \times 10^{-7}$ T, $\omega_m = 1.6 \times 10^7$ rad/s. The simulation covers the location of the atom over a period of 0.5 seconds. The colour gradient starts at blue for $t = 0$ and goes through to red at time $t = 0.5$ seconds.

In figure 7.2, we see that the atom's location is limited to a subsection of the potential shell near the equator. There is movement in both x and z, but the atom oscillates and stabilises around the equator. We want to take this model and move the stable region to the north pole of the system. We will first consider a purely

vertically driven system such as the one utilised in the mechanical Kapitza system to see if, in this new model of the system, a stable region can be maintained at the north pole of the potential.

7.2 Vertically driven system

By utilising Kapitza mechanics to maintain a stable region at the north pole, some changes need to be made. One of the first aspects that need to be changed is that, in its existing state, the system has a hole located at the north pole, which means that the atoms will not be trapped at the north pole and can escape the trapping potential. We, therefore, require a change to the trapping geometry. In particular, we want to adjust the Rabi frequency component so that the hole is located elsewhere on the trapping surface. We introduce a circular polarisation to the system to achieve this moving of the hole on the potential surface. A general expression for an RF field applied in the $x-y$ plane can be written in the following vector form [69, 110]:

$$\mathbf{B}_{RF} = B^0_{RF} \begin{pmatrix} \cos(\omega t) \\ \lambda \cos(\omega t - \alpha) \\ 0 \end{pmatrix} \tag{7.20}$$

The coupling is found by finding the perpendicular component $B_\perp$ to a static B-field by rotating from a coordinate system aligned along the quadrupole field to the lab frame coordinate system. In doing this the following expression might be obtained [69]:

$$\begin{aligned} \left(\frac{B_\perp}{B^0_{RF}}\right)^2 =& \frac{\lambda^2 x^2 + y^2}{x^2+y^2} + \frac{4z^2}{x^2+y^2+4z^2}\left(\frac{x^2+\lambda^2 y^2}{x^2+y^2}\right) \\ & - \frac{2\lambda xy\cos(\alpha)}{x^2+y^2+4z^2} + \frac{4\lambda z \sin(\alpha)}{\sqrt{x^2+y^2+4z^2}}. \end{aligned} \tag{7.21}$$

In a circularly polarised system $\lambda = 1$ and $\alpha = \pm\pi/2$. This simplifies the previous expression to

$$\left(\frac{B_\perp}{B^0_{RF}}\right)^2 = 1 + \frac{4z^2}{x^2+y^2+4z^2} \pm \frac{4z}{\sqrt{x^2+y^2+4z^2}}. \tag{7.22}$$

We want to choose whether α is positive or negative since it determines the nature of the system. Since we are looking to create a maximum coupling at the north pole of the trapping potential where z is positive. Given this, the correct polarisation of the RF field, therefore, for resonance is. Therefore, $\alpha = \pi/2$ gives us the expression

$$\left(\frac{B_\perp}{B^0_{RF}}\right)^2 = 1 + \frac{4z^2}{x^2+y^2+4z^2} + \frac{4z}{\sqrt{x^2+y^2+4z^2}}. \tag{7.23}$$

This can be further simplified so that

$$\left(\frac{B_\perp}{B^0_{RF}}\right)^2 = \left(1 + \frac{4z}{\sqrt{x^2+y^2+4z^2}}\right)^2. \tag{7.24}$$

The Rabi frequency term therefore takes the form of the expression

$$\begin{aligned}\Omega_0(x,y,z,t) =& \frac{|\alpha B_{rf}(t)|}{2b'}\sqrt{\left(1 + \frac{2z}{\sqrt{x^2+y^2+4z^2}}\right)^2} \\ =& \frac{|\alpha B_{rf}|}{2b'}\left(1 + \frac{2z}{\sqrt{x^2+y^2+4z^2}}\right).\end{aligned} \tag{7.25}$$

Since we are vertically driving the system, we need to modify the Rabi frequency term so that the field is displaced vertically through the transformation $z \to z - z_0$, with

$$z_0 = \frac{B_m}{2b'}\sin(\omega_m t). \tag{7.26}$$

This gives a final expression for the Rabi frequency in the following form:

$$\Omega_0(x,y,z,t) = \frac{|\alpha B_{rf}(t)|}{2b'}\left(1 + \frac{2\left(z - \frac{B_m}{2b'}\sin(\omega_m t)\right)}{\sqrt{x^2+y^2+4\left(z-\frac{B_m}{2b'}\sin(\omega_m t)\right)^2}}\right). \tag{7.27}$$

In addition to this change in the Rabi frequency we choose to set the frequency and magnitude of the rf-frequency to be constant meaning $\omega_{rf}(t) = \omega_{rf}$ and $B_{rf}(t) = B_1$. Substituting these expressions into our final result, we get an equation for the potential,

$$\begin{aligned} V =& gmz + m'_F\hbar\left[\frac{\alpha^2 B_1^2}{4b'^2}\left(1 + \frac{2\zeta(t)}{\sqrt{x^2+y^2+4\zeta(t)^2}}\right)^2\right. \\ &\left. + \left(-\omega_{rf} + \alpha\sqrt{x^2+y^2+4\zeta(t)^2}\right)^2\right]^{\frac{1}{2}}, \end{aligned} \tag{7.28}$$

with

$$\zeta(t) = z - \frac{B_m}{2b'}\sin(\omega_m t). \tag{7.29}$$

The resulting equations of motion for this system take on the following form:

$$\frac{\partial x}{\partial t} = X, \tag{7.30}$$

$$\frac{\partial y}{\partial t} = Y, \tag{7.31}$$

$$\frac{\partial z}{\partial t} = Z, \tag{7.32}$$

$$\frac{\partial X}{\partial t} = -\frac{\alpha\hbar m'_F x}{2m} \times \frac{2\alpha - \frac{2\omega_{rf}}{\sqrt{x^2+y^2+4\zeta(t)^2}} - \frac{\alpha B_1^2 \zeta(t)\left(-2\zeta(t)+\sqrt{x^2+y^2+4\zeta(t)^2}\right)}{b'^2(x^2+y^2+4\zeta(t)^2)^2}}{\sqrt{\frac{\alpha^2 B_1^2}{4b'}\left(1+\frac{2\zeta(t)}{\sqrt{x^2+y^2+4\zeta(t)^2}}\right)^2 + \left(\omega_{rf} - \alpha\sqrt{x^2+y^2+4\zeta(t)^2}\right)^2}}, \tag{7.33}$$

$$\frac{\partial Y}{\partial t} = -\frac{\alpha\hbar m'_F y}{2m} \times \frac{2\alpha - \frac{2\omega_{rf}}{\sqrt{x^2+y^2+4\zeta(t)^2}} - \frac{\alpha B_1^2 \zeta(t)\left(-2\zeta(t)+\sqrt{x^2+y^2+4\zeta(t)^2}\right)}{b'^2(x^2+y^2+4\zeta(t)^2)^2}}{\sqrt{\frac{\alpha^2 B_1^2}{4b'}\left(1+\frac{2\zeta(t)}{\sqrt{x^2+y^2+4\zeta(t)^2}}\right)^2 + \left(\omega_{rf} - \alpha\sqrt{x^2+y^2+4\zeta(t)^2}\right)^2}} \tag{7.34}$$

and

$$\frac{\partial Z}{\partial t} = -g - \frac{\hbar m'_F}{2m} \times \frac{8\alpha\zeta(t)\left(\alpha - \frac{\omega_{rf}}{\sqrt{x^2+y^2+4\zeta(t)^2}}\right) + \frac{\alpha^2 B_1^2}{b'^2}\frac{(x^2+y^2)\left(-2\zeta(t)+\sqrt{x^2+y^2+4\zeta(t)^2}\right)}{(x^2+y^2+4\zeta(t)^2)^2}}{\sqrt{\frac{\alpha^2 B_1^2}{4b'}\left(1+\frac{2\zeta(t)}{\sqrt{x^2+y^2+4\zeta(t)^2}}\right)^2 + \left(\omega_{rf} - \alpha\sqrt{x^2+y^2+4\zeta(t)^2}\right)^2}}. \tag{7.35}$$

One aspect of this system that differs from the mechanical Kapitza system is the potential term. In the z direction, we find that the system is in a harmonic potential. With the change in the system, we need to make sure that this is still the case with our new model. Since this is not automatically the case, this brings more conditions on the stability, which potentially makes it more difficult to find a stable system compared to the relative ease that we had in finding stable systems for the mechanical system. Indeed, if we test a system that we know is stable in the mechanical Kapitza regime in this new atomic Kapitza regime, we find the system unstable.

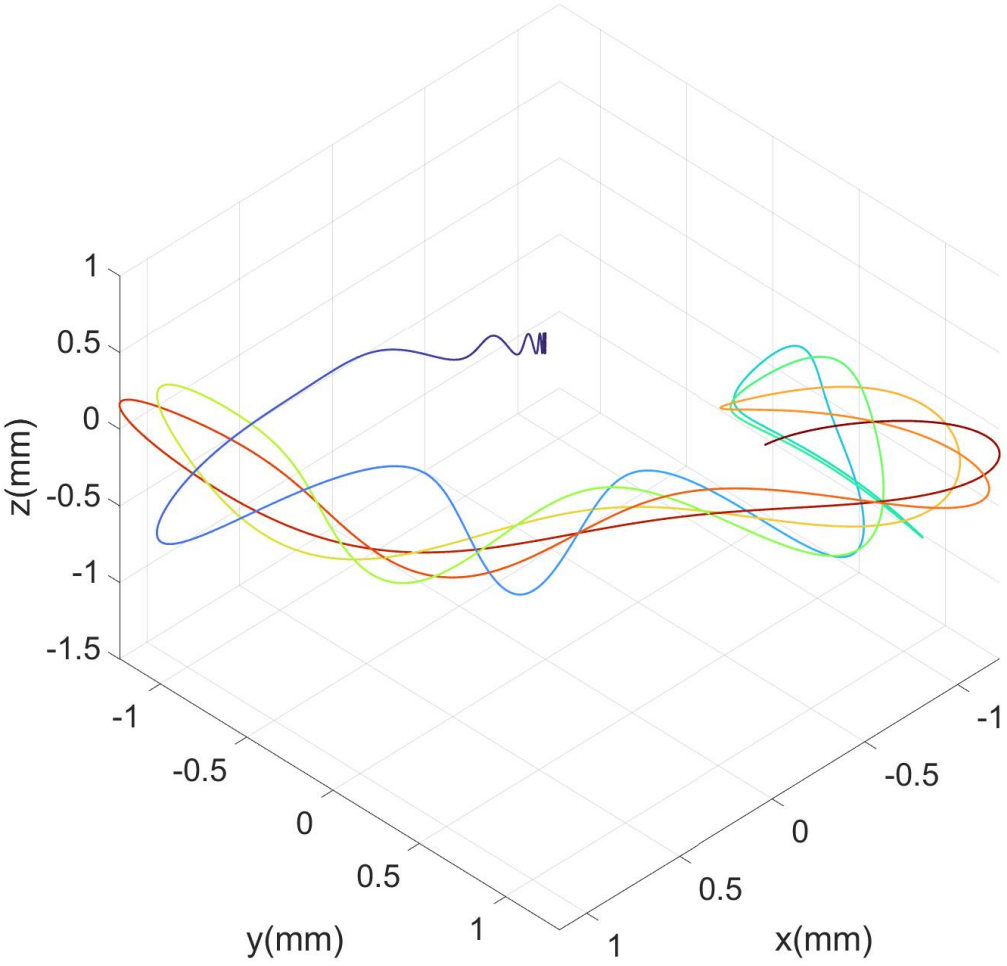

Figure 7.2: Typical path of an unstable system with vertical driving. The trapping potential is initialised with the atom located at a distance from the centre of the trap of 6.25×10^{-4}m, a polar angle of $\theta = 10^{-5}$ and an azimuthal angle of $\phi = -\pi/4$, setting $B_m = 2.5 \times 10^{-5}$ T, $\omega_{rf} = 2.75 \times 10^7$ rad/s, $B_1 = 1.3191 \times 10^{-7}$ T, $\omega_m = 1.6 \times 10^4$ rad/s. The simulation covers the location of the atom over a period of 0.5 seconds. The colour gradient starts at blue for $t = 0$ and goes through to red at time $t = 0.5$ seconds.

If we plot the individual components, we can see how the system is evolving to understand how the system is unstable. We can see that in figure 7.3 that the x component of the system exponentially increases over time, taking the atom away from the inverted position until the atom passes over the equator when it starts to oscillate across the southern hemispheroid meaning that the system is not stabilised in the inverted position and is instead finding the gravitationally

favourable position below the equator. In the mechanical Kapitza system, we expect the atom to oscillate in x over the north pole instead of drifting away from the north pole, highlighting that this new system is unstable.

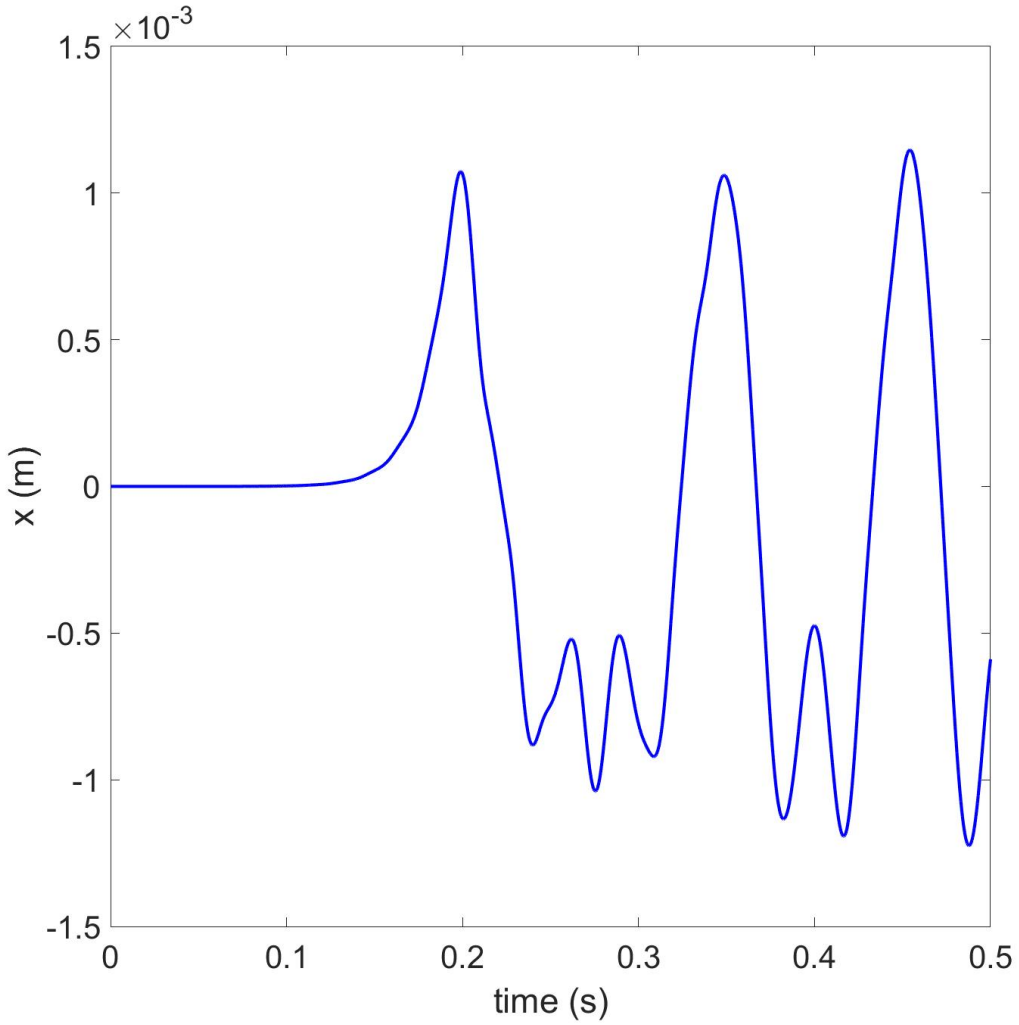

Figure 7.3: Evolution in x for an unstable atom The trapping potential is initialised with the atom located at a distance from the centre of the trap of 6.25×10^{-4}m, a polar angle of $\theta = 10^{-5}$ and an azimuthal angle of $\phi = -\pi/4$, setting $B_m = 2.5 \times 10^{-5}$ T, $\omega_{rf} = 2.75 \times 10^7$ rad/s, $B_1 = 1.3191 \times 10^{-7}$ T, $\omega_m = 1.6 \times 10^4$ rad/s.

In figure 7.4, we see that initially, the system oscillates in the z direction, which is typically for the mechanical system; however, the maximum amplitude is slowly decreasing over time, indicating instability. This decrease in amplitude increases over time until the atom is no longer above the equator when it begins to oscillate like a conventional pendulum, albeit one with more complex dynamics due to vertical

driving. This result indicates that such a system is unstable when its mechanical counterpart is stable.

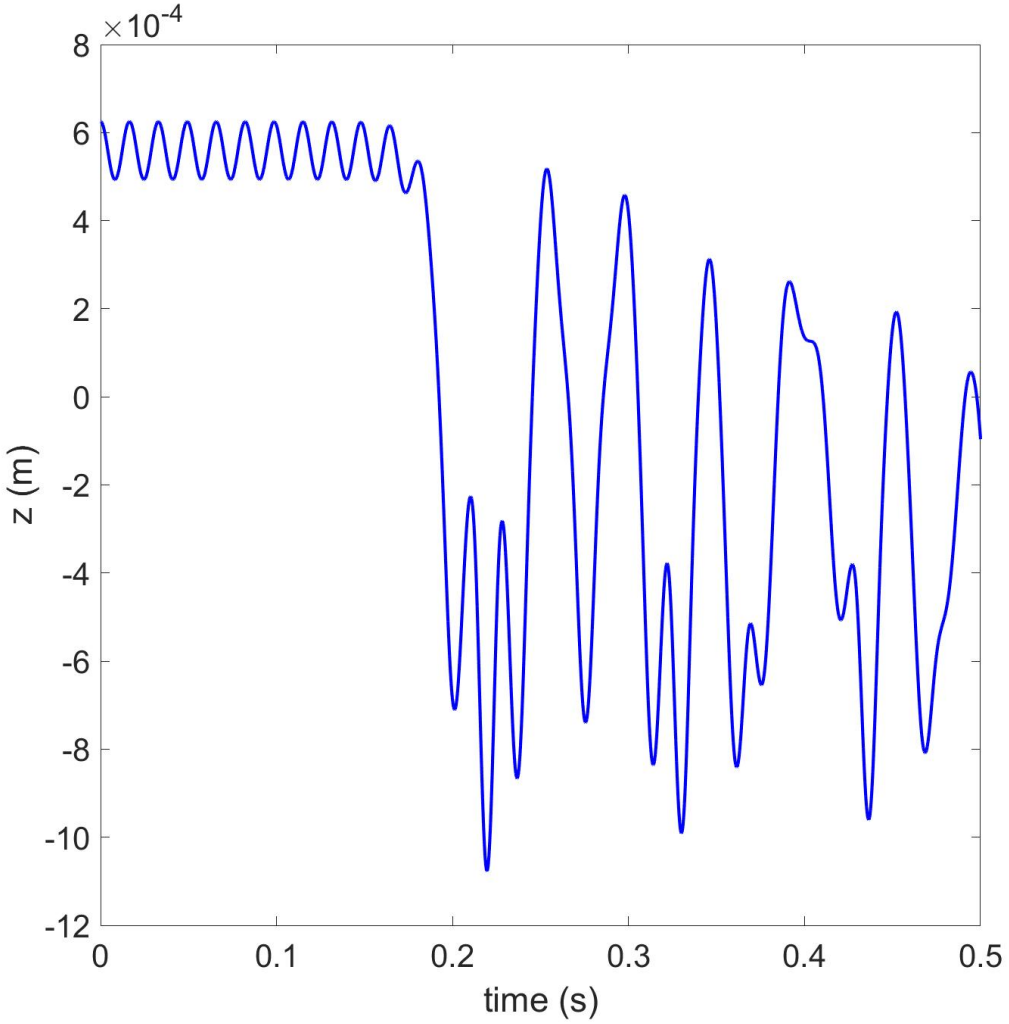

Figure 7.4: Evolution in z for an unstable atom The trapping potential is initialised with the atom located at a distance from the centre of the trap of 6.25×10^{-4} m, a polar angle of $\theta = 10^{-5}$ and an azimuthal angle of $\phi = -\pi/4$, setting $B_m = 2.5 \times 10^{-5}$ T, $\omega_{rf} = 2.75 \times 10^7$ rad/s, $B_1 = 1.3191 \times 10^{-7}$ T, $\omega_m = 1.6 \times 10^4$ rad/s. The simulation covers the location of the atom over a period of 0.5 seconds.

We then tested a wide range of known stable conditions for the mechanical Kapitza system in this new atomic Kapitza scheme and found that all of these systems became unstable. These findings indicate that finding stable systems in the atomic trapping scheme appears to be significantly more challenging than for the mechanical system and that other factors are involved in the stability of such a sys-

tem. If we look at the Lagrangian of both systems, we might begin to understand why this is the case. Both systems have the same kinetic energy term and gravitational potential energy; however, the formulation of the spring term is different between the two systems. In particular, the mechanical Kapitza system this spring term is defined as

$$V_{\text{mech-spring}} = \frac{\kappa}{2}\left(\sqrt{x^2+y^2+\zeta(t)^2}-\ell_0\right)^2, \tag{7.36}$$

whereas the equivalent term in the atomic system takes the form

$$\begin{aligned} V_{\text{atomic-spring}} =& m'_F\hbar\left[\frac{\alpha^2 B_1^2}{4b'^2}\left(1+\frac{2\zeta(t)}{\sqrt{x^2+y^2+4\zeta(t)^2}}\right)^2\right. \\ &\left.+\left(-\omega_{rf}+\alpha\sqrt{x^2+y^2+4\zeta(t)^2}\right)^2\right]^{\frac{1}{2}}. \end{aligned} \tag{7.37}$$

The mechanical system can be described to be in a harmonic regime which we can demonstrate through an expansion of the brackets, which gives the expression for the spring potential as

$$V_{\text{mech-spring}} = \frac{\kappa}{2}\left(x^2+y^2+\zeta(t)^2+2\ell_0\sqrt{x^2+y^2+\zeta(t)^2}+\ell_0^2\right). \tag{7.38}$$

This harmonic potential ensures the stability of the system when driven correctly. We want to ensure that our atomic Kapitza system is similarly in an harmonic regime as well. If we take a simplified version of the atomic spring potential, we get the expression

$$V = \sqrt{(\lambda z)^2+\Omega_0^2}. \tag{7.39}$$

In the limit $\lambda|z| \gg \Omega_0$ this becomes

$$V \approx \lambda|z|. \tag{7.40}$$

As a result, the potential function is then in a linear regime which appears to be unstable for our tested parameters, meaning that the Kapitza mechanics will not maintain a stable region in the inverted position. If, instead, we have a limit whereby $\lambda|z| \ll \Omega_0$, then the potential term might be written in the following manner:

$$V = \Omega_0 \sqrt{1 + \left(\frac{\lambda z}{\Omega_0}\right)^2} \tag{7.41}$$

The Taylor expansion of this equation is as follows:

$$V = \Omega_0 + \frac{\lambda^2 z^2}{2\Omega_0} + \mathcal{O}(z^4) \tag{7.42}$$

In this regime, the potential is harmonic; therefore, through careful selection of driving, a stable region might be found in the inverted position. This criterion is an additional challenge to utilising the Kapitza mechanism for an atomic trapping system. Relating this finding to our system, we find that, in general, the systems that we have tested thus far are generally in the linear regime, and therefore the resulting system is unstable. This system property makes finding a stable configuration utilising vertical Kapitza driving challenging. None of our stable mechanical systems tested in the previous chapters of this thesis has stable counterparts in the atomic trapping scheme. If a stable region were found utilising this technique, it would require the delicate balancing of multiple inequalities to obtain a stable configuration. Having tested a wide range of systems that are of the correct scale for an experimental system, we can conclude that either the stable system lies outside of the range of parameters tested and therefore outside of expected system parameters for an experimental system or that a stable system might still be found within this range. However, the stability regions may be significantly smaller, making them experimentally and numerically challenging to find. Instead, we focus on a different configuration of the system to achieve trapping at the north pole of the potential field. As such, we now focus on trying to achieve the same effect, namely a stabilisation around the north pole of the trapping potential that does not rely on this

Kaptiza style driving to maintain stability.

7.3 Rapid horizontal driving at the north pole

Experimentally, there is an excellent degree of control over how the potential is manipulated for an atomic trapping scheme. More complicated modes of control than simple vertical driving might be considered to achieve a stable system at the north pole of a trapping potential. One alternative approach we propose utilises a horizontal driving in both x and y to generate a stable region at the north pole of the trapping potential, much like a vertical driving can achieve a time-averaged adiabatic potential at the equator [65, 51]. Indeed Lesanovsky and von Klitzing [65] proposes a circular driving scheme to stabilise an atom within a dumbbell-like structure. This paper uses a circular motion to achieve its results within the same trapping potential. This system has zero coupling and thus a hole when the atoms are at the north pole of the trapping potential. In this section of the thesis, we will explore our own circular driving of the system with a modified potential such as to avoid the presence of a hole; we will also show that the system exhibits properties that indicate the formation of a time-averaged adiabatic potential located around the north pole of the potential. We choose a polarisation of the magnetic field tangential to the surface of the potential utilised in the stable system at the equator. By making this choice, we obtain an expression for the system's Rabi frequency in the form of

$$\Omega_0(x,y,z,t) = \frac{|\alpha B_1|}{4b'}\left(1 + \frac{x+y+2z}{\sqrt{x^2+y^2+4z^2}}\right). \tag{7.43}$$

We then introduce a modulation in the x and y terms so that the Rabi frequency becomes

$$\Omega_0(x,y,z,t) = \frac{|\alpha B_1|}{4b'}\left(1 + \frac{X_t+Y_t+2z}{\sqrt{X_t^2+Y_t^2+4z^2}}\right), \tag{7.44}$$

with

$$X_t = \frac{B_m}{2b'} \sin(\omega_m t) \tag{7.45}$$

and

$$Y_t = \frac{B_m}{2b'} \cos(\omega_m t). \tag{7.46}$$

We will keep all the remaining terms the same as the Kapitza style inverted atomic system to give an overall Lagrangian for the system in the following form:

$$\begin{aligned} L =& \frac{m}{2}\left(\left(\frac{\partial x}{\partial t}\right)^2 + \left(\frac{\partial y}{\partial t}\right)^2 + \left(\frac{\partial z}{\partial t}\right)^2\right) - mgz \\ & - m'_F\hbar \left[\frac{\alpha^2 B_1^2}{16b'^2}\left(1 + \frac{X_t + Y_t + 2z}{\sqrt{X_t^2 + Y_t^2 + 4z^2}}\right)^2\right. \\ & \left. + \left(\omega_{rf} - \alpha\sqrt{X_t^2 + Y_t^2 + 4z^2}\right)^2\right]^{\frac{1}{2}}. \end{aligned} \tag{7.47}$$

From this Lagrangian we derive the equations of motion for the system. These equations of motions are

$$\frac{\partial x}{\partial t} = X, \tag{7.48}$$

$$\frac{\partial y}{\partial t} = Y, \tag{7.49}$$

$$\frac{\partial z}{\partial t} = Z, \tag{7.50}$$

$$\begin{aligned}\frac{\partial X}{\partial t} =& -\frac{m'_F\hbar}{2m}\left[\frac{\alpha^2 B_1^2}{8b'^2}\frac{\left(Y_t^2+4z^2-X_t\left(Y_t+2z\right)\right)}{\left(X_t^2+Y_t^2+4z^2\right)^2}\right.\\ &\times\left(X_t+Y_t+2z+\sqrt{X_t^2+Y_t^2+4z^2}\right)\\ &\left.+2X_t\alpha\left(\alpha-\frac{\omega_{rf}}{\sqrt{X_t^2+Y_t^2+4z^2}}\right)\right]\\ &\times\left[\frac{\alpha^2 B_1^2}{16b'^2}\left(1+\frac{X_t+Y_t+2z}{\sqrt{X_t^2+Y_t^2+4z^2}}\right)^2+\left(\omega_{rf}-\alpha\sqrt{X_t^2+Y_t^2+4z^2}\right)^2\right]^{-\frac{1}{2}},\end{aligned} \tag{7.51}$$

$$\begin{aligned}\frac{\partial Y}{\partial t} =& -\frac{m'_F\hbar}{2m}\left[\frac{\alpha^2 B_1^2}{8b'^2}\frac{\left(X_t^2+4z^2-Y_t\left(X_t+2z\right)\right)}{\left(X_t^2+Y_t^2+4z^2\right)^2}\right.\\ &\times\left(X_t+Y_t+2z+\sqrt{X_t^2+Y_t^2+4z^2}\right)\\ &\left.+2Y_t\alpha\left(\alpha-\frac{\omega_{rf}}{\sqrt{X_t^2+Y_t^2+4z^2}}\right)\right]\\ &\times\left[\frac{\alpha^2 B_1^2}{16b'^2}\left(1+\frac{X_t+Y_t+2z}{\sqrt{X_t^2+Y_t^2+4z^2}}\right)^2+\left(\omega_{rf}-\alpha\sqrt{X_t^2+Y_t^2+4z^2}\right)^2\right]^{-\frac{1}{2}}\end{aligned} \tag{7.52}$$

and

$$\begin{aligned}\frac{\partial Z}{\partial t} =& -g-\frac{m'_F\hbar}{2m}\left[\frac{\alpha^2 B_1^2}{4b'^2}\frac{\left(X_t^2+Y_t^2-2z\left(X_t+Y_t\right)\right)}{\left(X_t^2+Y_t^2+4z^2\right)^2}\right.\\ &\times\left(X_t+Y_t+2z+\sqrt{X_t^2+Y_t^2+4z^2}\right)\\ &\left.+8\zeta(t)\alpha\left(\alpha-\frac{\omega_{rf}}{\sqrt{X_t^2+Y_t^2+4z^2}}\right)\right]\\ &\times\left[\frac{\alpha^2 B_1^2}{16b'^2}\left(1+\frac{X_t+Y_t+2z}{\sqrt{X_t^2+Y_t^2+4z^2}}\right)^2+\left(\omega_{rf}-\alpha\sqrt{X_t^2+Y_t^2+4z^2}\right)^2\right]^{-\frac{1}{2}}.\end{aligned} \tag{7.53}$$

We can then numerically simulate the system to check the system stability. For example, in figure 7.5 we plot a typical path for a stable system in this regime.

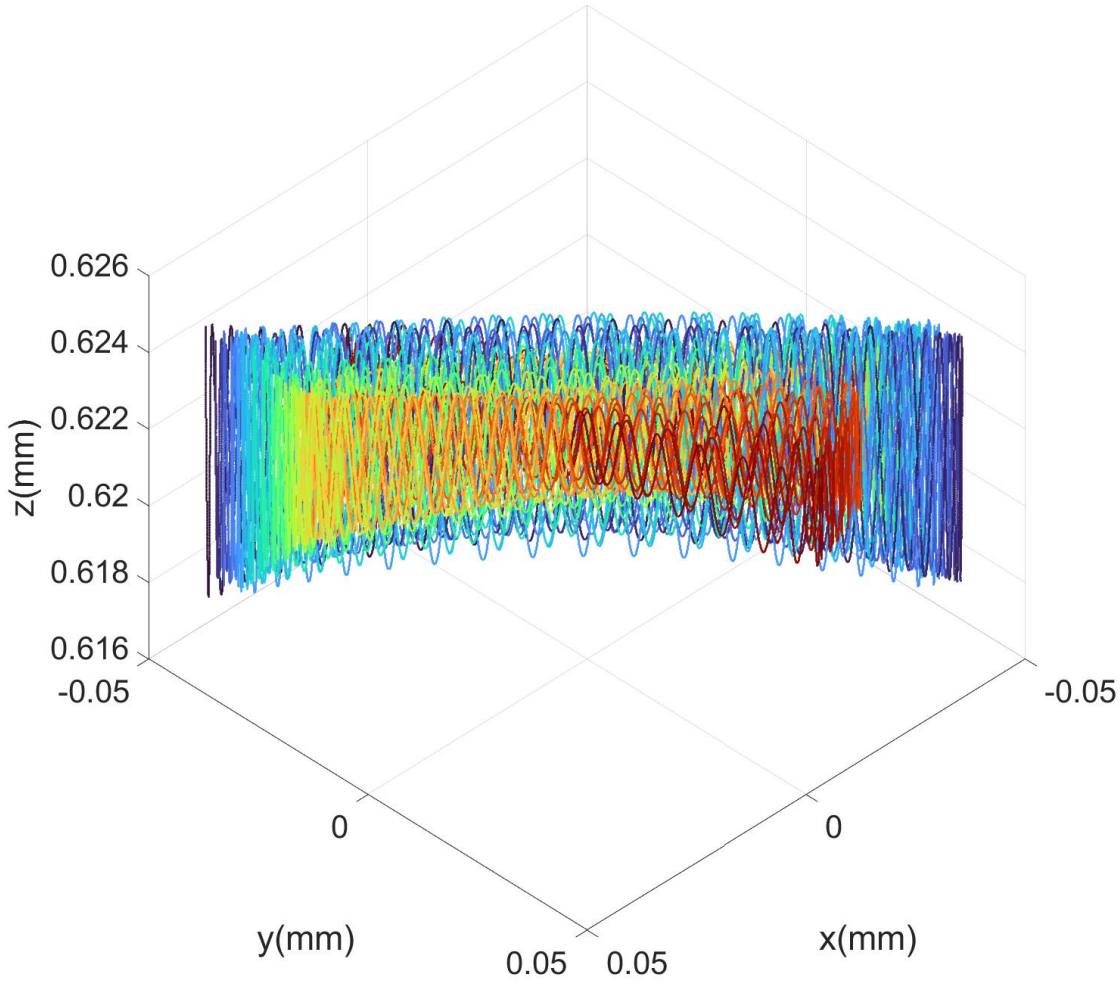

Figure 7.5: Typical path of an atom in a horizontally driven system and initially located near the north pole of a quadrupole. We set the initial position of the atom at a distance from the centre of the potential of 6.25×10^{-4} metres and an angle to the vertical of $\theta = \pi/32$ radians, setting $B_m = 2.5 \times 10^{-4}$ T, $\omega_{rf} = 5.5 \times 10^7$ rad/s, $B_{rf} = 1.3191 \times 10^{-7}$ T, $\omega_m = 1.6 \times 10^7$ rad/s. The simulation covers the location of the atom over a period of 1 second. The colour gradient starts at blue for $t = 0$ and goes through to red at time $t = 1$ second.

We can see that the atom remains stable around the north pole of the quadrupole with oscillations in the x, y and z directions. We can better understand the system's dynamics by plotting the x and z components.

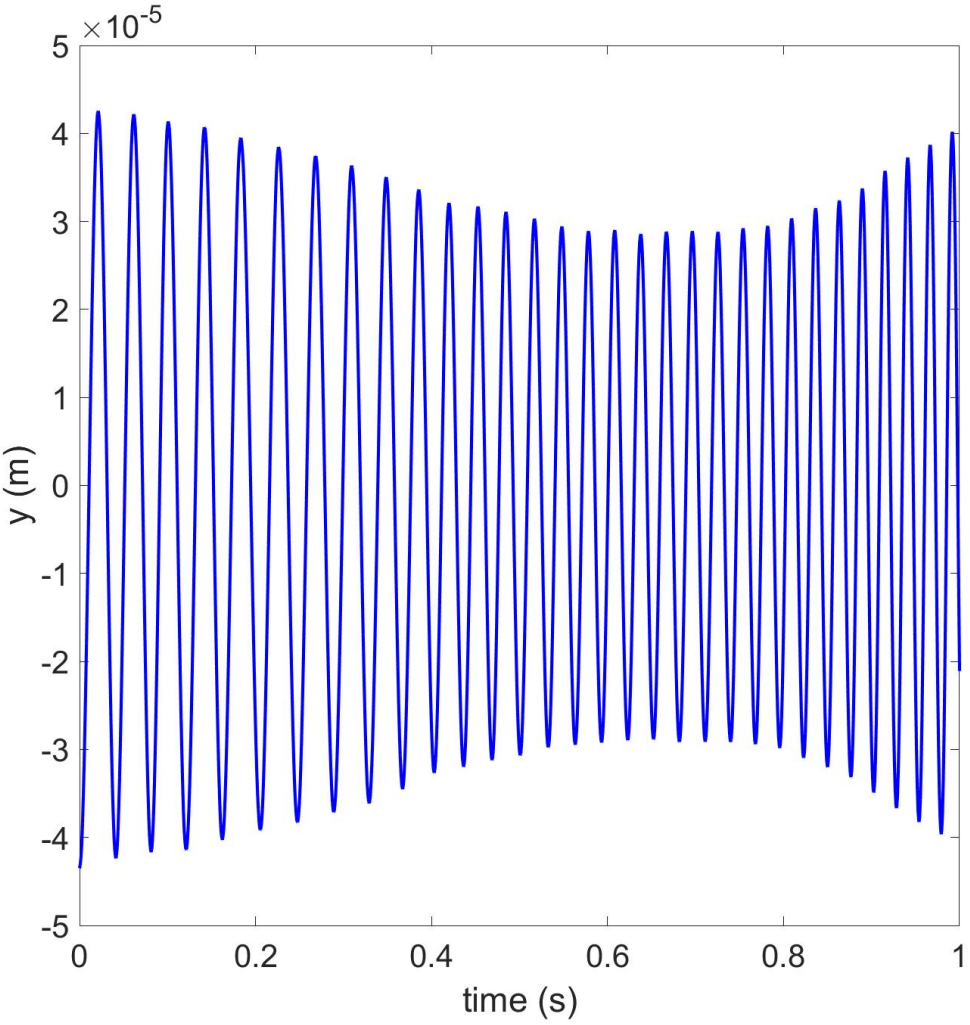

Figure 7.6: Evolution in y of an atom in a horizontally driven system and located near the north pole of a quadrupole. We set the initial position of the atom at a distance from the centre of the potential of 6.25×10^{-4} metres and an angle to the vertical of $\theta = \pi/32$ radians, setting $B_m = 2.5 \times 10^{-4}$ T, $\omega_{rf} = 5.5 \times 10^7$ rad/s, $B_{rf} = 1.3191 \times 10^{-7}$ T, $\omega_m = 1.6 \times 10^7$ rad/s. The simulation covers the atom's location over 1 second.

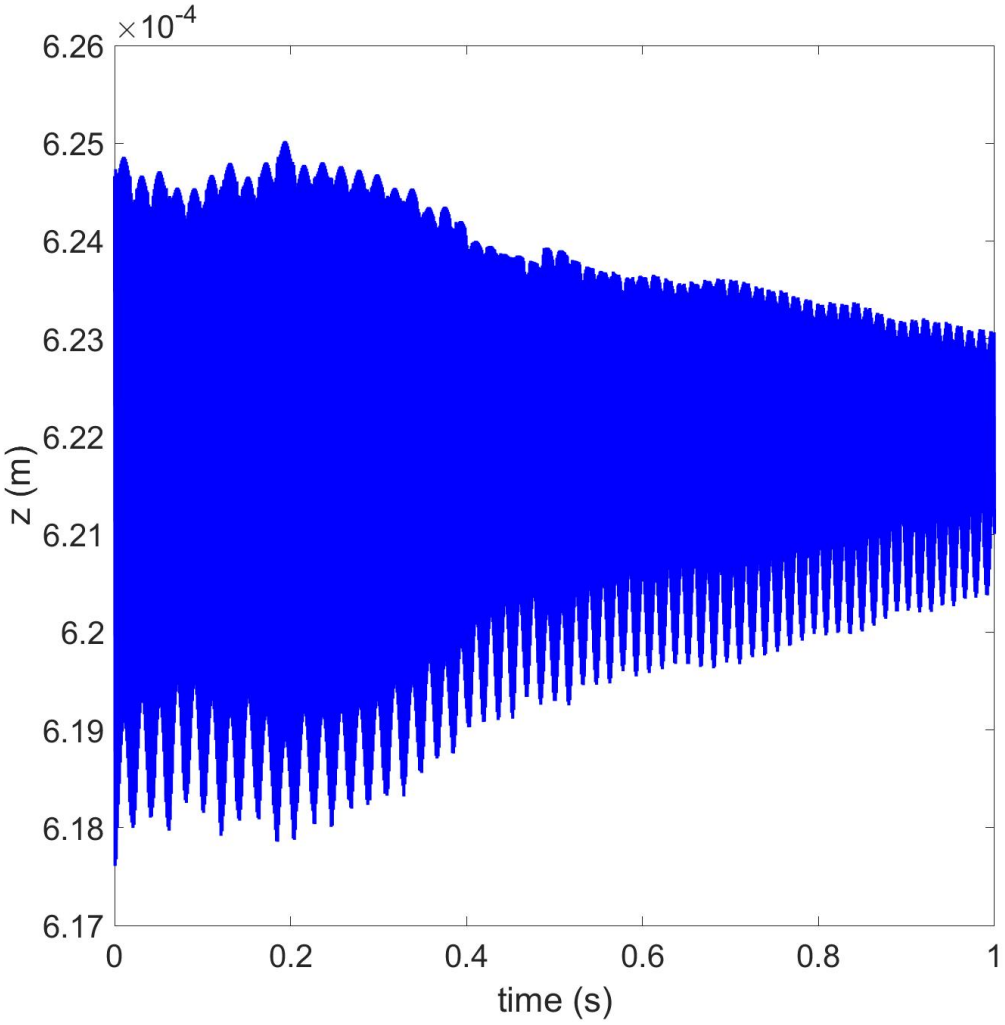

Figure 7.7: Evolution in z of an atom in a horizontally driven system located near the north pole of a quadrupole. We set the initial position of the atom at a distance from the centre of the potential of 6.25×10^{-4} metres and an angle to the vertical of $\theta = \pi/32$ radians, setting $B_m = 2.5 \times 10^{-4}$ T, $\omega_{rf} = 5.5 \times 10^7$ rad/s, $B_{rf} = 1.3191 \times 10^{-7}$ T, $\omega_m = 1.6 \times 10^7$ rad/s. The simulation covers the atom's location over 1 second.

From figures 7.6-7.7, we can see that the two components are oscillating back and forth around the north pole of the quadrupole and do not exhibit the same drift observed in the previous section with the vertically driven potential. This behaviour demonstrates that this trapping scheme stabilises the atom around the north pole. We note that the oscillations in the z direction decrease in magnitude over time; however, there is no drift in the median position in z over time, meaning that the system is stable over the interval simulated. This system is in marked contrast

to the results we saw when looking at the vertically driven system, which would immediately begin to drift away from the north pole when initialised. Given that this approach is similar to the approach used to stabilise the equator, we expected this result. We note that in the equator stabilised system, the atom oscillates a little below the equator, largely due to gravitational sagging of the trapping potential. In this system, this feature is not noticeable given that the sagging effect is symmetric about the north pole and, therefore, will affect the atom symmetrically. Having shown that this system behaves to stabilise the atoms at the north pole of the trapping potential, we will now look to show that we have a time-averaged adiabatic potential. To time-average the potential, we use the integral

$$V_{ta} = \frac{k\omega_m}{2\pi} \int_0^{\frac{2\pi}{k\omega_m}} V dt, \tag{7.54}$$

with k a whole integer representing the total number of full oscillation cycles to integrate over. We note that the potential we have utilised does not appear to have an analytical solution to the integration. Instead, we take the power series expansion of the potential in t and utilise this in our integration. For this thesis, we will be looking over the first four cycles to average out any variations; therefore, we set $k = 4$. To demonstrate that this system does behave as a time-averaged adiabatic potential, we expect to see that the time-averaged potential function will exhibit a characteristic harmonic potential shape in x and y at the north pole of the trapping potential. Additionally, the frequency of oscillations in x and y will be consistent with a harmonic potential of a similar shape.

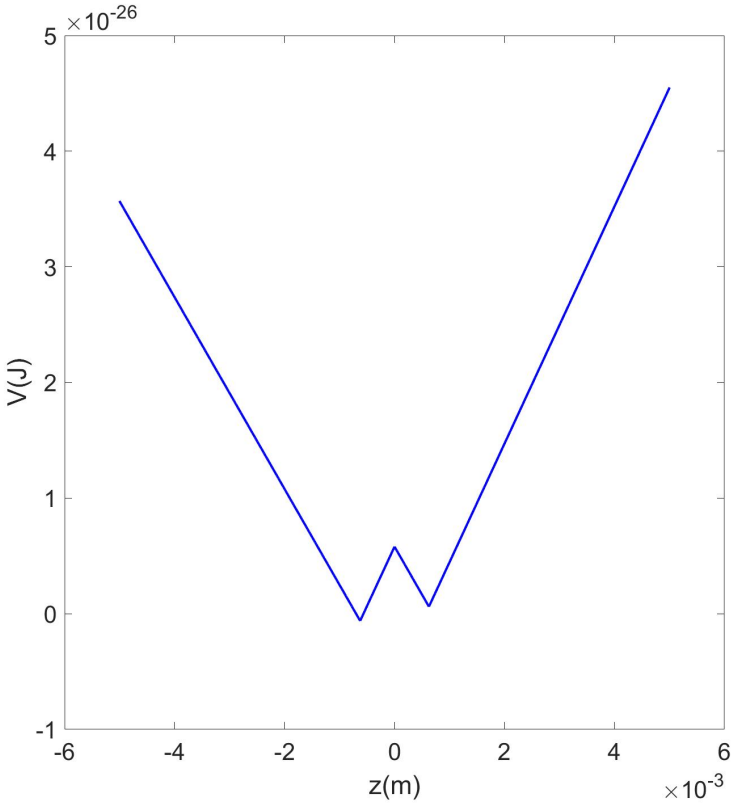

Figure 7.8: The time-averaged potential field in z along the z-axis. With $B_m = 2.5 \times 10^{-4}$ T, $\omega_{rf} = 5.5 \times 10^7$ s^{-1}, $B_{rf} = 1.3191 \times 10^{-7}$ T, $\omega_m = 1.6 \times 10^7$ s^{-1}.

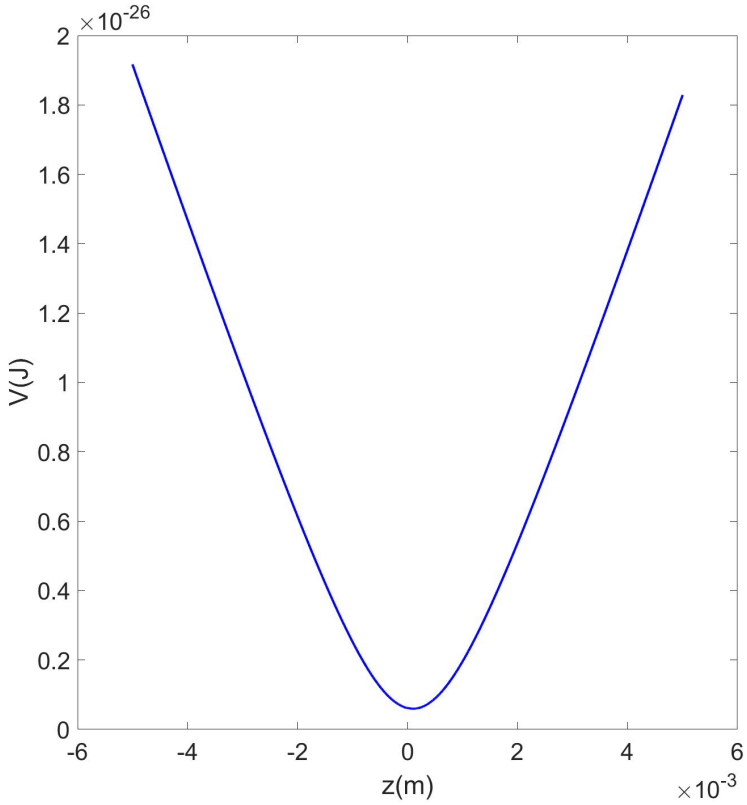

Figure 7.9: The time-averaged potential field in x at the north pole of the trapping potential. With $B_m = 2.5 \times 10^{-4}$ T, $\omega_{rf} = 5.5 \times 10^7$ s^{-1}, $B_{rf} = 1.3191 \times 10^{-7}$ T, $\omega_m = 1.6 \times 10^7$ s^{-1}.

In figure 7.8, we observe two local minima associated with the top and bottom of the trapping potential. The potential energy is lower for the minima located in negative z primarily since the gravitational potential energy is lower for this location on the potential. In figure 7.9, we see that, indeed, the time-averaged potential does appear to form a harmonic potential. This property would indicate that under this time-averaging approach, we do observe that we have a harmonic potential, explaining the emergence of a stable region at the north pole of the trapping potential. To verify that this time-averaged harmonic potential is responsible for the systems behaviour, we look at the number of oscillations per second observed in figure 7.6. From this number of oscillations, we are then able to describe a harmonic potential in the form of the expression

$$V = \frac{1}{2} m\omega^2 x^2 \tag{7.55}$$

which has the same frequency of oscillations. We then plot this potential, with an offset so that the minimum for this and the time-averaged potential are the same, in figure 7.10.

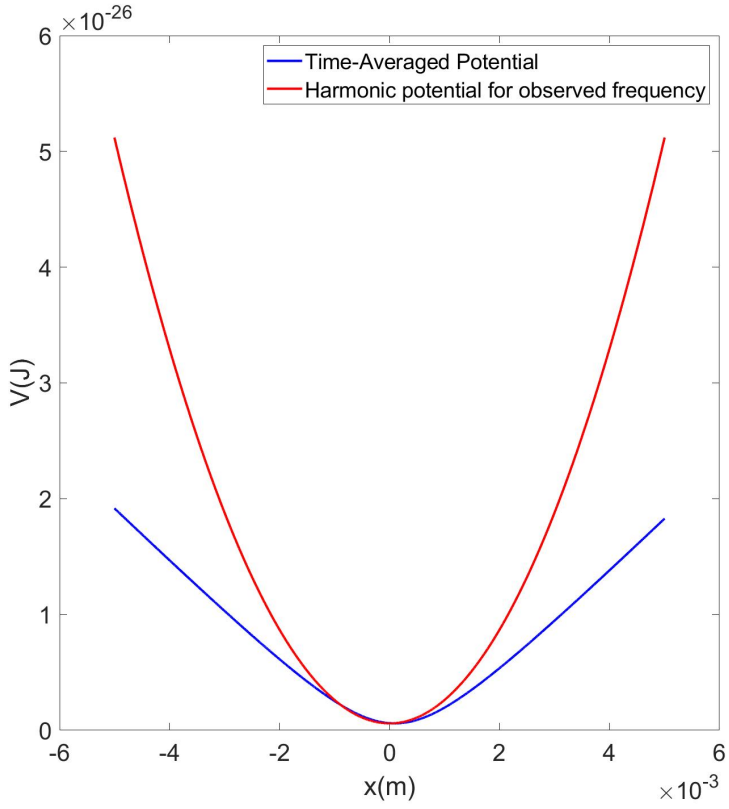

Figure 7.10: The time-averaged potential field in x at the north pole of the trapping potential is plotted in blue and a trapping potential consistent with the oscillations observed in x is plotted in red. With $B_m = 2.5 \times 10^{-4}$ T, $\omega_{rf} = 5.5 \times 10^7$ s^{-1}, $B_{rf} = 1.3191 \times 10^{-7}$ T, $\omega_m = 1.6 \times 10^7$ s^{-1}.

In figure 7.10, we see that the two potentials appear similar, especially in the region around the north pole. Since the system is not an harmonic oscillator and its behaviour is more complex, we would expect that results do not perfectly line up but should be consistent, and this is what we see here, with the two curves following a similar line, particularly around the minimum. As a result, this indicates that, indeed, the behaviour of the atom in such a system is being governed by a time-averaged adiabatic potential.

Overall, we have demonstrated that such a system can be utilised to stabilise an atom in an inverted position.

7.4 Conclusions

In this chapter, we have demonstrated that, although a mechanical Kapitza system will be stable on an atomic trapping scale when we apply the same driving to the atomic system, the result appears to be unstable. Given the results outlined in chapter 5 of this thesis which indicate that a system on this scale can be stable we must conclude that the instability is a result of an-harmonicity in the potential and not due to the choice of scale, or the use of atoms. Since this is a result of the potential for the given system it may prove fruitful in future work beyond this thesis to consider what changes might be made to the potential to resolve the an-harmonicity given the indication that a stable system might be possible on this scale. We have suggested that this is due to the quadrupole being in a linear regime under the same input conditions as the mechanical system. Any stable systems that utilise these mechanics will likely be challenging to find, both experimentally and numerically. Instead, we have proposed an alternative approach utilising a horizontal driving of the system in the x and y directions with a full Rabi coupling at the north pole of the trapping potential, demonstrating that such a system can be stabilised at the north pole of the quadrupole. This approach of multi-directional driving was demonstrated previously in this thesis in the previous chapter for a purely mechanical system on an atomic trapping scale, and we have also subsequently demonstrated that this technique works for the atomic quadrupole. This approach provides a mechanism by which the inverted position may be stabilised and keep atoms in gravitationally unfavourable positions.

Chapter 8

Conclusions

In this thesis, we have been looking at the dynamics of atoms within the context of atom trapping schemes.

In chapter two of this thesis, we have derived expressions for the free expansion of both the toroidal (2.24) and hollow shell (2.92) wave-packets in three dimensions. Additionally, we have derived expressions for the fringe visibility for both systems, demonstrating their asymptotic nature, allowing for a greater understanding of what to expect experimentally. The visibility expressions might also help design experiments to look specifically at the free expansion of these geometries to obtain high visibility interference fringes.

In chapter three, we then demonstrated that our results mirror those achieved through the implementation of the Split-Step Fourier Method (SSFM), with direct comparisons yielding a high fidelity across all results. We observed that in both systems, a high-density central peak emerges, which in the toroidal geometry produces a central column. This central peak depended on the initial radius (R) and its ratio with the initial width (σ). Additional simulations of the system were conducted using the Gross-Pitaevskii equation and determined that the effects of this non-linearity on the overall system were minimal, particularly for systems with fewer than 10^4 atoms.

In chapter four, we looked at how our methodology might be applied to asymmetric systems to demonstrate the versatility of our approach. We demonstrated

how a numerical integration might be used when the system does not lead to an integral that has an analytic solution, showing that the numerical integration rapidly converges upon the correct solution as the number of steps utilised increases. We additionally showed that the divergence of our analytic expressions to the numerical simulation was slow, further verifying the accuracy of our approach in the asymmetric regime. Finally in this chapter, we identified the emergence of anti-nodes in the free expansion of the asymmetric hollow shell and the torus. These anti-nodes were highly dependent on the initial state and could be used experimentally to identify the properties of the original system.

In chapter five, we have demonstrated the viability of an atomic trapping scale inverted elastic pendulum. We have shown a broad range of variable combinations on this scale that lead to a stable system. Additionally, we have demonstrated the relative robustness of such a system such that a spread of starting conditions may still result in stable systems. We have shown an approximate Mathieu stability zone for these systems and then discussed and tested the reliability, showing that the Mathieu stability may only be used as a guide due to the linearisation approximations necessary with this approach. We showed that a system is more stable if the driving frequency is less than the radial trapping frequency and if the rest length is significantly larger than the driving amplitude. We found that the overall initial system velocity did not seem to affect stability except for a velocity in the θ direction, with the system relatively robust to initial velocities otherwise. The system does, however, appear to be more dependent on starting angle and length with the greater the starting angle, the more likely that system is to be unstable.

In chapter six, we looked at further variations on the mechanical Kapitza pendulum. Specifically, we found a reduction in the system's driving frequency and a reduction in the system's total energy as a function of time. This property we then verified analytically utilising the linearised approximation of the system. We also looked at how driving the system in multiple directions might be used to control the location of the pendulum, moving the stable region away from the inverted position

to other locations and maintaining its stability over the horizontal.

Finally, in chapter seven, we took our understanding of the mechanical Kapitza pendulum and applied it to an rf-dressed three-dimensional quadrupole magnetic field. We found that the vertical driving of this quadrupole did not produce a stable system as straightforwardly as the mechanical system. One possibility for this is that the system occupies a linear regime and not an harmonic one required for stability. We instead proposed an alternative driving scheme to create a stable region at the north pole of this quadrupole by driving the system in the x and y directions. We showed that this system was able to stabilise the inverted position of this quadrupole and therefore provides an alternative approach to trapping the atoms that stabilise the north pole.

Through the research undertaken in writing this thesis, several avenues can now be explored beyond the scope of the work presented here. Firstly, with the free expansion of wave packets, we have demonstrated the versatility of our analytical approach, which indicates that the methodology might be applied to a wide range of different systems depending on the areas of experimental interest. Additionally, we presented one type of asymmetry that our new methodology could study, but, given how the interference pattern of any system is highly dependent on its initial state, many more might be of interest. Furthermore, we compared our results to numerical simulations, aiming to demonstrate what might be seen experimentally; however, it would be a good test of both our methodology and our simulations to compare these results to ones obtained through experiment. Secondly, other trapping schemes might be tested with the inverted pendulum style trapping to check whether stable configurations may be found more easily. Also, experimentally testing our alternative approach to stabilising the atom utilising a horizontal driving is of interest to check whether this might be an experimentally viable alternative. Finally, a further investigation into what parameters might lead to a stable Kapitza-style driving in the atomic system could provide insight into whether there is an experimentally viable set of parameters where this mechanism might be applied to

achieve stability at the north pole of the trapping potential.

Appendix A

Alternative method for the toroidal wave-packet

In this appendix, we will be looking at an alternative method for finding equations for the free-expanding three-dimensional torus. This approach utilises the wave-function density and therefore omits any phase considerations. This methodology may be preferable depending on whether the concern is just for the shape of the wave function and what one might expect to see experimentally. The idea behind this method of approach is the same basis as the other method used in the main part of this thesis. With this second methodology, we start with the following expression for a Gaussian wave-packet which was adapted from Pauli [111] by J.-M. Martin in his thesis [112]. This expression is as follows:

$$\begin{aligned}\psi_0(\mathbf{r},t,v_{\mathbf{r}},v_{\Delta},k_{\mathbf{r}},\omega_{\mathbf{r}},\Delta k) =& \frac{1}{\sqrt{N}}\exp\left(-\frac{(\mathbf{r}-v_{\mathbf{r}}t)^2}{4\sigma(t)^2}\right)\\ &\times\exp\left(i\frac{v_{\Delta}t}{\sigma_0}\frac{(\mathbf{r}-v_{\mathbf{r}}t)^2}{4\sigma(t)^2}+i\left(k_{\mathbf{r}}\cdot\mathbf{r}-\omega_{\mathbf{r}}t\right)\right)\\ &\times\exp\left(-\frac{i}{2}\arccos\left(\frac{1}{2\sigma(t)\Delta k}\right)\right),\end{aligned} \tag{A.1}$$

where $\mathbf{r}$ is a spatial coordinate, $v_{\mathbf{r}}$ the initial velocity, $k_{\mathbf{r}}$ is the momentum, $\omega_{\mathbf{r}}$ is the trapping frequency and N is a general normalisation constant. In the specific case we are looking at, namely the free expansion of a toroidal wave packet, we

can impose certain conditions on the system. Firstly, we assume that the toroidal wave-packet is initially static, therefore meaning $v_{\mathbf{r}} = 0$; we also impose that the initial momentum of the system is also zero meaning $k_{\mathbf{r}} = 0$. Additionally, since we are looking at free expansion, the trapping frequency can also be set to zero. At this point, it is possible to make rewrite several terms in our expression so that they are in terms of the constants σ_0, $\hbar$ and m with

$$\Delta k = \frac{1}{2\sigma_0} \tag{A.2}$$

and

$$v_\Delta = \frac{\hbar}{2m\sigma_0} \tag{A.3}$$

For ease, we shall leave our $\Delta\mathbf{r}(t)^2$ term in the following derivation, but it is important to note that this can be expressed in terms of the same constants $\sigma_{\mathbf{r}}$, $\hbar$ and m such that

$$\sigma(t)^2 = \sigma_0^2 + \frac{\hbar^2 t^2}{4m^2\sigma_0^2}. \tag{A.4}$$

Making all these substitutions results in the following expression:

$$\begin{aligned}\psi_0(\mathbf{r}, t, \omega_{\mathbf{r}}) =& \frac{1}{\sqrt{N}} \exp\left(-\frac{\mathbf{r}^2}{4\sigma(t)^2}\right) \\ &\times \exp\left(\frac{i\hbar t}{8m\sigma_0^2\sigma(t)^2}\mathbf{r}^2 - i\omega_{\mathbf{r}} t - \frac{i}{2}\arccos\left(\frac{\sigma_0}{\sigma(t)}\right)\right).\end{aligned} \tag{A.5}$$

This is the wave-function expression for a free Gaussian distribution located at the origin. We want to now introduce a transformation to centre the Gaussian at a location we will label $\mathbf{r}_0$ which gives the following expression for the wave-function:

$$\begin{aligned}\psi_0(\mathbf{r}, t, \omega_{\mathbf{r}}) =& \frac{1}{\sqrt{N}} \exp\left(-\frac{(\mathbf{r} - \mathbf{r}_0)^2}{4\sigma(t)^2}\right) \\ &\times \exp\left(\frac{i\hbar t}{8m\sigma_0^2\sigma(t)^2}(\mathbf{r} - \mathbf{r}_0)^2 - i\omega_{\mathbf{r}} t - \frac{i}{2}\arccos\left(\frac{\sigma_0}{\sigma(t)}\right)\right).\end{aligned} \tag{A.6}$$

Since the system we are considering is built of an infinite number of interacting Gaussian distributions, it makes sense to create a density matrix for two Gaussian wave packets with

$$\rho_0(\mathbf{r}, \mathbf{r}', t) = \psi_0(\mathbf{r}, t) \times \psi_0^\dagger(\mathbf{r}', t). \tag{A.7}$$

Since we are only interested in the magnitude of the final wave-function in this methodology we shall only be using terms on the diagonal when $\mathbf{r} = \mathbf{r}'$. By taking the density matrix, all imaginary terms that are independent of the coordinate $\mathbf{r}$ cancel giving the expression

$$\begin{aligned}\rho(\mathbf{r}, t) =& \frac{1}{N} \exp\left(-\frac{(\mathbf{r} - \mathbf{r}_0)^2 + (\mathbf{r} - \mathbf{r}_0')^2}{4\sigma(t)^2}\right) \\ &\times \exp\left(\frac{i\hbar t}{8m\sigma_0^2\sigma(t)^2}\left[(\mathbf{r} - \mathbf{r}_0)^2 - (\mathbf{r} - \mathbf{r}_0')^2\right]\right),\end{aligned} \tag{A.8}$$

where N is some normalisation factor as yet undetermined. Now that we have a general expression, let us rewrite it in Cartesian coordinates where

$$(\mathbf{r} - \mathbf{r}_0)^2 = (x - x_0)^2 + (y - y_0)^2 + (z - z_0)^2. \tag{A.9}$$

We will assume that the Gaussian's width is uniform in all directions, but this is not a necessary assumption to make. Indeed, we will consider what happens when this is not the case. Since the initial width is the same in all dimensions, the dispersion expression $\sigma(t)$ remains the same for each coordinate. Rewriting our equation (A.8)

in Cartesian coordinates gives us

$$\begin{aligned}\rho\left(x,y,z,t\right) =& \frac{1}{N}\exp\left(-\frac{\left(x-x_0\right)^2+\left(y-y_0\right)^2+\left(z-z_0\right)^2}{4\sigma(t)^2}\right)\\ &\times\exp\left(-\frac{\left(x-x_0'\right)^2+\left(y-y_0'\right)^2+\left(z-z_0'\right)^2}{4\sigma(t)^2}\right)\\ &\times\exp\left(\frac{i\hbar t}{8m\sigma_0^2\sigma(t)^2}\left(\left(x-x_0\right)^2+\left(y-y_0\right)^2+\left(z-z_0\right)^2\right)\right)\\ &\times\exp\left(\frac{-i\hbar t}{8m\sigma_0^2\sigma(t)^2}\left(\left(x-x_0'\right)^2+\left(y-y_0'\right)^2+\left(z-z_0'\right)^2\right)\right).\end{aligned} \tag{A.10}$$

We must now define the location of these Gaussian distributions. Our end result we are aiming for is a toroidal wave-packet. As such we want these Gaussians to lie somewhere on the torus. To do this we will set our initial locations in x, y and z as follows:

$$x_0 = R\cos(\theta), \tag{A.11}$$

$$x_0' = R\cos(\theta'), \tag{A.12}$$

$$y_0 = R\sin(\theta), \tag{A.13}$$

$$y_0' = R\sin(\theta'), \tag{A.14}$$

and

$$z_0 = z_0' = 0, \tag{A.15}$$

where R is the distance to the origin, θ is the angle that at which the wave-function is located and θ' is the location of the interfering wave-packet. By setting $r^2 = x^2 + y^2$ and then expanding and simplifying our two functions we get the following

expression:

$$\begin{aligned}\rho\left(r,\theta,\theta',z,t\right) =& \frac{1}{N}\exp\left(-\frac{r^2+R^2+z^2}{2\sigma(t)^2}\right)\exp\left(\left(\frac{1}{2\sigma(t)^2}-\frac{i\hbar t}{4m\sigma_0^2\sigma(t)^2}\right)Rr\cos(\theta)\right)\\ &\times\exp\left(\left(\frac{1}{2\sigma(t)^2}+\frac{i\hbar t}{4m\sigma_0^2\sigma(t)^2}\right)Rr\cos(\theta')\right).\end{aligned} \tag{A.16}$$

This expression is for two interacting Gaussian wave packets. However, we want instead to use an infinite summation of these to form our torus. To do this, we will integrate θ and θ' through the circumference of a torus. We then need to renormalise the resulting expression giving us

$$\begin{aligned}\rho_{\text{torus}}\left(r,\theta,\theta',z,t\right) =& \frac{1}{N}\exp\left(-\frac{r^2+R^2+z^2}{2\sigma(t)^2}\right)\\ &\times\int_0^{2\pi}\int_0^{2\pi}\exp\left(\left(\frac{1}{2\sigma(t)^2}-\frac{i\hbar t}{4m\sigma_0^2\sigma(t)^2}\right)Rr\cos(\theta)\right)\\ &\times\exp\left(\left(\frac{1}{2\sigma(t)^2}+\frac{i\hbar t}{4m\sigma_0^2\sigma(t)^2}\right)Rr\cos(\theta')\right)d\theta d\theta'.\end{aligned} \tag{A.17}$$

When we perform the integration, we must use the following identity,

$$I_0(z)=\frac{1}{\pi}\int_0^{\pi}\exp(z\cos(\theta))d\theta \tag{A.18}$$

Using this and normalising expression we get the final expression for a toroidal wave-packet in the following form:

$$\begin{aligned}\rho_{\text{torus}}\left(r,z,t\right) =& \frac{1}{(2\pi\sigma(t)^2)^{\frac{3}{2}}\exp\left(-\frac{R^2}{4\sigma_0^2}\right)I_0\left(\frac{R^2}{4\sigma_0^2}\right)}\exp\left(-\frac{r^2+R^2+z^2}{2\sigma(t)^2}\right)\\ &\times\left|I_0\left(Rr\left(\frac{1}{2\sigma(t)^2}+\frac{i\hbar t}{4m\sigma_0^2\sigma(t)^2}\right)\right)\right|^2.\end{aligned} \tag{A.19}$$

Rewriting this expression using the variables in the main part of this thesis, we find that we get the same expression we found using the other methodology in equation (2.38) for the wave-function density we obtain the expression

$$|\psi_{\text{3dtorus}}|^2=\frac{1}{(2\pi)^{\frac{3}{2}}\sigma(\tau)^3}\exp\left(-\frac{(r^2+R^2+z^2)}{2\sigma(\tau)^2}+\frac{R^2}{4\sigma_0^2}\right)\frac{\left|I_0\left(\frac{rR(1-i\tau)}{2\sigma(\tau)^2}\right)\right|^2}{I_0\left(\frac{R^2}{4\sigma_0^2}\right)}. \tag{A.20}$$

Since we have demonstrated that we arrive at the same density function using either of our approaches, we can conclude that either approach is valid, and therefore it is a matter of preference as to which approach is used with the method used in the main body of this thesis providing phase data whereas this approach does not.

Appendix B

Alternative method for the hollow shell wave-packet

As with the toroidal geometry, we use the equation (A.10) as a starting point. We therefore begin with the expression

$$\begin{aligned}\rho\left(x,y,z,t\right) =& \frac{1}{N}\exp\left(-\frac{\left(x-x_0\right)^2+\left(y-y_0\right)^2+\left(z-z_0\right)^2}{4\sigma(t)^2}\right)\\ &\times\exp\left(-\frac{\left(x-x_0'\right)^2+\left(y-y_0'\right)^2+\left(z-z_0'\right)^2}{4\sigma(t)^2}\right)\\ &\times\exp\left(\frac{i\hbar t}{8m\sigma_0^2\sigma(t)^2}\left(\left(x-x_0\right)^2+\left(y-y_0\right)^2+\left(z-z_0\right)^2\right)\right)\\ &\times\exp\left(\frac{-i\hbar t}{8m\sigma_0^2\sigma(t)^2}\left(\left(x-x_0'\right)^2+\left(y-y_0'\right)^2+\left(z-z_0'\right)^2\right)\right).\end{aligned} \tag{B.1}$$

For a hollow shell wave-packet we locate the Gaussians on the shell such that the wave-packets are centred at the following location:

$$x_0 = R\sin(\phi)\cos(\theta), \tag{B.2}$$

$$x_0' = R\sin(\phi')\cos(\theta'), \tag{B.3}$$

$$y_0 = R\sin(\phi)\sin(\theta), \tag{B.4}$$

$$y_0' = R\sin(\phi')\sin(\theta'), \tag{B.5}$$

$$z_0 = R\cos(\phi) \tag{B.6}$$

and

$$z_0' = R\cos(\phi'), \tag{B.7}$$

where R is the desired radius of the hollow shell, θ and θ' the polar angle and ϕ and ϕ' the azimuthal angular location of the two wave-packets. The prime differentiates between the two interacting wave packets. We can then take the above and substitute it into our equation (A.10). In doing so we obtain the expression

$$\begin{aligned}\rho =& \frac{1}{N}\exp\left(-\frac{(x-R\sin(\phi)\cos(\theta))^2+(y-R\sin(\phi)\sin(\theta))^2+(z-R\cos(\phi))^2}{4\sigma(t)^2}\right)\\ &\times\exp\left(-\frac{(x-R\sin(\phi')\cos(\theta'))^2+(y-R\sin(\phi')\sin(\theta'))^2+(z-R\cos(\phi'))^2}{4\sigma(t)^2}\right)\\ &\times\exp\left(\frac{i\hbar t}{8m\sigma_0^2\sigma(t)^2}\left((x-R\sin(\phi)\cos(\theta))^2+(y-R\sin(\phi)\sin(\theta))^2\right)\right)\\ &\times\exp\left(\frac{-i\hbar t}{8m\sigma_0^2\sigma(t)^2}\left((x-R\sin(\phi')\cos(\theta'))^2+(y-R\sin(\phi')\sin(\theta'))^2\right)\right)\\ &\times\exp\left(\frac{i\hbar t}{8m\sigma_0^2\sigma(t)^2}\left(z-R\cos(\phi)\right)^2\right)\\ &\times\exp\left(\frac{-i\hbar t}{8m\sigma_0^2\sigma(t)^2}\left(z-R\cos(\phi')\right)^2\right).\end{aligned} \tag{B.8}$$

Having obtained this density function for two interacting Gaussians, we wish to simplify the expression. If we consider the following term:

$$(x-R\sin(\phi)\cos(\theta))^2+(y-R\sin(\phi)\sin(\theta))^2+(z-R\cos(\phi))^2. \tag{B.9}$$

As before, with the toroidal wave packet, we can utilise symmetry. This time, the hollow shell is spherically symmetric, and as a result, we can define the system such that $x = y = 0$ and $z = r$. With this substitution, the above expression can be written as

$$\begin{aligned}
&(x - R\sin(\phi)\cos(\theta))^2 + (y - R\sin(\phi)\sin(\theta))^2 + (z - R\cos(\phi))^2 \\
\rightarrow\ & R^2\sin^2(\phi)\cos^2(\theta) + R^2\sin^2(\phi)\sin^2(\theta) + r^2 - 2Rr\cos(\phi) + R^2\cos^2(\phi) \\
&= r^2 + R^2 - 2Rr\cos(\phi).
\end{aligned} \tag{B.10}$$

With this knowledge, the density function can be simplified into the following form:

$$\begin{aligned}
\rho\left(r, \phi, \phi', \theta, \theta', t\right) =& \frac{1}{N}\exp\left(-\frac{r^2 + R^2 - 2Rr\cos(\phi)}{4\sigma(t)^2}\right) \\
&\times \exp\left(-\frac{r^2 + R^2 - 2Rr\cos(\phi')}{4\sigma(t)^2}\right) \\
&\times \exp\left(\frac{i\hbar t}{8m\sigma_0^2\sigma(t)^2}\left(r^2 + R^2 - 2Rr\cos(\phi)\right)\right) \\
&\times \exp\left(\frac{-i\hbar t}{8m\sigma_0^2\sigma(t)^2}\left(r^2 + R^2 - 2Rr\cos(\phi')\right)\right).
\end{aligned} \tag{B.11}$$

Now that we have the expression for two interacting Gaussian distributions located on the hollow shell, we want to integrate through the angles θ, θ', ϕ and ϕ'. This integration is the equivalent of taking the sum of an infinite number of similar Gaussians. All of these Gaussians we locate on the surface of a hollow shell. The integral we will be evaluating is

$$\begin{aligned}
\rho\left(r, \phi, \phi', \theta, \theta', t\right) =& \frac{1}{N}\int_0^{2\pi} d\theta \int_0^{2\pi} d\theta' \\
&\times \int_0^{\pi}\int_0^{\pi} \exp\left(-\frac{r^2 + R^2 - 2Rr\cos(\phi)}{4\sigma(t)^2}\right) \\
&\times \exp\left(-\frac{r^2 + R^2 - 2Rr\cos(\phi')}{4\sigma(t)^2}\right) \\
&\times \exp\left(\frac{i\hbar t}{8m\sigma_0^2\sigma(t)^2}\left(r^2 + R^2 - 2Rr\cos(\phi)\right)\right) \\
&\times \exp\left(\frac{-i\hbar t}{8m\sigma_0^2\sigma(t)^2}\left(r^2 + R^2 - 2Rr\cos(\phi')\right)\right)\sin(\phi)\sin(\phi')d\phi d\phi'.
\end{aligned} \tag{B.12}$$

Since the above function is independent in θ and θ', these integrals will result in an

additional $4\pi^2$ term. Since we still need to find the normalisation factor, we will absorb this term into N. The integral in ϕ and ϕ' is not trivial. First of all, we can extract terms independent of these two angles. This results in the following formulation:

$$\begin{aligned}\rho\left(r,\phi,\phi',\theta,\theta',t\right) =& \frac{1}{N}\exp\left(-\frac{r^2+R^2}{2\sigma(t)^2}\right)\\ &\times\int_0^{\pi}\int_0^{\pi}\exp\left(\frac{Rr}{2\sigma(t)^2}\left(1-\frac{i\hbar t}{2m\sigma_0^2}\right)\cos(\phi)\right)\\ &\times\exp\left(\frac{Rr}{2\sigma(t)^2}\left(1+\frac{i\hbar t}{2m\sigma_0^2}\right)\cos(\phi')\right)\sin(\phi)\sin(\phi')d\phi d\phi'.\end{aligned} \tag{B.13}$$

We now integrate this function, we can do so using the integral identity

$$\int_0^{\pi}\exp\left(A\cos(\phi)\right)\sin(\phi)d\phi = \frac{2}{A}\sinh(A). \tag{B.14}$$

Performing these integrations we get the following expression:

$$\begin{aligned}\rho\left(r,t\right) =& \frac{1}{N}\exp\left(-\frac{r^2+R^2}{2\sigma(t)^2}\right)\\ &\times\frac{4\sigma(t)^2}{Rr\left(1-\frac{i\hbar t}{2m\sigma_0^2}\right)}\sinh\left(Rr\left(\frac{1}{2\sigma(t)^2}-\frac{i\hbar t}{4m\sigma_0^2\sigma(t)^2}\right)\right)\\ &\times\frac{4\sigma(t)^2}{Rr\left(1+\frac{i\hbar t}{2m\sigma_0^2}\right)}\sinh\left(Rr\left(\frac{1}{2\sigma(t)^2}+\frac{i\hbar t}{4m\sigma_0^2\sigma(t)^2}\right)\right).\end{aligned} \tag{B.15}$$

We simplify this expression by absorbing any common multiplying terms that are constant in r and t and performing the multiplication of terms we obtain the expression

$$\begin{aligned}\rho\left(r,t\right) =& \frac{1}{N}\frac{16\sigma(t)^4}{R^2r^2\left(1+\frac{\hbar^2t^2}{4m^2\sigma_0^4}\right)}\exp\left(-\frac{r^2+R^2}{2\sigma(t)^2}\right)\\ &\times\left|\sinh\left(Rr\left(\frac{1}{2\sigma(t)^2}+\frac{i\hbar t}{4m\sigma_0^2\sigma(t)^2}\right)\right)\right|^2.\end{aligned} \tag{B.16}$$

Normalising the density function gives us the following final expression:

$$\begin{aligned}\rho\left(r,t\right) =& \frac{1}{\sqrt{2}\pi^{\frac{3}{2}} r^2 \sigma(t)\left(1-\exp\left(-\frac{R^2}{2\sigma_0^2}\right)\right)} \exp\left(-\frac{r^2+R^2}{2\sigma(t)^2}\right) \\ & \times \left|\sinh\left(Rr\left(\frac{1}{2\sigma(t)^2}+\frac{i\hbar t}{4m\sigma_0^2\sigma(t)^2}\right)\right)\right|^2 .\end{aligned} \tag{B.17}$$

This equation may be re-written as

$$\begin{aligned}\left|\psi_{\mathrm{hs}}(r,\tau)\right|^2 =& \frac{1}{(2\pi)^{\frac{3}{2}} r^2 \sigma(\tau)\left(1-\exp\left(-\frac{R^2}{2\sigma_0^2}\right)\right)} \left[\exp\left(-\frac{(r^2+R^2)}{2\sigma(\tau)^2}\right)\right. \\ & \left. \times \left(\cosh\left(\frac{rR}{\sigma(\tau)^2}\right)-\cos\left(\frac{rR\tau}{\sigma(\tau)^2}\right)\right)\right].\end{aligned} \tag{B.18}$$

Given that both approaches again lead to the same density function, it indicates that either approach is valid.

Appendix C

Runge-Kutta-Fehlberg algorithm

The Runge-Kutta-Fehlberg algorithm uses a large number of rational coefficients [104]. We detail the value of the coefficients here. The first lot of coefficients are

used in the intermediary step between the time steps,

$$
\begin{aligned}
c_{20} &= 1/4 \\
c_{21} &= 1/4 \\
c_{30} &= 3/8 \\
c_{31} &= 3/32 \\
c_{32} &= 9/32 \\
c_{40} &= 12/13 \\
c_{41} &= 1932/2197 \\
c_{42} &= -7200/2197 \\
c_{43} &= 7296/2197 \\
c_{50} &= 1 \\
c_{51} &= 439/216 \\
c_{52} &= -8 \\
c_{53} &= 3680/513 \\
c_{54} &= -845/4104 \\
c_{60} &= 1/2 \\
c_{61} &= -8/27 \\
c_{62} &= 2 \\
c_{63} &= -3544/2565 \\
c_{64} &= 1859/4104 \\
c_{65} &= 11/40
\end{aligned}
\tag{C.1}
$$

The following coefficients are used to calculate the new values after the time step,

$$\begin{aligned} y_{c1} &= 25/216 \\ y_{c3} &= 1408/2565 \\ y_{c4} &= 2197/4101 \\ y_{c5} &= -1/5 \end{aligned} \tag{C.2}$$

Finally these coefficients are used to calculate the error estimator,

$$\begin{aligned} z_{c1} &= 16/135 \\ z_{c3} &= 6566/12825 \\ z_{c4} &= 28561/56430 \\ z_{c5} &= -9/50 \\ z_{c6} &= 2/55 \end{aligned} \tag{C.3}$$

The algorithm for the Runge-Kutte-Fehlberg algorithm for the inverted elastic pendulum is as follows. We define x_i, X_i, y_i, Y_i, z_i and Z_i as the initial values for each parameter and x_{i+1}, X_{i+1}, y_{i+1}, Y_{i+1}, z_{i+1} and Z_{i+1} as the values after one full step. Finally we define δt as the time-step. The subscript on the a, b, c, d, e and f terms indicate which step of the algorithm the equation is a part of.

$$a_0 = \delta t \left(X_i \right) \tag{C.4}$$

$$b_0 = \delta t \left(\frac{\kappa l_0 x_i}{m\sqrt{x_i^2 + y_i^2 + z_i^2}} - \frac{\kappa x_i}{m} \right) \tag{C.5}$$

$$c_0 = \delta t \left(Y_i \right) \tag{C.6}$$

$$d_0 = \delta t \left(\frac{\kappa l_0 y_i}{m\sqrt{x_i^2 + y_i^2 + z_i^2}} - \frac{\kappa y_i}{m} \right) \tag{C.7}$$

$$e_0 = \delta t \left(Z_i \right) \tag{C.8}$$

$$f_0 = \delta t \left(\frac{\kappa l_0 z_i}{m\sqrt{x_i^2 + y_i^2 + z_i^2}} - \frac{\kappa z_i}{m} + A\Omega^2 \cos(\Omega t) - g \right) \tag{C.9}$$

$$a_1 = \delta t \left(X_i + c_{21} b_0 \right) \tag{C.10}$$

$$b_1 = \delta t \left(\frac{\kappa l_0 \left(x_i + c_{21} a_0 \right)}{m\sqrt{\left(x_i + c_{21} a_0 \right)^2 + \left(y_i + c_{21} c_0 \right)^2 + \left(z_i + c_{21} e_0 \right)^2}} - \frac{\kappa \left(x_i + c_{21} a_0 \right)}{m} \right) \tag{C.11}$$

$$c_1 = \delta t \left(Y_i + c_{21} d_0 \right) \tag{C.12}$$

$$d_1 = \delta t \left(\frac{\kappa l_0 \left(y_i + c_{21} c_0 \right)}{m\sqrt{\left(x_i + c_{21} a_0 \right)^2 + \left(y_i + c_{21} c_0 \right)^2 + \left(z_i + c_{21} e_0 \right)^2}} - \frac{\kappa \left(y_i + c_{21} c_0 \right)}{m} \right) \tag{C.13}$$

$$e_1 = \delta t \left(Z_i + c_{21} f_0 \right) \tag{C.14}$$

$$f_1 = \delta t \left(\frac{\kappa l_0 (z_i + c_{21} e_0)}{m\sqrt{(x_i + c_{21} a_0)^2 + (y_i + c_{21} c_0)^2 + (z_i + c_{21} e_0)^2}} \right. \tag{C.15}$$

$$\left. - \frac{\kappa (z_i + c_{21} e_0)}{m} + A\Omega^2 \cos(\Omega \left(t + c_{20} \delta t \right)) - g \right) \tag{C.16}$$

$$a_2 = \delta t \left(X_i + c_{31} b_0 + c_{32} b_1 \right) \tag{C.17}$$

$$b_2 = \delta t \left(\frac{\kappa l_0 \left(x_i + c_{31}a_0 + c_{32}a_1\right)}{m\sqrt{\left(x_i + c_{31}a_0 + c_{32}a_1\right)^2 + \left(y_i + c_{31}c_0 + c_{32}c_1\right)^2 + \left(z_i + c_{31}e_0 + c_{32}e_1\right)^2}} - \frac{\kappa \left(x_i + c_{31}a_0 + c_{32}a_1\right)}{m} \right) \tag{C.18}$$

$$c_2 = \delta t \left(Y_i + c_{31}d_0 + c_{32}d_1\right) \tag{C.19}$$

$$d_2 = \delta t \left(\frac{\kappa l_0 \left(y_i + c_{31}c_0 + c_{32}c_1\right)}{m\sqrt{\left(x_i + c_{31}a_0 + c_{32}a_1\right)^2 + \left(y_i + c_{31}c_0 + c_{32}c_1\right)^2 + \left(z_i + c_{31}e_0 + c_{32}e_1\right)^2}} - \frac{\kappa \left(y_i + c_{31}c_0 + c_{32}c_1\right)}{m} \right) \tag{C.20}$$

$$e_2 = \delta t \left(Z_i + c_{31}f_0 + c_{32}f_1\right) \tag{C.21}$$

$$f_2 = \delta t \left(\frac{\kappa l_0 \left(z_i + c_{31}e_0 + c_{32}e_1\right)}{m\sqrt{\left(x_i + c_{31}a_0 + c_{32}a_1\right)^2 + \left(y_i + c_{31}c_0 + c_{32}c_1\right)^2 + \left(z_i + c_{31}e_0 + c_{32}e_1\right)^2}} - \frac{\kappa \left(z_i + c_{31}e_0 + c_{32}e_1\right)}{m} + A\Omega^2 \cos(\Omega \left(t + c_{30}\delta t\right)) - g \right) \tag{C.22}$$

$$a_3 = \delta t \left(X_i + c_{41}b_0 + c_{42}b_1 + c_{43}b_2\right) \tag{C.23}$$

$$b_3 = \delta t \left(\frac{\kappa l_0 \left(x_i + c_{41}a_0 + c_{42}a_1 + c_{43}a_2\right)}{m} \Big(\left(x_i + c_{41}a_0 + c_{42}a_1 + c_{43}a_2\right)^2 + \left(y_i + c_{41}c_0 + c_{42}c_1 + c_{43}c_2\right)^2 + \left(z_i + c_{41}e_0 + c_{42}e_1 + c_{43}e_2\right)^2 \Big)^{-\frac{1}{2}} - \frac{\kappa \left(x_i + c_{41}a_0 + c_{42}a_1 + c_{43}a_2\right)}{m} \right) \tag{C.24}$$

$$c_3 = \delta t \left(Y_i + c_{41}d_0 + c_{42}d_1 + c_{43}d_2\right) \tag{C.25}$$

$$\begin{aligned} d_3 =&\delta t\Bigg(\frac{\kappa l_0\left(y_i + c_{41}c_0 + c_{42}c_1 + c_{43}c_2\right)}{m}\Bigg(\left(x_i + c_{41}a_0 + c_{42}a_1 + c_{43}a_2\right)^2 \\ &+ \left(y_i + c_{41}c_0 + c_{42}c_1 + c_{43}c_2\right)^2 + \left(z_i + c_{41}e_0 + c_{42}e_1 + c_{43}e_2\right)^2\Bigg)^{-\frac{1}{2}} \\ &- \frac{\kappa\left(y_i + c_{41}c_0 + c_{42}c_1 + c_{43}c_2\right)}{m}\Bigg) \end{aligned} \tag{C.26}$$

$$e_3 = \delta t\left(Z_i + c_{41}f_0 + c_{42}f_1 + c_{43}f_2\right) \tag{C.27}$$

$$\begin{aligned} f_3 =&\delta t\Bigg(\frac{\kappa l_0\left(z_i + c_{41}e_0 + c_{42}e_1 + c_{43}e_2\right)}{m}\Bigg(\left(x_i + c_{41}a_0 + c_{42}a_1 + c_{43}a_2\right)^2 \\ &+ \left(y_i + c_{41}c_0 + c_{42}c_1 + c_{43}c_2\right)^2 + \left(z_i + c_{41}e_0 + c_{42}e_1 + c_{43}e_2\right)^2\Bigg)^{-\frac{1}{2}} \\ &- \frac{\kappa\left(z_i + c_{41}e_0 + c_{42}e_1 + c_{43}e_2\right)}{m} + A\Omega^2\cos(\Omega\left(t + c_{40}\delta t\right)) - g\Bigg) \end{aligned} \tag{C.28}$$

$$a_4 = \delta t\left(X_i + c_{51}b_0 + c_{52}b_1 + c_{53}b_2 + c_{54}b_3\right) \tag{C.29}$$

$$\begin{aligned} b_4 =&\delta t\Bigg(\frac{\kappa l_0\left(x_i + c_{51}a_0 + c_{52}a_1 + c_{53}a_2 + c_{54}a_3\right)}{m}\Bigg(\left(x_i + c_{51}a_0 + c_{52}a_1 + c_{53}a_2 + c_{54}a_3\right)^2 \\ &+ \left(y_i + c_{51}c_0 + c_{52}c_1 + c_{53}c_2 + c_{54}c_3\right)^2 + \left(z_i + c_{51}e_0 + c_{52}e_1 + c_{53}e_2 + c_{54}e_3\right)^2\Bigg)^{-\frac{1}{2}} \\ &- \frac{\kappa\left(x_i + c_{51}a_0 + c_{52}a_1 + c_{53}a_2 + c_{54}a_3\right)}{m}\Bigg) \end{aligned} \tag{C.30}$$

$$c_4 = \delta t\left(Y_i + c_{51}d_0 + c_{52}d_1 + c_{53}d_2 + c_{54}d_3\right) \tag{C.31}$$

$$
\begin{aligned}
d_4 =&\delta t\Bigg(\frac{\kappa l_0\left(y_i + c_{51}c_0 + c_{52}c_1 + c_{53}c_2 + c_{54}c_3\right)}{m} \\
&\times\Bigg(\left(x_i + c_{51}a_0 + c_{52}a_1 + c_{53}a_2 + c_{54}a_3\right)^2 + \\
&\left(y_i + c_{51}c_0 + c_{52}c_1 + c_{53}c_2 + c_{54}c_3\right)^2 + \left(z_i + c_{51}e_0 + c_{52}e_1 + c_{53}e_2 + c_{54}e_3\right)^2\Bigg)^{-\frac{1}{2}} \\
&- \frac{\kappa\left(y_i + c_{51}c_0 + c_{52}c_1 + c_{53}c_2 + c_{54}c_3\right)}{m}\Bigg)
\end{aligned}
\tag{C.32}
$$

$$
e_4 = \delta t\left(Z_i + c_{51}f_0 + c_{52}f_1 + c_{53}f_2 + c_{54}f_3\right) \tag{C.33}
$$

$$
\begin{aligned}
f_4 =&\delta t\Bigg(\frac{\kappa l_0\left(z_i + c_{51}e_0 + c_{52}e_1 + c_{53}e_2 + c_{54}e_3\right)}{m} \\
&\times\Bigg(\left(x_i + c_{51}a_0 + c_{52}a_1 + c_{53}a_2 + c_{54}a_3\right)^2 \\
&+ \left(y_i + c_{51}c_0 + c_{52}c_1 + c_{53}c_2 + c_{54}c_3\right)^2 + \left(z_i + c_{51}e_0 + c_{52}e_1 + c_{53}e_2 + c_{54}e_3\right)^2\Bigg)^{-\frac{1}{2}} \\
&- \frac{\kappa\left(z_i + c_{51}e_0 + c_{52}e_1 + c_{53}e_2 + c_{54}e_3\right)}{m} + A\Omega^2\cos(\Omega\left(t + c_{50}\delta t\right)) - g\Bigg)
\end{aligned}
\tag{C.34}
$$

$$
a_5 = \delta t\left(X_i + c_{61}b_0 + c_{62}b_1 + c_{63}b_2 + c_{64}b_3 + c_{65}b_4\right) \tag{C.35}
$$

$$
\begin{aligned}
b_5 =&\delta t\Bigg(\frac{\kappa l_0\left(x_i + c_{61}a_0 + c_{62}a_1 + c_{63}a_2 + c_{64}a_3 + c_{65}a_4\right)}{m} \\
&\Bigg(\left(x_i + c_{61}a_0 + c_{62}a_1 + c_{63}a_2 + c_{64}a_3 + c_{65}a_4\right)^2 \\
&+ \left(y_i + c_{61}c_0 + c_{62}c_1 + c_{63}c_2 + c_{64}c_3 + c_{65}c_4\right)^2 \\
&+ \left(z_i + c_{61}e_0 + c_{62}e_1 + c_{63}e_2 + c_{64}e_3 + c_{65}e_4\right)^2\Bigg)^{-\frac{1}{2}} \\
&- \frac{\kappa\left(x_i + c_{61}a_0 + c_{62}a_1 + c_{63}a_2 + c_{64}a_3 + c_{65}a_4\right)}{m}\Bigg)
\end{aligned}
\tag{C.36}
$$

$$c_5 = \delta t \left(Y_i + c_{61} d_0 + c_{62} d_1 + c_{63} d_2 + c_{64} d_3 + c_{65} d_4 \right) \tag{C.37}$$

$$\begin{aligned} d_5 = & \delta t \Bigg(\frac{\kappa l_0 \left(y_i + c_{61} c_0 + c_{62} c_1 + c_{63} c_2 + c_{64} c_3 + c_{65} c_4 \right)}{m} \\ & \Big(\left(x_i + c_{61} a_0 + c_{62} a_1 + c_{63} a_2 + c_{64} a_3 + c_{65} a_4 \right)^2 \\ & + \left(y_i + c_{61} c_0 + c_{62} c_1 + c_{63} c_2 + c_{64} c_3 + c_{65} c_4 \right)^2 \\ & + \left(z_i + c_{61} e_0 + c_{62} e_1 + c_{63} e_2 + c_{64} e_3 + c_{65} e_4 \right)^2 \Big)^{-\frac{1}{2}} \\ & - \frac{\kappa \left(y_i + c_{61} c_0 + c_{62} c_1 + c_{63} c_2 + c_{64} c_3 + c_{65} c_4 \right)}{m} \Bigg) \end{aligned} \tag{C.38}$$

$$e_5 = \delta t \left(Z_i + c_{61} f_0 + c_{62} f_1 + c_{63} f_2 + c_{64} f_3 + c_{65} f_4 \right) \tag{C.39}$$

$$\begin{aligned} f_5 = & \delta t \Bigg(\frac{\kappa l_0 \left(z_i + c_{61} e_0 + c_{62} e_1 + c_{63} e_2 + c_{64} e_3 + c_{65} e_4 \right)}{m} \\ & \Big(\left(x_i + c_{61} a_0 + c_{62} a_1 + c_{63} a_2 + c_{64} a_3 + c_{65} a_4 \right)^2 \\ & + \left(y_i + c_{61} c_0 + c_{62} c_1 + c_{63} c_2 + c_{64} c_3 + c_{65} c_4 \right)^2 \\ & + \left(z_i + c_{61} e_0 + c_{62} e_1 + c_{63} e_2 + c_{64} e_3 + c_{65} e_4 \right)^2 \Big)^{-\frac{1}{2}} \\ & - \frac{\kappa \left(z_i + c_{61} e_0 + c_{62} e_1 + c_{63} e_2 + c_{64} e_3 + c_{65} e_4 \right)}{m} \\ & + A\Omega^2 \cos(\Omega \left(t + c_{60} \delta t \right)) - g \Bigg) \end{aligned} \tag{C.40}$$

We now have all of the components necessary to calculate the next time step. For this methodology we need both the fourth and fifth order approximations.

$$x_{i+1} = x + y_{c1} a_0 + y_{c3} a_2 + y_{c4} a_3 + y_{c5} a_4 \tag{C.41}$$

$$x_{\text{error}(i+1)} = x + z_{c1}a_0 + z_{c3}a_2 + z_{c4}a_3 + z_{c5}a_4 + z_{c6}a_5 \tag{C.42}$$

$$\left(\frac{\partial x}{\partial t}\right)_{i+1} = \frac{\partial x}{\partial t} + y_{c1}b_0 + y_{c3}b_2 + y_{c4}b_3 + y_{c5}b_4 \tag{C.43}$$

$$\left(\frac{\partial x}{\partial t}\right)_{\text{error}(i+1)} = \frac{\partial x}{\partial t} + z_{c1}b_0 + z_{c3}b_2 + z_{c4}b_3 + z_{c5}b_4 + z_{c6}b_5 \tag{C.44}$$

$$y_{i+1} = y + y_{c1}c_0 + y_{c3}c_2 + y_{c4}c_3 + y_{c5}c_4 \tag{C.45}$$

$$y_{\text{error}(i+1)} = y + z_{c1}c_0 + z_{c3}c_2 + z_{c4}c_3 + z_{c5}c_4 + z_{c6}c_5 \tag{C.46}$$

$$\left(\frac{\partial y}{\partial t}\right)_{i+1} = \frac{\partial y}{\partial t} + y_{c1}d_0 + y_{c3}d_2 + y_{c4}d_3 + y_{c5}d_4 \tag{C.47}$$

$$\left(\frac{\partial y}{\partial t}\right)_{\text{error}(i+1)} = \frac{\partial y}{\partial t} + z_{c1}d_0 + z_{c3}d_2 + z_{c4}d_3 + z_{c5}d_4 + z_{c6}d_5 \tag{C.48}$$

$$z_{i+1} = z + y_{c1}e_0 + y_{c3}e_2 + y_{c4}e_3 + y_{c5}e_4 \tag{C.49}$$

$$z_{\text{error}(i+1)} = z + z_{c1}e_0 + z_{c3}e_2 + z_{c4}e_3 + z_{c5}e_4 + z_{c6}e_5 \tag{C.50}$$

$$\left(\frac{\partial z}{\partial t}\right)_{i+1} = \frac{\partial z}{\partial t} + y_{c1}f_0 + y_{c3}f_2 + y_{c4}f_3 + y_{c5}f_4 \tag{C.51}$$

$$\left(\frac{\partial z}{\partial t}\right)_{\text{error}(i+1)} = \frac{\partial z}{\partial t} + z_{c1}f_0 + z_{c3}f_2 + z_{c4}f_3 + z_{c5}f_4 + z_{c6}f_5 \tag{C.52}$$

We then take the difference between the iterated function and the error approximator for each equation. If this difference falls outside of the established error range, then the time step is either decreased or increased, and the whole step is repeated until it does fall within an acceptable range. Sometimes a system may vary so rapidly that the result is wildly outside the accepted error range, and it can be helpful to set a minimum acceptable time step so that the simulation may still progress, but with the caveat that results might not be that accurate.

Appendix D

Equations of motion in Cartesian coordinates

We start with the Lagrangian of the system in three dimensions with driving in multiple directions,

$$\begin{aligned} L = \frac{m}{2}\left[\left(\frac{\partial x}{\partial t}\right)^2 + \left(\frac{\partial y}{\partial t}\right)^2 + \left(\frac{\partial z}{\partial t}\right)^2\right] - mz\left(g - A_z\Omega_z^2\cos\left(\Omega_z t\right)\right) \\ +mxA_x\Omega_x^2\cos(\Omega_x t) + myA_y\Omega_y^2\cos(\Omega_y t) - \frac{\kappa}{2}\left(\sqrt{x^2+y^2+z^2} - l_0\right)^2 \end{aligned} \tag{D.1}$$

Applying Lagrangian mechanics to the system.

$$\frac{\partial}{\partial t}\frac{\partial L}{\partial \dot{x}} - \frac{\partial L}{\partial x} = 0 \tag{D.2}$$

$$\frac{\partial}{\partial t}\frac{\partial L}{\partial \dot{y}} - \frac{\partial L}{\partial y} = 0 \tag{D.3}$$

$$\frac{\partial}{\partial t}\frac{\partial L}{\partial \dot{z}} - \frac{\partial L}{\partial z} = 0 \tag{D.4}$$

Substituting in our Lagrangian we get the following equations,

$$\ddot{x} = \frac{\kappa l_0 x}{m\sqrt{x^2+y^2+z^2}} - \frac{\kappa x}{m} + A_x\Omega_x^2\cos(\Omega_x t) \tag{D.5}$$

$$\ddot{y} = \frac{\kappa l_0 y}{m\sqrt{x^2+y^2+z^2}} - \frac{\kappa y}{m} + A_y\Omega_y^2\cos(\Omega_y t) \tag{D.6}$$

$$\ddot{z} = \frac{\kappa l_0 z}{m\sqrt{x^2+y^2+z^2}} - \frac{\kappa z}{m} + A_z\Omega_z^2\cos(\Omega_z t) - g \tag{D.7}$$

Setting tolerance bounds and ascertaining whether or not the difference between the fourth and fifth-order approximation falls outside of these bands can be used to adjust the time step. For instance, if we found that the difference between the fourth and fifth-order approximation was greater than our tolerance threshold, we can half the time step and repeat the simulation over this new time step. Similarly, if all fall below our tolerance bound, the time step may be doubled to ensure simulation run times are as short as possible.

Bibliography

[1] M. Planck, "Über das gesetz der energieverteilung im normalspectrum," *Annalen der Physik*, vol. 309, no. 3, p. 553–563, 1901.

[2] A. Einstein, "Über einen die erzeugung und verwandlung des lichtes betreffenden heuristischen gesichtspunkt," *Annalen der Physik*, vol. 322, no. 6, p. 132–148, 1905.

[3] L. de Broglie, "Waves and quanta," *Nature*, vol. 112, no. 2815, p. 540–540, 1923.

[4] W. Heisenberg, "Über quantentheoretische umdeutung kinematischer und mechanischer beziehungen.," *Zeitschrift für Physik*, vol. 33, no. 1, p. 879–893, 1925.

[5] M. Born and P. Jordan, "Zur quantenmechanik," *Zeitschrift für Physik*, vol. 34, no. 1, p. 858–888, 1925.

[6] M. Born, W. Heisenberg, and P. Jordan, "Zur quantenmechanik. ii.," *Zeitschrift für Physik*, vol. 35, no. 8-9, p. 557–615, 1926.

[7] E. Schrödinger, "Quantisierung als eigenwertproblem," *Annalen der Physik*, vol. 386, no. 18, p. 109–139, 1926.

[8] W. Heisenberg, "Über den anschaulichen inhalt der quantentheoretischen kinematik und mechanik," *Zeitschrift für Physik*, vol. 43, no. 3-4, p. 172–198, 1927.

[9] E. H. Kennard, "Zur quantenmechanik einfacher bewegungstypen," *Zeitschrift für Physik*, vol. 44, no. 4-5, p. 326–352, 1927.

[10] H. M. Weyl, *The theory of groups and quantum mechanics*. Dover Publ., 1930.

[11] H. Igel, A. Cochard, J. Wassermann, A. Flaws, U. Schreiber, A. Velikoseltsev, and N. P. Dinh, "Broad-band observations of earthquake-induced rotational ground motions," *Geophysical Journal International*, vol. 168, no. 1, p. 182–196, 2007.

[12] J. M. McGuirk, G. T. Foster, J. B. Fixler, M. J. Snadden, and M. A. Kasevich, "Sensitive absolute-gravity gradiometry using atom interferometry," *Phys. Rev. A*, vol. 65, p. 033608, Feb 2002.

[13] A. Peters, K. Y. Chung, and S. Chu, "High-precision gravity measurements using atom interferometry," *Metrologia*, vol. 38, no. 1, p. 25–61, 2001.

[14] C. M. Will, "The confrontation between General Relativity and experiment," *Living Reviews in Relativity*, vol. 4, no. 1, p. 4, 2001.

[15] A. Wicht, E. Hensley, Joel M andSarajlic, and S. Chu, "A preliminary measurement of the finestructure constant based on atom interferometry," *Physica scripta*, vol. 2002, no. 1, pp. 82–, 2002.

[16] A. Bertoldi, G. Lamporesi, L. Cacciapuoti, M. D. Angelis, M. Fattori, T. Petelski, A. Peters, M. Prevedelli, J. Stuhler, G. M. Tino, and et al., "Atom interferometry gravity-gradiometer for the determination of the newtonian gravitational constant g," *The European Physical Journal D*, vol. 40, no. 2, p. 271–279, 2006.

[17] J. B. Fixler, G. T. Foster, J. M. Mcguirk, and M. A. Kasevich, "Atom interferometer measurement of the newtonian constant of gravity," *Science*, vol. 315, p. 74–77, May 2007.

[18] H. Müntinga, H. Ahlers, M. Krutzik, A. Wenzlawski, S. Arnold, D. Becker, K. Bongs, H. Dittus, H. Duncker, N. Gaaloul, C. Gherasim, E. Giese, C. Grzeschik, T. W. Hänsch, O. Hellmig, W. Herr, S. Herrmann, E. Kajari,

S. Kleinert, C. Lämmerzahl, W. Lewoczko-Adamczyk, J. Malcolm, N. Meyer, R. Nolte, A. Peters, M. Popp, J. Reichel, A. Roura, J. Rudolph, M. Schiemangk, M. Schneider, S. T. Seidel, K. Sengstock, V. Tamma, T. Valenzuela, A. Vogel, R. Walser, T. Wendrich, P. Windpassinger, W. Zeller, T. van Zoest, W. Ertmer, W. P. Schleich, and E. M. Rasel, "Interferometry with Bose-Einstein condensates in microgravity," *Physical Review Letters*, vol. 110, p. 093602, Feb 2013.

[19] T. van Zoest, N. Gaaloul, Y. Singh, H. Ahlers, W. Herr, S. T. Seidel, W. Ertmer, E. Rasel, M. Eckart, E. Kajari, S. Arnold, G. Nandi, W. P. Schleich, R. Walser, A. Vogel, K. Sengstock, K. Bongs, W. Lewoczko-Adamczyk, M. Schiemangk, T. Schuldt, A. Peters, T. Könemann, H. Müntinga, C. Lämmerzahl, H. Dittus, T. Steinmetz, T. W. Hänsch, and J. Reichel, "Bose-Einstein Condensation in microgravity," *Science*, vol. 328, no. 5985, pp. 1540–1543, 2010.

[20] R. Geiger, V. Ménoret, G. Stern, N. Zahzam, P. Cheinet, B. Battelier, A. Villing, F. Moron, M. Lours, Y. Bidel, A. Bresson, A. Landragin, and P. Bouyer, "Detecting inertial effects with airborne matter-wave interferometry," *Nature communications*, vol. 2, no. 1, pp. 474–474, 2011.

[21] J. F. Schaff, T. Langen, and J. Schmiedmayer, "Interferometry with atoms," 2015.

[22] T. L. Gustavson, A. Landragin, and M. A. Kasevich, "Rotation sensing with a dual atom-interferometer Sagnac gyroscope," *Classical and Quantum Gravity*, vol. 17, p. 2385–2398, Aug 2000.

[23] K. Jiang, H. Lee, C. C. Gerry, and J. P. Dowling, "Super-resolving quantum radar: Coherent-state sources with homodyne detection suffice to beat the diffraction limit," *The Rochester Conferences on Coherence and Quantum Optics and the Quantum Information and Measurement meeting*, 2013.

[24] M. Lanzagorta, "Quantum radar," *Synthesis Lectures on Quantum Computing*, vol. 3, no. 1, p. 1–139, 2011.

[25] M. Taylor, "Biological measurement beyond the quantum limit," *Quantum Microscopy of Biological Systems*, p. 143–151, 2015.

[26] M. A. Taylor and W. P. Bowen, "Quantum metrology and its application in biology," *Physics Reports*, vol. 615, p. 1–59, 2016.

[27] Bose, "Plancks gesetz und lichtquantenhypothese," *Zeitschrift für Physik*, vol. 26, no. 1, p. 178–181, 1924.

[28] S. Bose, "Planck's law and the light quantum hypothesis," *Journal of Astrophysics and Astronomy*, vol. 15, no. 1, p. 3–7, 1994.

[29] A. Einstein, *Quantentheorie des einatomigen idealen Gases*. John Wiley Sons, Ltd, 2005.

[30] M. H. Anderson, J. R. Ensher, M. R. Matthews, C. E. Wieman, and E. A. Cornell, "Observation of Bose-Einstein Condensation in a dilute atomic vapor," *Science*, vol. 269, no. 5221, p. 198–201, 1995.

[31] K. B. Davis, M. O. Mewes, M. R. Andrews, N. J. van Druten, D. S. Durfee, D. M. Kurn, and W. Ketterle, "Bose-Einstein Condensation in a gas of sodium atoms," *Physical Review Letters*, vol. 75, pp. 3969–3973, Nov 1995.

[32] C. Cohen-Tannoudji and D. Guery-Odelin, *Advances in atomic physics: An overview*. World Scientific, 2011.

[33] S. Chu, "Nobel lecture: The manipulation of neutral particles," *Reviews of Modern Physics*, vol. 70, no. 3, p. 685–706, 1998.

[34] C. N. Cohen-Tannoudji, "Nobel lecture: Manipulating atoms with photons," *Reviews of Modern Physics*, vol. 70, no. 3, p. 707–719, 1998.

[35] W. D. Phillips, "Nobel lecture: Laser cooling and trapping of neutral atoms," *Reviews of Modern Physics*, vol. 70, no. 3, p. 721–741, 1998.

[36] A. Roy and D. Angom, "Finite temperature expansion dynamics of Bose–Einstein condensates in ring traps," *Physics Letters A*, vol. 381, no. 31, p. 2483–2488, 2017.

[37] A. Roy and D. Angom, "Ramifications of topology and thermal fluctuations in quasi-2d condensates," *Journal of Physics B: Atomic, Molecular and Optical Physics*, vol. 50, no. 22, p. 225301, 2017.

[38] L. A. Toikka, "Self-interference of a toroidal Bose–Einstein condensate," *New Journal of Physics*, vol. 16, no. 4, p. 043011, 2014.

[39] C. Ryu, K. C. Henderson, and M. G. Boshier, "Creation of matter wave Bessel beams and observation of quantized circulation in a Bose–Einstein Condensate," *New Journal of Physics*, vol. 16, no. 1, p. 013046, 2014.

[40] A. Stephenson, "On induced stability," *The London, Edinburgh, and Dublin Philosophical Magazine and Journal of Science*, vol. 15, no. 86, pp. 233–236, 1908.

[41] P. Kapitza, "Dynamic stability of a pendulum when its point of suspension vibrates," *Soviet Phys. JETP*, vol. 21, p. 588–597, 1951.

[42] C. F. Squire, "Collected papers of P. L. Kapitza, vol ii: 1938–1964," *Journal of the Franklin Institute*, vol. 282, p. 263, Oct 1966.

[43] L. D. Landau and E. M. Lifshits, *Mechanics*. Pergamon, 1960.

[44] F. M. Phelps and J. H. Hunter, "An analytical solution of the inverted pendulum," *American Journal of Physics*, vol. 33, p. 285–295, Apr 1965.

[45] E. Butikov, "On the optical path length in refracting media," *Citation: American Journal of Physics*, vol. 86, p. 268, 2018.

[46] J. A. Blackburn, H. J. T. Smith, and N. Gronbech-Jensen, "Stability and hopf bifurcations in an inverted pendulum," *American Journal of Physics*, vol. 60, p. 903–908, Oct 1992.

[47] C. E. Mazzilli, "A theoretical and experimental analysis of support-excited non-linear vibrations of the extensible pendulum," *IMA Journal of Applied Mathematics*, vol. 34, no. 2, p. 137–154, 1985.

[48] A. Arinstein and M. Gitterman, "Inverted spring pendulum driven by a periodic force: linear versus nonlinear analysis," *European Journal of Physics*, vol. 29, p. 385–392, Feb 2008.

[49] G. Ryland and L. Meirovitch, "Stability boundaries of a swinging spring with oscillating support," *Journal of Sound and Vibration*, vol. 51, no. 4, p. 547–560, 1977.

[50] A. L. Migdall, J. V. Prodan, W. D. Phillips, T. H. Bergeman, and H. J. Metcalf, "First observation of magnetically trapped neutral atoms," *Physical Review Letters*, vol. 54, no. 24, p. 2596–2599, 1985.

[51] H. Perrin and B. M. Garraway, "Trapping atoms with radio frequency adiabatic potentials," *Advances In Atomic, Molecular, and Optical Physics*, p. 181–262, 2017.

[52] O. Morizot, C. L. Garrido Alzar, P.-E. Pottie, V. Lorent, and H. Perrin, "Trapping and cooling of rf-dressed atoms in a quadrupole magnetic field," *Journal of Physics B: Atomic, Molecular and Optical Physics*, vol. 40, no. 20, p. 4013–4022, 2007.

[53] K. Merloti, R. Dubessy, L. Longchambon, A. Perrin, P.-E. Pottie, V. Lorent, and H. Perrin, "A two-dimensional quantum gas in a magnetic trap," *New Journal of Physics*, vol. 15, no. 3, p. 033007, 2013.

[54] A. Vitt and G. Gorelik, "Oscillations of an elastic pendulum as an example of the oscillations of two parametrically coupled linear systems," *Zhurnal Tekhniceskoj Fiziki*, vol. 3, no. 2-3, pp. 294–307, 1933.

[55] M. G. Rusbridge, "Motion of the sprung pendulum," *American Journal of Physics*, vol. 48, no. 2, p. 146–151, 1980.

[56] J. H. Heinbockel and R. A. Struble, "Resonant oscillations of an extensible pendulum," *Zeitschrift für angewandte Mathematik und Physik ZAMP*, vol. 14, no. 3, p. 262–269, 1963.

[57] R. Carretero-Gonzalez, H. N. Nunez-Yepez, and A. L. Salas-Brito, "Regular and chaotic behaviour in an extensible pendulum," *European Journal of Physics*, vol. 15, no. 3, p. 139–148, 1994.

[58] E. P. Gross, "Structure of a quantized vortex in Boson systems," *Il Nuovo Cimento*, vol. 20, no. 3, p. 454–477, 1961.

[59] O. Carnal and J. Mlynek, "Young's double-slit experiment with atoms: A simple atom interferometer," *Physical Review Letters*, vol. 66, no. 21, p. 2689–2692, 1991.

[60] M. Kasevich and S. Chu, "Atomic interferometry using stimulated Raman transitions," *Physical Review Letters*, vol. 67, no. 2, p. 181–184, 1991.

[61] D. W. Keith, C. R. Ekstrom, Q. A. Turchette, and D. E. Pritchard, "An interferometer for atoms," *Physical Review Letters*, vol. 66, pp. 2693–2696, May 1991.

[62] E. Schwartz, "Sagnac effect in an off-center rotating ring frame of reference," *European Journal of Physics*, vol. 38, no. 1, p. 015301, 2016.

[63] R. B. Hurst, J.-P. R. Wells, and G. E. Stedman, "An elementary proof of the geometrical dependence of the Sagnac effect," *Journal of Optics A: Pure and Applied Optics*, vol. 9, no. 10, p. 838–841, 2007.

[64] T. Fernholz, R. Gerritsma, P. Krüger, and R. J. C. Spreeuw, "Dynamically controlled toroidal and ring-shaped magnetic traps," *Physical Review A*, vol. 75, no. 6, 2007.

[65] I. Lesanovsky and W. V. Klitzing, "Time-Averaged Adiabatic potentials: Versatile matter-wave guides and atom traps," *Physical Review Letters*, vol. 99, no. 8, 2007.

[66] K. Henderson, C. Ryu, C. Maccormick, and M. G. Boshier, "Experimental demonstration of painting arbitrary and dynamic potentials for Bose–Einstein condensates," *New Journal of Physics*, vol. 11, no. 4, p. 043030, 2009.

[67] A. Ramanathan, K. C. Wright, S. R. Muniz, M. Zelan, W. T. Hill, 3rd, C. J. Lobb, K. Helmerson, W. D. Phillips, and G. K. Campbell, "Superflow in a toroidal Bose-Einstein condensate: an atom circuit with a tunable weak link," *Physical Review Letters*, vol. 106, no. 13, pp. 130401–130401, 2011.

[68] S. Beattie, S. Moulder, R. J. Fletcher, and Z. Hadzibabic, "Persistent currents in spinor condensates," *Physical Review Letters*, vol. 110, no. 2, pp. 025301–025301, 2013.

[69] W. H. Heathcote, E. Nugent, B. T. Sheard, and C. J. Foot, "A ring trap for ultracold atoms in an rf-dressed state," *New Journal of Physics*, vol. 10, p. 043012, Oct 2008.

[70] G. E. Marti, R. Olf, and D. M. Stamper-Kurn, "Collective excitation interferometry with a toroidal Bose-Einstein condensate," *Physical Review. A, Atomic, molecular, and optical physics*, vol. 91, no. 1, 2015.

[71] J. A. Sauer, M. D. Barrett, and M. S. Chapman, "Storage ring for neutral atoms," *Physical Review Letters*, vol. 87, no. 27 Pt 1, pp. 270401–270401, 2001.

[72] A. S. Arnold, C. S. Garvie, and E. Riis, "Large magnetic storage ring for Bose-Einstein condensates," *Physical Review. A, Atomic, molecular, and optical physics*, vol. 73, no. 4, 2006.

[73] P. Navez, S. Pandey, H. Mas, K. Poulios, T. Fernholz, and W. V. Klitzing, "Matter-wave interferometers using TAAP rings," *New Journal of Physics*, vol. 18, no. 7, p. 075014, 2016.

[74] S. Pandey, H. Mas, G. Drougakis, P. Thekkeppatt, V. Bolpasi, G. Vasilakis, K. Poulios, and W. V. Klitzing, "Hypersonic Bose–Einstein condensates in accelerator rings," *Nature*, vol. 570, no. 7760, p. 205–209, 2019.

[75] O. Zobay and B. M. Garraway, "Atom trapping and two-dimensional Bose-Einstein condensates in field-induced adiabatic potentials," *Physical Review. A, Atomic, molecular, and optical physics*, vol. 69, no. 2, 2004.

[76] N. Lundblad, R. A. Carollo, C. Lannert, M. J. Gold, X. Jiang, D. Paseltiner, N. Sergay, and D. C. Aveline, "Shell potentials for microgravity Bose–Einstein condensates," *npj Microgravity*, vol. 5, no. 1, p. 30, 2019.

[77] "Cold atom laboratory." `https://coldatomlab.jpl.nasa.gov/`.

[78] C. Lannert, T.-C. Wei, and S. Vishveshwara, "Dynamics of condensate shells: Collective modes and expansion," *Physical Review A*, vol. 75, p. 013611, Oct 2007.

[79] A. Tononi and L. Salasnich, "Bose-Einstein condensation on the surface of a sphere," *Physical Review Letters*, vol. 123, no. 16, p. 160403, 2019.

[80] K. Padavić, K. Sun, C. Lannert, and S. Vishveshwara, "Physics of hollow Bose-Einstein condensates," *EPL (Europhysics Letters)*, vol. 120, p. 20004, Jan 2017.

[81] J. A. C. Weideman and B. M. Herbst, "Split-Step Methods for the Solution of the Nonlinear Schrödinger Equation," *SIAM Journal on Numerical Analysis*, vol. 23, no. 3, p. 485–507, 1986.

[82] J. Janszky, P. Domokos, and P. Adam, "Coherent states on a circle and quantum interference," *Phys. Rev. A*, vol. 48, pp. 2213–2219, Sep 1993.

[83] R. E. Gaunt, "Inequalities for modified Bessel functions and their integrals," *Journal of Mathematical Analysis and Applications*, vol. 420, no. 1, pp. 373–386, 2014.

[84] W. Lewoczko-Adamczyk, A. Peters, T. V. Zoest, E. Rasel, W. Ertmer, A. Vogel, S. Wildfang, G. Johannsen, K. Bongs, K. Sengstock, and et al., "Rubidium Bose–Einstein condensate under microgravity," *International Journal of Modern Physics D*, vol. 16, no. 12b, p. 2447–2454, 2007.

[85] C. Lotz, T. Froböse, A. Wanner, L. Overmeyer, and W. Ertmer, "Einstein-elevator: A new facility for research from g to 5 g," *Gravitational and Space Research*, vol. 5, no. 2, p. 11–27, 2017.

[86] B. Barrett, L. Antoni-Micollier, L. Chichet, B. Battelier, T. Lévèque, A. Landragin, and P. Bouyer, "Dual matter-wave inertial sensors in weightlessness," *Nature Communications*, vol. 7, no. 1, pp. 13786–13786, 2016.

[87] W. Bao and Q. Du, "Computing the ground state solution of Bose–Einstein condensates by a normalized gradient flow," *SIAM Journal on Scientific Computing*, vol. 25, no. 5, p. 1674–1697, 2004.

[88] G. Strang, "On the construction and comparison of difference schemes," *SIAM Journal on Numerical Analysis*, vol. 5, no. 3, p. 506–517, 1968.

[89] R. Deiterding, R. Glowinski, H. Oliver, and S. Poole, "A reliable split-step fourier method for the propagation equation of ultra-fast pulses in single-mode optical fibers," *Journal of Lightwave Technology*, vol. 31, no. 12, p. 2008–2017, 2013.

[90] R. Jozsa, "Fidelity for mixed quantum states," *Journal of Modern Optics*, vol. 41, no. 12, p. 2315–2323, 1994.

[91] P. Pitaevskii, L, "Vortex lines in an imperfect Bose gas," *Soviet Physics Jetp*, vol. 13, p. 451–454, Aug 1961.

[92] V. Fock, "Näherungsmethode zur lösung des quantenmechanischen mehrkörperproblems," *Zeitschrift für Physik*, vol. 61, no. 1-2, p. 126–148, 1930.

[93] M. Egorov, B. Opanchuk, P. Drummond, B. V. Hall, P. Hannaford, and A. I. Sidorov, "Measurement of s-wave scattering lengths in a two-component Bose-Einstein condensate," *Physical Review A*, vol. 87, no. 5, p. 053614, 2013.

[94] C. Pethick and H. Smith, *Bose-Einstein condensation in dilute gases*. Cambridge University Press, 2008.

[95] P. G. Kevrekidis, D. J. Frantzeskakis, and R. Carretero-González, *Emergent nonlinear phenomena in Bose-Einstein condensates: theory and experiment*, vol. 45. Springer, 2008.

[96] V. E. Zakharov and A. B. Shabat, "Exact Theory of Two-dimensional Self-focusing and One-dimensional Self-modulation of Waves in Nonlinear Media," *Soviet Journal of Experimental and Theoretical Physics*, vol. 34, p. 62, Jan. 1972.

[97] L. H. Thomas, "The calculation of atomic fields," *Mathematical Proceedings of the Cambridge Philosophical Society*, vol. 23, no. 5, p. 542–548, 1927.

[98] E. Fermi, "Un metodo statistico per la determinazione di alcune priorieta dell'atome," *Rend. Accad. Naz. Lincei*, vol. 6, no. 602-607, p. 32, 1927.

[99] N. Bogoliubov, "On the theory of superfluidity," *J. Phys*, vol. 11, no. 1, p. 23, 1947.

[100] P. Lynch, "Resonant motions of the three-dimensional elastic pendulum," *International Journal of Non-Linear Mechanics*, vol. 37, p. 345–367, 2002.

[101] L. Meirovitch, *Methods of analytical dynamics*. McGraw-Hill, 1970.

[102] F. W. J. Olver, D. W. Lozier, R. F. Boisvert, C. W. Clark, N. I. O. Standards, and Technology, *NIST handbook of mathematical functions*. Cambridge New York Melbourne Cambridge University Press Cambridge New York Melbourne Cambridge University Press, 2010.

[103] J. H. E. Cartwright and O. Piro, "The dynamics of Runge-Kutta methods," *Int. J. Bifurcation and Chaos*, vol. 2, pp. 427–49, 1992.

[104] E. Fehlberg, *Low-order classical Runge-Kutta formulas with stepsize control and their application to some heat transfer problems*. National Aeronautics And Space Administration, 1969.

[105] "Even Mathieu function: Series representations (subsection 06/01/03)." `https://functions.wolfram.com/MathieuandSpheroidalFunctions/MathieuC/06/01/03/`.

[106] "Characteristic value of an even Mathieu function: Series representations (subsection 06/01/01)." `https://functions.wolfram.com/MathieuandSpheroidalFunctions/MathieuCharacteristicA/06/01/01/`.

[107] D. E. Pritchard, "Cooling neutral atoms in a magnetic trap for precision spectroscopy," *Physical Review Letters*, vol. 51, no. 15, p. 1336–1339, 1983.

[108] M. Gildemeister, E. Nugent, B. E. Sherlock, M. Kubasik, B. T. Sheard, and C. J. Foot, "Trapping ultracold atoms in a time-averaged adiabatic potential," *Physical Review A*, vol. 81, no. 3, p. 031402, 2010.

[109] B. E. Sherlock, M. Gildemeister, E. Owen, E. Nugent, and C. J. Foot, "Time-averaged adiabatic ring potential for ultracold atoms," *Physical Review A*, vol. 83, no. 4, 2011.

[110] M. Gildemeister, *Trapping ultracold atoms in time-averaged adiabatic potentials*. PhD thesis, Oxford University, 2010.

[111] W. Pauli and C. P. Enz, *Pauli lectures on physics. vol. 5: Wave mechanics.* Cambridge, 1973.

[112] J.-M. Martin, *An atomchip gyro: theory and experiment.* PhD thesis, University of Sussex, June 2020.